UNIVERSITY OF CALIFORNIA
RIVERSIDE

An Investigation of Surface and Crown Fire Dynamics in Shrub Fuels

A Dissertation submitted in partial satisfaction
of the requirements for the degree of

Doctor of Philosophy

in

Mechanical Engineering

by

Jesse Sandoval Lozano

August 2011

Dissertation Committee:
Dr. Shankar Mahalingam, Chairperson
Dr. David Weise
Dr. Marko Princevac

Copyright by
Jesse Sandoval Lozano
2011

The Dissertation of Jesse Sandoval Lozano is approved:

_____

_____

_____
Committee Chairperson

University of California, Riverside

Acknowledgements

There as many people I would like to thank and acknowledge without whom this would not be possible. Professor Shankar Mahalingam is the first person I would like to thank. Throughout my career as a student he has encouraged me and has been an invaluable source for guidance. When I struggled with my course work or research he was there to reassure me and provide me confidence. As an advisor he helped guide my research in the right direction while at the same time allowing me to think freely without constraint. He gave a lot of his time to review and provide valuable comments on the articles we published together and on my dissertation. I would also like to thank Dr. David Weise who provided thoughtful insight and suggestions that helped improve my experiments and overall results. He was always available when I needed guidance and also gave a lot of his time to review and provide valuable feedback on the article we published together and on my dissertation. I also want to express my appreciation and gratitude to Professor Marko Princevac for providing a wealth of knowledge and guidance in incorporating the Particle Image Velocimetry system into my experiments and for all the constructive comments he gave that improved my experiment results.

This research was made possible due to the support and sponsorship by the Department of Mechanical Engineering and agreement 06-JV-11272166-058 with the USDA Forest Service Pacific Southwest Research Station in Riverside, California.

I would like to thank Joey Chong, Physical Science Technician at the USDA Forest Service fire laboratory, for all the laboratory technical assistance and field work.

He drove me to the North Mountain Experimental Area and helped me cut and collect fuel for my experiments more times than I can remember. Joey set up all the data acquisition software which coordinated all the experiment devices and made it possible to collect all the data from the experiments that were conducted. I would also like to thank Tachajapong Watcharapong who taught me how to setup and conduct the preliminary experiments and who provided valuable assistance in conducting the numerical study. Also special thanks to Andy Amaya and Diego Villaseñor who provided valuable technical assistance when I initially started using Linux and when hardware and software problems presented themselves. Thanks to Sam Pournazeri who assisted in troubleshooting all and any problems experienced when using the Particle Image Velocimetry system. Thank you to Dallan Prince of Brigham Young University in Utah for developing and providing me an invaluable Matlab code which assisted me in analyzing portions of the collected experiment data.

Last but not least I would like to express my deep appreciation and gratitude to all the students and individuals who took time from their busy schedules to assist me in performing all the experiments: Chris Richardson, Gerardo Cervantes, David Becerra, Christian Bartolome, William Cakiraga, Ramon Rodriquez, Ambarish Dahale, Manuel Lozano, Ricardo Miranda and Hansheng Pan. Without their assistance there is no doubt that I would not have been able to complete all the experiments in the timeline I had set for this study.

Dedication

I would like to dedicate this work to my family and friends who have supported me in everything I have done. To my father, Jacinto Lozano, who from an early age taught me to be disciplined and to always work hard. He taught me how to build and repair things and through this sparked in me an intellectual curiosity. To my mother, Adela Casas, who along with my father raised me and taught me to be self reliant. Without my parents' bravery and sacrifice to migrate to the United States I would not be where I am today. I would like to thank my siblings Alex Casas, Mary Lozano, and Manuel Lozano for all their encouragement.

I am very fortunate to be where I am today and to have had the opportunities I have had. There were many people along the way that steered me in the right direction. Over the years I have learned that not many individuals are presented with the opportunities that were presented to me and so I dedicate this work to those who have not had the opportunities to fulfill their potential.

I also dedicate this work to my wife, Helen Lozano and her family. She has been at my side every step of this long journey. We have experienced the good times and the bad times together. She has given me support and confidence in my abilities and her family has provided endless encouragement.

To my friends who throughout the years have become my family and provided me a great deal of support. Humberto Madrid, Javier Ramirez, Elizabeth Gurba, Daniel Fisch, Elvira Cuevas-Fisch, Dr. Gerald Fisch, Ricardo Miranda, Rafael Garcilazo, Yiyi

Wong, Ivan Marin, Frank Garcia, Diego Villaseñor and to all those whom I have not mentioned by name but nonetheless have been part of this journey and contributed to this accomplishment.

ABSTRACT OF THE DISSERTATION

An Investigation of Surface and Crown Fire Dynamics in Shrub Fuels

by

Jesse Sandoval Lozano

Doctor of Philosophy, Graduate Program in Mechanical Engineering
University of California, Riverside, August 2011
Dr. Shankar Mahalingam, Chairperson

The focus of this study was on spatially segregated multiple crown fuel matrices that model the crowns of discrete shrubs. The influence of the horizontal crown separation distance between crown fuel matrices on the transition process from surface fires to crown fires and on the rate of spread of surface fires in chaparral fuels was investigated experimentally and numerically. The experiments were carried out in a 1.20 m width × 1.20 m height × 7.4 m length, open-roof wind tunnel to ensure that flame-generated buoyancy effects were not suppressed. The surface fire was initiated in a fuel bed comprised of aspen (*Populus tremuloides Michx*) excelsior that was evenly distributed over an area of 0.8 m width × 2.8 m length to a depth of 0.10 m. Crown fuel matrices were composed of live chamise (*Adenostoma fasciculatum*) held in place by two 0.6 m length × 0.3 m height × 0.8 m width wire mesh baskets, at a height of 0.35 m from the surface of the fuel bed. Crown separation distances (CSD) investigated range from 0.1 m to 0.3 m.

At a CSD of 0.1 m, as the fire front approached and ignited the downwind crown fuel matrix, the surface fire and upwind crown fires merged into a single fire. Following

ignition of the downwind crown fuel, a single merged fire, comprising the surface and two crown fires, results. At larger crown separation distances of 0.2 m and 0.3 m, the surface and upwind crown fires were segregated, appearing as two distinct fire fronts, with the ignition of the downstream crown fuel matrix occurring earlier in time for the lower CSD case. In addition, a Particle Image Velocimetry system was utilized to investigate the influence of CSD on the flow field between adjacent crown fuel matrices.

Table of Contents

1 Introduction 1

1.1 Problem Statement 1

1.2 Objectives 9

1.3 Scope 9

2 Background 10

2.1 Properties Influencing Fires Spread 10

2.2 Particle Image Velocimetry 21

2.3 Large Eddy Simulation 23

3 Experimental Setup Descriptions 28

3.1 Experiment Location 28

3.2 Wind Tunnel Setup 28

3.3 Fuel Bed Setup 34

3.4 Moisture Measurements 36

3.5 Fire Front Behavior Data 36

3.6 Particle Image Velocimetry System Arrangement 38

4 Large Eddy Simulation Setup 42

4.1 LES Model Parameters 42

5 Previous Studies 46

6 Results – Rate of Spread Analysis 55

6.1 Surface Fuel Only and Single Crown Configurations 57

6.2 Multiple Crown Fuel Configurations 79

7 Results – Particle Image Velocimetry Analysis 142

8 Results – Large Eddy Simulation 162

8.1 Surface Fire Front Rate of Spread 162

8.2 Flow Field between Crown Fuels 174

9 Conclusions and Future Work 189

9.1 Conclusions 189

9.2 Future Work 194

Bibliography 196

Appendix A 205

Appendix B 213

List of Figures

Figure 3.1: Schematic of wind tunnel showing push fan, flow conditioner section and the test section. 29

Figure 3.2: Flow characterization vertical plane showing locations above fuel bed where velocity measurements are performed. 30

Figure 3.3: Wind speed profile along the surface fuel bed length representing an average value across a vertical plane of 0.51 m wide by 1.02 m high starting at 0.10 m from fuel bed surface. 32

Figure 3.4: Wind speed profile with height above the surface fuel bed at 1.0 m from the leading edge of the fuel bed (location of the crown fuel). 33

Figure 3.5: Schematic of surface fuel bed and crown setup at a crown separation distance (CSD) of 10 cm showing location of fuel bed thermocouples (labeled TC1 thru TC10). Thermocouples are placed 2.5 cm above the surface fuel. RC01 heat flux sensor is position 0.3 m downstream of crown-two. Note: crown fuel matrices 1 and 2 are referred to as C1 and C2. The width perpendicular to the sketch is 0.8 m for the surface and crown fuel matrices. 38

Figure 3.6: Schematic showing area to be imaged using the PIV system. 41

Figure 4.1: Illustration of LES computational setup 43

Figure 5.1: Fuel bed thermocouple setup used to determine surface fire rate of spread *R*. A total of 10 thermocouples (15 cm apart). 50

Figure 5.2: Schematic of surface fuel bed with crown fuel system and appropriate dimensions. Also shown is the PIV region of interest (ROI). 50

Figure 5.3: (a) Image showing location of Nd: YAG laser which produces the vertical laser sheet that spans the length of the wind tunnel; (b) Image showing position of CCD camera used to capture PIV images to resolve the flow field within and surrounding a propagating fire front. 52

Figure 6.1: Illustration for view factors between rectangles having a common edge and forming an arbitrary angle. 61

Figure 6.2: Average rate of spread at each thermocouple location plot for a surface fuel only configuration for the three wind speed cases of: (a) 0.0 m/s; (b) 1.1 m/s; (c) 1.9 m/s; with standard deviation error bars. 62

Figure 6.3: Time evolution of surface flame depth for fuel configuration a during a wind condition of: (a) 0.0 m/s; (b) 1.1 m/s; (c) 1.9 m/s. 64

Figure 6.4: Tabulated view factor values and corresponding plot for a surface fuel only configuration at a wind condition of 0.0 m/s. Left side of plot represents leading edge of fuel bed while right side of plot represents the downstream edge of the fuel bed. 67

Figure 6.5: Surface fuel and crown 1 configuration plots for the three wind speed cases of 0.0 m/s, 1.1 m/s and 1.9 m/s of: (a) Average rate of spread at each thermocouple location; (b) Average surface fuel mass loss rate at each thermocouple location. 69

Figure 6.6: Plot of total heat flux impinging onto the surface fuel at the downstream edge of the fuel bed for a surface fuel and crown 1 configuration at a wind speed of 1.1 m/s. Note: curves for x76 (experiment 76) and x80 have been time shift to all start at the instant crown 1 ignites in x77..... 71

Figure 6.7: Plot of total heat flux impinging onto the surface fuel at the downstream edge of the fuel bed for a surface fuel only configuration at a wind speed of 1.1 m/s. Note: curves for x35 (experiment 35), x36, and x37 have been time shift. 72

Figure 6.8: Plot of total heat flux impinging onto the surface fuel at the downstream edge of the fuel bed for a surface fuel and crown 1 configuration at a wind speed of 1.9 m/s. Note: curves for x74 (experiment 74), x75, and x79 have been time shift. 73

Figure 6.9: Plot of total heat flux impinging onto the surface fuel at the downstream edge of the fuel bed for a surface fuel only configuration at a wind speed of 1.9 m/s. Note: curves for x66 (experiment 66), x71, and x72 have been time shift. 74

Figure 6.10: Surface fuel and crown 2 configuration plots for the three wind speed cases of 0.0 m/s, 1.1 m/s and 1.9 m/s of: (a) Average rate of spread at each thermocouple location; (b) Average surface fuel mass loss rate at each thermocouple location. 76

Figure 6.11: Plot of total heat flux impinging onto the surface fuel at the downstream edge of the fuel bed for a surface fuel and crown 2 configuration at a wind speed of 1.1 m/s. Note: curves for x69 (experiment 69) and x70 have been time shift. 77

Figure 6.12: Plot of total heat flux impinging onto the surface fuel at the downstream edge of the fuel bed for a surface fuel and crown 2 configuration at a wind speed of 1.9 m/s. Note: curves for x62 (experiment 62), x63 and x64 have been time shift. 78

Figure 6.13: Average rate of spread and surface fuel mass loss rate at each thermocouple location plot for a crown separation distance of 10 cm during a no wind condition. Left axis represents values for rate of spread and right axis represents values for surface fuel mass loss rate. 82

Figure 6.14: Images from experiment 23 at (a) t = 282 s at time of crown 1 ignition; (b) t = 330 s during crown 1 combustion; (c) t = 340 s at time of crown 2 ignition..... 83

Figure 6.15: Tabulated view factor values and corresponding plot for a crown 1 and crown 2 configuration for a CSD of 10 cm at a wind condition of 0.0 m/s. Left side of plot represents leading edge of fuel bed while right side of plot represents the downstream edge of the fuel bed..... 84

Figure 6.16: Plots for a surface fuel and crown 1 and two configuration at a crown separation distance of 10 cm for a no wind condition of: (a) total heat flux and convection heat flux produced during experiment 23; (b) branch and air temperature history during experiment 23; (c) total heat flux and convection heat flux produced during experiment 24; (b) branch and air temperature history during experiment 24; 85

Figure 6.17: Average rate of spread and surface fuel mass loss rate at each thermocouple location plot for a crown separation distance of 20 cm during a no wind condition. Left axis represents values for rate of spread and right axis represents values for surface fuel mass loss rate. 87

Figure 6.18: Images from experiment 21 at (a) t = 236 s at time of crown 1 ignition; (b) t = 285 s during crown 1 combustion; (c) t = 296 s at time of crown 2 ignition..... 89

Figure 6.19: Tabulated view factor values and corresponding plot for a crown 1 and crown 2 configuration for a CSD of 20 cm at a wind condition of 0.0 m/s. Left side of plot represents leading edge of fuel bed while right side of plot represents the downstream edge of the fuel bed..... 90

Figure 6.20: Plots for a surface fuel and crown 1 and two configuration at a crown separation distance of 20 cm for a no wind condition of: (a) total heat flux and convection heat flux produced during experiment 21; (b) branch and air temperature history during experiment 21. 91

Figure 6.21: Average rate of spread and surface fuel mass loss rate at each thermocouple location plot for a crown separation distance of 30 cm during a no wind condition. Left axis represents values for rate of spread and right axis represents values for surface fuel mass loss rate. 93

Figure 6.22: Images from experiment 17 at (a) t = 230 s at time of crown 1 ignition; (b) t = 265 s during crown 1 combustion; (c) t = 297 s at time of crown 2 ignition..... 95

Figure 6.23: Tabulated view factor values and corresponding plot for a crown 1 and crown 2 configuration for a CSD of 30 cm at a wind condition of 0.0 m/s. Left side of plot represents leading edge of fuel bed while right side of plot represents the downstream edge of the fuel bed..... 96

Figure 6.24: Plots for a surface fuel and crown 1 and two configuration at a crown separation distance of 30 cm for a no wind condition of: (a) total heat flux and convection heat flux produced during experiment 17; (b) branch and air temperature history during experiment 17. 97

Figure 6.25: Total heat flux and convection heat flux curves for a surface fuel and crown 1 only configuration at a crown separation distance of 30 cm for a no wind condition during experiment 12. 98

Figure 6.26: Average rate of spread and surface fuel mass loss rate at each thermocouple location plot for a crown separation distance of 10 cm during a 1.1 m/s wind condition. Left axis represents values for rate of spread and right axis represents values for surface fuel mass loss rate: (a) raw data; (b) average surface fuel mass loss rate shifted backwards. 101

Figure 6.27: Images from experiment 60 at (a) t = 120 s at time of crown 1 ignition; (b) t = 155 s during crown 1 combustion; (c) t = 162 s at time of crown 2 ignition..... 103

Figure 6.28: Tabulated view factor values and corresponding plot for a crown 1 and crown 2 configuration for a CSD of 10 cm at a wind condition of 1.1 m/s. Left side of plot represents leading edge of fuel bed while right side of plot represents the downstream edge of the fuel bed..... 104

Figure 6.29: Plots for a surface fuel and crown 1 and two configuration at a crown separation distance of 10 cm for a 1.1 m/s wind condition of: (a) total heat flux and convection heat flux produced during experiment 60; (b) branch and air temperature history during experiment 60. 105

Figure 6.30: Average rate of spread and surface fuel mass loss rate at each thermocouple location plot for a crown separation distance of 20 cm during a 1.1 m/s wind condition. Left axis represents values for rate of spread and right axis represents values for surface fuel mass loss rate. 107

Figure 6.31: Images from experiment 52 at (a) t = 84 s at time of crown 1 ignition; (b) t = 115 s during crown 1 combustion; (c) t = 120 s at time of crown 2 ignition..... 108

Figure 6.32: Tabulated view factor values and corresponding plot for a crown 1 and crown 2 configuration for a CSD of 20 cm at a wind condition of 1.1 m/s. Left side of plot represents leading edge of fuel bed while right side of plot represents the downstream edge of the fuel bed..... 109

Figure 6.33: Plot for a surface fuel and crown 1 and two configuration at a crown separation distance of 20 cm for a 1.1 m/s wind condition of total heat flux and convection heat flux produced during experiment 52. 111

Figure 6.34: Average rate of spread and surface fuel mass loss rate at each thermocouple location plot for a crown separation distance of 30 cm during a 1.1 m/s wind condition. Left axis represents values for rate of spread and right axis represents values for surface fuel mass loss rate. 113

Figure 6.35: Images from experiment 38 at (a) t = 99 s at time of crown 1 ignition; (b) t = 115 s during crown 1 combustion; (c) t = 136 s at time of crown 2 ignition..... 114

Figure 6.36: Tabulated view factor values and corresponding plot for a crown 1 and crown 2 configuration for a CSD of 30 cm at a wind condition of 1.1 m/s. Left side of plot represents leading edge of fuel bed while right side of plot represents the downstream edge of the fuel bed..... 115

Figure 6.37: Plots for a surface fuel and crown 1 and two configuration at a crown separation distance of 30 cm for a 1.1 m/s wind condition of: (a) total heat flux and convection heat flux produced during experiment 38; (b) branch and air temperature history during experiment 38. 117

Figure 6.38: Total heat flux and convection heat flux curves for a surface fuel and crown 1 only configuration at a crown separation distance of 30 cm for a 1.1 m/s wind condition during experiment 77. 118

Figure 6.39: Average rate of spread and surface fuel mass loss rate at each thermocouple location plot for a crown separation distance of 10 cm during a 1.9 m/s wind condition. Left axis represents values for rate of spread and right axis represents values for surface fuel mass loss rate. 120

Figure 6.40: Tabulated view factor values and corresponding plot for a crown 1 and crown 2 configuration for a CSD of 10 cm at a wind condition of 1.9 m/s. Left side of plot represents leading edge of fuel bed while right side of plot represents the downstream edge of the fuel bed..... 122

Figure 6.41: Images from experiment 29 at (a) t = 81 s at time of crown 1 ignition; (b) t = 85 s during crown 1 combustion; (c) t = 92 s at time of crown 2 ignition. 123

Figure 6.42: Plots for a surface fuel and crown 1 and two configuration at a crown separation distance of 10 cm for a 1.9 m/s wind condition of: (a) total heat flux and convection heat flux produced during experiment 29; (b) branch and air temperature history during experiment 29. 124

Figure 6.43: Average rate of spread and surface fuel mass loss rate at each thermocouple location plot for a crown separation distance of 20 cm during a 1.9 m/s wind condition. Left axis represents values for rate of spread and right axis represents values for surface fuel mass loss rate. 126

Figure 6.44: Images from experiment 30 at (a) t = 56 s at time of crown 1 ignition; (b) t = 65 s during crown 1 combustion; (c) t = 75 s at time of crown 2 ignition. 128

Figure 6.45: Tabulated view factor values and corresponding plot for a crown 1 and crown 2 configuration for a CSD of 20 cm at a wind condition of 1.9 m/s. Left side of plot represents leading edge of fuel bed while right side of plot represents the downstream edge of the fuel bed..... 129

Figure 6.46: Plots for a surface fuel and crown 1 and two configuration at a crown separation distance of 20 cm for a 1.9 m/s wind condition of: (a) total heat flux and convection heat flux produced during experiment 30; (b) branch and air temperature history during experiment 30. 131

Figure 6.47: Average rate of spread and surface fuel mass loss rate at each thermocouple location plot for a crown separation distance of 30 cm during a 1.9 m/s wind condition. Left axis represents values for rate of spread and right axis represents values for surface fuel mass loss rate. 133

Figure 6.48: Tabulated view factor values and corresponding plot for a crown 1 and crown 2 configuration for a CSD of 30 cm at a wind condition of 1.9 m/s. Left side of plot represents leading edge of fuel bed while right side of plot represents the downstream edge of the fuel bed..... 134

Figure 6.49: Images from experiment 30 at (a) t = 56 s at time of crown 1 ignition; (b) t = 65 s during crown 1 combustion; (c) t = 75 s at time of crown 2 ignition. 136

Figure 6.50: Plot for a surface fuel and crown 1 and 2 configuration at a crown separation distance of 30 cm for a 1.9 m/s wind condition of total heat flux and convection heat flux produced during experiment 49. 137

Figure 6.51: Total heat flux and convection heat flux curves for a surface fuel and crown 1 only configuration at a crown separation distance of 30 cm for a 1.9 m/s wind condition during experiment 73. 138

Figure 7.1: Velocity vector field plot for a surface fuel and crown 1 and 2 configuration at a crown separation distance of 10 cm for a 0.0 m/s wind condition during experiment 90 showing ambient air entrainment at t = 9.1 s; Note: time shown here is time during PIV capturing not time during the actual experiment. 143

Figure 7.2: (a) Velocity vector plot at t = 0.7 s showing the formation of a 3.6 cm diameter vortex within the open area of a 10 cm CSD and a 0.0 m/s wind condition; (b) corresponding vorticity contour plot used to calculate vorticity of 14.9 s^{-1} clockwise; experiment 90; Note: time shown here is time during PIV capturing not time during the actual experiment. 145

Figure 7.3: (a) Velocity vector plot at t = 3.1 s showing the formation of a 2.1 cm diameter vortex within the open area of a 10 cm CSD and a 0.0 m/s wind condition; (b) corresponding vorticity contour plot used to calculate vorticity of 19.8 s^{-1} clockwise; experiment 90; Note: time shown here is time during PIV capturing not time during the actual experiment. 146

Figure 7.4: (a) Velocity vector plot at t = 10.8 s showing the formation of a 2.1 cm diameter vortex within the open area of a 10 cm CSD and a 0.0 m/s wind condition; (b) corresponding vorticity contour plot used to calculate vorticity of 65 s^{-1} clockwise; experiment 91; Note: time shown here is time during PIV capturing not time during the actual experiment. 148

Figure 7.5: (a) Velocity vector plot at t = 3.9 s showing the formation of a 1.7 cm diameter vortex within the open area of a 10 cm CSD and a 1.1 m/s wind condition; (b) corresponding vorticity contour plot used to calculate vorticity of 60.5 s^{-1} clockwise; experiment 57; Note: time shown here is time during PIV capturing not time during the actual experiment. 149

Figure 7.6: (a) Velocity vector plot at t = 12.3 s showing the formation of a 2.1 cm diameter vortex within the open area of a 10 cm CSD and a 1.1 m/s wind condition; (b) corresponding vorticity contour plot used to calculate vorticity of 34.3. s^{-1} clockwise; experiment 57; Note: time shown here is time during PIV capturing not time during the actual experiment. 150

Figure 7.7: Velocity vector field plots of: (a) ambient air entrainment as the fire front approaches the ROI from the left at t = 0.2 s for experiment 50 (b) fire front propagating along the ROI at t = 4.9 s for experiment 53; Note: times shown here are times during PIV capturing not times during the actual experiment. 152

Figure 7.8: Velocity vector field plots of: (a) ambient air entrainment as the fire front approaches the ROI from the left at t = 4.7 s for experiment 38 (b) fire front propagating along the ROI at t = 15.3 s for experiment 39; Note: times shown here are times during PIV capturing not times during the actual experiment. 154

Figure 7.9: Velocity vector plot at t = 1.61 s as the fire front propagates along the ROI for a 10 cm CSD configuration with a 1.9 m/s wind condition..... 155

Figure 7.10: (a) Velocity vector plot at t = 1.1 s showing the formation of a 1.5 cm diameter vortex within the open area of a 10 cm CSD and a 1.9 m/s wind condition; (b) corresponding vorticity contour plot used to calculate vorticity of 238.1 s^{-1} clockwise; experiment 88; Note: time shown here is time during PIV capturing not time during the actual experiment. 156

Figure 7.11: Velocity vector field plots of: (a) ambient air entrainment as the fire front approaches the ROI from the left at t = 4.0 s for experiment 85 (b) fire front propagating along the ROI at t = 7.0 s for experiment 85; Note: times shown here are times during PIV capturing not times during the actual experiment. 158

Figure 7.12: Velocity vector field plots of: (a) ambient air entrainment as the fire front approaches the ROI from the left at t = 2.4 s for experiment 46 (b) fire front propagating along the ROI at t = 1.07 s for experiment 46; Note: times shown here are times during PIV capturing not times during the actual experiment. 160

Figure 8.1: LES results at a midplane of air temperature and velocity field for a CSD of 10 cm at: (a) C1 ignition; t = 104.0 s. Instantaneous *R* is 1.8 cm/s and radiation energy transfer rate per unit volume between 1.7 m and 1.8 m is 4.18 kW/m^3; (b) C2 ignition; t = 114.0 s. Instantaneous *R* is 1.4 cm/s and radiation energy transfer rate per unit volume between 1.7 m and 1.8 m is 73.6 kW/m^3..... 163

Figure 8.2: LES results at a midplane of air temperature and velocity field for a CSD of 20 cm at: (a) C1 ignition; t = 106.1 s. Instantaneous *R* is 1.4 cm/s and radiation energy transfer rate per unit volume between 1.7 m and 1.8 m is 0.43 kW/m^3; (b) C2 ignition; t = 128.7 s. Instantaneous *R* is 1.4 cm/s and radiation energy transfer rate per unit volume between 1.7 m and 1.8 m is 510.5 kW/m^3..... 165

Figure 8.3: LES results at a midplane of air temperature and velocity field for a CSD of 30 cm at: (a) C1 ignition; t = 96.5 s. Instantaneous *R* is 1.2 cm/s and radiation energy transfer rate per unit volume between 1.7 m and 1.8 m is 0.76 kW/m^3; (b) C2 ignition; t = 115.2 s. Instantaneous *R* is 1.2 cm/s and radiation energy transfer rate per unit volume between 1.7 m and 1.8 m is 34.18 kW/m^3..... 166

Figure 8.4: LES results at a midplane of air temperature and velocity field for a CSD of 10 cm at: (a) C1 ignition; t = 74.5 s. Instantaneous *R* is 1.0 cm/s and radiation energy transfer rate per unit volume between 1.7 m and 1.8 m is 1.05 kW/m^3; (b) C2 ignition; t = 89.5 s. Instantaneous *R* is 0.6 cm/s and radiation energy transfer rate per unit volume between 1.7 m and 1.8 m is 20.74 kW/m^3..... 168

Figure 8.5: LES results at a midplane of air temperature and velocity field for a CSD of 20 cm at: (a) C1 ignition; t = 66.1 s. Instantaneous *R* is 0.4 cm/s and radiation energy transfer rate per unit volume between 1.7 m and 1.8 m is 0.38 kW/m^3; (b) C2 ignition; t = 86.1 s. Instantaneous *R* is 1.0 cm/s and radiation energy transfer rate per unit volume between 1.7 m and 1.8 m is 75.17 kW/m^3..... 170

Figure 8.6: LES results at a midplane of air temperature and velocity field for a CSD of 30 cm at: (a) C2 ignition; t = 96.4 s. Instantaneous *R* is 1.4 cm/s and radiation energy transfer rate per unit volume between 1.7 m and 1.8 m is 5.5 kW/m^3; (b) C1 ignition; t = 101.8 s. Instantaneous *R* is 1.2 cm/s and radiation energy transfer rate per unit volume between 1.7 m and 1.8 m is 13.7 kW/m^3..... 172

Figure 8.7: LES results at a midplane of air temperature and velocity field for a CSD of 10 cm and a 0.0 m/s wind condition as the fire front propagates: (a) beneath C1; (b) through area between C1 and C2; (c) beneath C2. 176

Figure 8.8: LES results at a midplane of air temperature and velocity field for a CSD of 20 cm and a 0.0 m/s wind condition as the fire front propagates: (a) beneath C1; (b) through area between C1 and C2; (c) beneath C2. 177

Figure 8.9: LES results at a midplane of air temperature and velocity field for a CSD of 30 cm and a 0.0 m/s wind condition as the fire front propagates: (a) beneath C1; (b) through area between C1 and C2; (c) beneath C2. 180

Figure 8.10: LES results at a midplane of air temperature and velocity field for a CSD of 10 cm and a 0.8 m/s wind condition as the fire plume propagates: (a) beneath C1; (b) through area between C1 and C2; (c) beneath C2. 181

Figure 8.11: LES results at a midplane of air temperature and velocity field for a CSD of 20 cm and a 0.8 m/s wind condition as the fire plume propagates: (a) beneath C1; (b) through area between C1 and C2; (c) beneath C2. 183

Figure 8.12: LES results at a midplane of air temperature and velocity field for a CSD of 30 cm and a 0.8 m/s wind condition as the fire plume propagates: (a) beneath C1; (b) through area between C1 and C2; (c) beneath C2. 184

List of Tables

Table 6.1: Average rate of spread at each thermocouple location for a surface fuel only configuration for the three wind cases (0.0 m/s, 1.1 m/s, 1.9 m/s).....58

Table 6.2: Average rate of spread at each thermocouple location for a surface fuel and crown 1 configuration for the three wind cases (0.0 m/s, 1.1 m/s, 1.9 m/s)...68

Table 6.3: Average rate of spread at each thermocouple location for a surface fuel and crown 2 configuration for the three wind cases (0.0 m/s, 1.1 m/s, 1.9 m/s)...75

Table 6.4: Average rate of spread and average surface fuel mass loss rate data at each thermocouple location for a crown separation distance of 10 cm during a no wind condition. 79

Table 6.5: Average rate of spread and average surface fuel mass loss rate data at each thermocouple location for a crown separation distance of 20 cm during a no wind condition. 86

Table 6.6: Average rate of spread and average surface fuel mass loss rate data at each thermocouple location for a crown separation distance of 30 cm during a no wind condition. 92

Table 6.7: Average rate of spread and average surface fuel mass loss rate data at each thermocouple location for a crown separation distance of 10 cm during a 1.1 m/s wind condition. 100

Table 6.8: Average rate of spread and average surface fuel mass loss rate data at each thermocouple location for a crown separation distance of 20 cm during a 1.1 m/s wind condition. 106

Table 6.9: Average rate of spread and average surface fuel mass loss rate data at each thermocouple location for a crown separation distance of 30 cm during a 1.1 m/s wind condition. 112

Table 6.10: Average rate of spread and average surface fuel mass loss rate data at each thermocouple location for a crown separation distance of 10 cm during a 1.9 m/s wind condition. 119

Table 6.11: Average rate of spread and average surface fuel mass loss rate data at each thermocouple location for a crown separation distance of 20 cm during a 1.9 m/s wind condition. 125

Table 6.12: Average rate of spread and average surface fuel mass loss rate data at each thermocouple location for a crown separation distance of 30 cm during a 1.9 m/s wind condition. 132

1 Introduction

1.1 Problem Statement

Fires burn large areas in California and around the world annually. California experiences numerous wildland fires that affect the lives of thousands of citizens every year. In 2000 the U.S. census bureau reported that 33.8 million people resided in California. The last census in 2010 showed California population had grown to 37.3 million people. As a consequence of the increase in California's population, new communities continue to be constructed on the wildland-urban interface. The proximity of people and homes to the wildlands has resulted in the continued efforts to understand fire phenomena for the purpose of successfully and safely managing fires in these areas. In 2011 the National Interagency Fire Center reported that in the first six months 34,095 fires had burned 4.6 million acres nationwide. The 10-year average (2001-2011) for the first six months was 37,095 fires with 1.9 million acres burned. In southern California fires burn in area that consists of chaparral fuels [73]. Much of new growth in chaparral fuels grow in sparse configurations.

Chaparral is a complex of shrubby vegetation characterized by evergreen sclerophyll shrubs such as chamise (*Adenostoma fasciculatum*), hoaryleaf ceanothus (*Ceanothus crassifolius*), and manzanita (*Arctostaphylos glandulosa*) which dominates many sites at low to middle elevations throughout California, Arizona, and Mexico [11]. Chaparral usually burns with high intensity crown fires and is important because, for the majority, it is located in the wildland-urban interface [23]. Chamise is one of the most

hazardous wildland fuels and is known to burn hot and fast with physical characteristics that are conducive to a rapid rate of energy release [24]. Fires in chaparral fuels are generally categorized as crown fires due to the elevated nature of the fuel.

Many different mathematical models have been developed to predict different aspects of wildland fire behavior. These models are designed to predict the evolution of a fire as a function of fuel properties, mean wind speed and direction, and terrain topography. The merits and assumptions of the various models have been reviewed previously and the interested reader is encouraged to examine these reviews [19, 74, 70, 98]. Current operational fire models such as BEHAVE [8], FARSITE [36] and BRNPLN [44] are computer implementations of the Rothermel spread model [4, 81]. Another implementation of the Rothermel model in southern California called FIRECAST [22] added chaparral fuel beds based on Rothermel and Philpot's work (1973). These models make various parameter simplification and assumptions that are inconsistent with field observations [9, 68, 69]. Rothermel's model assumes uniform fuel, dominated by dead material close to the ground, and constant environmental conditions. Predicting fire behavior is also highly dependent upon knowledge of fuel characteristics [24]. Current operational models do not include a two-way coupling between the fire and the atmosphere. Research or physical models of fire behavior, on the other hand, focus on improved methodologies and are often limited in scope and designed to better understand specific physical processes. The earliest coupled atmosphere-fire research model is due to Grishin (1992). Since then, Clark *et al.* (1996), Linn *et al.* (2002), and Mell *et al.* (2007) have also developed such coupled models, and applied them to relatively large

scales, with the smallest, unresolved length scales ranging from 1 to 10 meters. To validate existing physical models for fire behavior, it is important to perform experiments and collect data that can be compared to model predictions. Although data exist that describe fire spread rate and some qualitative aspects of wildfire behavior, little data have explicitly revealed the small time and spatial scales in the convective processes that may determine the rate of fire spread [20] and overall fire behavior. A comprehensive survey and discussion of various types of surface fire spread models developed during the period 1990-2007 is presented in Sullivan (2009) [88, 89, 90].

Fire spread within wildland fuels is maintained by thermal energy release from fuel combustion, flame and ember radiation heat transfer, convective heat transfer, and through advection effects such as rolling embers and spotting [91]. In order to estimate the convective energy transfer, it is necessary to characterize the buoyant plume, namely its dimensions, temperature, and air velocity distribution [28, 29].

Flow measurements in the vicinity of large fires have been performed in field settings using anemometers and other devices [21, 62, 74, 95]. Various researchers have measured instantaneous two-dimensional velocity fields in turbulent flows involving combustion [53, 80, 106]. Reuss *et al*. (1990) used a Particle Image Velocimetry system to obtain the instantaneous velocity field over a 24 mm by 32 mm area within a two-stroke engine. They were able to resolve the velocity integral-length scales utilizing the PIV data. Zhou and Garner (1995) used a PIV system to investigate flame propagation and unburned gas velocity fields within a cylindrical combustion chamber to determine the local flame speed. Long *et al.* (2006) utilized a PIV system, with an imaging area of

138 mm by 108 mm, to examine how flame fronts interact with simple toroidal vortex structures in a controlled environment. The PIV allowed them to investigate how the toroidal vortices distorted the flame front, and how the progression of the flame was affected. Three vortex sizes each resulting from air being pushed through different orifice sizes 40, 30 and 20 mm, by a progressing flame front, were investigated. From the analysis it was determined that there were three distinct modes of flame-vortex interaction: 1) at an orifice size of 40 mm the flame propagates around the vortex following the streamlines, pushing the vortex ahead of the flame and slowly consuming the mixture in the vortex, 2) at an orifice size of 30 mm the flame initially propagates around the vortex and then rapidly consumes the vortex, and 3) at an orifice size 20 mm the flame immediately and rapidly consumes the mixture in the vortex.

Using a Particle Image Velocimetry (PIV) method, the velocity vector fields of the three fire regions (continuous, intermittent, thermal plume) and their surroundings were computed for non-wind aided fire spread across a fuel bed of uniformly distributed aspen (*Populus tremuloides Michx*) excelsior [55]. Flames encountered in forest fires are generally classified as diffusion flames in which all three regions exist [58]. Results showed that vortices were present in all three flame regions ranging from 4.4 cm to 5.8 cm in diameter. Because of the size of the vortices and their proximity to the surface fuel, along with corroborating thermocouple data, it was determined that the main heat transfer mechanism for fire spread in a non-wind aided propagating fire was radiation preheating of the unburned fuel elements directly ahead of the fire front. Using the same PIV system and a thermocouple system, fluid dynamic structure and temperature data

were gathered that were essential in the study of wind-aided fire spread across an array of small diameter discrete fuel elements in a low speed wind tunnel operating at a wind speed of 0.6 m/s [54]. The fuel type used in this study was bamboo skewers with diameter, length, and dry mass per unit length of 3.0 mm, 5.0 cm, and 0.062 g/cm, respectively. Two fuel loading cases were investigated, high fuel loading of 3.12 kg/m^2 (total dry fuel mass per unit fuel bed area) and low fuel loading of 0.78 kg/m^2. Results showed that vortices were only present in the high fuel loading case. It was determined that experiments conducted at a higher fuel loading resulted in a lower rate of spread (0.26 cm/s), higher intensity fire front, and development of strong vortices. For the high fuel loading, the vortices captured using the PIV system indicated the presence of convection that preheated the fuel elements further ahead of the fire front. This preheating was deduced from the thermocouple data. It was determined that the average rate of spread was inversely proportional to the square root of the burnt fuel mass load (defined and used as per Carrier et *al.*, 1991), consistent with theoretical predictions in the literature.

Much research had been undertaken in understanding fire spread through surface and crown fuels. Lindenmuth and Davis (1973) performed fire behavior research at the prescribe fire experiment area in the Prescott National Forest. Chaparral brush in that area covered approximately six-million acres with 85% consisting of shrub live oak. They observed that fuels grew in clumps and that those fuels were fairly homogeneous within clumps. It was also observed that fuel clumps were surrounded by strips of virtually bare ground. From their finding they developed a statistical model to predict

rate of spread in the Arizona oak chaparral fuels. Fernandes (2001) performed fire spread research in evergreen sclerophyll shrublands dominated by broadleaf or heath species in Portugal. Shrublands occupy approximately four-million acres (18% of the country). Fuels investigated were from the northwestern, Central, northeastern and southern regions of Portugal. Through his results he derived several empirical models to predict rate of fire spread in Portuguese shrub stands to be used in prescribed burning conditions. Bradstock and Gill (1993) performed fire spread research between fuel arrays at the Yathong Nature Research in New South Wales Australia. The fuel consisted of a principal overstory of Eucalyptus (3-4 m in height), a shrub layer of Acacia (1-3 m in height) and a near surface layer of Triodia Irritans (< 0.8 m height). From their results they determined that the near-surface layer had a major role in fire spread by flame contact across the gaps between fuel elements. They also found that eucalyptus may contribute to fire spread through the production of fire brands and the initiation of spot fires downwind.

The International Crown Fire Modeling Experiment in the northwest territories of Canada by Clark et al. (1999) investigated crown fire behavior in an overstory of jack pine and an understory of black spruce. Through their investigation they observed titling vortices that played an important role in the convection heat transfer phenomena. Van Wagner (1977) developed a semi-empirical model for crown fire initiation. In this model crown ignition occurs when the surface fire intensity per unit length of fire line (kW/m) is equal to or greater than the critical fire line intensity per unit length of fire line required to initiate crowning (kW/m), $I_s \geqslant I_o$. Cruz et al. (2006) [27, 28] developed a Crown Fuel

Ignition Model (CFIM) based on heat transfer theory. The model generated temperature of the crown fuel particles that are assumed to ignite upon achieving ignition temperature. The model predicts ignition of crown fuels but does not determine the onset of crown fire spread. Scott and Reinhardt (2001) developed crown fire initiation model that is a torching index which is the wind speed at which a crown fire is expected to ignite. The crown fuel will ignite if the rate of spread of a surface fire, R_s, is greater than the critical rate of spread for crown fire ignition, R_o.

Tachajapong et al. (2008) concluded that propagating surface fires through excelsior fuel beds led to ignition of crown fuel matrices composed of live chamise when the crown base height was located within either the continuous (0.00 m to 0.15 m from the surface fuel) or intermittent flame regions (0.15 m to 0.45 m from the surface fuel). The crown base height is defined as the vertical distance between the surface fuel and the lowest height at which the canopy fuel density exceeds 0.011 kg/m^3 [7, 86]. Experiments were performed with the crown fuel base within the intermittent flame region and for crown fuel bulk densities of 0.75, 1.75, and 2.75 kg/m^3, where crown fuel bulk density refers to the oven dry mass of foliage and small twigs (less than 3 mm in diameter) per unit volume of canopy [5, 36, 48, 96]. Experiment results were compared to those attained through use of a Large Eddy Simulation (LES) model. It was concluded that the LES results and the experimental measurements were within reasonable agreement. The higher crown fuel bulk density enhances the probability of crown fire ignition. An increase in crown fuel bulk density results in the increased ability by the crown fuel

matrix to retain thermal energy while at the same time reducing the convective heat losses to the surroundings. These results were also evident in the LES model results.

Another outcome of Tachajapong's (2008) research was the observation that the fire behavior under open conditions was quite different from that observed under conditions in which lateral entrainment was suppressed by the side walls of a wind tunnel. His experiments attempted to model situations corresponding to segregated crown fuels, and more continuous distribution of crown fuel. In all cases though, a single crown fuel matrix was utilized. The focus of this study is on the transition from a surface to a crown fire with the objective of gaining an in depth understanding of the heat transfer mechanisms by which this phenomenon occurs under conditions in which multiple crown fuel elements that are spatially segregated are present. The goal is to understand crown fire behavior under these circumstances, and to identify the potential influence of the crown fire on the surface fire behavior. The experimental results will be compared to those of an LES mathematical model. A non-intrusive velocity measurement technique will be deployed to directly measure the velocities within a fire environment with the expectation of shedding light into conditions that could potentially cause spotting in which firebrands are lofted from the fire, possibly landing in regions containing unburned fuel. It is expected that by performing laboratory and model experiments, it will be possible to better understand the dynamics of fire behavior from marginal burning to intense fire spread conditions.

1.2 Objectives

The objective of this study is to gain a better insight and understanding into the heat transfer mechanisms that contribute to the transition from a surface fire to a crown fire for various environmental and fuel conditions. Comparing LES results against those attained from the experiments can further validate the LES model used in this study.

1.3 Scope

In this study, the emphasis is on investigating the various environmental and fuel characteristics that affect fire behavior by performing experiments and utilizing mathematical models. This study will be performed in the following steps:

1) Evaluate the effect of crown fuel separation on surface fire behavior and thus on the convective and radiation heat transfer for pre-heating of the crown fuel matrices and of the unburned surface fuel elements.
2) Evaluate the effect of crown fuel separation on the flow speed between adjacent crown fuel matrices of the hot gaseous products of combustion from a propagating fire .
3) Compare experimental results to those attained through use of the LES mathematical model.

2 Background

2.1 Properties Influencing Fire Spread

Fire Classifications

Fire behavior is strongly dependent on the nature of the fuel and environmental conditions. Wildland fires are classified as ground fires, surface fire or crown fires. Ground fires occurring in the accumulated, decomposed organic materials can have spread rates on the scale of cm/hr [38]. Surface fires involve loose dead fuels on the forest floor or grasses in open land. Surface fires in loose dead forest fuels travel at rates of 100-200 m/hr while wind-driven fires in grass and shrublands may travel at rates of 15-20 km/hr [77]. Crown fires spread though consumption of fuel in elevated canopies of trees and occur in extensive brush fields in Mediterranean regions of the world, in dense coniferous forests in northern temperate and boreal regions, and in eucalyptus forests in Australia. Large surface fires and crown fires are typically the most damaging fires to life, property, and natural resources. The distribution of crown fuel can range from a contiguous arrangement of elevated fuels to situations in which crown fuel elements may be segregated in space with contiguous surface fuel underneath. Fire behavior under these differing circumstances is not well understood and forms the bases of the research presented here.

Physical characteristics that affect fire dynamics can be classified into environment properties and fuel properties. Important environment parameters in fire prediction are relative humidity, wind speed and direction, ambient temperature, and

topography. For surface and crown fires, the fuel properties affecting fire behavior are fuel type, fuel moisture content, fuel density, fuel loading, fuel surface-to-volume ratio, fuel bulk density, and crown fuel base height. Fuel and environmental properties affect fire characteristics such as intensity, ignition time, residence time, and burning time. The environment and fuel properties will be discussed briefly.

Wind Conditions

Wind is an important variable that influences fire initiation. The effects of wind on surface fires and crown fires vary. If the wind is in the direction of fire propagation, the flame tilt angle, measured from the vertical, between the fire front and the surface fuel can increase, impinging large quantities of radiation and convection heat to the unburned surface fuels ahead of the fire front. The result is an increase in combustion rate, higher flow velocities, increased flame heights, and increased rate of spread and higher burning intensity [97]. Merrill and Alexander (1987) define the flame height as the average maximum vertical distance between the flame tip and surface fuel and the flame tile angle as the angle of the center of the fire front from the horizontal direction. In this study the flame tilt angle is measured from the vertical direction. If the wind is in the opposite direction of fire propagation the flame tilt angle, as measured in this study, will become negative. As a result less radiation and convection heat will impinge onto the unburned surface fuels ahead of the fire front leading to a decrease in combustion rate and overall rate of spread. Wind both assists and hampers crown fuel ignition. Wind aids crown fire initiation by increasing the rate of spread of the surface fire which increases flame lengths, thereby resulting in increased heat release from the surface fire.

At high wind speed crown fuel ignition is hindered because the increase in the rate of spread also decreases the residence time, which is the time the surface fire transfers heat by radiation and convection to the crown fuel. The residence time is decreased because the surface fire traverses the crown fuel area at a higher rate. This causes a reduction in the quantity of radiation and convection heat flux transferred between the advancing surface fire and stationary crown fuel. The presence of the wind may result in a cooling effect, where the gaseous products of combustion and crown fuel particles are cooled by the wind before the hot gases reach the crown fuel [28, 29]. Wind aids fire propagation by producing rolling embers which can ignite large fires at various distances from the source fire. Koo et al. (2010) studied the role of firebrands in fire propagation and the important parameters involved in spot fire development and they performed a review on firebrand behavior. It was observed that conifer needles, pollen cones, cone scales, bracts and wood fragments were transported by wind and subsequently deposited up to 20 km from a forest fire [72]. Firebrand impact is influenced by weather conditions, especially wind and humidity. Wind transports the firebrands and humidity is a key parameter in determining whether ignition by firebrand will occur [49]. It was observed [18, 97, 105, 107] that under wind-aided conditions, convective energy transfer plays a more prominent role in ignition of unburned fuel in contrast to no wind conditions where radiation dominates. Morvan et al. (2002) performed a numerical study to determine the effect of wind on wildfire propagation through Mediterranean shrubs and grasses for various wind speeds ranging from 1 m/s to 10 m/s. They show the existence of two

propagation modes, corresponding to situations dominated by radiation heat transfer, plume dominated fires, and by convection heat transfer, wind driven fires.

Relative Humidity and Ambient Temperature

Relative humidity influences fire behavior by limiting the rate at which the fuel is desiccated. Relative humidity is considered as the drying power of the ambient air and thus influences the rate at which moisture is removed from the fuel [33]. Many studies have been performed that show the influence of relative humidity on fire spread [26, 30, 33, 76, 84]. Although these studies show a correlation between fire spread and relative humidity, it has been observed that there is not some constant prevailing, but instead there is a mixture of danger variables, which combine to produce conditions for a major fire to occur.

Topography

Topography can have great or no effect on fire spread. Inclined terrain will have a similar affect on a propagating surface fire as wind speed, but without cooling effect experienced during wind driven fires. If a surface fire is propagating up a hill the flame will be in closer proximity to the unburned fuel and as a result a larger quantity of radiative heat will impinge on the unburned fuels ahead of the fire front. The unburned fuels will reach ignition temperature sooner and the propagation rate will be faster in comparison to a fire spreading on horizontal terrain. If a surface fire is propagating down a hill the flame will be tilted backward, opposite the unburned fuels. The view factor will decrease and therefore the radiative heat transferred to the unburned fuels will be minimal when compared to the radiative heat transferred to the unburned fuels within the

reaction zone. The view factor of a flame with $\theta = 30°$ is 5 time greater than the corresponding value for the same flame inclined backward with $\theta = 150°$ [97].

Live and Dead Fuels

An important consideration is whether fuels are live fuels or dead fuels. In generally, fuels that burn in a forest fires are categorized into two classes, living fuels and dead fuels. Living fuels, consisting of leaves, twigs, and stems of growing plants do not burn readily by themselves. These live fuels require the presence of dead fuels to assist the ignition process [59]. Live fuels absorb and desorb moisture actively, which means they acquire moisture as needed from the environment or from the soil. They regulate their moisture and are less responsive to changes in ambient temperature, relative humidity, and wind. Generally the moisture content of living fuels is significantly high to sustain combustion, even during the drought season. Flammability of live fuels is thus strongly related to the availability of dead stems, litter, and desiccated herbs and forbs [41, 92].

Fires that start in dry dead fuels spread rapidly. After one or two decades, chaparral brush will sustain fast-spreading and high intensity fires, depending upon the ratio of live-to-dead fuel [83]. Dead fuels absorb and expel moisture passively. Dead fuel moisture levels respond quickly to ambient environment conditions and are critical in determining fire potential. For example, 1-hour fuels (particles less than 0.6 cm in diameter) reach equilibrium with ambient relative humidity within an hour, while 1000-hour fuels (7.6 to 20.3 cm diameter) require 1000 hours to reach equilibrium with the ambient relative humidity [85]. Dead chamise responds to changes in moisture dictated

by daily fluctuations in humidity, precipitation, and temperature. Knowledge of the amount of fine and medium-sized dead fuel in forests is critical for the understanding and prediction of fire behavior [17].

Fuel Moisture

Fuel moisture content has a major impact on the ignition, development and spread of fires [43]. Moisture content *M*, is the ratio of the mass of water to the dry mass of fuel,

$$M = \frac{m_w}{m_d} \tag{2.1}$$

where m_w is the mass of water and m_d is the mass of the dry fuel. Fuel moisture is an important parameter that influences fire ignition in surface and crown fires, and is dependent on age, fuel type, and environmental conditions. High fuel moisture content increases the amount of energy required to increase fuel temperature [28]. In a surface fire, as the fire propagates, the fuel downwind of the fire front is preheated by radiation and under certain conditions, convection. As the unburned fuel is heated, its temperature increases so that the moisture within the fuel begins to evaporate. Once the fuel is desiccated, its temperature continues to increase until ignition occurs. If an insufficient quantity of moisture has evaporated by the time the fire front reaches the unburned fuel, the fuel will not ignite upon fire front arrival. The fire will then extinguish. For crown fuels, the moisture vaporization process is similar, but the thermal energy that raises the temperature of the crown fuel so that moisture vaporization occurs and the fuel can reaches ignition temperature, originates from the surface fire propagating beneath the crown fuel. Fuel moisture content of live fuels is governed by the the season and the

quantity of groundwater available. Plant moisture content is the lowest at the onset of fall and highest in spring and early summer in southern California. The lack of fuel moisture is attributed to the fuels losing moisture throughout the four months of summer and to the lack of rain during the summer season. During the late fall and winter months, the moisture content of live Chamise remains relatively constant, typically between 80% and 110% of the dry weight. Between March and May, new growth has very high moisture content, sometimes over 200% of the dry weight [24]. Dead fuel moisture content depends on environmental conditions such as humidity and temperature, and is much lower than in live fuels. When a fuel has less than 30% moisture, it is considered a dead fuel [22]. As with live fuels, dead fuels are also the driest in late fall and the lack of moisture is attributed to low humidity and high temperatures throughout the summer.

Fuel loading

Fuel loading is defined as the dry mass of fuel per unit area of fuel bed. The average fuel loading for chamise is [24] 2.2 kg/m^2. Fuel loading is known to influences the rate of fire spread [18]. The more fuel that a fire front must pre-heat the slower it will propagate.

Intensity

Fire intensity is proportional to the amount of fuel consumed per unit area and the rate of fire spread [17],

$$I = Hm_b R \tag{2.2}$$

where H is the heat yield of fuel (kJ/kg), m_b is the amount of fuel burned per unit area (kg/m^2), and R is the rate of fire spread (m/s). Intensity is a measure of heat energy released during a fire per fire line length (W/m). An increase of fire intensity is followed by an increase in flame height, radiative heating, and conductive heating. The result is that fuel ahead of the propagating flame front is preheated as the flame front approaches. Increased fire intensity is due to the increased amount of fuel being burned or the increased rate of spread. A larger quantity of fuel releases a larger amount of pyrolysis gases that are then ignited when they are hot enough and are oxidized. The combustion of larger quantities of pyrolysis gases results in larger flames. More radiation and convection heat energy impinge onto unburned surface fuels as a result of the larger flames. There are various methods of measuring intensity such as pyrometers, calorimeters, and thermocouple data. In savannas of northern Australia, fire intensities may range from 500 to 10,000 kilowatts per meter (kW/m), and rarely exceed 20,000 kW/m. In southern Australian eucalyptus forests, where fuel has accumulated to near maximum levels, in excess of 30 tons per hectare (t/ha), fire intensities can be as high as 50,000-100,000 kW/m [104].

Surface Area-to-Volume Ratio

Heat transfer to the interior of fuel elements occurs by conduction through the surface. Larger surface area to volume ratios will result in fuels being heated at a greater rate because there is a larger surface for the heat to flow through in comparison to the volume. In dead fuels, surface area-to-volume ratio affects moisture content. Moisture in dead fuels is absorbed and desorbed through the fuel's surface, thus if the surface to volume ratio is large, greater amounts of moisture will be absorbed or desorbed. In chaparral fuels, the average surface to volume ratio for chamise, ceanothus, and manzanita are 66 cm^{-1}, 58 cm^{-1}, and 41 cm^{-1} respectively [99].

Bulk Density

Fuel bulk density is important in both surface and crown fires. Bulk density is the mass of fuel per unit volume of fuel configuration (kg/m^3) and can very dependent on the arrangement of the fuel in question. In surface and crown fuels, it affects the ignition success and the rate of fire spread. Bulk densities in conifer forests range from 0.09 kg/m^3 to 0.96 kg/m^3 [6, 27, 48] and in chaparral shrub they range from 0.20 kg/m^3 to 2.10 kg/m^3 [24]. If the bulk density is high, then a surface fire will propagate slowly in comparison to a low bulk density case. The lower rate of fire spread in a high bulk density case is due to the increased amount of fuel that the fire front must preheat and ignite before it can continue to propagate. In addition, a higher bulk density restricts the flow of oxygen to the fire and minimizes cooling effects. In crown fires, if the bulk density is high, larger quantities of thermal energy will be stored within the crown fuel matrix, thereby increasing temperature of the crown fuel and promoting ignition. When

the bulk density is significantly low, then the hot gaseous products of combustion will be allowed to flow through the crown fuel matrix without increasing the temperature of the crown fuel sufficiently to reach ignition temperature. High crown fuel bulk densities restrict fuel pyrolysis gases from escaping and low temperature air from entering the crown fuel matrix, thereby allowing the gases to reach ignition temperature. Low crown fuel bulk densities allow pyrolyzed gases to escape and lower temperature air to enter the crown fuel matrix, preventing ignition. For crown fuels, the probability of transition from surface to crown fires increases as the bulk density of the crown increases.

Crown Fuel Base Height

Crown fuel base height is defined as the lowest height above the ground at which there is sufficient canopy fuel to propagate fire vertically through the canopy, figure 2.2 [96]. The crown fuel height, along with other factors, has a considerable effect on the probability of a surface fire transitioning to a crown fire [15]. During a surface fire, the crown fuel height determines the section within the fire regime where the crown will be located. The crown fuel will be located in one of the three fire regimes, continuous flame region, intermittent flame region, or plume region. The continuous flame region is where the flame extends vertically covering the entire observation area in the vertical direction. Vertical distance of the continuous flame region is measured from the top of the surface fuel to the lowest flame height observed. Intermittent flame region is where the flame is present in the observation area, but is not continuous in the vertical direction. Vertical distance to the lower and the upper boundaries of the intermittent flame region is from the top of the surface fuel to the lowest and highest observed flame height, respectively.

Hot gaseous products of combustion from the surface fire represent the plume region. In this region, no flame is visible. The lower boundary of the plume region is measured from the top of the surface fuel to the highest flame height observed. The fire regime where the crown fuel is located will affect the amount of thermal energy that will transfer to the crown fuel. Tachajapong (2008) a performed crown base height investigation.

2.2 Particle Image Velocimetry

Particle Image Velocimetry (PIV) is a non-intrusive technique that allows for the measurement of instantaneous 2-D velocity field without significantly disturbing the flow field [3, 45, 101, 2, 50, 40]. The PIV technique measures the velocity in a fluid by correlating images of the particle-seeded flow (1). Ideally, the tracer particles should match the density of the medium as closely as possible. The particle size must be chosen to allow for optimal flow tracking and enhanced light scattering [61]. Response time is an indicator of whether a particle type is suitable for PIV applications. Assuming Stokes flow for particle drag, the response time (time required for particle to reach 63% of the flow velocity) of particles can be estimated using a first-order inertial response to a constant flow acceleration [79].

$$\tau_P = \frac{d_P^2 \rho_P}{18\mu} \tag{2.1}$$

In Equation 2.1, d_p is the diameter of the particle, ρ_P is the density of the particle, and μ is the dynamic viscosity of the fluid.

In PIV the flow of interest is seeded with seed particles of a chosen material. For fire application the seed particles chosen are generally aluminum oxide (Al_2O_3). These particles are chosen for their high refractive index and high melting point. Once the flow field is seeded, a double-pulsed Nd:YAG laser generates a laser sheet with a wavelength of 532 nm at a specified frequency, Δt, thus illuminating the seed particles. Laser pulse frequency is determined by flow velocity estimations. A high-speed flow field merits a

larger laser pulse frequency, smaller time between laser pulses, and a low-speed flow requires a larger time between laser pulses. The resulting laser sheet is expanded to a desired thickness utilizing sheet forming optics such as spherical and cylindrical lenses. The spherical and cylindrical lenses ensure that the waist of the laser sheet is located at the center of the region of interest. The cylindrical lens will determine the height of the light sheet at the point of interest and the spherical lens will determine the distance from the lens where the waist thickness will be minimal. Laser waist location is important to minimize errors that arise from illuminated particles that are in front or behind the plane of interest. As the laser pulses, light is incident on the seed particles within the flow field that is then scattered and captured by a CCD (charge-coupled device) camera [50] functioning at a specified frequency. If the objective is to record the evolution of fluid dynamic structures, a higher capture frequency is recommended, but if all that is required is the velocity field, then lower capture frequencies are sufficient.

The instantaneous velocity field of the flow is then calculated by comparing a sequence of captured images. Individual images are decomposed into small interrogation windows. Interrogation window from subsequent images are cross-correlated with each other [101, 78] resulting in a signal peak from which the particles displacement in the x-direction, dx, and y-direction, dy, is determined [46, 47, 60]. Dividing by the time between laser pulses, Δt, the horizontal and vertical components of velocity (V_x and V_y) are computed, thus the local velocity of the flow field is resolved. The cross-correlation process is repeated for the entire image resulting in the velocity vector field of the flow.

2.3 Large Eddy Simulation

The Large Eddy Simulation (LES) model is based on a detailed description of the complex heat transfer processes and simple combustion mechanism contributing to the ignition of solid fuel and fire spread that was developed by Zhou et al. (2007). The LES code used is described in detail by Tachajapong (2008). Only the major equations are described here.

Spatial filtering is utilized to separate the gas phase turbulent flow fields into resolved large-scale and unresolved small-scale contributions. The large-scales are resolved in a time-dependent simulation using a set of filtered equations that are computed directly. Suitable closure models are used to model the small-scales. The filtering operation uses a length scale, Δ, to distinguish between large-scales and small-scales. Eddies that are larger than Δ are distinguished as large eddies and eddies smaller than Δ are considered small eddies. The key processes for fire spread occurring between the gas and solid phases are the transfer of mass, momentum, and energy. It is assumed that the large eddies transport mass, momentum, energy, and species mass fractions while the effect of small eddies on turbulent transport is modeled through suitable sub-grid scale closure models.

The combustion of solid fuel is calculated by solving mass and energy equations, which include the effects of drying, pyrolysis, and char combustion and the exchanges of mass, momentum, and energy with the surrounding gas. Many fuel and environmental variables such as fuel geometry, fuel moisture, fuel bulk density, ambient temperature, wind speed and relative humidity can be studied through use of the LES code. In the

LES these quantities can be independently specified to gain a better understanding of the role of the various variables on both the surface fire spread process and transition to a crown fire. A uniform grid system is used to span the computational domain. The fuel bed is placed in the center of the computational domain in the horizontal direction. Introducing a volumetric heat source over the entire fuel bed depth and along the fuel bed width simulates ignition of the fuel bed.

Transport Equations

Gas Phase

The set of transport equations for the resolved field as per Tachajapong (2008) are as follows. The filtered gas phase continuity equation is

$$\frac{\partial \overline{\rho}}{\partial t} + \frac{\partial \overline{\rho} \widetilde{u}_i}{\partial x_i} = \overline{S}_{s-g} \tag{2.2}$$

where $\overline{\rho}$ is the filtered gas mixture density, x_i is the tensor notation for the position vector, $\widetilde{u}_i$ is the Favre-filtered velocity component along x_i, and $\overline{S}_{s-g}$ is the filtered mass production rate that arises from the decomposition of solid fuel to the gaseous phase. The filtered gas phase momentum equation is

$$\frac{\partial \overline{\rho} \widetilde{u}_i}{\partial t} + \frac{\partial \overline{\rho} \widetilde{u}_j \widetilde{u}_i}{\partial x_j} = \frac{\partial}{\partial x_j}\left\{ -\overline{\rho}\left(\widetilde{u_i u_j} - \widetilde{u}_i \widetilde{u}_j\right)\right\} - \frac{\partial \overline{p}}{\partial x_i} + \frac{\partial \overline{\tau}_{ij}}{\partial x_j} + \overline{\rho} g_i - \overline{F}_{s,i} \tag{2.3}$$

where $\overline{p}$ is the filtered pressure, g_i is the acceleration vector, $\overline{F}_{s,i}$ is the filtered i-th component of the drag force arising from the gas and solid phase interaction, and $\overline{\tau}_{ij}$ represents the filtered viscous stress. The filtered gas phase energy equation is

$$\frac{\partial \overline{\rho}\widetilde{h}}{\partial t}+\frac{\partial \overline{\rho}\widetilde{u}_j\widetilde{h}}{\partial x_j}=\frac{\partial}{\partial x_j}\left\{-\overline{\rho}\left(\widetilde{u_j h}-\widetilde{u}_j\widetilde{h}\right)\right\}-\frac{\partial \overline{q}_i}{\partial x_i}-\overline{q}_{conv}+\overline{q}_{rad}+\left(1-X_c\right)\overline{\dot{m}}_{s,char}L^{char} \tag{2.4}$$

where $\widetilde{h}$ is the gas mixture enthalpy, $\overline{q}_i$ is the filtered heat flux vector, $\overline{q}_{conv}$ is the convection heat transfer rate per unit volume between the solid and gas phase, $\overline{q}_{rad}$ is the radiation heat transfer rate per unit volume. The final term on the right hand side represents part of the heat transfer rate released from the heterogeneous combustion between oxygen and char. In this term $\overline{\dot{m}}_{s,char}$ is the consumption rate of char mass per unit volume and L^{char} is the specific enthalpy associated with char combustion.

The filtered gas phase species transport equation is

$$\frac{\partial \overline{\rho}\widetilde{Y}_K}{\partial t}+\frac{\partial \overline{\rho}\widetilde{u}_j\widetilde{Y}_K}{\partial x_j}=\frac{\partial}{\partial x_j}\left\{-\overline{\rho}\left(\widetilde{u_j Y_k}-\widetilde{u}_j\widetilde{Y}_K\right)\right\}+\frac{\partial \overline{q}_{Y_{K,i}}}{\partial x_i}+\overline{S}_{s-g,K}+\overline{\omega}_K \tag{2.5}$$

where $\overline{q}_{Y_{K,i}}$ is the filtered species diffusion flux vector, $\overline{S}_{s-g,K}$ is the filtered production rate of gas species *K* resulting from solid fuel decomposition accompanied by vaporization, pyrolysis, and oxidation of char, and $\overline{\omega}_K$ is the filtered production rate of species *K* through chemical reactions occurring in the gas phase. In each of equations (2.3), (2.4), and (2.5), the first term on the right hand side represents subgrid scale terms that require modeling. Details of this modeling are presented briefly in Zhou et al., (2007) and in more detail in Tachajapong (2008).

Solid Phase

The solid fuel is modeled as consisting of two phases: foliage and branches. These two phases have different densities but are assumed to have the same moisture content. It is assumed that the fuel initially includes water, pyrolyzates, char, and

noncombustible ash. Let $\overline{m}_s$ denote the mass of the solid, and the associated subscripts the contributions to the total mass due to the water, pyrolyzates, and char. Taking into account water vaporization, pyrolysis, and char combustion within the preheating and burning processes, the resulting mass balance equation for the solid phase is

$$\frac{\partial \overline{m}_s}{\partial t} = -\overline{\dot{m}}_{s,H_2O} - \overline{\dot{m}}_{s,pyr} - \overline{\dot{m}}_{s,char} \tag{2.6}$$

Assuming that the solid fuel particles are thermally thin, the energy balance equation for the solid phase is

$$\frac{\partial \overline{c}_{p,s} \overline{m}_s \overline{T}_s}{\partial t} = \overline{q}_{conv} + \overline{q}_{rad,s} + \overline{q}_{mass} \tag{2.7}$$

where $\overline{c}_{p,s}$ is the filtered specific heat of the solid phase, $\overline{T}_s$ is the filtered solid phase temperature. $\overline{q}_{rad,s}$, $\overline{q}_{conv}$, and $\overline{q}_{mass}$ are the filtered energy transfer rates per unit volume. The variation in solid phase temperature gives rise to $\overline{q}_{rad,s}$ and $\overline{q}_{conv}$ as a result of radiation and convection transfer rates between the solid and the gas phase. Also influencing the solid phase temperature is the heat loss/absorption rate $\overline{q}_{mass}$, which is a result of the water vaporization, pyrolysis, and char oxidation. The filtered convection heat transfer rate between the gas and solid phase from equation 2.7 is modeled as

$$\overline{q}_{conv} = Ah_c\left(\tilde{\overline{T}} - \overline{T}_s\right) \tag{2.8}$$

where the heat transfer coefficient h_c is deduced from the Nusselt number (Nu) of the solid phase as

$$Nu = \frac{h_c d}{\lambda} = 0.683\,\mathrm{Re}^{0.466} \tag{2.9}$$

where λ is the conductive heat transfer coefficient of the gas phase, and the Reynolds number (Re) is based on *d* and the filtered gas phase velocity and kinematic viscosity. The filtered rate of heat release arising from water vaporization, pyrolysis, and char combustion in equation 2.7 is modeled as

$$\overline{q}_{mass} = -\overline{\dot{m}}_{s,H_2O} L^{H_2O} - \overline{\dot{m}}_{s,pyr} L^{pyr} + X_c \overline{\dot{m}}_{s,char} L^{char} \tag{2.10}$$

where L^{H_2O}, L^{pyr}, and L^{char} represent the enthalpies for the process of vaporization, pyrolysis, and char combustion. The variable X_c is a sharing coefficient detailing the distribution of the heat from char combustion between the solid and gas phases.

The governing equations are discretized in a three dimensional Cartesian coordinate system. Explicit quadratic upstream second order accurate scheme in space and time is utilized to numerically integrate the governing equations (QUICKEST) [51, 31], while the SIMPLER method [71] is used to treat the velocity and pressure coupling [75]. A three dimensional Discrete Ordinates (DO) method [65] calculates the radiation through the solid fuel and radiation heat transfer between solid and gas phases.

Utilizing the computational LES model, it is possible to investigate and identify the factors that determine a successful transition from a surface fire to a crown fire.

3 Experimental Setup Descriptions

3.1 Experiment Location

Experiments are performed at the fire laboratory located at the United States Department of Agriculture Forest Service (USDAFS) facility in Riverside, California. The laboratory is a 13 x 13 m metal building with 6.1 m walls and a vented peaked roof, which is 7.6 m above the concrete floor. Air is introduced at ground level to force smoke up through the roof ventilation system. To provide uniform surface fire spread a homogenous bed of aspen (*Populus tremuloides* Michx) excelsior was used. Excelsior is shredded wood and was used to produce a flame height of 0.3-0.5 m. Excelsior is dead wood and its moisture content will equilibrate with ambient temperature and relative humidity given sufficient time and steady conditions as most forest surface fuels [67]. Chamise (*Adenostoma fasciculatum*), a common species in chaparral, was used as the crown fuel for all investigations. It was collected from the North Mountain Experimental Area.

3.2 Wind Tunnel Setup

For this study, a wind tunnel with a cross section of 1.20 m wide × 1.20 m height and is 7.4 m in total length, Figure 3.1, was constructed [93, 94]. Located upstream of the test section is a 48” axial fan, driven by a 1 hp, three-phase, 240V, electric motor. A micro inverter controls wind speed with an output frequency ranging from 0 to 50.0 Hz and a resolution of 0.1 Hz. Turbulence effects from the push fan are minimized by

directing air flow through a flow conditioning section that creates an initially uniform flow within the test region of the wind tunnel. The flow conditioning section consists of a honeycomb followed by a series of three screens, Figure 3.1. For all experiments, the fuel bed is located within the test section, which is 3.40 m in length. The top of the test section remained opened, allowing the fire front to propagate without any constraints [105].

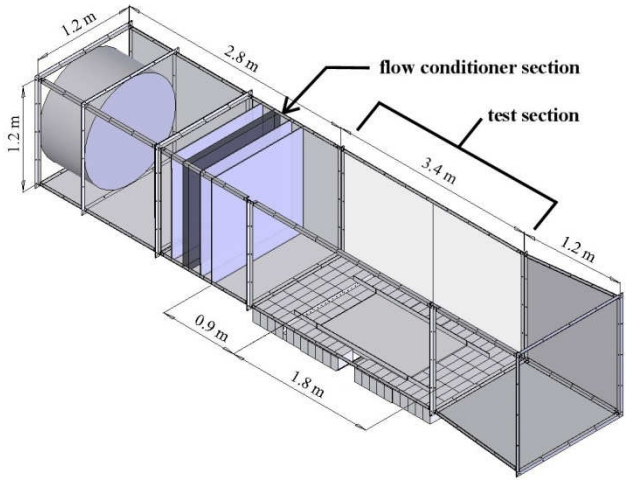


Figure 3.1: Schematic of wind tunnel showing push fan, flow conditioner section and the test section.

Before experimentation it was necessary to characterize the flow field to determine the wind speed at specified locations within the test section of the wind tunnel. To perform this flow characterization the test section was divided into four vertical planes measuring 0.51 m in width by 1.02 m in height with measurements starting at 0.10 m and concluding at 1.12 m from the fuel bed surface. The four planes were located within the test section of the wind tunnel. The first plane was positioned at 0.05 m from the last flow conditioner screen. The second, third, and fourth measurement planes were located at 1.0 m, 1.5 m and 2.0 m from the last flow conditioning screen. Vertical and

horizontal distance between each measurement point is 12.8 cm and 25.5 cm, respectively, Figure 3.2. Each measured plane consisted of 3 columns with 9 points per column. Velocity measurements were performed using a constant temperature hot-wire anemometer (Omega, Inc., model FMA-604-V) and each measurement was recorded for approximately 5 minutes. The frequencies analyzed were 20 Hz and 50 Hz, which are the lowest and highest frequencies the push-fan is capable of producing. Measurements are performed for all four vertical planes. The average of the twenty-seven velocity measurements was calculated and reported as the average flow velocity at the specified plane. Velocity measurements were repeated several days later using a different setup to adjust the horizontal and vertical position of the hot-wire anemometer to demonstrate repeatability of the measurements. A total of two hundred and sixteen velocity measurements were performed.

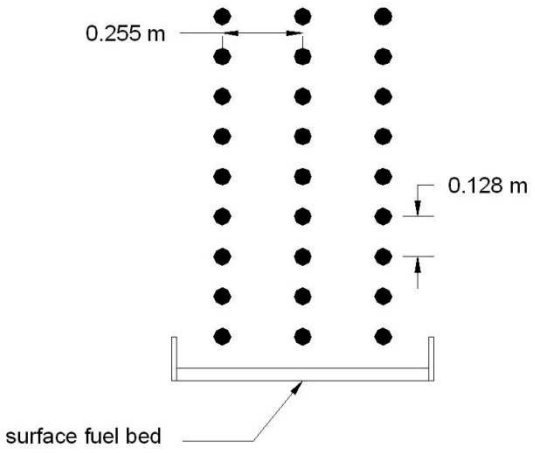


Figure 3.2: Flow characterization vertical plane showing locations above fuel bed where velocity measurements are performed.

Figure 3.3 shows the average velocity at each plane for the initial and repeated measurements within the test section of the wind tunnel for the lowest and highest frequencies possible. Data shows excellent repeatability of the velocity measurements with the largest differences of 5% and 4% appearing at leading edge of the fuel bed for both frequencies. The minimum difference appears at the crown fuel section (1.0 m from the leading edge of the fuel bed) at 20 Hz with a difference value of 1%. The recorded data shows that at 20 Hz the difference between flow speed at the test section entrance (plane 1) and the flow speed at the crown fuel matrix location (plane 4) is 7%. This difference value is the same for the repeat test at 20 Hz. At 50 Hz, the difference between flow speed at plane 1 and plane 4 is 6% for the initial measurement and 5% for the repeat measurement.

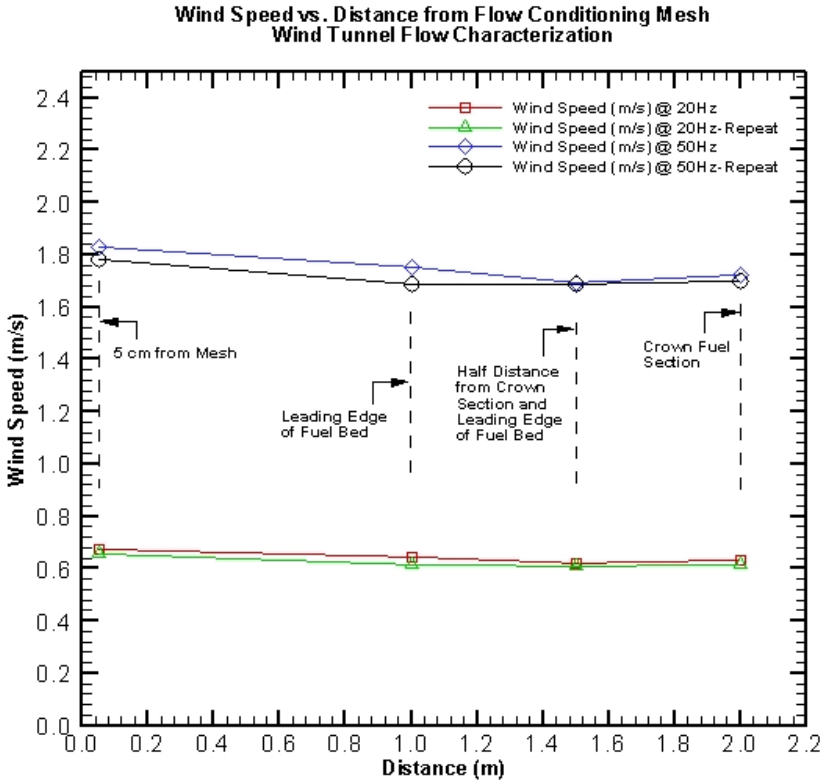


Figure 3.3: Wind speed profile along the surface fuel bed length representing an average value across a vertical plane of 0.51 m wide by 1.02 m high starting at 0.10 m from fuel bed surface.

Figure 3.4 shows velocity with height plotted at the crown fuel matrix location (1.0 m from the fuel bed leading edge) for the initial and repeat measurements. At both frequencies the variation between measurements at a given height is not greater than 6.5%. Within the intermittent flame region (0.15 m to 0.45 m) the variation in wind speed with height is approximately 5% at 20 Hz and 8% at 50 Hz. Wind speed begins to decrease above 0.8 m. The greatest variation was found above 0.9 m with a variation of 46% at 50 Hz. At 20 Hz flow speed variation was less than 34%. Flow speed diminishes with increasing height because the top of the wind tunnel is open and the air is allowed to

flow out through the top as opposed to the area near the fuel bed where the air is forced to flow forward maintaining a more stable flow speed.

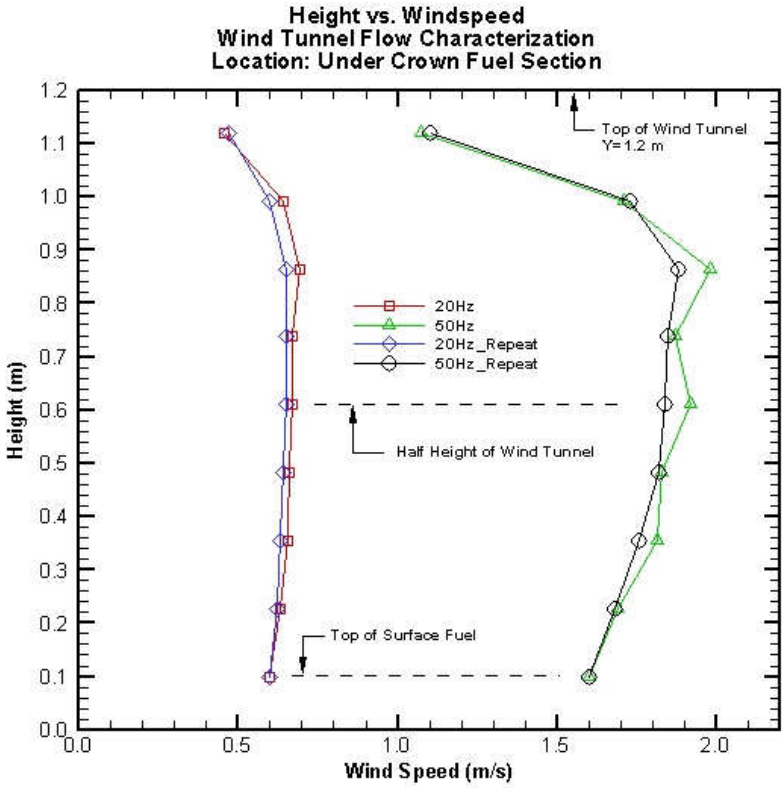


Figure 3.4: Wind speed profile with height above the surface fuel bed at 1.0 m from the leading edge of the fuel bed (location of the crown fuel).

Previous analysis has identified nearly 30 dimensionless groups related to fire and explosions [102] with Reynolds number and Froude number as the most important quantities. Since the focus of the present study is fluid flow within and surrounding a propagating fire, the Froude number is perhaps the most appropriate group to use [103]. The appropriate Froude number is defined as $Fr = U^2/gH$ where U is a characteristic inertial velocity typically measured as wind speed at mid flame height, and H is the characteristic flame height. Froude number scaling maintains balance between

convective and gravitational effects during experimentation. Buoyancy or plume dominated fires are characterized by small Froude numbers ($F_r \leq 1$) whereas wind driven fires occur for larger Froude numbers ($F_r > 1$) [59]. Using wind speed data attained from the California State University San Bernardino virtual weather station, Froude numbers were estimated to range from 0 to 4.8 for a mid flame wind speed of 15 m/s and typical flame heights of 5 m to 10 m. In southern California prescribed burns are performed during marginal burning conditions [99] where wind speeds at mid flame height are significantly lower than 15 m/s. Mid flame wind speeds measured at an elevation of 6.1 m (measured during prescription burning) with an applied wind reduction factor of 0.6 [82], are less than 3.3 m/s. The wind reduction factor accounts for the influence of stand and canopy structures on wind. Froude numbers under these conditions are in the range of 0 to 1.1 according to an estimated flame height of 1.0 m. Accordingly, during experimentation under no wind conditions, the Froude numbers were in the range of 0 to 1.3 for a mid flame wind speed of 2.3 m/s and a characteristic flame height of 40 cm.

3.3 Fuel Bed Setup

In large-scale wildland fires the fire front is represented as a curve that separates burned and unburned fuel regions. At a small region of a wildfire or in a controlled laboratory-scale fire, the fire front can be approximated as having a nearly linear shape, and fire spread through the fuel bed is assumed to be perpendicular to the fire front [107]. The experimental setup at the USDAFS burn facility is thus modeled as a fuel bed in

which the fire front has a linear shape and fire spread is perpendicular to the fire front. This fuel bed is set inside a wind tunnel.

A mass of 0.90 kg of aspen excelsior was evenly distributed over the fuel bed to a depth of 0.10 m resulting in a fuel loading of 0.313 kg/m^2 and a bulk density of 3.13 kg/m^3. The packing ratio (bulk density/fuel particle density) of the fuel beds was 0.008. Two crown fuel baskets consisting of two wire mesh cubes were positioned at the far downstream side of the test section. The wire mesh baskets were set at a height of 35 cm from the surface of the fuel bed and were kept constant for all experiments in this study. The surface fuel bed was situated atop a 0.4 m x 0.3 m precision balance (Sartorius model CPA34001S) with a range of 34 kg and readability of 0.1 g to record surface fuel mass loss rate, $\dot{m}$. To ignite the surface fuel in a line ignition, approximately 59 cc of isopropyl alcohol was placed in a metal channel that was positioned parallel to the width of the fuel bed (0.80 m) underneath the surface fuel approximately 0.5 m upstream from the leading edge of the fuel bed.

To determine the crown separation distances that would be investigated a field study was performed on a 10 m × 10 m plot at the North Mountain Experimental Area. The plot contained twenty-seven chamise bushes. The diameter of individual chamise bushes and the separation distance between adjacent chamise bushes was measured. Average diameter and separation distance were calculated to be 0.8 m and 0.6 m respectively. Due to the size constraint of the wind tunnel it was deemed satisfactory to use a crown length of 0.6 m instead of 0.8 m. A 0.6 m separation distance could not be achieved in the wind tunnel thus a maximum separation distance of 0.3 m was used.

3.4 Moisture Measurements

The fuel moisture content of chamise and excelsior was measured using an Arizona Instruments Computrac 1000 moisture analyzer. Accuracy of the moisture analyzer was determined using the Arizona Instruments application data sheet for the Computrac 1000 moisture analyzer. The data sheet contains percent moisture of sixty-four materials that was determined using the moisture analyzer and oven drying method. From this data the average difference between the moisture measurements from the two methods was approximately 1% with the moisture analyzer giving a moisture reading 1% higher than that attained through the over drying method.

3.5 Fire Front Behavior Data

A Canon-FS200 and Canon-FS300 digital camera capturing at 30 Hz was used to record each experiment. Fire front behavior and crown fuel ignition times are then determined from the captured images. The instantaneous rate of spread is defined as the distance traversed by a fire in a direction normal to itself per unit time. The fuel bed and crown fuel setup allows for temperature measurements using a set of 30 gauge (0.25 mm diameter) type K (Chromel-alumel) thermocouples with a response time of 0.3 seconds. These thermocouples can be placed anywhere on the surface of the fuel bed and crown fuel matrix. For this study, ten thermocouples were placed 2.5 cm above the surface fuel along the fuel bed starting at 40 cm from the leading edge of the fuel bed, Figure 3.5. The distance between each subsequent thermocouple was 20 cm. Two thermocouples were placed in each crown fuel matrix with one thermocouple from each matrix placed

within a section of branch to record branch temperature as the fire front approached and ignited the corresponding crown fuel matrix.

Heat release rate is an important factor contributing to the severity of a fire [10, 87]. To measure heat flux from the fire front to adjacent crown fuel matrices, a heat flux sensor (Hukseflux model RC01) was position 0.3 m downstream from crown-two. Sensor RC01 has dimensions of 65 mm x 65 mm x 13 mm, response time of 1.5 s, maximum allowable heat flux of 400 kW/m2, and is capable of measuring radiation and convection heat flux. To measure heat flux from the fire front to unburned surface fuels, heat flux sensor (Hukseflux model SBG01) was situated at the downstream edge of the surface fuel. The position of both sensors is shown in Figure 3.5. In Chapter 6 (Results and Discussion) section 6.1 (Rate of Spread), Sensor SBG01 is used in the heat flux analysis for surface fuel only and single crown configurations while sensor RC01 is used in the heat flux analyses for multiple crown fuel configurations.

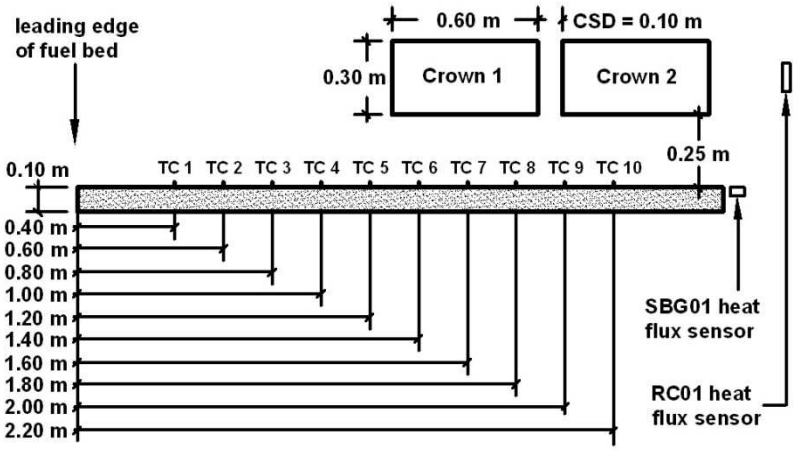


Figure 3.5: Schematic of surface fuel bed and crown setup at a crown separation distance (CSD) of 10 cm showing location of fuel bed thermocouples (labeled TC1 thru TC10). Thermocouples are placed 2.5 cm above the surface fuel. RC01 heat flux sensor is position 0.3 m downstream of crown-two. Note: crown fuel matrices 1 and 2 are referred to as C1 and C2. The width perpendicular to the sketch is 0.8 m for the surface and crown fuel matrices.

3.6 Particle Image Velocimetry System Arrangement

A Particle Image Velocimetry (PIV) system was used to capture the instantaneous velocity field within and surrounding a propagating flame through an excelsior fuel bed and transitioning to a crown fire. The PIV technique measures the velocity in a fluid by correlating images of the particle-seeded flow [1]. Approximately 200 g of aluminum oxide (Al_2O_3) per experiment was utilized as the seeding particles. The particle size ranged from 1 to 3 μm and particle density is 3970 kg/m^3. These particles were chosen because they are readily available at low cost, and most importantly, are able to withstand the high temperatures within a fire (≈2345 K) [61]. Particle response times range from 4 μs to 0.04 ms for particle sizes of 1 μm and 3 μm respectively. The aluminum oxide has a refractive index, *m*, of 1.76. Response time is in the range of the smallest time between

laser pulses, and thus is reasonable. Since velocity measurements were performed within the fire, and the fire also emits light, the chosen particles have to reflect a greater quantity of light than is emitted from the fire to allow for particle tracking.

An aerosol generator based on the design by Glass and Kennedy (1977) and adapted by Sun (2006a) was utilized to seed the test section. Air at 345 kPa was injected into the aerosol generator, which created a cloud of particles that was expelled through the top of the aerosol generator. The air flow rate was controlled by a series of valves. Expelled particles were fed through two seeding pipes (113 cm in length and 1.7 cm in diameter) that are composed of 25, 2 mm diameter, horizontal perforations (perforations are along the same line), ejecting the seed particles horizontally outward. One seed pipe was placed vertically approximately 1.0 m downstream from the trailing edge of the fuel bed, and the second seed pipe was also placed at the trailing edge of the fuel bed but positioned horizontally parallel to the length of the fuel bed. As the fire front burned through the crown fuel section, air containing seed particles was entrained into the fire column.

As the fire front approached the test section, the seed particles were illuminated in a plane at the center of the experimental fuel bed parallel to the direction of fire spread. A double-pulsed Nd:YAG (neodymium-doped yttrium aluminium garnet, Nd:$Y_3Al_5O_{12}$) laser (Big Sky Laser Technologies, Inc, model CFR400) located 2 m from the area of interest generated a vertical laser sheet with a wavelength of 532 nm (with energy of 388 mJ/pulse) that illuminated the seed particles. The laser beam was expanded into a 567 mm high and 0.212 mm thick sheet that illuminated the seed particles in a vertical plane

within the area of interest parallel to the length of the fuel bed. To properly position the waist of the laser sheet, sheet-forming optics, which includes a spherical lens (2000 mm focal length) and a cylindrical lens (15 mm focal length), were used. A LASERPULSE Synchronizer (TSI Inc.) was utilized to trigger the laser pulse and the camera with correct sequences and timing through a 2.66 GHz dual processor workstation (Intel Xeon^{TM}). The laser sheet was synchronized with a high resolution (1600 x 1192 pixel) POWERVIEW 2M CCD camera (TSI Inc., model 630157) with a 50 mm Nikkor lens and PK-12 ring and an exposure time of 400 μs. The camera aperture was set to 8 with a 10 Hz capture rate. The camera was placed 0.74 m from the area of interest perpendicular to the vertical laser sheet and set to capture 160 PIV image sets per experiment. The time difference between successive images was optimized for the best PIV quality to Δt = 50 μs. This Δt was chosen through experimentation to minimize processing errors obtained when the seed particles, from frame to frame, exit the interrogation regions during PIV data processing. Particle images were captured in a 20.0 cm (horizontal) x 14.0 cm (vertical) domain. A black background was placed perpendicular to the CCD camera, on the opposite side of the experimental fuel bed, to prevent any light scattering that can introduce background noise in the raw images. To reduce the luminosity of the fire and the amount of noise captured by the camera, a 532 nm laser line filter was attached to the camera lens. This ensured that only green light (532 nm) was recorded. The velocity fields were obtained using the INSIGHT 3G (version 7.2.0) analysis software.

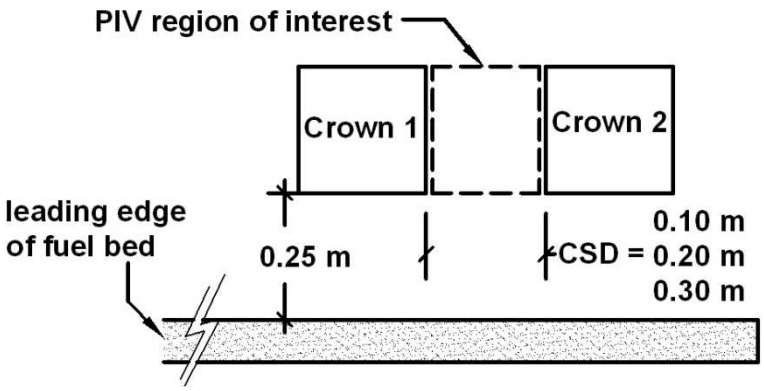


Figure 3.6: Schematic showing area to be imaged using the PIV system.

The region between the two crown fuels was investigated using the described PIV setup. Figure 3.6 shows a dashed square indicating the area that was analyzed. The area between the crown fuels was analyzed to determine variation in flow speed that affects convective preheating of the crown fuel elements.

4 Large Eddy Simulation Setup

4.1 LES Model Parameters

Large Eddy Simulation code was used to investigate the effect of crown fuel separation on the dynamics of multiple crown fire initiation. All variables except crown fuel separation and wind speed remained constant. In LES these quantities were independently specified to acquire a greater insight on the role of the effect of these variables on both the surface fire spread process and transition to a crown fire.

In the LES model, a surface fuel and multiple crown fuels were modeled with two block plates along the fuel bed sides and the setup was within the boundaries of a wind tunnel. All the boundaries except the bottom were open boundaries in which all the primary flow variables at the boundaries had zero gradient conditions. To calculate radiation and convection heat transfer, mass loss rate of surface and crown fuels, and moisture loss rate of surface and crown fuels, the computational domain was decomposed into a system of uniform grids. Along the fire propagation direction, the *x*-domain was 2.1 m in length and was composed of 107 horizontal uniform grids. The *z*-domain was 0.8 m in width and was constructed of 50 horizontal uniform grids. The *y*-domain was 1.1 m in height and was comprised of 57 vertical uniform vertical grids. In all, the computational domain was composed of a system of 304,950 cells, Figure 4.1. Tachajapong et al. (2008) performed a grid independence test and concluded that the grid resolution utilized in this study was sufficient to investigating the ignition process.

The setup for the LES was smaller than the experiment itself to save on computation time. The fuel bed was 1.9 m in length and was situated at the center of the computational domain starting at 0.1 m from the left and ending at 2.0 m from the left of the computational domain. Fuel depth was 0.1 m starting from the bottom of the computational domain. The width of the fuel bed was 0.4 m. The surface fuel was aspen (*Populus tremuloides*) excelsior with bulk density, moisture content, pyrolysis content, char content, surface area-to-volume ratio, and fuel particle density of 3.125 kg/m^3, 7%, 84.3%, 15.4%, 4500 m^{-1}, and 400 kg/m^3 respectively.

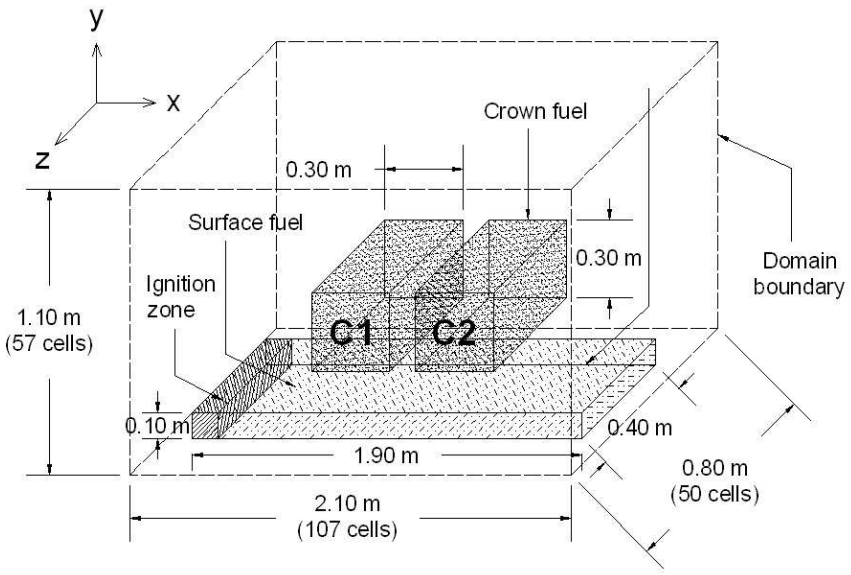


Figure 4.1: Illustration of LES computational setup

The crown fuel section consisted of two crown fuel elements shown as C1 (crown 1) and C2 (crown 2) in Figure 4.1. During experimentation the position of crown 2 was fixed while the position of crown 1 varied to study the effect of crown fuel separation on the dynamics of multiple crown fire initiation. The crown fuel dimensions were 0.3 m ×

0.3 m × 0.4 m ($L \times H \times W$). Crown 2 spanned from 1.5 to 1.8 in the *x*-coordinate, 0.35 to 0.65 in the *y*-coordinate, and 0.2 to 0.6 in the *z*-coordinate while the position of crown 1 will depended on the specific case being investigated. Both crown fuel elements consisted of live chamise (*Adenostoma fasciculatum*) with foliage diameter of 0.5 mm and branch diameter of 3.5 mm with foliage comprising 53% of the chamise and 47% is branch material. The foliage has bulk density of 3.98 kg/m^3, 36% moisture content, 67.9% pyrolysis content, 28.6% char content, surface area-to-volume ratio of 8000 m^{-1}, and particle density of 500 kg/m^3. The branch has bulk density of 3.53 kg/m^3, 36% moisture content, 79% pyrolysis content, 15.4% char content, surface area-to-volume ratio of 1800 m^{-1}, and particle density of 600 kg/m^3. All the fuels, surface and crown (foliage and branch), were set at an initial temperature of 308 K.

To ignite the fuel, an ignition zone was created at the front of the fuel bed with dimensions of 0.1 × 0.1 × 0.4 m (Figure 4.1). The ignition zone spanned from 0.1 to 0.2 m in the *x*-direction, 0.0 to 0.1 in the *y*-direction, and 0.2 to 0.6 in the *z*-direction. The heat source was maintained until 70% of the fuel in the ignition zone was burnt. Two block plates were included in the model to prevent radiation heat loss from the side of the fuel bed, thus ensuring that the fire front maintained a linear shape as opposed to a curved shape. These block plates were situated along the length of the fuel bed and were 1.9 m in length and 0.1 m in height with negligible thickness. The block plates spanned from 0.1 to 2.0 m in the *x*-coordinate, 0.0 to 0.1 m in the y-coordinated, and were positioned at 0.2 and 0.6 m in the *z*-plane.

The environment properties were 308 K and 101.325 kPa for the ambient temperature and atmospheric pressure, respectively. During experimentation, only distance between crown fuels and wind speed was varied while efforts were made to maintain all other conditions constant. Crown separation distances investigated ranged from 0.1 m to 0.3 m, wind speeds ranged from 0.0 m/s to 1.9 m/s, and crown fuel bulk density was kept constant at 5.5 kg/m^3. Solid fuel temperature and air temperature within the crown fuel matrix was measured. By investigating the ignition of multiple crowns it will be possible to better understand the transition process.

5 Previous Studies

Prior to the experimental and numerical results which are the focus of this study, various sets of experiments were performed to determine what the important variables were that necessitated an investigation and to improve the experimental setup that would subsequently be utilized to perform the experiments presented in this study. All previous studies were performed in multiple crown fuel environments situated within a wind tunnel.

The first set of experiments, performed in the Fall of 2009, multiple crown fire initiation in shrubs was investigated via laboratory experiments to determine the influence of separation distance between adjacent crown fuel matrices on the fire transition process from surface fuels to crown fuels, and between crown matrices at a constant wind speed of 1.1 m/s. The experiments were performed in the same facility and wind tunnel described in Chapter 3. Dimensions of the wind tunnel in the Fall of 2009 were 1.20 m width × 1.20 m height × 6.4 m length, which was 1.0 m shorter than the current wind tunnel length of 7.4 m. A mass of 0.45 kg of shredded aspen (*Populus tremuloides Michx*) excelsior was evenly distributed over the 0.8 m width × 1.8 m length of the surface fuel bed to a depth of 0.10 m. The current length of the surface fuel bed is 3.6 m. A crown stand consisting of two wire mesh platforms was set at the far downstream side of the fuel bed. The platforms were at a fixed height of 30 cm from the surface fuel. Chamise, with an average moisture content of 36%, was used as the crown fuel for all investigations and is collected from brush grown outside the burn laboratory, described in Chapter 3. Three crown separation distances were investigated, 0.1 m, 0.2 m

and 0.3 m. A constant crown fuel bulk density of 5.5 kg m^{-3} was used for all the experiments. That same bulk density is used for the experiments presented in this study. A series of 30 gauge type K thermocouples was used to capture temperature data at the surface fuel and crown fuel locations. Four thermocouples were placed on the surface of the fuel, at 0.3 m distance between adjacent thermocouples, to assist in determining surface fire local rate of spread *R*. Two thermocouples were situated within each crown fuel matrix with one thermocouple from each matrix placed within a sample of branch, thus the thermocouples recorded branch temperature and air temperature within the crown as a fire front propagated across the fuel bed.

Data showed that the average rate of spread was influence by the variation in crown separation distances. The average rate of spread for the three cases were 3.6 cm/s, 2.9 cm/s, and 3.0 cm/s for crown separation distance of 0.1 m, 0.2 m and 0.3 m respectively. Analysis of the recorded images for a crown separation distance of 0.1 m showed that as the fire front approached and ignited crown two, the surface fire and crown one fire were one merged fire. When crown two ignited, the result was a larger merged fire that included the surface fire and crown one and crown two fires. The investigation of crown separation distances of 0.2 m and 0.3 m showed that as crown two ignited, the surface fire and crown one fires were two separate fires. From the recorded images it was deduced that the larger crown one flame heights, in the case of a crown separation distance of 0.2 m in comparison to a crown separation distance of 0.3 m, produced a large quantity of thermal heating that resulted in the ignition of crown two sooner in case two and in case three.

These preliminary experiments showed that indeed crown separation distance was a variable that merited a dedicated investigation. It was also possible to determine what aspects of the experiment could be improved. When investigation the crown separation distance of 0.3 m, it was observed that ignition of crown 1 mainly occurred at the bottom of crown 1 at the downstream edge. This was a consequence of the relatively short length of the surface fuel bed, which did not allow for an adequate amount time for the surface fire front to transfer sufficient heat energy to crown 1 as to result in ignition at the upstream edge of the crown. The length of the surface fuel bed was increased by 1.8 m to a total length of 3.6 m to ensure proper ignition of crown 1. To accommodate the length of the new fuel bed, the wind tunnel test section length was increase by 1.0 m, which resulted in an overall wind tunnel length of 7.4 m. It was also determined that four thermocouples were insufficient to achieve a proper representation of the surface fire front rate of spread. To improve rate of spread measurements a new thermocouple system was designed to attain a greater number of local rate of spread R measurements. The improved system consisted of ten thermocouples with each thermocouple placed 0.15 m apart from each other. The fuel bed itself was also redesigned to allow for the measurement of surface fuel mass loss rate. The new fuel bed was constructed of an aluminum frame to reduce weight and included a support strip at each end of the fuel bed to allow the edges to be supported atop four 11.0 kg capacity load cells (model LC302-25), one per corner. The crown stand consisting of the two wire mesh platforms did not allow for the mass loss rate measurements of the individual crown fuels. The crown fuel system was redesigned to consist of two cantilever beams, each holding a wire mesh

basket. An 11.0 kg capacity load cell (model LC302-25) was placed beneath each cantilever beam to measure the mass loss rate of the crown fuels as the fire consumed the fuel. The improved overall system was used to conduct a similar set of experiment in the Summer of 2010.

The Summer 2010 set of experiments were performed in the same facility as described in Chapter 3. The focus of these experiments was on spatially segregated multiple crown fuel elements, as was the case in the Fall 2009 experiments, which model the crowns of discrete shrubs. The influence of (horizontal) separation distance between crown fuel matrices on the transition process from surface fires to crown fires in chaparral fuels was investigated experimentally. These experiments were performed at a constant wind speed of 1.1 m/s. A mass of 0.9 kg of shredded aspen (*Populus tremuloides Michx*) excelsior was evenly distributed over an area 0.8 m width × 3.6 m length to a depth of 0.10 m and ignited using isopropyl alcohol spread along the leading edge of the fuel bed producing a surface fire with flame heights 0.3 to 0.5 m. Two cantilever beams, each holding a wire mesh basket, were set at the far downstream side of the fuel bed. The baskets were at a fixed height of 30 cm from the surface fuel. Live chamise branches and foliage, collected near Riverside, CA, comprised the crown fuel matrices. To ensure that crown ignition occurred for all experiments performed, a constant crown fuel bulk density of 5.5 kg m^{-3} was used and moisture content of the live chamise ranged from 28% to 37%. A series of 30 gauge (0.25 mm) type K (chromel-alumel) thermocouples measured air temperature at the top of the surface bed and within the crown fuel matrices. Figure 5.1 shows ten thermocouples were placed on the surface

of the fuel bed at 0.15 m apart. Two thermocouples were situated within each crown fuel matrix to measure branch temperature and air temperature adjacent to the branch. A Canon-FS200 digital video camera was used to record each experiment. The resulting images were used to observe and document fire behavior.

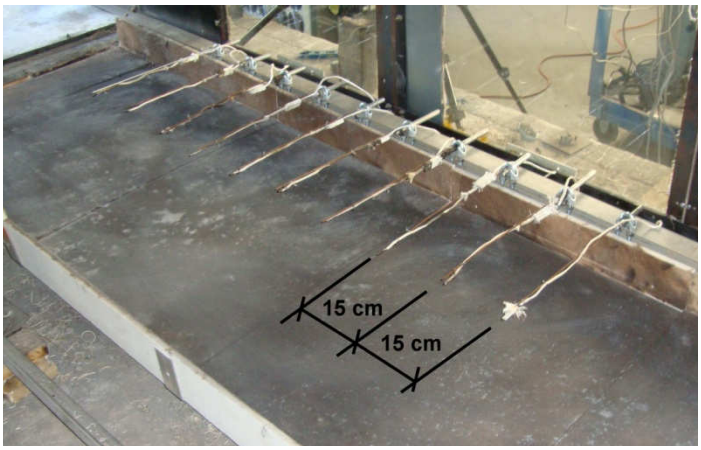


Figure 5.1: Fuel bed thermocouple setup used to determine surface fire rate of spread *R*. A total of 10 thermocouples (15 cm apart).

A new addition to these set of experiments was the Particle Image Velocimetry (PIV) system which was used to measure the flow field within and ahead of the propagating fire front in the region between the surface fuel and the crown fuel matrix, Figure 5.2.

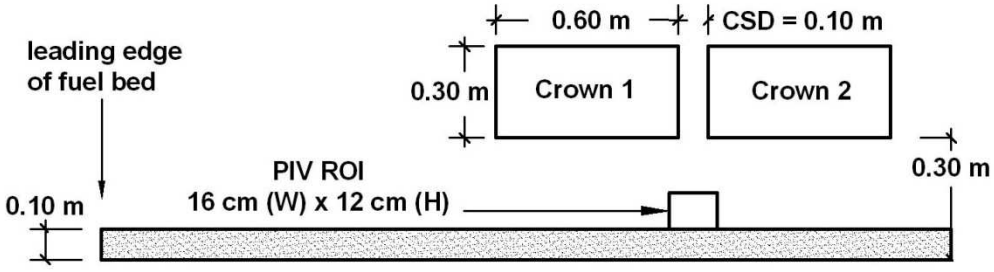
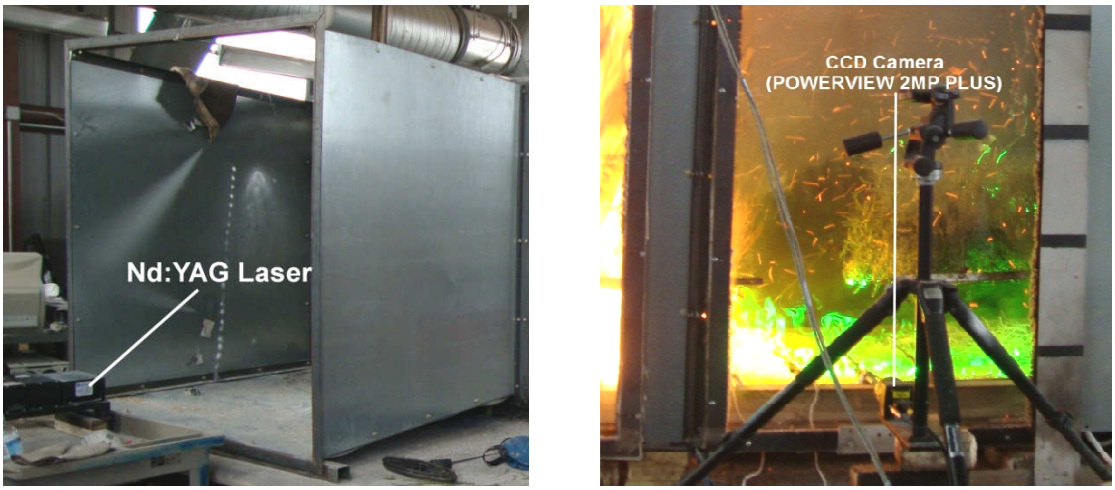


Figure 5.2: Schematic of surface fuel bed with crown fuel system and appropriate dimensions. Also shown is the PIV region of interest (ROI).

The PIV theory is described in detail in Chapter 2. The setup was similar as described in Chapter 3. A compressed air line with a pressure of 517 kPa and flow rate of 24.5 l/minute was connected to an aerosol generator containing the seed particles. For these experiments, Al_2O_3 particles (1-2 μm in diameter) with particle response times ranging between 4 to 20 μs were chosen. These particles were selected for their high refractive index (≈1.76) and high melting point (≈2345 K) [61]. The seed particles within the aerosol generator were mixed by the incoming air and ejected out through the top of the aerosol generator which was connected to a transport line that was attached to a long length of steel tube (2.5 cm OD) placed along the centerline within the surface fuel. The seed particles were then injected horizontally into the fire through perforations located along the length of the tube. Once the flow field was seeded a double-pulsed Nd: YAG laser, Figure 5.3a, (Big Sky Laser Technologies, Inc, model CFR400), located 2.0 m from the region of interest, generated a vertical laser sheet with a wavelength of 532 nm and energy of 388 mJ/pulse, thus illuminating the seed particles. A spherical lens (2000 mm focal length) and cylindrical lens (15 mm focal length) ensured that the thinnest section of the laser sheet (waist) was situated at the center of the region of interest. Particle images were captured by a high resolution (1600 x 1200 pixel) POWERVIEW PLUS 2MP CCD camera, Figure 5.3b, (TSI Inc., model 630057) with a 50 mm f/2.8 Nikkor lens and a laser pulse delay and PIV camera exposure time of 600 μs and 800 μs respectively. A 532 nm filter was attached to the camera lens to reduce the flame luminosity. The distance between the laser sheet and camera was 75.0 cm. The particle

images were captured in a 12.0 cm (vertical) x 16.0 cm (horizontal) domain at 2 Hz. The frame straddling technique was applied to measure the velocity field (TSI Inc). Two sequential particles images with a time difference of 300 μs were used to find the velocity field in each interrogation region of 128 x 128 pixels using INSIGHT^{TM} 3.5 software package (TSI Inc).



(a) **(b)**

Figure 5.3: (a) Image showing location of Nd: YAG laser which produces the vertical laser sheet that spans the length of the wind tunnel; (b) Image showing position of CCD camera used to capture PIV images to resolve the flow field within and surrounding a propagating fire front.

From the analysis performed on the data gathered it was determined that horizontal separation distance between crown matrices affected the average surface fire rate of spread. The overall average rate of spread *R* for the cases investigated were 2.03 cm/s, 1.06 cm/s, and 2.06 cm/s for crown separation distances of 0.1 m, 0.2 m and 0.3 m respectively. Analysis of the recorded images for a crown separation distance of 0.1 m showed that as the fire front approached and ignited crown 2, after igniting crown 1, the

surface fire and crown 1 fire front were one merged fire with flame lengths exceeding 1.1 m. This resulted in a greater quantity of radiative energy impinging on crown 2 than for the crown separation distances of 0.2 m and 0.3 m, which both showed that at the instant crown 2 ignited, the surface fire and crown 1 fire were two separate fires with flame lengths not exceeding 0.6 m. From these same images a flame tilt analysis showed that as the fire front propagated towards crown 1 the average flame tilt angle ranged from 26° to 28°. Once the fire front arrived at the location of crown 1 the average flame tilt angle decreased between 14° and 15°.

Using the Particle Image Velocimetry system allowed the flow field at the surface of the surface fuel, between crown 1 and crown 2, to be resolved. Through the analysis of the PIV images for the time when the fire front was at the upstream boundary of the region of interest, it was calculated that the average horizontal component of velocity (velocity of ambient air entrained into the fire front) was 0.28 m/s. When the fire front was within the boundaries of the region of interest, with the fire enveloping the entire domain, the average vertical component of velocity was 1.18 m/s (velocity of the hot gaseous products of combustion).

The experiment of Summer 2010 resulted in further improvements to the overall system. The fuel bed system consisting of the 11.0 kg capacity load cells (model LC302-25) that were placed at the four corners of the surface fuel bed to measure mass loss rate did not function well. Measurements attained through use of this system were deemed not useful as it was difficult to distinguish between data points due to actual mass loss and data points due to vibration of the surface fuel bed as a result of the incoming 1.1 m/s

wind. The fuel bed was redesigned to be situated atop a 0.4 m x 0.3 m precision balance (Sartorius model CPA34001S) with a range of 34 kg and readability of 0.1 g to record surface fuel mass loss rate. Further additions to the measurement system were made by adding the capability to measure heat flux. To measure heat flux from the fire front to adjacent crown fuel matrices, a heat flux sensor (Hukseflux model RC01) is position 0.3 m downstream from crown 2. Sensor RC01 has dimensions of 65 mm x 65 mm x 13 mm, response time of 1.5 s, maximum allowable heat flux of 400 kW/m^2, and is capable of measuring radiation and convection heat flux. To measure heat flux from the fire front to unburned surface fuels, when possible, heat flux sensor (Hukseflux model SBG01) is situated at the downstream edge of the surface fuel. The position of both sensors is shown in Figure 3.5. Through analysis of the PIV data it was determined that it would be more useful to resolve the flow field directly between the crown fuel matrices instead of resolving the flow field at the surface of the fuel bed, as has been done in previous studies [54, 55, 56].

6 Results – Rate of Spread Analysis

The rate of spread, *R*, is investigated for various fuel configurations and environmental conditions. Fuel configurations with increasing complexity of arrangement are investigated. They are (a) surface fuel only configuration, (b) single crown at location crown 1 with surface fuel, (c) single crown at location crown 2 with surface fuel, and (d) surface fuel and both crown configurations with varying distance between crowns. The horizontal distance between crowns investigated is 0.1 m, 0.2 m and 0.3 m. This distance will henceforth be referred to as the crown separation distance, CSD, crown 1 is located upstream from crown 2. For each fuel configuration the wind speed is varied between the following wind conditions: 0.0 m/s (no wind), 1.1 m/s (low wind), and 1.9 m/s (high wind). Temperature data is recorded at 10 Hz, as the fire front propagated along the length of the surface fuel bed. Using a reference temperature, 500 K, and determining the time required by each of the ten thermocouples (TC) to reach the reference temperature allows for the calculation of the rate of spread at each thermocouple location. The experiments for each case are repeated at least 3 times, and the average *R* reported is calculated from all the data in a given case.

Temperature readings from devices such as thermocouples can be significantly affected by radiations errors that occur as a result of the thermocouple bead temperature not be in equilibrium with its surroundings. As the thermocouple beads increase in temperature, greater than the surrounding environment temperature, the temperature difference causes the thermocouple beads to loss heat in the form of radiation loss, thus the bead temperature decreases and the apparent thermocouple junction temperature is

different from the true gas temperature [16, 25, 57, 13]. To compensate of the decrease in temperature a radiation correction is applied to all the thermocouple data which is collected. The radiation correction is based on Ballantyne et al. (1976) work where it was determined that in a fluctuating temperature field the difference in mean temperature between the surrounding gas, *T*, and the thermocouple junction is given by

$$\frac{\sigma\varepsilon T^4}{h+4\sigma\varepsilon T^3} \tag{6.1}$$

where ε is the wire emissivity and σ is the Stefan-Boltzmann constant. The convection heat transfer coefficient *h* is determined using Whitaker's (1972) correlation for external flow over a sphere.

$$Nu = 2+\left(0.4Re^{0.5}+0.6Re^{2/3}\right)Pr^{0.4} \tag{6.2}$$

The Nusselt number, Reynolds number and Prandtl number are found via equations 6.3, 6.4 and 6.5.

$$Nu = \frac{hD_b}{k_g} \tag{6.3}$$

$$Re = \frac{\rho_g U_g D_b}{\mu_g} \tag{6.4}$$

$$Pr = \frac{c_{p,g}\mu_g}{k_g} \tag{6.5}$$

where D_b is the thermocouple bead diameter, U_g is the local gas velocity in the vicinity of the thermocouple bead, ρ_g, μ_g, $c_{p,g}$ and k_g are the density, viscosity, heat capacity at constant pressure and thermal conductivity of gas respectively. The Reynolds number and Prandtl number are used to determine Nusselts number via equation 6.2. Having

determined Nusselts number, equation 6.3 is used to determine the convection heat transfer coefficient *h* that is used to determine the radiation correction from equation 6.1.

6.1 Surface Fuel only and Single Crown Configurations

Baseline Case: Surface Fuel Only Configuration

Table 6.1 shows the average rate of spread for a surface fuel only configuration (configuration a) for the three wind cases of 0.0 m/s, 1.1 m/s and 1.9 m/s. The first column refers to the location of the TC's in relation to the leading edge of the fuel bed, thus, TC2, where the first *R* value is calculated, is located 60 cm from the leading edge of the fuel bed and each consecutive TC thereafter is 20 cm apart. From the data shown in Table 6.1, it is possible to observe how wind affects surface fire rate of spread at each thermocouple. *R* is 1.0 cm/s when the fire front reaches TC2 at 0.0 m/s wind condition. As the wind speed is increased to 1.1 m/s, *R* increases to 2.6 cm/s, and at a wind speed of 1.9 m/s, *R* is 13.7 cm/s. This same trend is observed at each thermocouple location, where the minimum *R* occurs during a no wind (0.0 m/s) condition, and the maximum *R* is during the high wind speed case of 1.9 m/s.

Surface fuel only			
Thermocouple Location (cm)	***R*** **in cm/s for wind speed = 0.0 m/s**	***R*** **in cm/s for wind speed = 1.1 m/s**	***R*** **in cm/s for wind speed = 1.9 m/s**
60	1.0	2.6	13.7
80	1.0	2.2	2.2
100	0.9	3.8	11.2
120	1.1	2.7	2.9
140	0.9	2.3	3.3
160	0.9	2.8	9.1
180	1.0	2.4	3.7
200	1.0	4.2	5.8
220	1.0	2.1	6.3

Table 6.1: Average rate of spread at each thermocouple location for a surface fuel only configuration for the three wind cases (0.0 m/s, 1.1 m/s, 1.9 m/s).

Figure 6.2 is a plot of the data presented in Table 6.1 with standard deviation error bars. It is evident that in the absence of wind, the average rate of spread remains fairly constant as the fire front propagates along the fuel bed with a minimum *R* of 0.9 cm/s and a maximum *R* of 1.1 cm/s, with a standard deviation of 0.1 cm/s. This trend is also observed for a wind speed case of 1.1 m/s where the minimum *R* is 2.1 cm/s and the maximum *R* is 4.2 cm/s with a standard deviation of 0.7 cm/s. When the wind speed is increased to 1.9 m/s, the rate of spread becomes unsteady with standard deviation, minimum and maximum *R* values of 4.0 cm/s, 2.2 cm/s and 13.7 cm/s respectively. The term unsteady as used here refers to the large spatial fluctuation in *R* over the course of the evolution of the fire along the length of the fuel bed.

The increase in *R* can be attributed to how the wind affects the view factors between the surface fire front and the unburned surface fuel during the three wind conditions. As the wind increases from 0.0 m/s to 1.9 m/s the flame tilt angle will increase affecting the view factors. The flame tilt angle is related to fire acceleration and is affected by fire size and stage of growth and can be caused by wind, slope, or the

interaction with other fires [37]. In this study the flame tilt angle is measured from the vertical and is extracted from the recorded video data. During a wind condition of 0.0 m/s the average flame tilt angle as the fire front propagates along the fuel bed is -1°. At wind conditions of 1.1 m/s and 1.9 m/s the average flame tilt angle is 23° and 45°, respectively.

Since at a 0.0 m/s wind condition the flame is approximately vertical (90° from the surface fuel), the view factors can be calculated using Hamilton and Morgan's 1952 view factor equation, equation 6.6, for two finite rectangles, having one common edge, and at an angle of 90° to each other.

$$F_{1-2} = \frac{1}{\pi L}\left(L\tan^{-1}\left(\frac{1}{L}\right) + N\tan^{-1}\left(\frac{1}{N}\right) - \sqrt{\left(N^2+L^2\right)}\tan^{-1}\frac{1}{\sqrt{N^2+L^2}} \right. \tag{6.6}$$

$$\left. + \frac{1}{4}\ln\left\{ \frac{\left(1+L^2\right)\left(1+N^2\right)}{1+L^2+N^2}\left[\frac{L^2\left(1+L^2+N^2\right)}{\left(1+L^2\right)\left(L^2+N^2\right)}\right]^{W^2}\left[\frac{N^2\left(1+N^2+L^2\right)}{\left(1+N^2\right)\left(N^2+L^2\right)}\right]^{H^2} \right\} \right)$$

The view factors during the low and high wind conditions can be calculated using Hamilton and Morgan's 1952 view factor equation, equation 6.7, for two rectangles having a common edge and forming an arbitrary angle, but utilizing the table of numerical values calculated by Feingold (1966).

$$F_{1-2} = \frac{1}{\pi L}\left(-\frac{1}{4}\sin 2\Phi\left[NL\sin\Phi + \left(\frac{1}{2}\pi - \Phi\right)\left(N^2 + L^2\right) + L^2\tan^{-1}\left(\frac{N - L\cos\Phi}{L\sin\Phi}\right)\right.\right. \tag{6.7}$$

$$\left. + N^2\tan^{-1}\left(\frac{L - N\cos\Phi}{N\sin\Phi}\right)\right] + \frac{1}{4}\sin^2\Phi\ln\left\{\left[\frac{\left(1+N^2\right)\left(1+L^2\right)}{1+N^2+L^2-2NL\cos\Phi}\right]^{\csc^2\Phi+\cot^2\Phi}\right.$$

$$\left.\left[\frac{L^2\left(1+N^2+L^2-2NL\cos\Phi\right)}{\left(1+L^2\right)\left(N^2+L^2-2NL\cos\Phi\right)}\right]^{L^2}\right\} + \frac{1}{4}N^2\sin^2\Phi\ln\left[\left(\frac{N^2}{N^2+L^2-2NL\cos\Phi}\right)\right.$$

$$\left.\left[\frac{L^2\left(1+N^2+L^2-2NL\cos\Phi\right)}{\left(1+L^2\right)\left(N^2+L^2-2NL\cos\Phi\right)}\right]^{L^2}\right\} + \frac{1}{4}N^2\sin^2\Phi\ln\left[\left(\frac{N^2}{N^2+L^2-2NL\cos\Phi}\right)\right.$$

$$\left.\left(\frac{1+N^2}{1+N^2+L^2-2NL\cos\Phi}\right)\cos^2\Phi\right] + L\tan^{-1}\left(\frac{1}{L}\right) + N\tan^{-1}\left(\frac{1}{N}\right) - \sqrt{\left(N^2+L^2-2NL\cos\Phi\right)}$$

$$\cot^{-1}\sqrt{\left(N^2+L^2-2NL\cos\Phi\right)} + \frac{1}{2}N\sin\Phi\sin 2\Phi\sqrt{\left(1+N^2\sin^2\Phi\right)}\left[\tan^{-1}\left(\frac{N\cos\Phi}{\sqrt{\left(1+N^2\sin^2\Phi\right)}}\right)\right.$$

$$\left. + \tan^{-1}\left(\frac{L - N\cos\Phi}{\sqrt{\left(1+N^2\sin^2\Phi\right)}}\right)\right] + \cos\Phi\int_0^L \sqrt{\left(1+z^2\sin^2\Phi\right)}\left[\tan^{-1}\left(\frac{N - z\cos\Phi}{\sqrt{\left(1+z^2\sin^2\Phi\right)}}\right)\right.$$

$$\left.\left. + \tan^{-1}\left(\frac{z\cos\Phi}{\sqrt{\left(1+z^2\sin^2\Phi\right)}}\right)\right] dz\right]$$

In equation 6.6 and 6.7, $N = a/b$ and $L = c/b$, Figure 6.1, where a is the flame height, c is the length of the fuel bed or section of surface fuel being investigated, and b is the width of the flame, which in this study is the same as the width of the fuel bed. When Φ is equal to 90°, equation 6.7 reduces to the simplified equation 6.6. For angles other than 90°, equation 6.7 is used. Feingold (1966) tabulated calculated view factors between rectangles having a common edge and forming an angle of 30°, 45°, 60°, 90°, 120°, 135° and 150°. In this study, the view factors during the wind-aided cases were calculated directly using equation 6.7. Figure 6.1 is used to determine *N* and *L*.

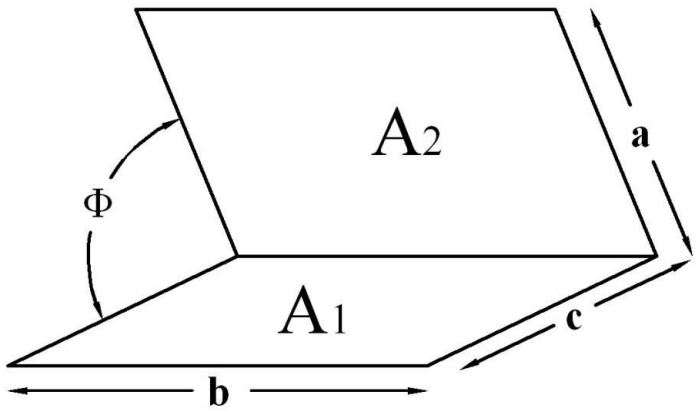
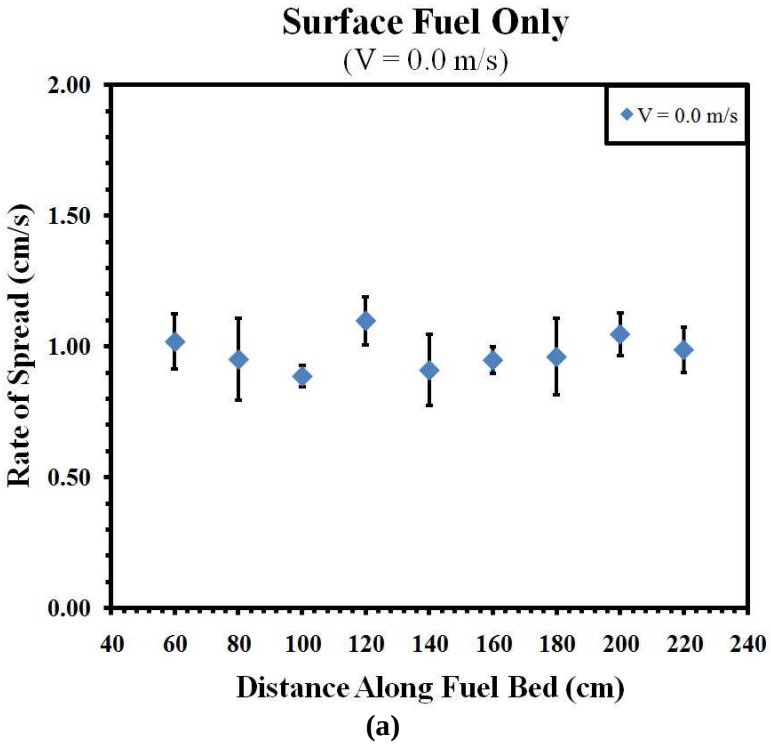
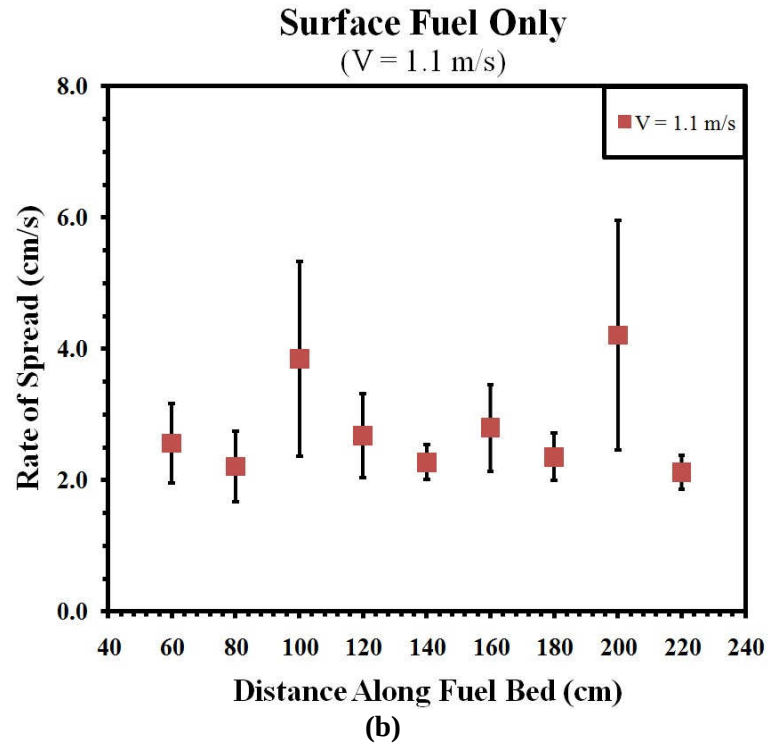


Figure 6.1: Illustration for view factors between rectangles having a common edge and forming an arbitrary angle.

High view factors will result in larger quantities of radiation flux impinging onto unburned surface fuel, leading to high *R* measurements, which are observed at a wind condition of 1.1 m/s and 1.9 m/s.



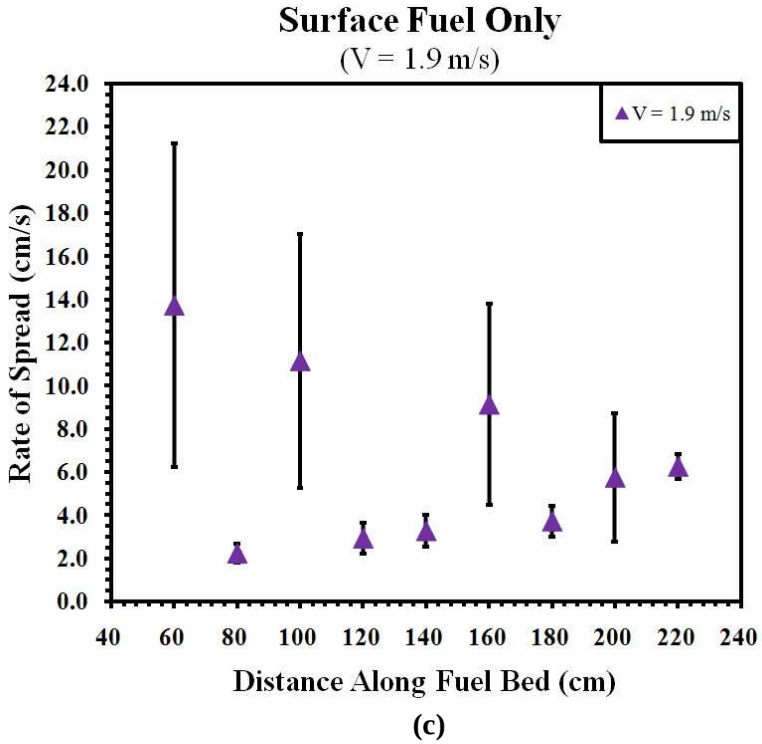
(a)



(b)

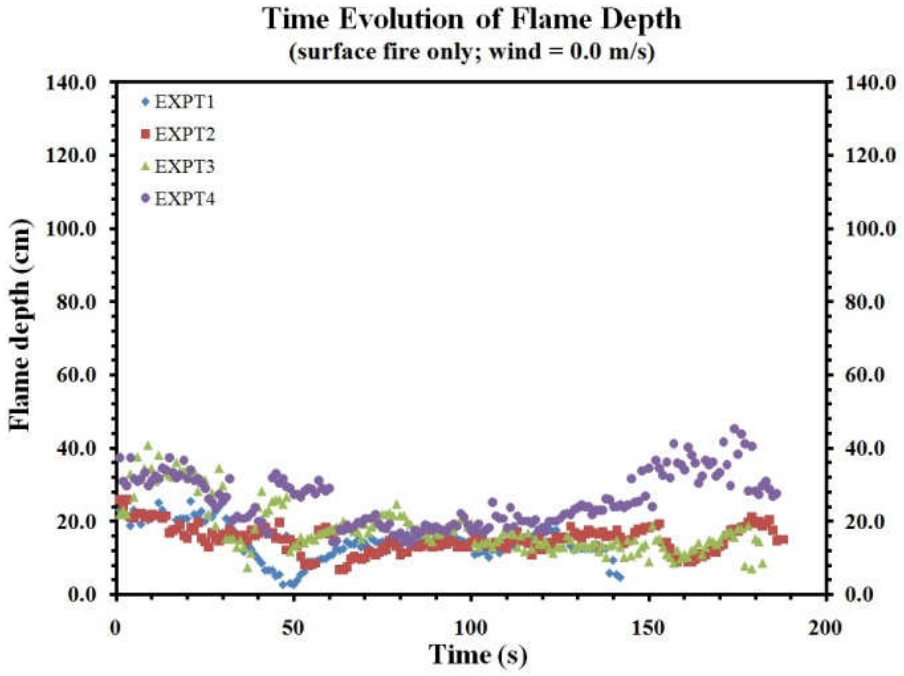
Figure 6.2: Average rate of spread at each thermocouple location plot for a surface fuel only configuration for the three wind speed cases of: (a) 0.0 m/s; (b) 1.1 m/s; (c) 1.9 m/s; with standard deviation error bars.

Figure 6.2 continued …

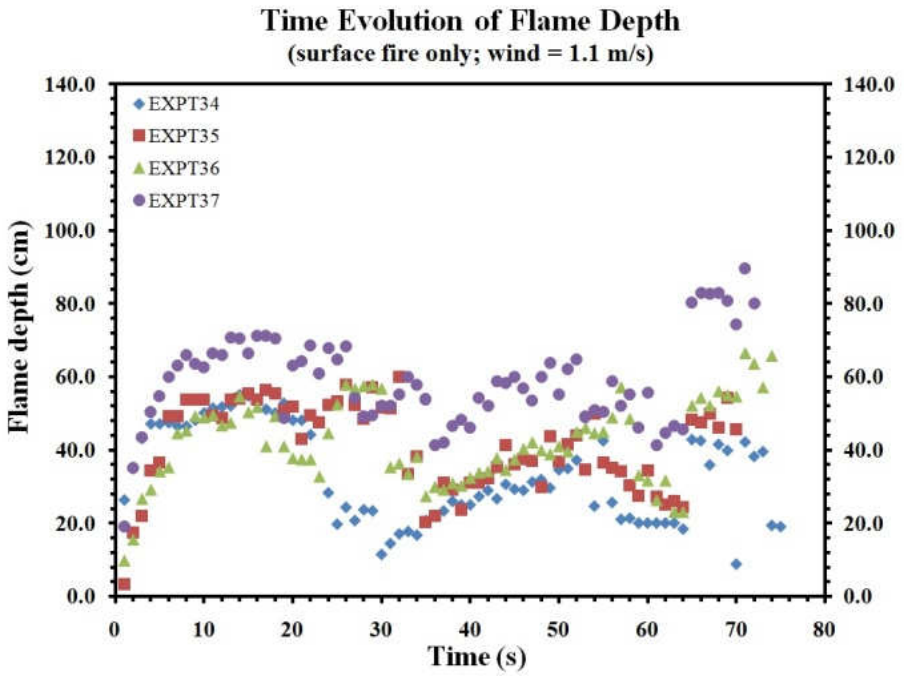


(c)

An analysis is performed to further investigate the instability of *R* between the three wind conditions. The time evolution of surface flame depth as the fire front propagates along the length of the surface fuel bed is extracted from the recorded video data. Figure 6.3 contains the plots for surface flame depth over the experiment time for all the experiments performed for a given wind condition for configuration a (surface fuel only). During a 0.0 m/s wind condition the flame depth ranges between 45.3 cm and 2.8 cm with an average flame depth of 18.5 cm. Figure 6.3a shows that flame depth over the experiment history does not vary significantly. The surface flame front has sufficient time and space to reach a steady combusting phase, thus *R* is quasi-steady as the fire front propagates along the fuel bed.



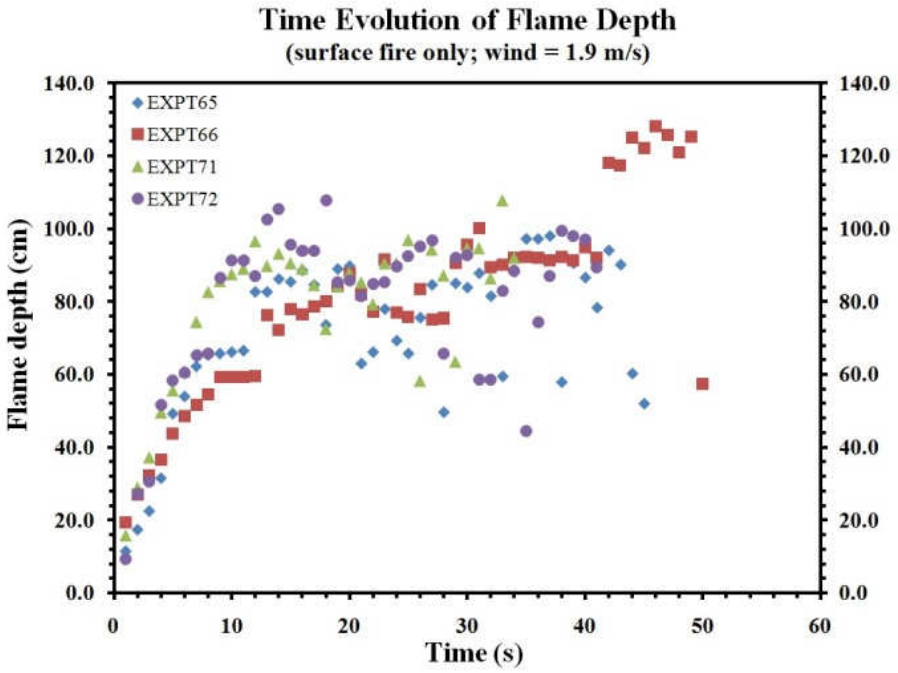
(a)



(b)

Figure 6.3: Time evolution of surface flame depth for fuel configuration a during a wind condition of: (a) 0.0 m/s; (b) 1.1 m/s; (c) 1.9 m/s.

Figure 6.3 continued …



(c)

Flame depth variation increases to a maximum and minimum of 89.6 cm and 3.4 cm, respectively, when the wind speed is increased to 1.1 m/s, Figure 6.3b. The large variation in flame depth results in a fairly unstable *R*. The largest flame depth variation is observed during a wind condition of 1.9 m/s where flame depth ranges between 128.2 cm and 9.4 cm, Figure 6.3c. At a wind speed of 1.9 m/s the surface fire front does not have sufficient time and space to achieve a steady combusting phase. As a result *R* is unstable as the fire front progresses along the fuel bed. A comparison of average flame depth during the three wind conditions shows that average flame depth is larger at a wind speed of 1.9 m/s by a factor of 1.8 and 4.2 in comparison to wind speeds of 1.1 m/s and 0.0 m/s, respectively.

Figure 6.4 shows the tabulated view factor values and corresponding plot for configuration a at a wind speed of 0.0 m/s. The fire front propagates from left to right in the plot and as such the view factors are plotted in the same fashion. The left side of the x-axis represents the leading edge of the fuel bed (at approximately x=3.5 m) and the right side of the x-axis represents the downstream edge of the fuel bed (at x=0.0 m). All view factor values at a wind condition of 0.0 m/s were calculated by determining an average flame length over the time of the experiments and using that average flame length and equation 6.6 to compute the view factors as the fire front propagated along the fuel bed. Observation of Figure 6.4 shows that as the fire front propagates towards the downstream edge of the fuel bed, the view factors exhibit an exponential behavior increasing considerably as the fire front approaches the downstream edge of the fuel bed. The minimum view factor of 0.033 was calculated at 3.6 m for the downstream edge of the fuel bed and the maximum view factor of 0.397 was calculated at 0.1 m from the downstream edge of the fuel bed.

Surface fuel only V = 0.0 m/s	
Distance from fuel bed downstream edge (m)	F_{1-2}
3.6	0.033
3.5	0.034
3.4	0.035
3.3	0.036
3.2	0.037
3.1	0.039
3.0	0.040
2.9	0.041
2.8	0.043
2.7	0.044
2.6	0.046
2.5	0.048
2.4	0.050
2.3	0.052
2.2	0.054
2.1	0.056
2.0	0.059
1.9	0.062
1.8	0.065
1.7	0.069
1.6	0.073
1.5	0.078
1.4	0.083
1.3	0.089
1.2	0.096
1.1	0.104
1.0	0.113
0.9	0.124
0.8	0.137
0.7	0.153
0.6	0.173
0.5	0.198
0.4	0.230
0.3	0.272
0.2	0.326
0.1	0.397

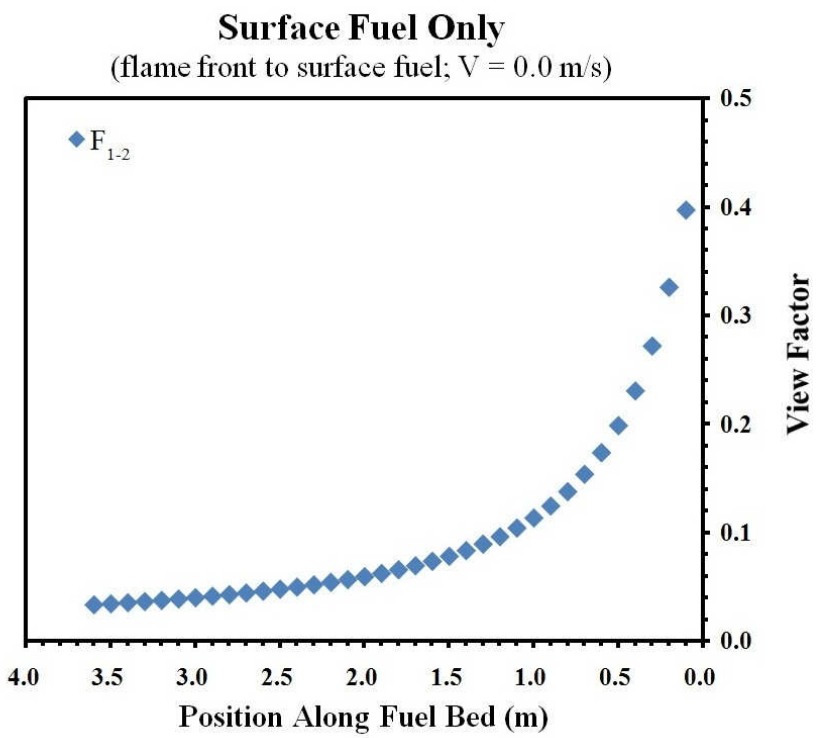


Figure 6.4: Tabulated view factor values and corresponding plot for a surface fuel only configuration at a wind condition of 0.0 m/s. Left side of plot represents leading edge of fuel bed while right side of plot represents the downstream edge of the fuel bed.

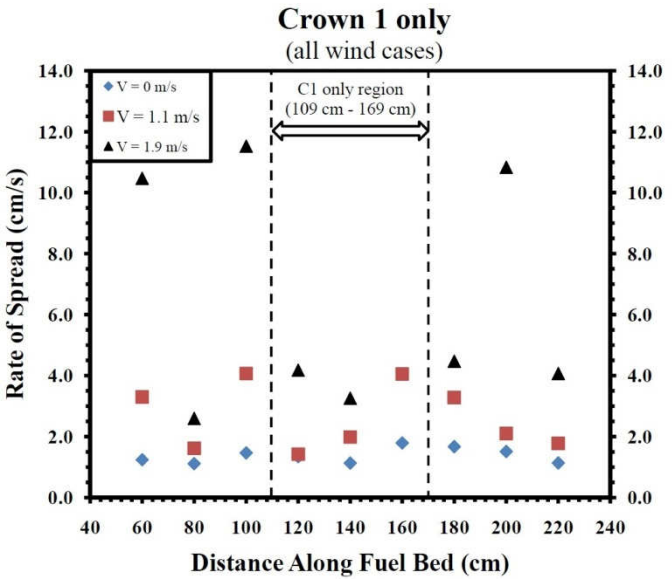
Surface Fuel and Crown 1 Configuration

Table 6.2 shows average rates of spread *R* for a surface fuel with crown 1 configuration, referred to as configuration b. Similar to configuration a, *R* is a minimum for the no wind condition while the maximum *R* occurs at the high wind speed case of 1.9 m/s for configuration b. Figure 6.5a is a plot of the data in Table 6.2. It shows that for a no wind condition, as the fire front propagates along the fuel bed, *R* remains quasi-steady with a standard deviation of 0.2 cm/s. When the wind speed is increased to 1.1 m/s and to 1.9 m/s, the rate of spread becomes increasing unsteady with standard deviations of 1.1 cm/s and 12.0 cm/s, respectively.

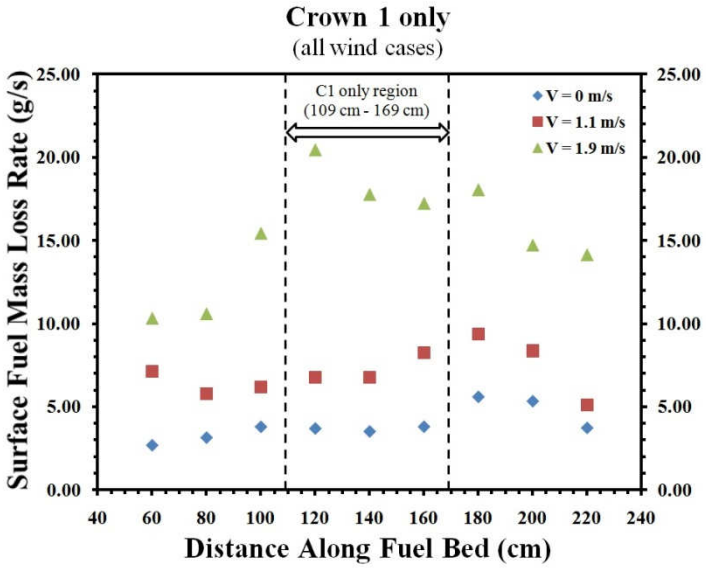
Crown 1 only			
Thermocouple Location (cm)	***R* in cm/s for wind speed = 0.0 m/s**	***R* in cm/s for wind speed = 1.1 m/s**	***R* in cm/s for wind speed = 1.9 m/s**
60	1.2	3.3	10.5
80	1.1	1.6	2.6
100	1.5	4.1	11.5
120	1.3	1.4	4.2
140	1.1	2.0	3.3
160	1.8	4.1	40.7
180	1.7	3.3	4.5
200	1.5	2.1	10.8
220	1.1	1.8	4.1

Table 6.2: Average rate of spread at each thermocouple location for a surface fuel and crown 1 configuration for the three wind cases (0.0 m/s, 1.1 m/s, 1.9 m/s).

A similar analysis is performed on the surface fuel mass loss rate, $\dot{m}$ at each thermocouple location, Figure 6.5b, and a comparison can be made to the *R* plot, Figure 6.5a. As the fire front propagates along the fuel bed $\dot{m}$ is quasi-steady with a minimum of 2.7 g/s and a maximum of 5.6 g/s with a standard deviation of 1.0 g/s. At a wind speed of 1.1 m/s the minimum and maximum values of $\dot{m}$ are 5.1 g/s and 9.4 g/s, respectively, with a standard deviation of 1.4 g/s, which is still quasi-steady. The surface fuel mass loss rate along the fuel bed becomes unsteady with minimum and maximum values of 10.3 g/s and 20.4 g/s, respectively, and a standard deviation of 3.4 g/s when the wind speed is increased to 1.9 m/s.



(a)



(b)

Figure 6.5: Surface fuel and crown 1 configuration plots for the three wind speed cases of 0.0 m/s, 1.1 m/s and 1.9 m/s of: (a) Average rate of spread *R* at each thermocouple location; *R* plots containing standard deviation error bars located in Appendix B; (b) Average surface fuel mass loss rate at each thermocouple location.

At a wind speed of 1.1 m/s, Figure 6.5a and b show that as the fire front reaches the upstream edge of crown 1, which is 109 cm from the leading edge of the fuel bed, both R and $\dot{m}$ increase from TC3 to TC4. Through the crown 1 region, area in Figure 6.5 plots shown between the dashed lines, R increases from 1.4 cm/s to 4.1 cm/s and $\dot{m}$ increases from 6.8 g/s to 8.3 g/s. A similar trend is observed for the no wind condition for both R and $\dot{m}$. Figure 6.6 can be used to explain the increase in R and $\dot{m}$.

Data from Figure 6.6 represent the total heat flux (kW/m^2) from the fire front impinging on the surface fuel at the downstream edge of the fuel bed (data from heat flux sensor SBG01). This plot shows the curves for all the experiments (experiments 76, 77 and 80) for a surface fuel and crown 1 configuration at a wind speed of 1.1 m/s plotted together. Heat flux data for experiments 76 and 80 have been time shifted so that all the curves begin at the instant of crown 1 ignition in experiment 77.

Figure 6.6 shows that as crown 1 ignites, the total heat flux impinging onto the surface fuel at the downstream edge of the surface fuel increases to an average maximum heat flux of 2.79 kW/m^2. This increase in heat flux preheats the unburned fuel ahead of the propagating fire front resulting in an increase of R and $\dot{m}$ from TC5 to TC7 as shown in Figure 6.5a and b, and previously mentioned, during a no wind and 1.1 m/s wind condition within the crown 1 boundaries. As the crown 1 fire begins to extinguish, the total heat flux begins to decrease to an average minimum plateau value of 0.70 kW/m^2. The decrease in total heat flux results in a decrease in both R and $\dot{m}$, from TC7 to TC10, for both of the low wind conditions (0.0 m/s and 1.1 m/s). During the no wind condition, R decreases from 1.7 cm/s to 1.1 cm/s and $\dot{m}$ decrease from 5.6 g/s to 3.7 g/s. At a wind

speed of 1.1 m/s, R decreases from 3.3 cm/s to 1.8 cm/s and $\dot{m}$ decrease from 9.4 g/s to 5.1 g/s.

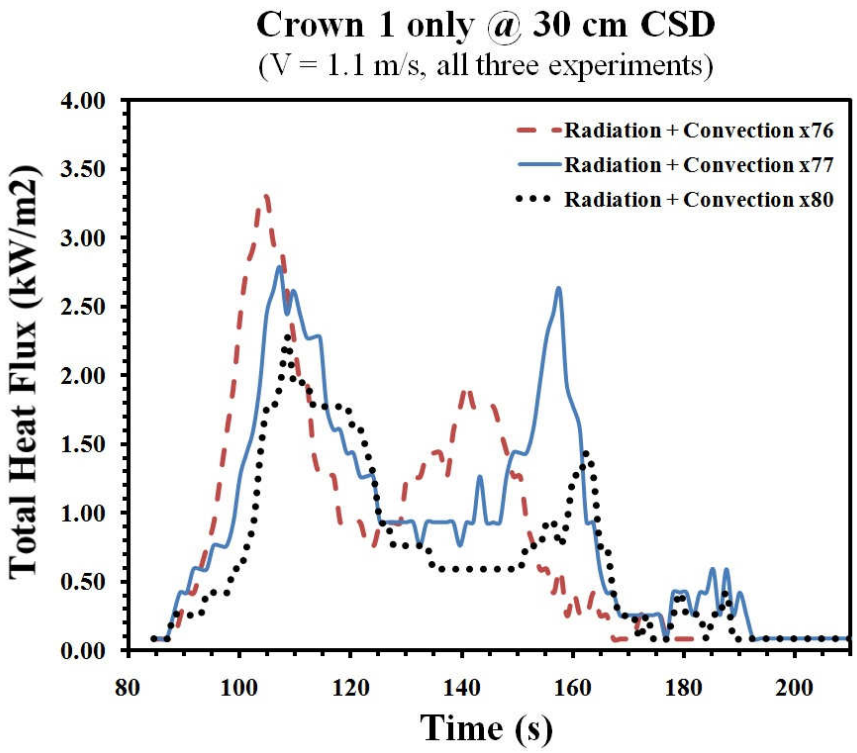


Figure 6.6: Plot of total heat flux impinging onto the surface fuel at the downstream edge of the fuel bed for a surface fuel and crown 1 configuration at a wind speed of 1.1 m/s. Note: curves for x76 (experiment 76) and x80 have been time shift to all start at the instant crown 1 ignites in x77.

After crown 1 extinguishes, the total heat flux reduces to a condition similar to what would have been present if no crown 1 fuel matrix had ignited and instead only a surface fire front under a 1.1 m/s wind speed existed, Figure 6.7. The total heat flux impinging on the fuel at the downstream edge of the fuel bed will increase as the fire front approaches with an average maximum total heat flux of 2.0 kW/m^2. When the fire front reaches the edge of the fuel bed and begins to completely exhaust the surface fuel supply, the total heat flux will then decrease until the fire is extinguished. At a wind

speed of 1.1 m/s and a surface fuel only configuration the maximum total heat flux that impinges on the fuel at the downstream edge of the fuel bed is 2.9 kW/m^2, Figure 6.7.

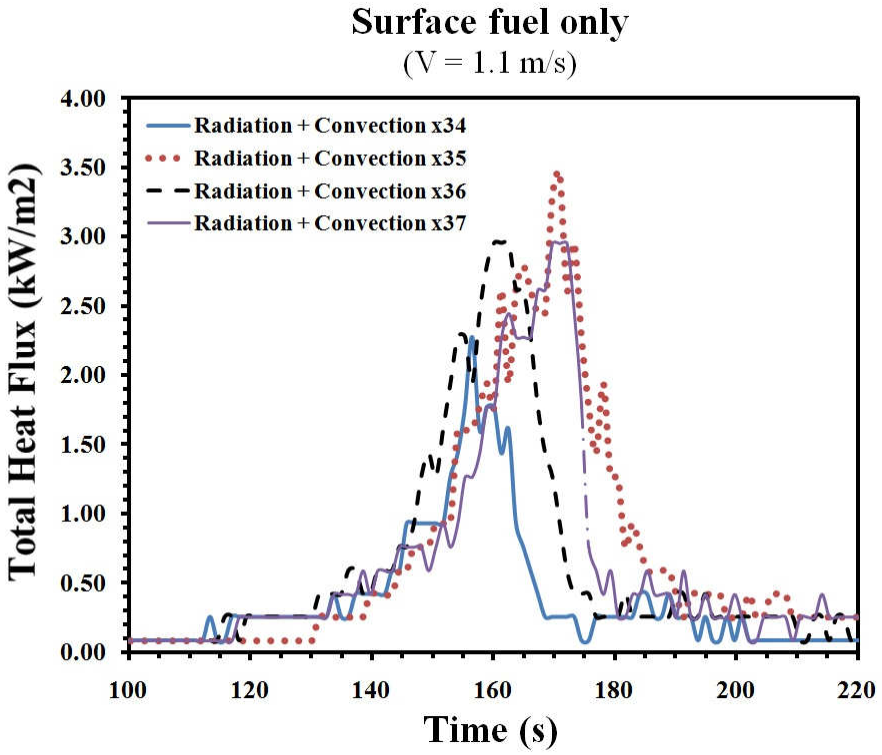


Figure 6.7: Plot of total heat flux impinging onto the surface fuel at the downstream edge of the fuel bed for a surface fuel only configuration at a wind speed of 1.1 m/s. Note: curves for x35 (experiment 35), x36, and x37 have been time shift.

Figure 6.8 shows that as wind speed is increased to 1.9 m/s from 1.1 m/s, the average maximum total heat flux after crown 1 ignition increases to 7.05 kW/m^2 from the 2.79 kW/m^2 in the 1.1 m/s wind speed case. Similarly at a wind speed of 1.9 m/s, as the crown 1 fire exhausts the crown fuel supply, the total heat flux begins to decrease to an average minimum plateau value, as was evident in the 1.1 m/s wind speed case for the same fuel configuration. At this plateau the average minimum total heat flux is 2.11 kW/m^2. After crown 1 extinguishes the surface fire front continues to propagate along

the fuel bed as it would have done otherwise if there was no crown 1 ignition, but instead a surface fuel only configuration with a 1.9 m/s wind. As the surface fire front continues propagating, after crown 1 fire extinction, the average maximum total heat flux impinged onto the unburned surface fuel ahead of the fire front is 4.01 kW/m^2.

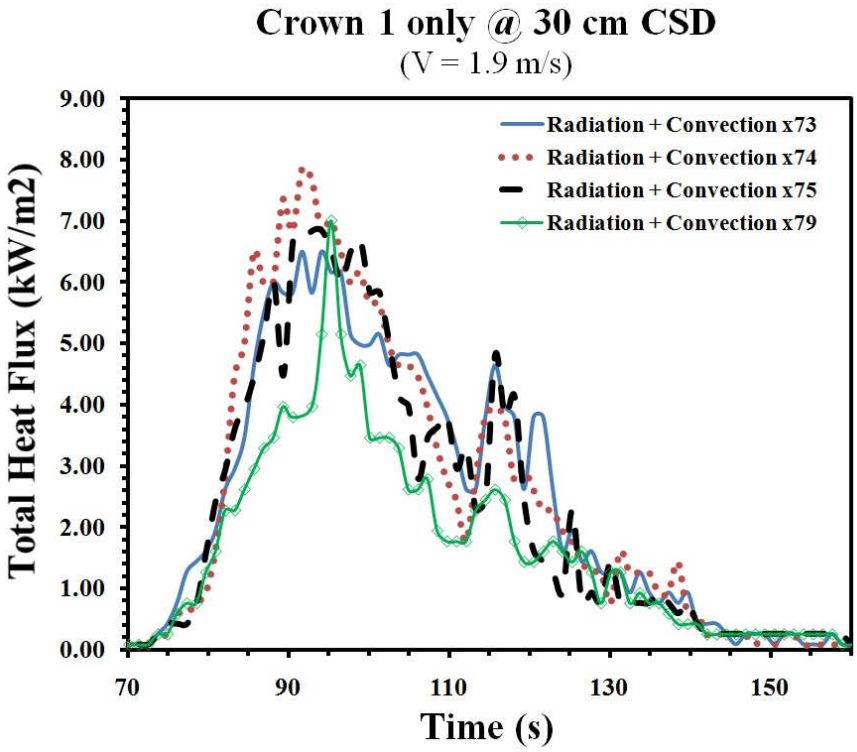


Figure 6.8: Plot of total heat flux impinging onto the surface fuel at the downstream edge of the fuel bed for a surface fuel and crown 1 configuration at a wind speed of 1.9 m/s. Note: curves for x74 (experiment 74), x75, and x79 have been time shift.

Under the same wind condition, but with a surface fuel only configuration, the average maximum total heat flux impinging on the unburned surface fuel at the downstream edge of the surface fuel bed is 7.85 kW/m^2, Figure 6.9. The same analysis is performed for the three wind cases for a surface fuel and crown 2 configuration.

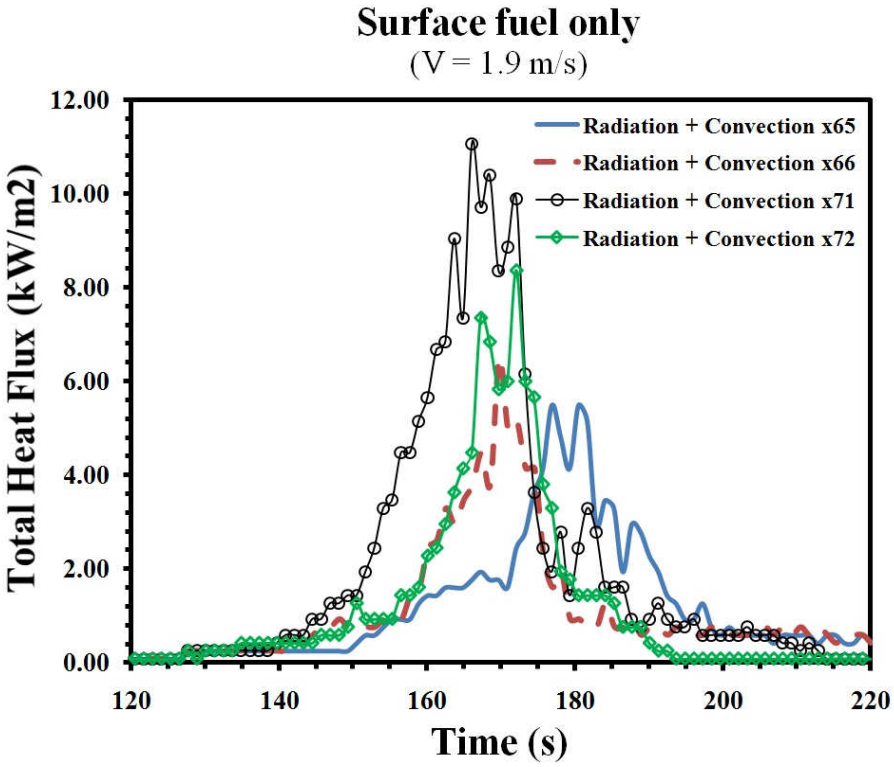


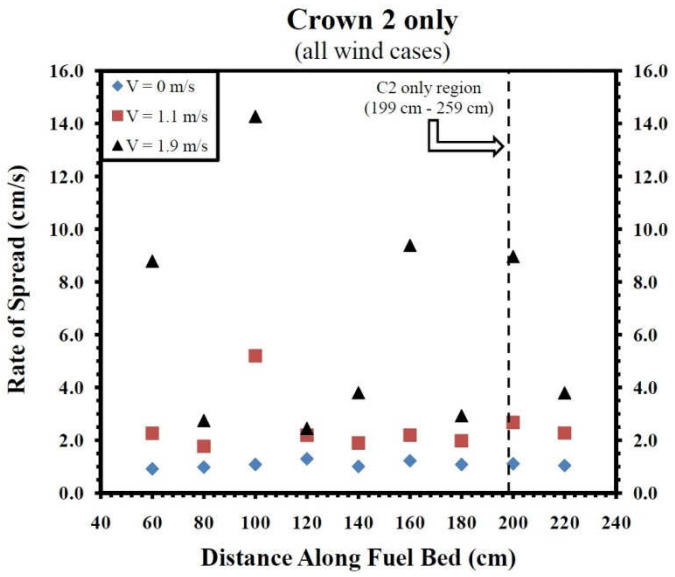
Figure 6.9: Plot of total heat flux impinging onto the surface fuel at the downstream edge of the fuel bed for a surface fuel only configuration at a wind speed of 1.9 m/s. Note: curves for x66 (experiment 66), x71, and x72 have been time shift.

As with the previous two fuel configurations, configurations a and b, the minimum and maximum *R* occurs at the no wind and 1.9 m/s conditions respectively. The standard deviation of *R* for the three wind cases is determined from the data of Table 6.3. At wind speeds of 0.0 m/s, 1.1 m/s and 1.9 m/s, the *R* standard deviation is 0.1 cm/s, 1.0 cm/s and 4.1 cm/s, respectively. The standard deviation of $\dot{m}$ is 0.3 g/s , 1.1g/s , and 1.3 g/s for wind speeds of 0.0 m/s, 1.1 m/s and 1.9 m/s respectively.

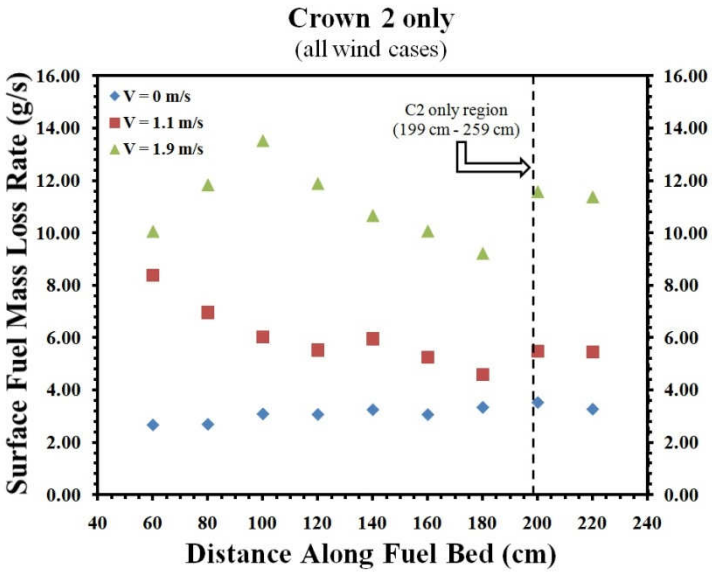
Crown 2 only			
Thermocouple Location (cm)	***R*** **in cm/s for wind speed = 0.0 m/s**	***R*** **in cm/s for wind speed = 1.1 m/s**	***R*** **in cm/s for wind speed = 1.9 m/s**
60	0.9	2.3	8.8
80	1.0	1.8	2.7
100	1.1	5.2	14.3
120	1.3	2.2	2.4
140	1.0	1.9	3.8
160	1.2	2.2	9.4
180	1.1	2.0	2.9
200	1.1	2.7	9.0
220	1.0	2.3	3.8

Table 6.3: Average rate of spread at each thermocouple location for a surface fuel and crown 2 configuration for the three wind cases (0.0 m/s, 1.1 m/s, 1.9 m/s).

Figure 6.10a and b show plots of R and $\dot{m}$, respectively, at each thermocouple location for the three wind cases for a surface fuel and crown 2 configuration, configuration c. The upstream edge of crown 2 is at 199 cm from the leading edge of the surface fuel bed. Both R and $\dot{m}$ curves show that during a no wind condition, rate of spread and surface fuel mass loss are fairly stable. During the no wind condition, the 95% confidence interval for the overall rate of spread is 1.08 cm/s ± 0.08 cm/s, and the corresponding $\dot{m}$ 95% confidence interval is 3.11 g/s ± 0.24 g/s. As the wind speed is increased to 1.1 m/s both R and $\dot{m}$, again, remain stable with 95% confidence intervals of 2.51 cm/s ± 0.31 cm/s and 5.96 g/s ± 0.38 g/s respectively. The stability can also be observed in Figure 6.11 where the total heat flux for the repeated experiments is plotted over the experiment time. The curves of Figure 6.11 show that as the fire front approaches crown 2, the total heat flux impinging on the unburned fuel at the downstream edge of the fuel bed is stable.



(a)



(b)

Figure 6.10: Surface fuel and crown 2 configuration plots for the three wind speed cases of 0.0 m/s, 1.1 m/s and 1.9 m/s of: (a) Average rate of spread at each thermocouple location; *R* plots containing standard deviation error bars located in Appendix B; (b) Average surface fuel mass loss rate at each thermocouple location.

As crown 2 ignites the total heat flux production continues to be stable resulting in smooth total heat flux curves for all repeated experiments with surface fuel and crown 2 configuration that are exposed to a 1.1 m/s wind. The average maximum total heat flux impinged unto the unburned surface fuel at the downstream edge of the fuel bed during crown 2 combustion is 10.5 kW/m^2.

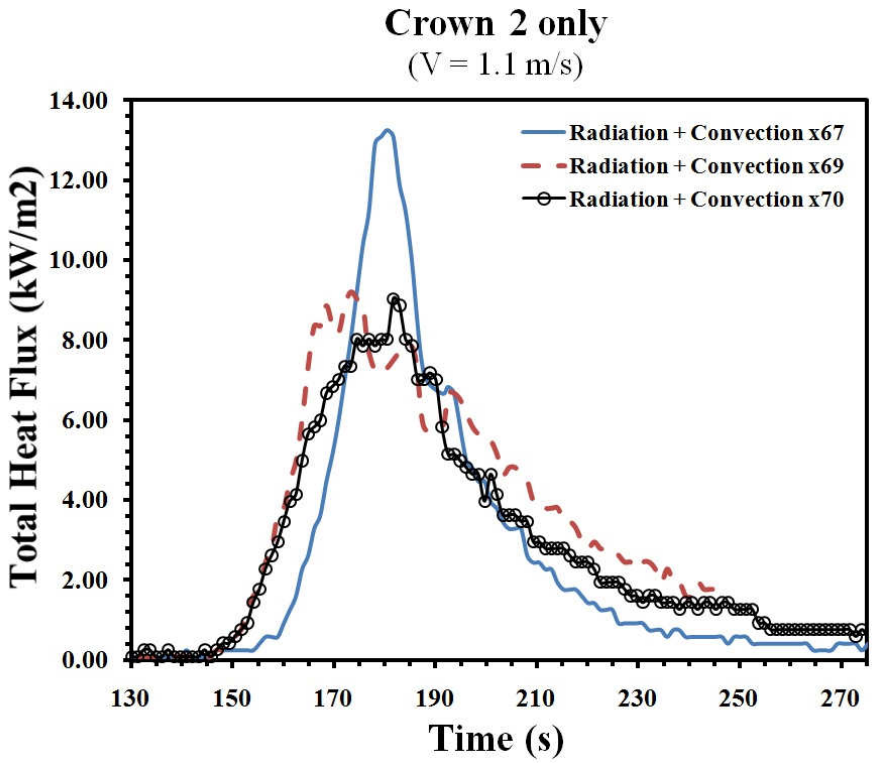


Figure 6.11: Plot of total heat flux impinging onto the surface fuel at the downstream edge of the fuel bed for a surface fuel and crown 2 configuration at a wind speed of 1.1 m/s. Note: curves for x69 (experiment 69) and x70 have been time shift.

Since the location of crown 2 is at the downstream edge of the surface fuel bed, as the surface fire front extinguishes so does the crown 2 fire, thus the curves of Figure 6.11 do not show a second total heat flux peak as was the case in configuration b.

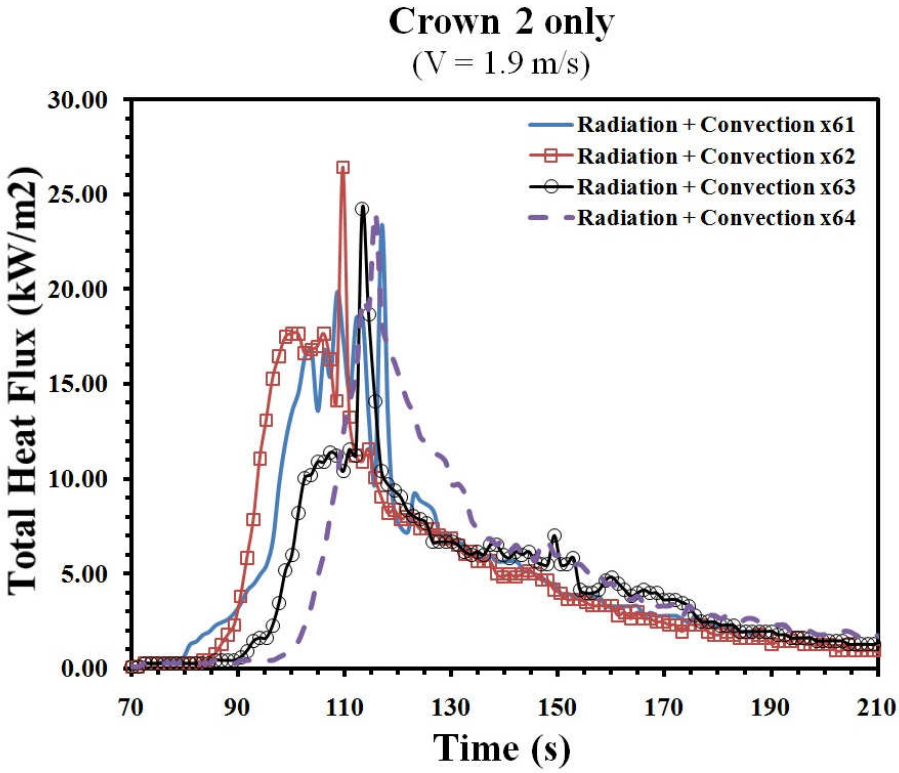


Figure 6.12: Plot of total heat flux impinging onto the surface fuel at the downstream edge of the fuel bed for a surface fuel and crown 2 configuration at a wind speed of 1.9 m/s. Note: curves for x62 (experiment 62), x63 and x64 have been time shift.

Figure 6.10a and b show that when wind speed is increased to 1.9 m/s both R and $\dot{m}$ along the fuel bed become very unstable. The instability is also observed in the total heat flux data for all repeated experiments in this case, Figure 6.12. During this wind condition the 95% confidence interval for R and $\dot{m}$ is 6.35 cm/s ± 0.69 cm/s and 11.14 g/s ± 1.06 g/s, respectively.

6.2 Multiple Crown Fuel Configurations

The next analysis performed is conducted in three parts. First, the wind speed is kept constant while the distance between crown fuel matrices is varied between 10 cm, 20 cm and 30 cm. This procedure is performed for a total of three wind speeds, 0.0 m/s, 1.1 m/s and 1.9 m/s. Fire front rate of spread and crown matrix ignition is investigated through use of the thermocouples to calculate rate of spread, and a heat flux sensor capable of recording total heat flux and convection heat flux. Heat flux sensor RC01 is placed vertically facing the upstream side of the wind tunnel at a location where an imaginary third crown fuel matrix at the downstream side of the wind tunnel would exist, which is approximately 289 cm from the leading edge of the fuel bed or 30 cm from the downstream face of crown 2. RC01 sensor will collect total heat flux and convection heat flux to investigate heat transfer phenomena to a would-be third crown fuel matrix located at the downstream side of the fuel configuration, henceforth referred to as crown 3.

Crown Separation Distance of 10 cm with No Wind

V = 0.0 m/s, Crown 1 and Crown 2 at 10 cm CSD			
TC #	Location (cm)	R (cm/s)	$\dot{m}$ (g/s)
2	60	0.9	3.2
3	80	0.9	2.9
4	100	1.1	3.2
5	120	1.0	3.3
6	140	1.0	3.3
7	160	1.1	3.4
8	180	1.4	4.2
9	200	1.7	4.8
10	220	1.3	4.7

Table 6.4: Average rate of spread and average surface fuel mass loss rate data at each thermocouple location for a crown separation distance of 10 cm during a no wind condition.

Table 6.4 shows the average rate of spread R and average surface fuel mass loss rate $\dot{m}$ at each thermocouple location along the fuel bed. Thermocouple 2, TC2, is located at 60 cm from the leading edge of the fuel bed and each consecutive TC is 20 cm apart. Recorded data stops at TC10, which is located 220 cm from the leading edge of the fuel bed. Data from Table 6.4 is plotted and shown in Figure 6.13. First the analysis at a CSD of 10 cm and a no wind condition is performed. Data for R is shown in Figure 6.13 as square markers while $\dot{m}$ is shown as diamonds, and the edges of crown 1 are indicated as dotted lines and the lead edge of crown 2 is indicated by a dashed line. Figure 6.14 shows images taken during experiment 24 capturing the combustion process from ignition of crown 1 to ignition of crown 2. As the fire front approaches the leading edge of crown 1, R begins to decrease from 1.1 cm/s, at TC4, to 1.0 cm/s, at TC6. The decrease in R is due to the heat from the fire front being reallocated to preheat crown 1 fuel matrix and the change in view factor due to the existence of crown 1 (e.i. crown 1 obstructing the heat flux from impinging onto the unburned surface fuel), as a result less heat is available to preheat the unburned surface fuel ahead of the fire front. As the fire front approaches crown 1, approximately 2.1 m from the downstream edge of the surface fuel, the view factor growth rate diminishes, growing at a slower rate when compared to the view factor growth rate in the region before crown 1, Figure 6.15. Figure 6.16 shows the total heat flux plot and the corresponding temperature at the crown fuel matrices plot for experiments 23 (Figure 6.16a and b) and 24 (Figure 6.16c and d) respectively. Figure 6.16c and d are shown to demonstrate experiment repeatability.

As crown 1 ignites in experiment 23 the air temperature preheating crown 1 reaching a maximum of 1,180 K. The warm air preheats the chamise branch to approximately 380 K before igniting and proceeding to enter the flaming phase reaching a maximum temperature of 1,126 K, Figure 6.16b. The preheating of the chamise branch to approximately 380 K before combustion, Figure 6.16b, is observed in all plots for this fuel configuration for a no wind condition. During the combustion of crown 1, the combined heat flux from the surface and crown 1 fire fronts assist in preheating the unburned surface fuel. The combustion of crown 1 causes an influx of oxygen to the fire front accelerating the combustion process, which is evident by the increase in flame lengths, Figure 6.14b, and an increase in heat flux output, Figure 6.16a. During crown 1 combustion, maximum flame length observed surpassed 1.8 m and maximum total heat flux and convection flux were 1.98 kW/m^2 and 0.18 kW/m^2 respectively. As a result of the increase in heat flux, R increases from 1.0 cm/s, TC6 at 1.4 m, to 1.7 cm/s, TC9 at 200 cm. The same trend is observed for $\dot{m}$ from TC6 to TC9 where $\dot{m}$ increases from 3.3 g/s to 4.8 g/s, respectively. The increase in flame lengths results in a significant increase in view factor growth rate from the instant crown 1 ignites (1.3 m from the downstream edge of the fuel bed) until the fire front reaches the downstream edge of the fuel bed, Figure 6.15. At the upstream edge of crown 1, the view factor is 0.069. The view factor increases exponentially reaching a maximum value of 0.375 as the fire front propagates towards the downstream edge of the surface fuel bed.

As the fire front approaches crown 2, the heat flux is obstructed from impinging on the unburned surface fuel ahead of the fire front and heat is reallocated to preheat and

ignite crown 2, Figure 6.14c. During crown 2 preheating and ignition, R decreases from 1.7 cm/s to 1.3 cm/s and $\dot{m}$ decreases from 4.8 g/s to 4.7 g/s. The hot gaseous products of combustion reach a maximum temperature of 1,358 K as crown 2 is consumed. The hot combustion gases preheat the chamise branch from crown 2 to approximately 380 K before it ignites and reaches a maximum temperature of 1,114 K as crown 2 burns. A maximum total and convection heat flux of 7.16 kW/m^2 and 0.67 kW/m^2, respectively, are impinged onto crown 3 at the downstream edge of the fuel bed.

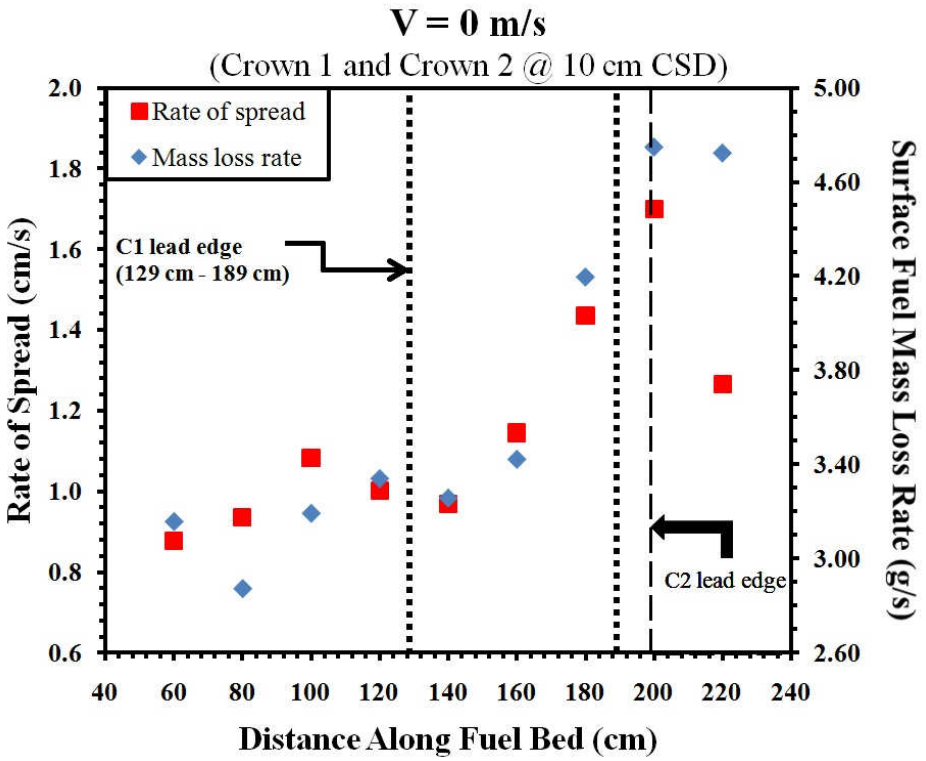
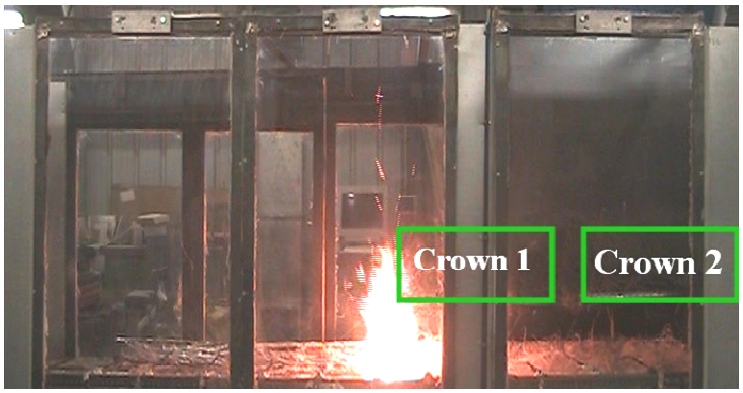


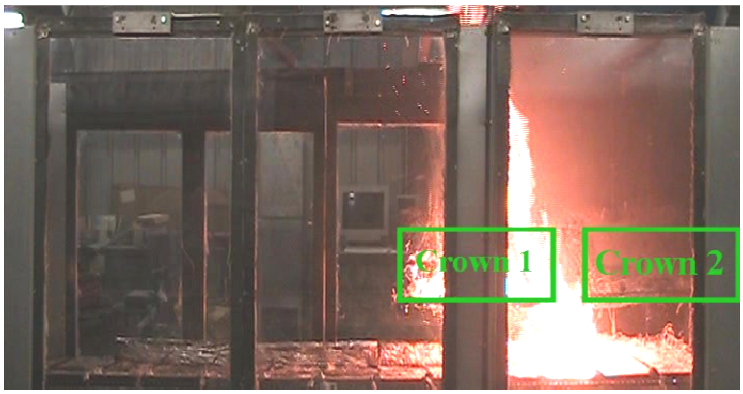
Figure 6.13: Average rate of spread and surface fuel mass loss rate at each thermocouple location plot for a crown separation distance of 10 cm during a no wind condition. Left axis represents values for rate of spread and right axis represents values for surface fuel mass loss rate; *R* plot containing standard deviation error bars located in Appendix B.



(a)



(b)



(c)

Figure 6.14: Images from experiment 23 at (a) t = 282 s at time of crown 1 ignition; (b) t = 330 s during crown 1 combustion; (c) t = 340 s at time of crown 2 ignition.

For the four experiments performed at a crown separation distance of 10 cm during a no wind condition, the average maximum total heat flux and convection heat flux is 8.88 kW/m^2 and 0.89 kW/m^2 respectively. The confidence values for the maximum total heat flux and convection flux is ± 1.75 kW/m^2 and ± 0.18 kW/m^2, respectively. The confidence interval for the overall R and $\dot{m}$ is 1.16 cm/s ± 0.18 cm/s and 3.66 g/s ± 0.98 g/s, respectively.

Crown 1 and 2 @ 10 cm CSD V = 0.0 m/s	
Distance from fuel bed downstream edge (m)	F_{1-2}
3.6	0.036
3.5	0.037
3.4	0.038
3.3	0.039
3.2	0.040
3.1	0.041
3.0	0.043
2.9	0.044
2.8	0.046
2.7	0.047
2.6	0.049
2.5	0.051
2.4	0.053
2.3	0.056
2.2	0.058
2.1	0.059
2.0	0.059
1.9	0.060
1.8	0.062
1.7	0.062
1.6	0.063
1.5	0.064
1.4	0.064
1.3	0.069
1.2	0.074
1.1	0.081
1.0	0.088
0.9	0.097
0.8	0.120
0.7	0.122
0.6	0.139
0.5	0.161
0.4	0.191
0.3	0.232
0.2	0.291
0.1	0.375

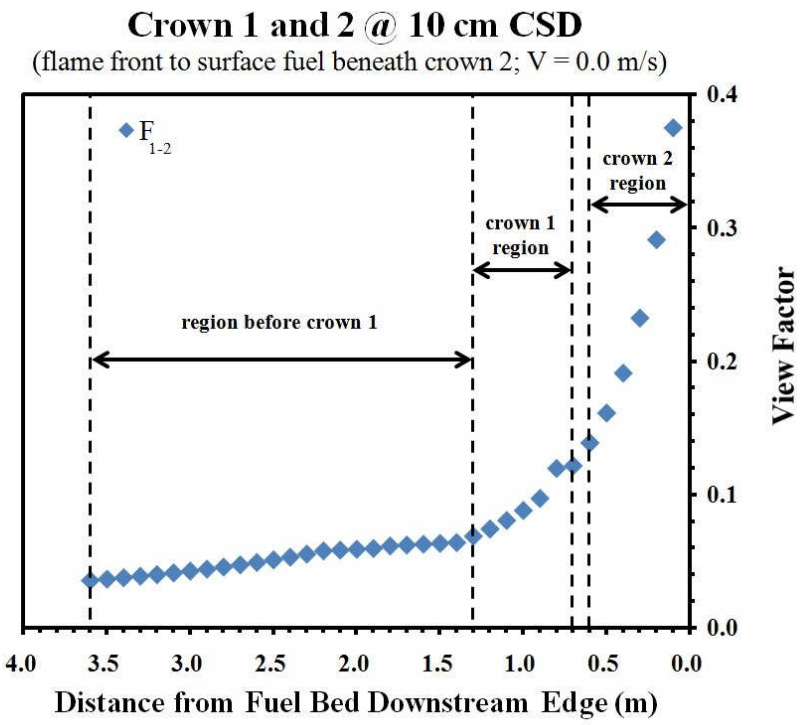


Figure 6.15: Tabulated view factor values and corresponding plot for a crown 1 and crown 2 configuration for a CSD of 10 cm at a wind condition of 0.0 m/s. Left side of plot represents leading edge of fuel bed while right side of plot represents the downstream edge of the fuel bed.

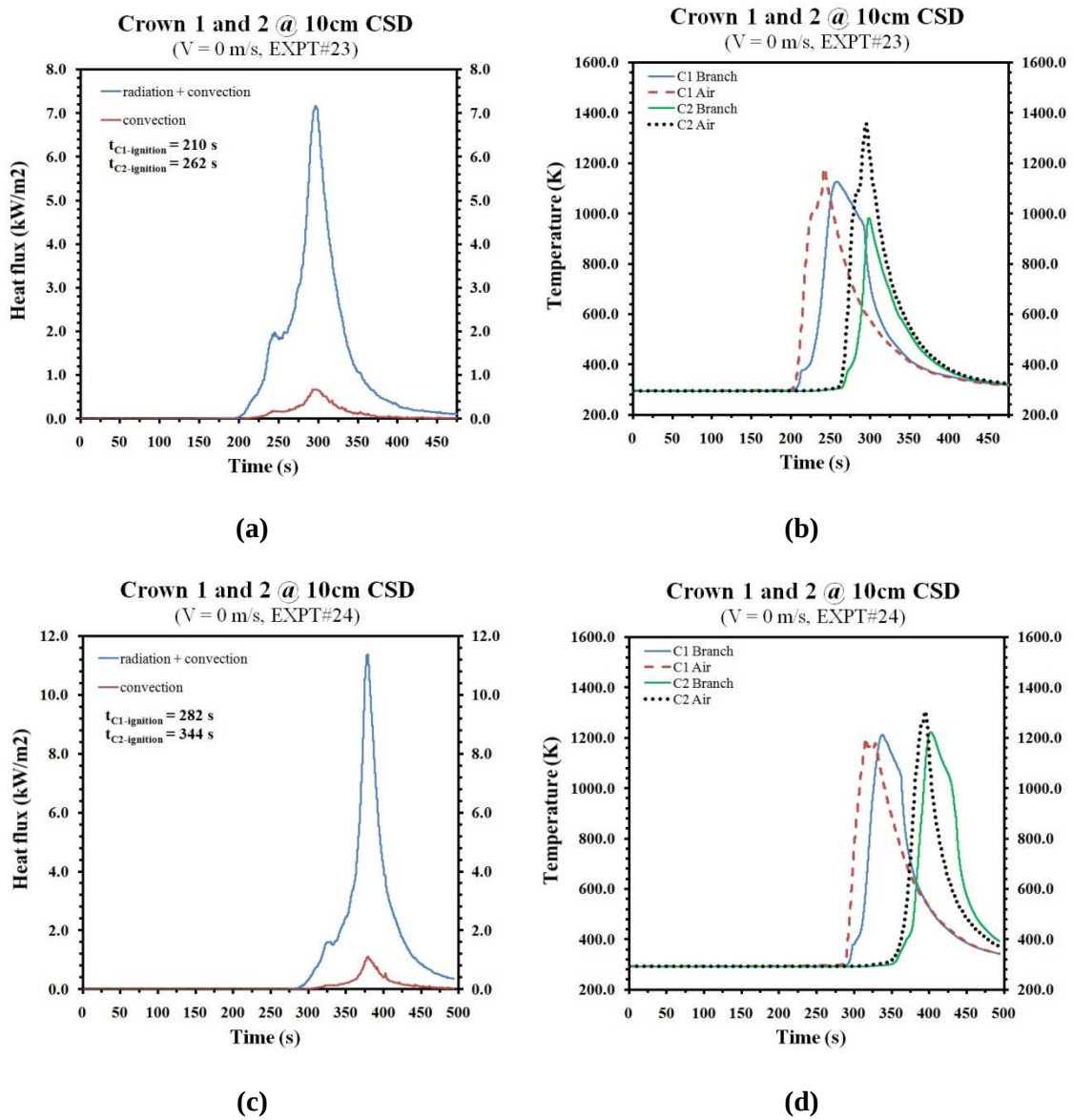


Figure 6.16: Plots for a surface fuel and crown 1 and two configuration at a crown separation distance of 10 cm for a no wind condition of: (a) total heat flux and convection heat flux produced during experiment 23; (b) branch and air temperature history during experiment 23; (c) total heat flux and convection heat flux produced during experiment 24; (b) branch and air temperature history during experiment 24;

Crown Separation Distance of 20 cm with No Wind

Table 6.5 shows average rate of spread and average surface fuel mass loss rate for the experimental case of a crown separation distances of 20 cm and no wind condition.

V =0.0 m/s, Crown 1 and Crown 2 at 20 cm CSD			
TC #	Location (cm)	R (cm/s)	$\dot{m}$ (g/s)
2	60	1.1	2.3
3	80	1.0	2.6
4	100	1.0	3.0
5	120	1.0	3.1
6	140	1.0	3.0
7	160	1.4	4.0
8	180	1.4	5.2
9	200	1.6	4.7
10	220	1.1	3.8

Table 6.5: Average rate of spread and average surface fuel mass loss rate data at each thermocouple location for a crown separation distance of 20 cm during a no wind condition.

R and $\dot{m}$ are plotted at each thermocouple location to determine how the crown separation distance of 20 cm affected the overall rate of spread, Figure 6.17. As the fire front propagates along the initial section of the surface fuel bed, before the crown 1 section, R remains steady with values ranging between 1.1 cm/s and 1.0 cm/s.

During the time before the fire front reaches crown 1, $\dot{m}$ increases from 2.3 g/s to 3.1 g/s. When the fire front reaches crown 1, Figure 6.18a, heat from the fire front is reallocated to preheat the crown 1 fuel matrix, while the crown fuel matrix also impedes heat flux from impinging on the unburned surface fuel. The overall effect is that R and $\dot{m}$ remain steady between TC5 and TC6, only varying by a magnitude of 0.1 as crown 1 is desiccated and reaches ignition temperature. As was the case for a CSD of 10 cm, as the fire front approaches crown 1, 2.0 m from the downstream edge of the surface fuel, the

view factor growth rate attenuates, increasing at a slower rate in comparison to the view factor growth rate in the region before crown 1, Figure 6.19. The combustion of crown 1 causes an influx of oxygen to the fire front increasing the combustion rate, thus increasing flame length and heat flux production. Figure 6.20 shows that crown 1 begins vigorous combustion at approximately 250 s. The crown temperature history plot, Figure 6.20b, shows that as crown 1 is being consumed the air temperature reaches a maximum of 1,083 K. The gaseous products of combustion preheat the chamise branch in crown 1 to approximately 380 K, before the branch elements ignite and combust reaching a maximum temperature of 1,020 K.

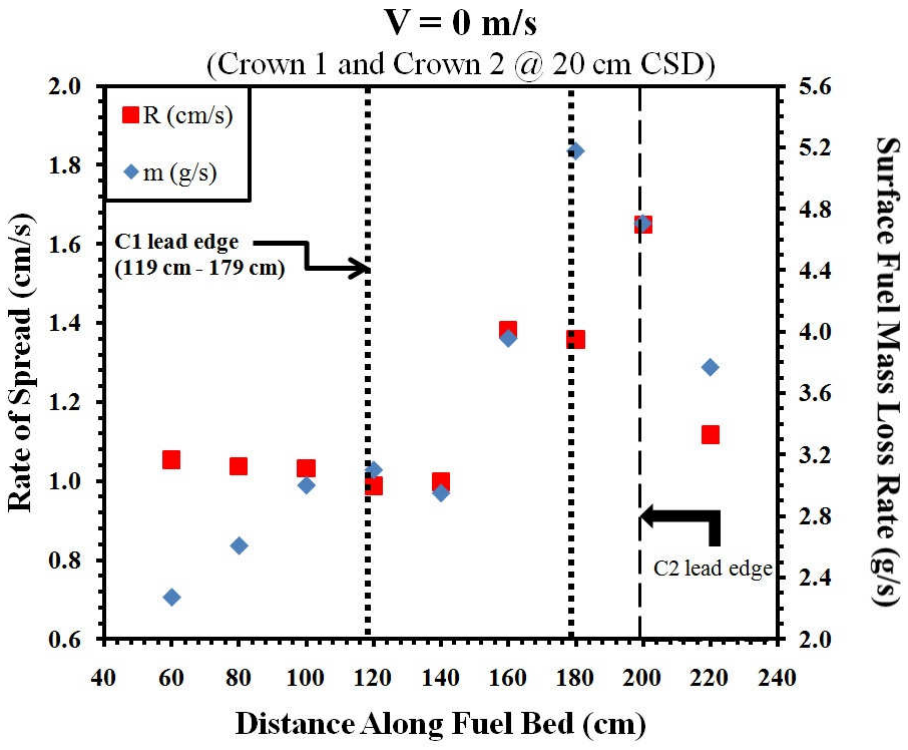


Figure 6.17: Average rate of spread and surface fuel mass loss rate at each thermocouple location plot for a crown separation distance of 20 cm during a no wind condition. Left axis represents values for rate of spread and right axis represents values for surface fuel mass loss rate; *R* plot containing standard deviation error bars located in Appendix B.

As crown 1 air and branch temperature reach their peak values, Figure 6.18b, the total heat flux and convection flux also reach a maximum of 1.39 kW/m^2 and 0.14 kW/m^2 respectively, Figure 6.20a. While crown 1 is being consumed, the increased heat flux produced by the fire front, with flame lengths exceeding 1.8 m in length, impinges onto and preheats the unburned surface fuel, resulting in an increase in R and $\dot{m}$. From TC6 to TC9, R increases from 1.0 cm/s to 1.6 cm/s respectively and $\dot{m}$ increase from 3.0 g/s to 5.2 g/s from TC6 to TC8 respectively. The increase in flame lengths again results in a considerable increase in view factor growth rate from the moment crown 1 ignites (1.4 m from the downstream edge of the fuel bed) until the fire front reaches the downstream edge of the fuel bed, Figure 6.19.

As the fire front approaches and reaches crown 2, R and $\dot{m}$ begin to decrease as a result of the decreasing amount of heat flux impinging onto the surface fuel due to the presence of crown 2. R decreases from 1.6 cm/s (TC9) to 1.0 cm/s (TC10) and $\dot{m}$ decreases from 5.2 g/s (TC8) to 3.8 g/s (TC10). The hot products of combustion from the fire front, 983 K, preheat the chamise branch to approximately 380 K, at which point the branch elements have been desiccated sufficiently to reach ignition temperature and enter the flaming phase, Figure 6.18c.

Figure 6.20 shows that crown 2 begins to vigorously combust at approximately 318 s, shown by the sharp increase in branch temperature and total heat flux to a maximum value of 1,270 K and 7.46 kW/m^2, respectively. Convection heat flux reaches a peak value of 0.78 kW/m^2. For the case of a crown separation distance of 20 cm and a 0.0 m/s wind condition, the confidence interval for the overall average rate of spread and

average surface fuel mass loss rate is 1.81 cm/s ± 0.09 cm/s and 3.51 g/s ± 0.43 g/s, respectively. The confidence interval for the maximum total heat flux is 8.23 kW/m^2 ± 0.95 kW/m^2 and 0.83 kW/m^2 ± 0.1 kW/m^2 for the maximum convection heat flux.

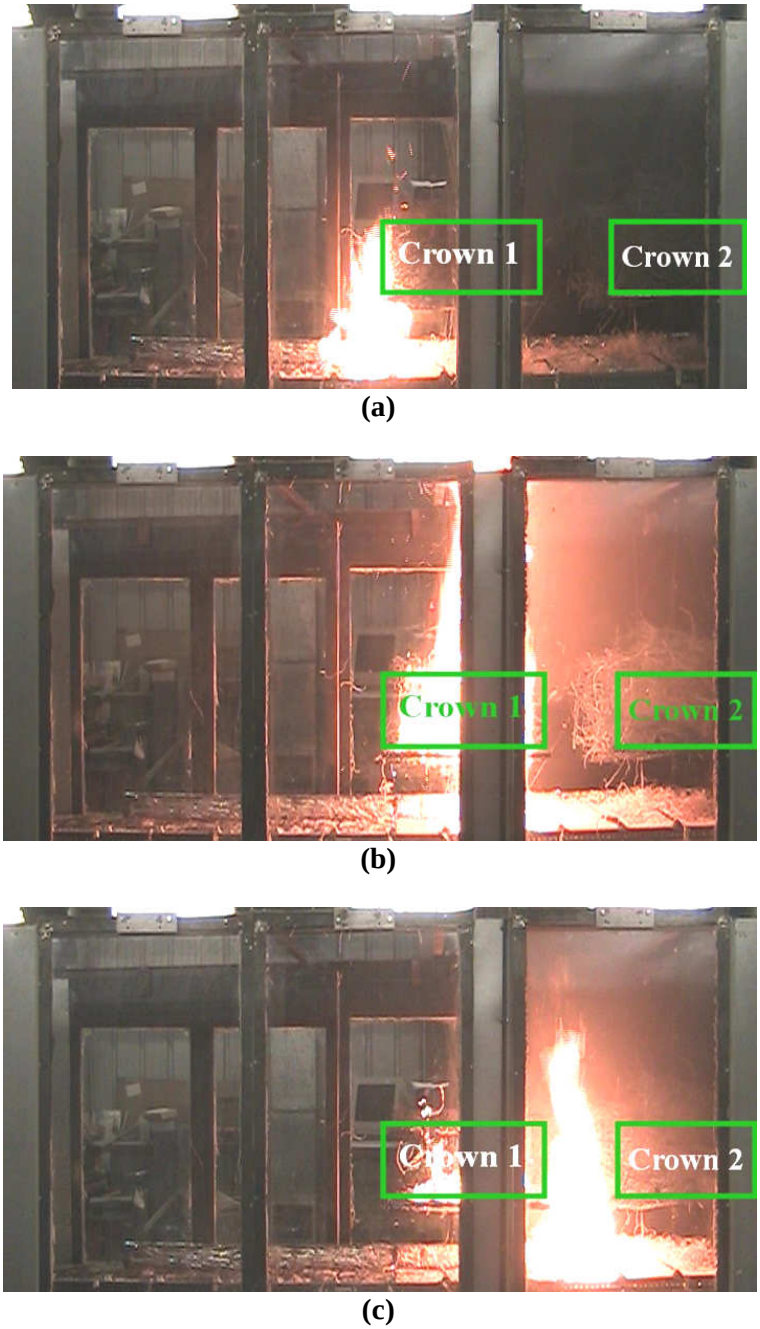


Figure 6.18: Images from experiment 21 at (a) t = 236 s at time of crown 1 ignition; (b) t = 285 s during crown 1 combustion; (c) t = 296 s at time of crown 2 ignition.

Crown 1 and 2 @ 20 cm CSD V = 0.0 m/s	
Distance from fuel bed downstream edge (m)	F_{1-2}
3.6	0.032
3.5	0.033
3.4	0.034
3.3	0.035
3.2	0.036
3.1	0.037
3.0	0.038
2.9	0.040
2.8	0.041
2.7	0.042
2.6	0.044
2.5	0.046
2.4	0.048
2.3	0.050
2.2	0.052
2.1	0.054
2.0	0.057
1.9	0.057
1.8	0.059
1.7	0.059
1.6	0.060
1.5	0.060
1.4	0.064
1.3	0.069
1.2	0.074
1.1	0.081
1.0	0.088
0.9	0.118
0.8	0.120
0.7	0.122
0.6	0.139
0.5	0.161
0.4	0.191
0.3	0.232
0.2	0.291
0.1	0.375

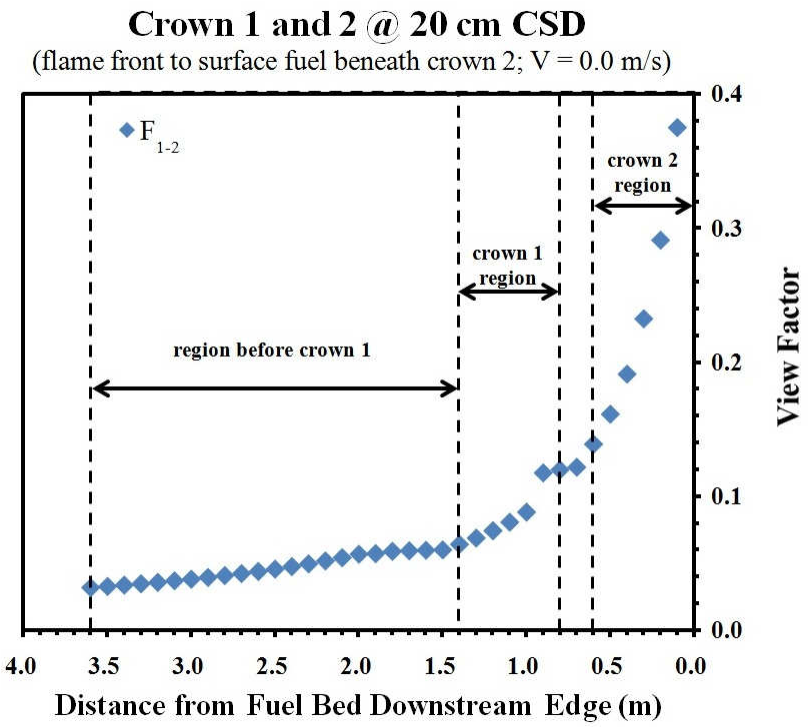
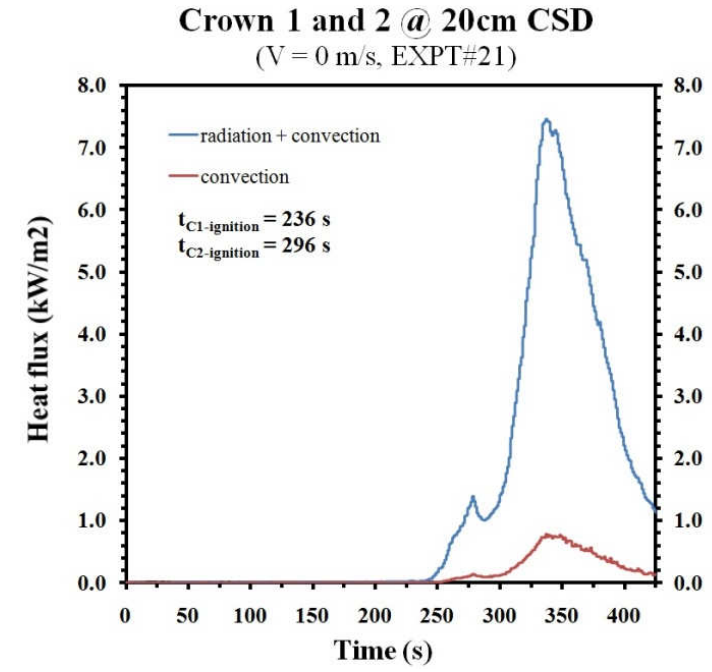
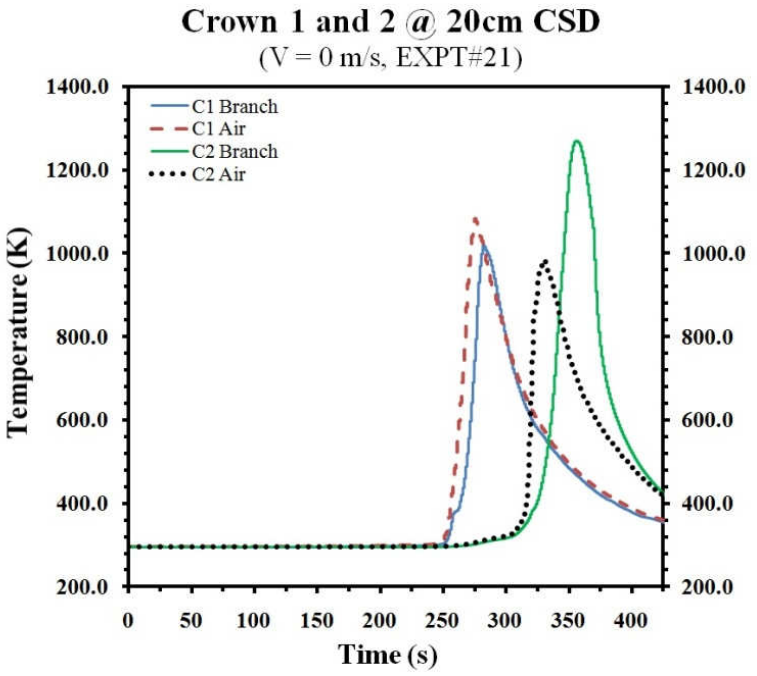


Figure 6.19: Tabulated view factor values and corresponding plot for a crown 1 and crown 2 configuration for a CSD of 20 cm at a wind condition of 0.0 m/s. Left side of plot represents leading edge of fuel bed while right side of plot represents the downstream edge of the fuel bed.



(a)



(b)

Figure 6.20: Plots for a surface fuel and crown 1 and two configuration at a crown separation distance of 20 cm for a no wind condition of: (a) total heat flux and convection heat flux produced during experiment 21; (b) branch and air temperature history during experiment 21.

Crown Separation Distance of 30 cm with No Wind

The next analyzes is performed by increasing the distance between crown fuel matrices to 30 cm while keeping the wind speed constant at 0.0 m/s. Table 6.6 contains data for the average rate of spread, R, and average surface fuel mass loss rate, $\dot{m}$, at each thermocouple location along the fuel bed. Figure 6.21 shows R and $\dot{m}$ plotted together to visualize how R and $\dot{m}$ change as the fire front propagates along the surface fuel bed.

V = 0.0 m/s, Crown 1 and Crown 2 at 30 cm CSD			
TC #	**Location (cm)**	**R (cm/s)**	**$\dot{m}$ (g/s)**
2	60	1.1	2.7
3	80	1.0	2.7
4	100	1.1	2.8
5	120	1.0	2.7
6	140	1.0	3.5
7	160	1.7	4.5
8	180	1.8	5.0
9	200	1.8	5.9
10	220	1.0	4.3

Table 6.6: Average rate of spread and average surface fuel mass loss rate data at each thermocouple location for a crown separation distance of 30 cm during a no wind condition.

All the experiments performed have similar trends and results, thus one experiment was chosen to represent the analysis in this discussion, experiment 17. The rate of spread is plotted on the left axis while the surface fuel mass loss rate is plotted on the right axis. As the fire front propagates along the surface fuel R and $\dot{m}$ remain steady from TC2 to TC4, section before crown 1 matrix, only varying by a magnitude of 0.1. As the fire front arrives at the location of crown 1, Figure 6.22a, heat from the fire front is reallocated to preheat crown 1 fuel elements. R decreases from TC4 to TC5 from 1.1 cm/s to 1.0 cm/s and $\dot{m}$ decreases from 2.8 g/s to 2.7 g/s as a result of the reduction of

heat flux impingement onto the unburned surface fuel. As the fire front nears crown 1, 2.2 m from the downstream edge of the surface fuel, the view factor growth rate abates, increasing at a slower rate in relation to the view factor growth rate in the region before crown 1, Figure 6.23.

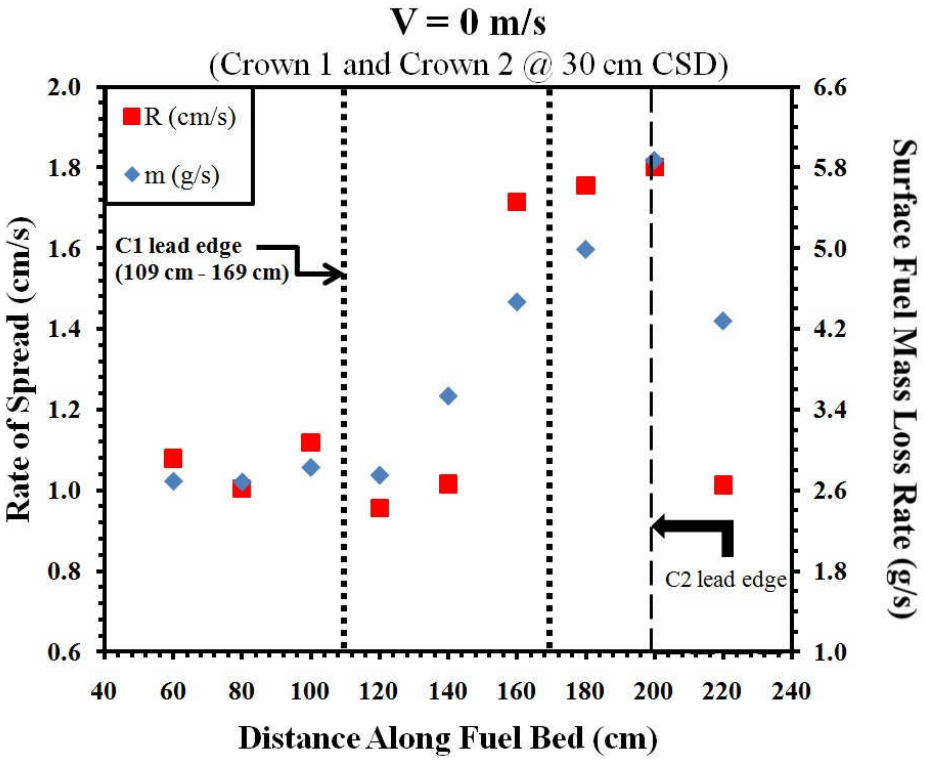


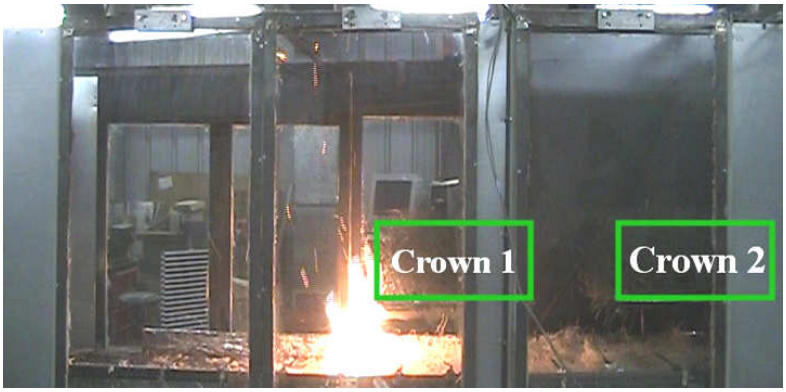
Figure 6.21: Average rate of spread and surface fuel mass loss rate at each thermocouple location plot for a crown separation distance of 30 cm during a no wind condition. Left axis represents values for rate of spread and right axis represents values for surface fuel mass loss rate; *R* plot containing standard deviation error bars located in Appendix B.

The gaseous products of combustion, with a maximum temperature of 1,107 K, from the fire front desiccate the chamise fuel matrix, raising the temperature of the chamise branch elements to approximately 380 K. Upon igniting, the chamise branch elements increase to a maximum temperature of 937 K, Figure 6.24b. The vigorous

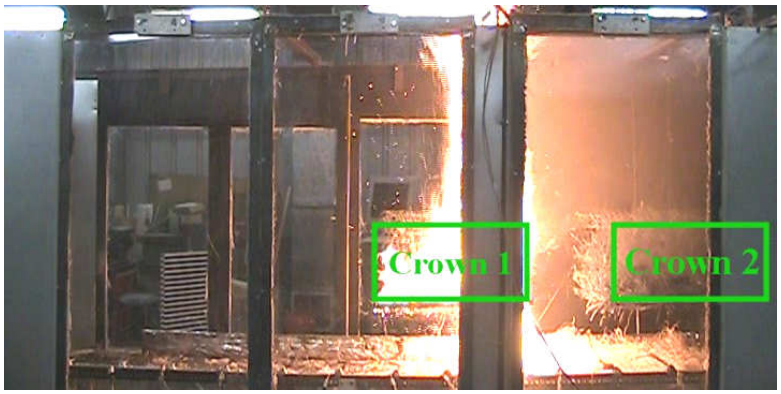
combustion of crown 1, Figure 6.22b, results in an increase of R and $\dot{m}$ between TC5 and TC7 (TCs beneath crown 1 section). R and $\dot{m}$ increase to 1.7 cm/s and 4.5 g/s respectively. At the peak of crown 1 combustion, t ≈ 278 s, the maximum total heat flux and convection flux is 1.50 kW/m^2 and 0.14 kW/m^2 respectively, Figure 6.24. The increased flame lengths after crown 1 ignition results in a substantial increase in view factor growth rate from the time crown 1 ignites (1.5 m from the downstream edge of the fuel bed) until the fire front reaches the downstream edge of the fuel bed.

The fire front then continues to propagate towards crown 2 along the surface fuel and crown fuel. R and $\dot{m}$ continue to increase in the section between the two crown fuels to 1.8 cm/s and 5.9 g/s respectively. The increase in R and $\dot{m}$ is due to the larger unobstructed open area between the two crown fuel matrices. This allows radiation to impinge on the unburned surface fuel ahead of the fire front for a longer period of time than was possible at CSD cases of 10 cm and 20 cm.

The crown 2 fuel matrix obstructs radiation flux from impinging onto the unburned surface fuel ahead of the fire front when the fire front reaches crown 2, Figure 6.22c, resulting in a decrease in R from 1.8 cm/s (TC9) to 1.0 cm/s (TC10) and a decrease in $\dot{m}$ from 5.9 g/s (TC9) to 4.3 g/s (TC10), respectively. The hot gaseous products of combustion, with maximum temperature of 1215 K, then proceed to preheat the chamise branch elements to approximately 380 K. After entering the flaming phase, branch temperature increases to a maximum of 1105K.



(a)



(b)



(c)

Figure 6.22: Images from experiment 17 at (a) t = 230 s at time of crown 1 ignition; (b) t = 265 s during crown 1 combustion; (c) t = 297 s at time of crown 2 ignition.

Crown 1 and 2 @ 30 cm CSD V = 0.0 m/s	
Distance from fuel bed downstream edge (m)	F_{1-2}
3.6	0.033
3.5	0.034
3.4	0.035
3.3	0.036
3.2	0.037
3.1	0.039
3.0	0.040
2.9	0.041
2.8	0.043
2.7	0.044
2.6	0.046
2.5	0.048
2.4	0.050
2.3	0.052
2.2	0.054
2.1	0.054
2.0	0.054
1.9	0.055
1.8	0.056
1.7	0.056
1.6	0.056
1.5	0.060
1.4	0.064
1.3	0.069
1.2	0.074
1.1	0.081
1.0	0.113
0.9	0.118
0.8	0.120
0.7	0.122
0.6	0.139
0.5	0.161
0.4	0.191
0.3	0.232
0.2	0.291
0.1	0.375

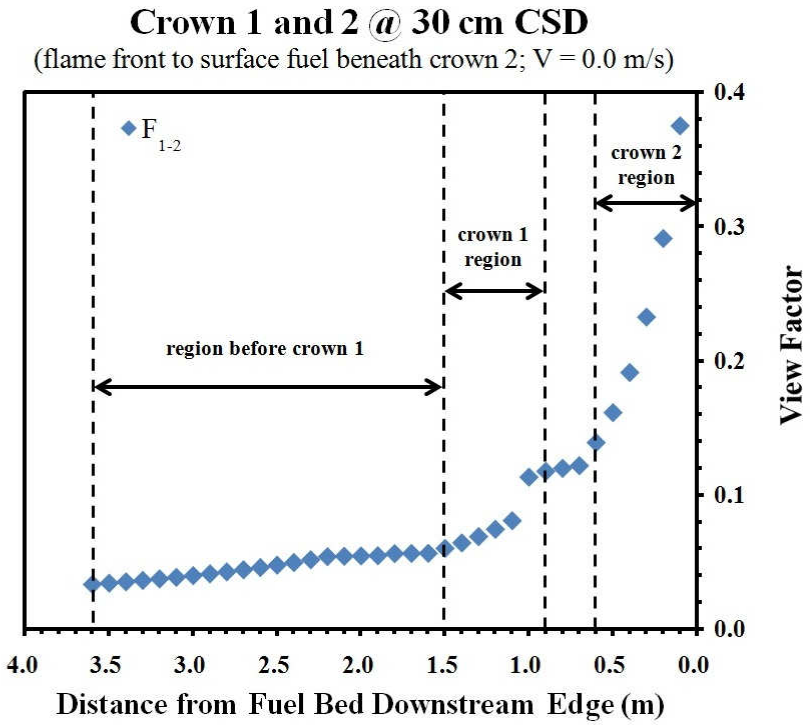
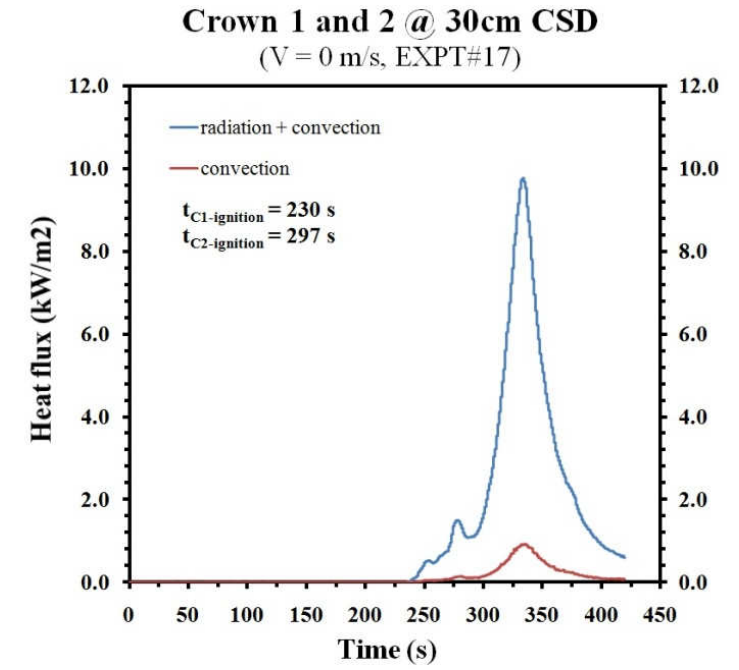


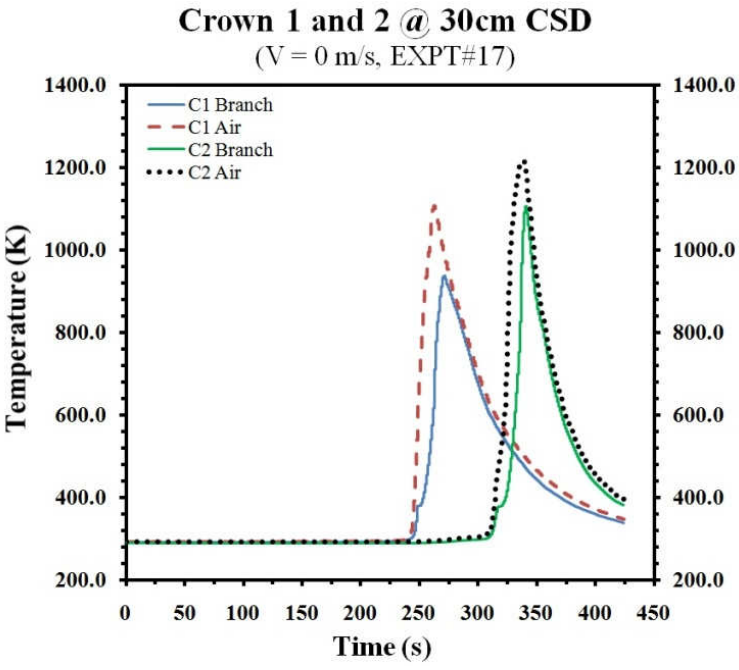
Figure 6.23: Tabulated view factor values and corresponding plot for a crown 1 and crown 2 configuration for a CSD of 30 cm at a wind condition of 0.0 m/s. Left side of plot represents leading edge of fuel bed while right side of plot represents the downstream edge of the fuel bed.

Maximum total and convection heat flux impingement onto crown 3 at the peak of crown 2 combustion is 9.77 kW/m^2 and 0.93 kW/m^2, respectively. The confidence interval for maximum total and maximum convection heat flux is 8.47 kW/m^2 ± 1.23 kW/m^2 and 0.80 kW/m^2 ± 0.12 kW/m^2, respectively. Confidence intervals for the overall R and the overall $\dot{m}$ are 1.27 cm/s ± 0.10 cm/s and 3.79 g/s ± 0.40 g/s, respectively.

To determine how the presence of crown two affects heat flux impingement onto crown 3 at the downstream side of the fuel configuration, an analysis is performed where crown two is removed and the results from this analysis are compared to those with an existing crown two fuel matrix configuration.



(a)



(b)

Figure 6.24: Plots for a surface fuel and crown 1 and two configuration at a crown separation distance of 30 cm for a no wind condition of: (a) total heat flux and convection heat flux produced during experiment 17; (b) branch and air temperature history during experiment 17.

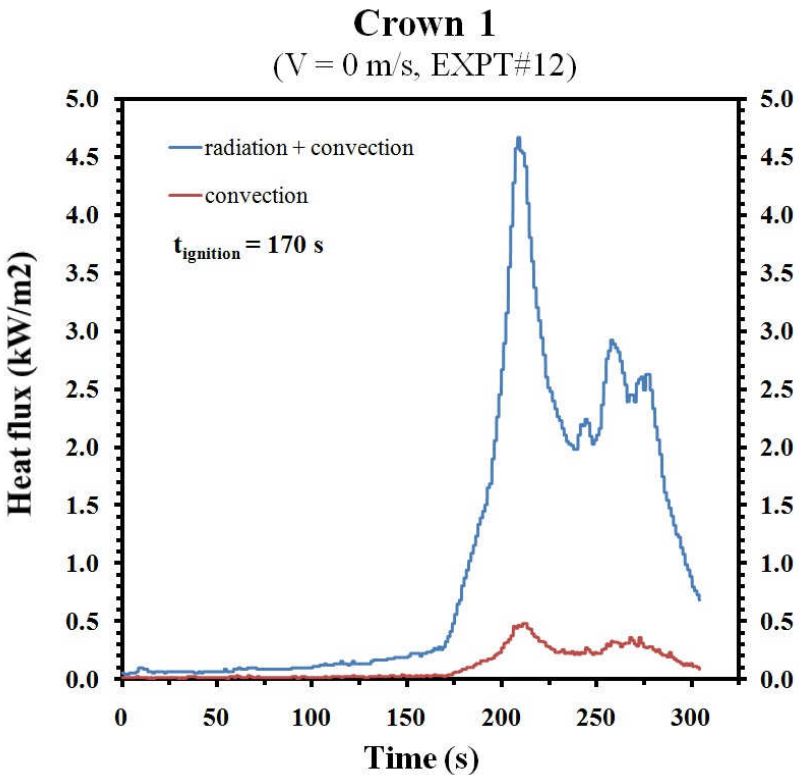


Figure 6.25: Total heat flux and convection heat flux curves for a surface fuel and crown 1 only configuration at a crown separation distance of 30 cm for a no wind condition during experiment 12.

Figure 6.25 shows a representation of the total and convection heat flux impinging on a third crown fuel matrix, as previously described. The average maximum total heat flux impinging onto crown 3 fuel matrix during combustion of crown one, where crown one is located at a distance of 30 cm from where crown two would normally be situated, is 4.69 kW/m^2. In comparison, when crown two is present and CSD is 30 cm, the average maximum total heat flux is 1.28 kW/m^2. The presence of crown two obstructs radiation and convection from impinging onto crown 3 fuel matrix, thus average maximum total heat flux impingement is reduced by a factor of 3.6. Lower amounts of heat flux impingement results in a slower *R* amongst crown fuel matrices.

Crown Separation Distance of 10 cm with a 1.1 m/s Wind

The next analysis is performed to investigate how the combination of crown separation distance and wind affects the overall heat transfer process to unburned surface fuel and unburned crown fuel. The crown separation distances studied are 10 cm, 20 cm and 30 cm at a constant wind speed of 1.1 m/s. Thermocouples located 2.5 cm above the surface fuel are utilized to calculate surface fire front rate of spread, while two thermocouples per crown are used to investigate crown fuel ignition as a result of heat transfer from a propagating surface fire and from burning adjacent crown fuel matrices.

Table 6.7 contains the data for average rate of spread and average surface fuel mass loss rate for the case of a CSD of 10 cm and a constant wind speed of 1.1 m/s. Unlike R at a no wind speed condition, R at 1.1 m/s is less stable with a standard deviation of 1.41 cm/s between TC's, which is greater than the standard deviation for the same fuel configuration at a no wind speed condition by a factor of 5.2. Observations of R and $\dot{m}$ curves in Figure 6.26a, suggest that under conditions of CSD 10 cm and 1.1 m/s wind speed, R and $\dot{m}$ respond differently when compared to one another, a staggered effect. Between TC2 and TC3 R decreases from 3.1 cm/s to 1.8 cm/s while $\dot{m}$ increases from 6.0 g/s to 6.4 g/s. From TC3 to TC4, R increases to 3.1 cm/s while $\dot{m}$ decreases to 5.6 g/s. Continued examination of Figure 6.26a shows the staggered pattern. R is reacting to the changing fuel configuration sooner than $\dot{m}$. Figure 6.26b shows R and $\dot{m}$ with $\dot{m}$ shifted backwards by one thermocouple location to better represent the staggered pattern between R and $\dot{m}$ from TC2 to TC7.

V = 1.1 m/s, Crown 1 and Crown 2 at 10 cm CSD			
TC #	Location (cm)	R (cm/s)	$\dot{m}$ (g/s)
2	60	3.1	6.0
3	80	1.8	6.4
4	100	3.1	5.6
5	120	2.0	6.3
6	140	1.8	5.9
7	160	6.2	5.2
8	180	2.1	6.3
9	200	2.9	7.7
10	220	1.7	5.6

Table 6.7: Average rate of spread and average surface fuel mass loss rate data at each thermocouple location for a crown separation distance of 10 cm during a 1.1 m/s wind condition.

As the fire front propagates along the fuel bed and approaches crown 1, from TC4 to TC5 *R* decreases, Figure 6.27a (experiment 60 which represents fire behavior for the current case under discussion). Heat flux is reallocated to preheat the crown 1 chamise fuel and heat flux impinging onto the unburned surface is hampered by the presence of crown 1 fuel matrix.

As the fire front approaches crown 1 the view factor increases from 0.097 (2.64 m from the downstream edge of the fuel bed) to 0.267 (1.52 m from the downstream edge of the fuel bed). Crown 1 then begins to obstruct radiation impingement onto the unburned surface fuel resulting in a lower view factor of 0.123 at 1.42 m from the downstream edge of the fuel bed, Figure 6.28. The hot gaseous products of combustion, ~ 905K, preheat the chamise branch element to approximately 380 K. Once branch elements have been sufficiently desiccated, ignition occurs achieving a maximum temperature of 857 K. As was established in the previous study at a no wind condition, once crown 1 ignites, *R* begins to increase, in this case from 1.8 cm/s (TC6) to 6.2 cm/s (TC7).

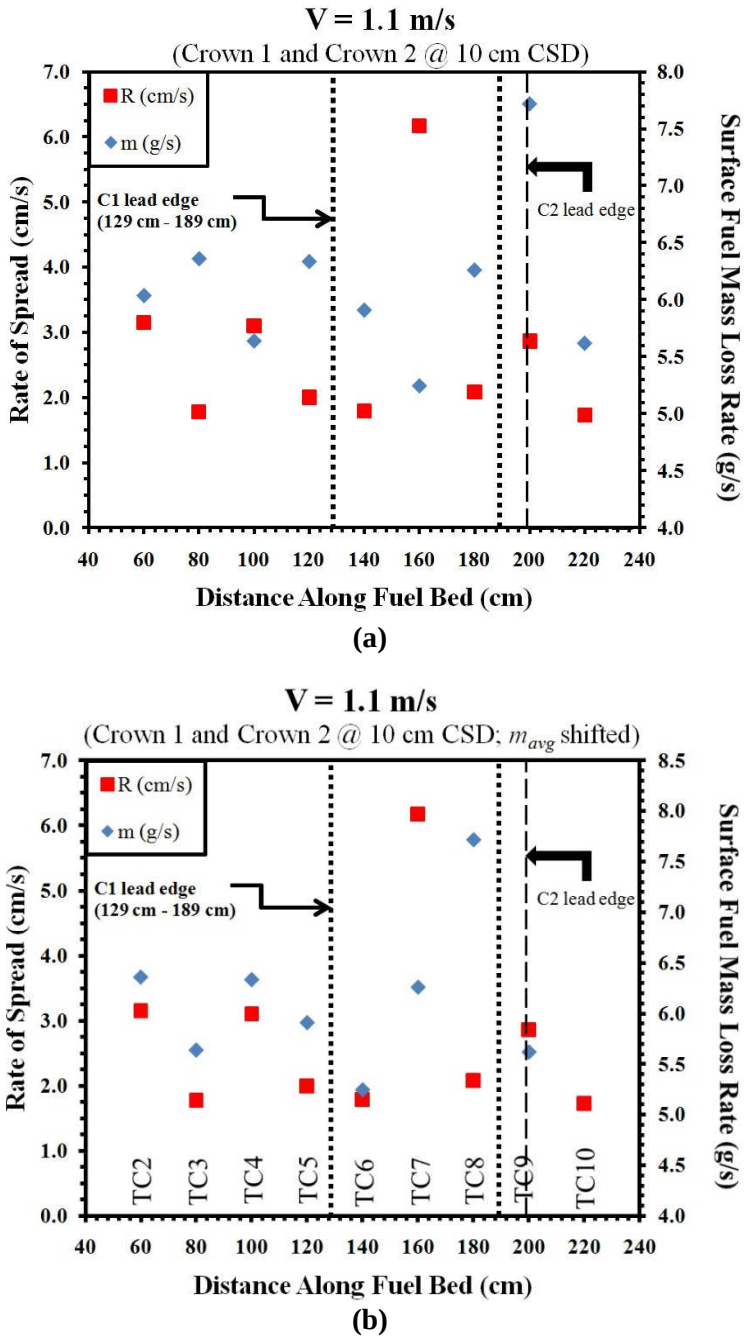
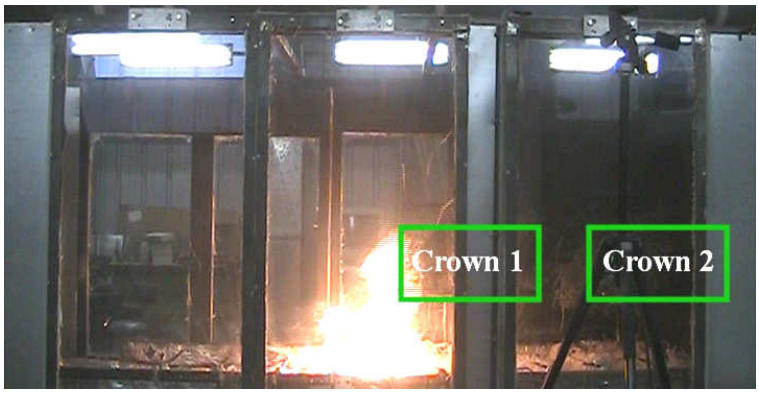


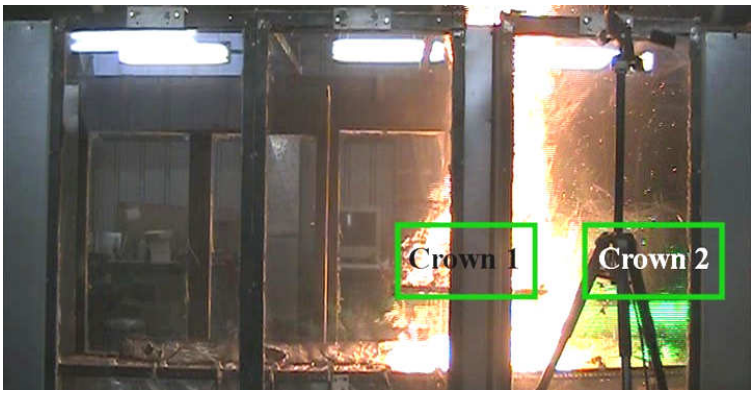
Figure 6.26: Average rate of spread and surface fuel mass loss rate at each thermocouple location plot for a crown separation distance of 10 cm during a 1.1 m/s wind condition. Left axis represents values for rate of spread and right axis represents values for surface fuel mass loss rate: (a) raw data; (b) average surface fuel mass loss rate shifted backwards; *R* plot containing standard deviation error bars located in Appendix B;

During the peak combustion of crown 1, Figure 6.29b, the fire front impinges a maximum total heat flux and convection flux of 2.54 kW/m^2 and 0.34 kW/m^2, respectively, onto crown 3 location at the leading edge of the surface fuel bed, shown as the first peak in Figure 6.29a. From the time crown 1 ignites, and the flame lengths increase, to when the fire front reaches the downstream edge of the fuel bed, the view factors increase exponentially reaching a maximum value of 0.596, Figure 6.28.

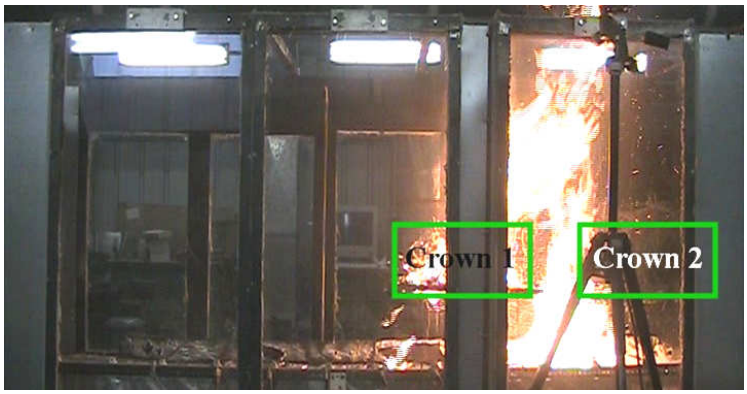
As the fire front continues propagating and arrives at crown 2, Figure 6.27c, *R* decreases from 6.2 cm/s (TC7) to 2.1 cm/s (TC8). The decrease in *R* is a result of the diminished amount of heat flux impinging on the unburned surface fuel due to the presence of crown 2, and the reallocation of heat to preheat crown 2 fuel matrix. The hot gaseous products of combustion, which reach a maximum temperature of 1031 K, Figure 6.29b, preheat the crown 2 branch element to approximately 380 K. Upon reaching the appropriate temperature, the branch elements ignite and achieve a maximum temperature of 1079 K. During combustion, the surface fire front and the crown fire front both impinge radiation and convection heat flux onto the unburned surface fuel, thus increasing *R* to 2.9 cm/s (TC9). A maximum total heat flux of 10.28 kW/m^2 and a maximum convection flux of 1.73 kW/m^2 is shown to impinge onto crown 3 fuel matrix. As the surface and crown fire fronts exhaust the crown and surface fuel supply, the flames begin to extinguish and *R* decreases to 1.7 cm/s (TC10).



(a)



(b)



(c)

Figure 6.27: Images from experiment 60 at (a) t = 120 s at time of crown 1 ignition; (b) t = 155 s during crown 1 combustion; (c) t = 162 s at time of crown 2 ignition.

Crown 1 and 2 @ 10 cm CSD V = 1.1 m/s	
Distance from fuel bed downstream edge (m)	F_{1-2}
2.64	0.097
2.58	0.097
2.35	0.104
2.26	0.102
2.14	0.107
1.99	0.127
1.90	0.154
1.80	0.162
1.67	0.173
1.64	0.188
1.52	0.267
1.42	0.123
1.32	0.130
1.22	0.148
1.12	0.158
1.02	0.170
0.92	0.184
0.82	0.219
0.72	0.241
0.62	0.267
0.52	0.299
0.42	0.386
0.32	0.444
0.22	0.511
0.12	0.596

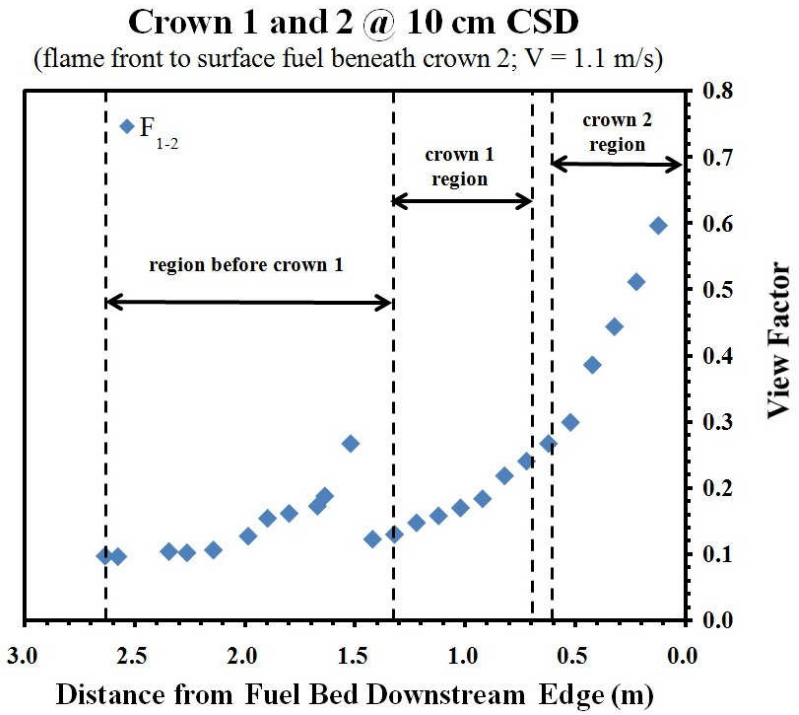


Figure 6.28: Tabulated view factor values and corresponding plot for a crown 1 and crown 2 configuration for a CSD of 10 cm at a wind condition of 1.1 m/s. Left side of plot represents leading edge of fuel bed while right side of plot represents the downstream edge of the fuel bed.

A total of five experiments were conducted for a CSD of 10 cm at a constant wind speed of 1.1 m/s. The confidence interval for maximum total and convection flux is 11.49 kW/m^2 ± 1.67 kW/m^2 and 1.72 kW/m^2 ± 0.16 kW/m^2 with standard deviations of 1.9 kW/m^2 and 0.18 kW/m^2, respectively. For overall R along the surface fuel bed, the confidence interval is 2.7 cm/s ± 0.3 cm/s with a standard deviation of 0.38 cm/s. The confidence interval for $\dot{m}$ is 6.13 g/s ± 0.53 g/s with a standard deviation of 0.54 g/s.

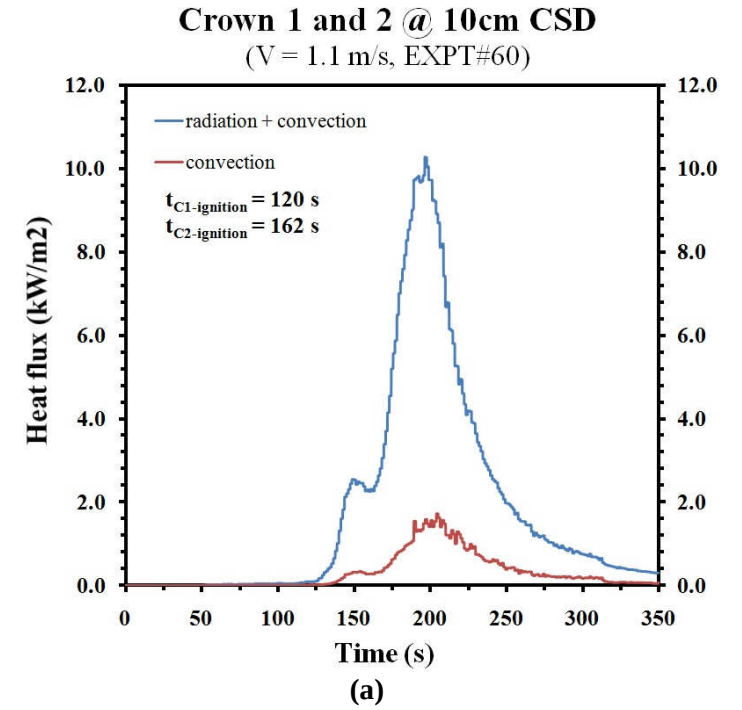


Figure 6.29: Plots for a surface fuel and crown 1 and two configuration at a crown separation distance of 10 cm for a 1.1 m/s wind condition of: (a) total heat flux and convection heat flux produced during experiment 60; (b) branch and air temperature history during experiment 60.

Crown Separation Distance of 20 cm with a 1.1 m/s Wind

Table 6.8 contains data for R and $\dot{m}$ at each thermocouple location along the surface fuel bed and Figure 6.30 contains the curves for the plotted data form Table 6.8. Visual inspection of the curves in Figure 6.30 show that in contrast to the no wind condition, for the same fuel configuration, R along the fuel bed is not very stable with a standard deviation of 0.86 cm/s compared to the standard deviation of 0.10 cm/s. R at 1.1 m/s is greater by a factor of 8.6.

V = 1.1 m/s, Crown 1 and Crown 2 at 20 cm CSD			
TC #	**Location (cm)**	***R* (cm/s)**	**$\dot{m}$ (g/s)**
2	60	3.1	8.1
3	80	1.9	7.5
4	100	3.0	7.8
5	120	1.9	8.5
6	140	2.1	8.9
7	160	6.2	8.9
8	180	2.4	10.2
9	200	2.9	8.6
10	220	1.4	6.2

Table 6.8: Average rate of spread and average surface fuel mass loss rate data at each thermocouple location for a crown separation distance of 20 cm during a 1.1 m/s wind condition.

Figure 6.31 consists of still images captured while performing experiment 52, which for this discussion will represent the fire behavior for a CSD of 20 cm experiencing a constant 1.1 m/s wind. As the fire front approaches crown 1, Figure 6.31a, heat from the fire front is reallocated to preheat the crown 1 fuel matrix, and heat flux impingement upon the unburned surface fuel ahead of the fire front begins to diminish due to the presence of the crown 1 matrix. In the region before crown 1 the view factor increases from 0.0.132 (2.11 m from the downstream edge of the fuel bed) to

0.222 (1.4 m from the downstream edge of the fuel bed). Crown 1 then begins to obstruct radiation impingement onto the unburned surface fuel resulting in a lower view factor of 0.138 at 1.3 m from the downstream edge of the fuel bed, Figure 6.32. With less heat to preheat the unburned surface fuel, *R* reduces from 3.0 cm/s (TC4) to 1.9 cm/s (TC5). As *R* decreases, the increase in $\dot{m}$ from thermocouple to thermocouple begins to decrease. From TC3 to TC5, $\dot{m}$ increases by 1.0 g/s, and from TC5 to TC7, $\dot{m}$ only increases by 0.4 g/s.

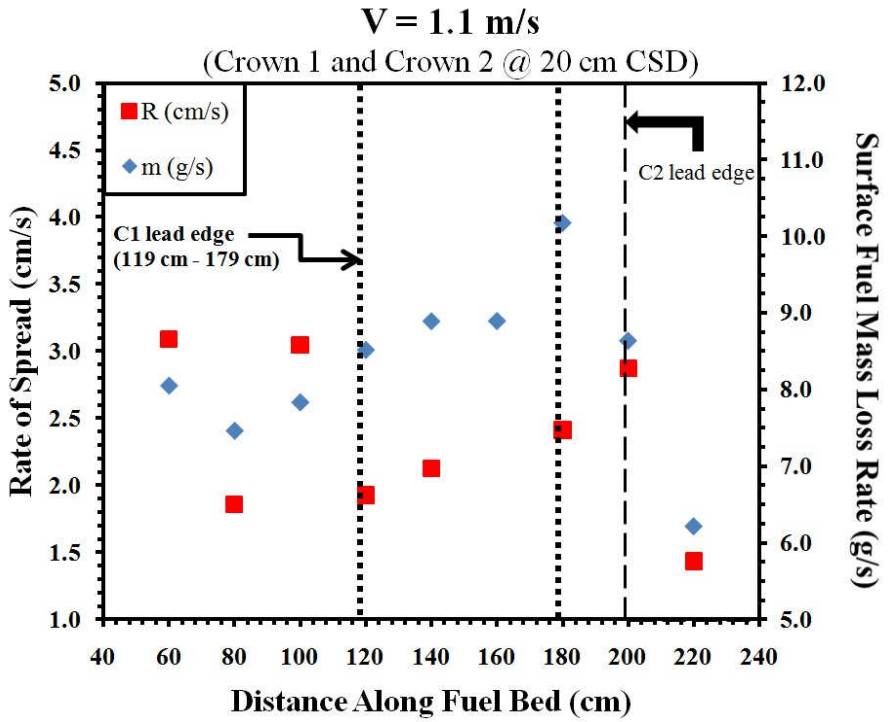
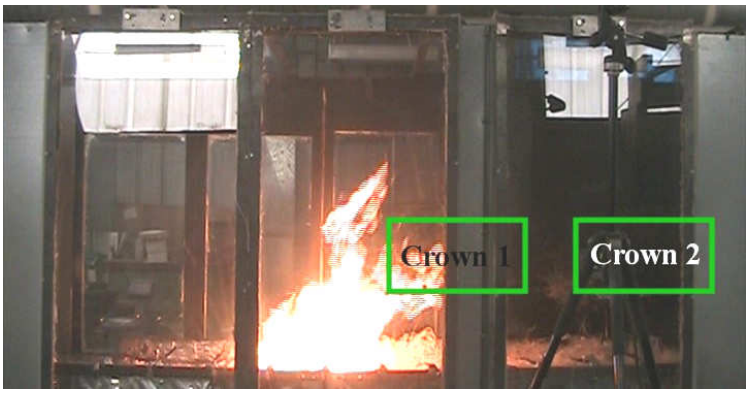
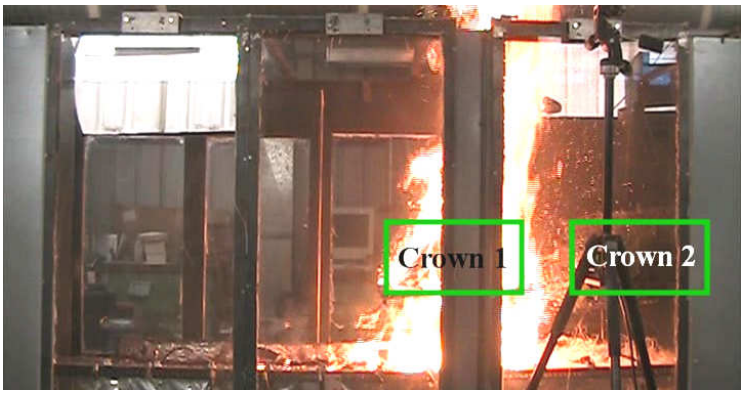


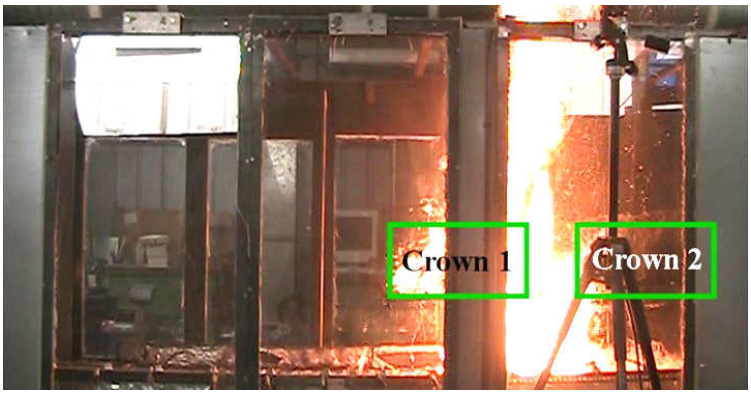
Figure 6.30: Average rate of spread and surface fuel mass loss rate at each thermocouple location plot for a crown separation distance of 20 cm during a 1.1 m/s wind condition. Left axis represents values for rate of spread and right axis represents values for surface fuel mass loss rate; *R* plot containing standard deviation error bars located in Appendix B.



(a)



(b)



(c)

Figure 6.31: Images from experiment 52 at (a) t = 84 s at time of crown 1 ignition; (b) t = 115 s during crown 1 combustion; (c) t = 120 s at time of crown 2 ignition.

Crown 1 and 2 @ 20 cm CSD V = 1.1 m/s	
Distance from fuel bed downstream edge (m)	F_{1-2}
2.11	0.132
2.06	0.132
1.98	0.138
1.94	0.144
1.88	0.118
1.78	0.180
1.74	0.146
1.68	0.065
1.58	0.175
1.52	0.198
1.47	0.210
1.40	0.222
1.30	0.138
1.20	0.148
1.10	0.158
1.00	0.184
0.90	0.200
0.80	0.219
0.70	0.241
0.60	0.299
0.50	0.338
0.40	0.386
0.30	0.444
0.20	0.596
0.10	0.644

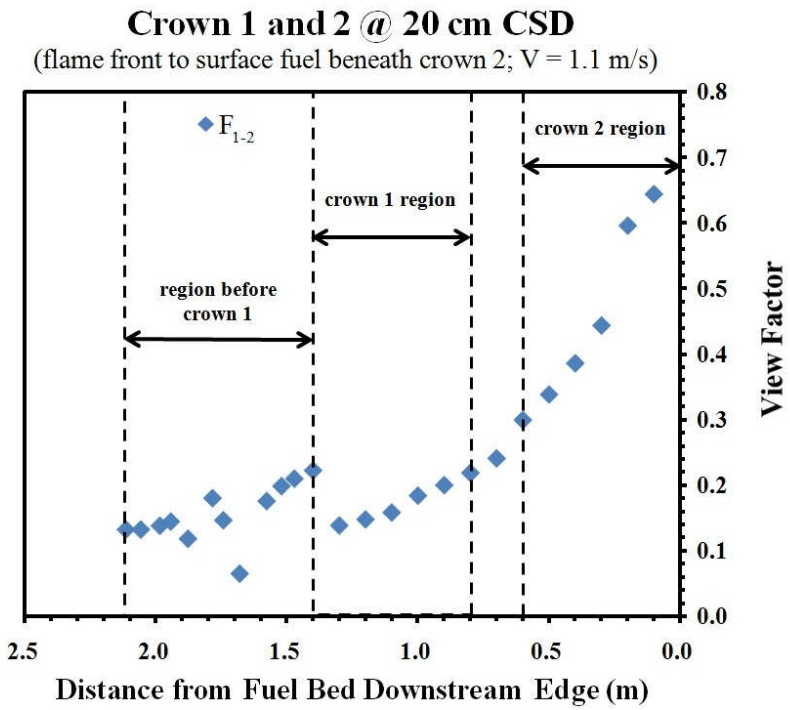


Figure 6.32: Tabulated view factor values and corresponding plot for a crown 1 and crown 2 configuration for a CSD of 20 cm at a wind condition of 1.1 m/s. Left side of plot represents leading edge of fuel bed while right side of plot represents the downstream edge of the fuel bed.

The hot gaseous products of combustion reach a maximum temperature of 1209 K and commence to preheat the chamise branch elements to approximately 308 K. Chamise fuel elements will desiccate until a sufficient quantity of water is evaporated, at which point the crown fuel element will continue to increase in temperature until reaching ignition temperature and entering the flaming phase. At the peak of crown 1 combustion, Figure 6.31b, the merged surface fire front and crown fire front impinge a maximum total heat flux and convection flux of 2.83 kW/m^2 and 0.36 kW/m^2, respectively, onto crown 3, Figure 6.33. As crown 1 burns, R and $\dot{m}$ increase to 2.4 cm/s (TC8) and 10.2 g/s (TC8) respectively.

The combusting of crown 1 results in increased flame lengths exceeding 2.0 m. From the moment crown 1 ignites to when the fire front reaches the downstream edge of the fuel bed, the view factors increase exponentially reaching a maximum value of 0.644. *R* continues to increase, from TC5 to TC8, while the fire fronts approach crown 2 as a result of the 20 cm open area between crown 1 and crown 2, which allows radiation and convection heat flux to impinge onto and preheat the unburned surface fuel. Again, the hot gaseous products of combustion preheat and then ignite the chamise crown fuel matrix. The maximum total and convection heat flux impinging onto crown 3 during the peak of crown 2 combustion is 15.95 kW/m^2 and 2.13 kW/m^2, respectively, Figure 6.33. *R* and $\dot{m}$ decrease during the last portion of the fuel section due to the diminishing surface and crown fuel supply.

Six experiments for a CSD of 20 cm at a constant 1.1 m/s wind speed were performed. The confidence interval for maximum total flux heat is 15.48 kW/m^2 ± 1.93 kW/m^2 and for the maximum convection heat flux the confidence interval is 2.0 kW/m^2 ± 0.15 kW/m^2. Standard deviations for maximum total and convection flux are 2.42 kW/m^2 and 0.18 kW/m^2, respectively. The confidence interval for *R* and $\dot{m}$ is 2.8 cm/s ± 0.69 cm/s and 6.13 g/s ± 0.53 g/s, respectively, with standard deviations of 0.86 cm/s and 0.54 g/s, respectively.

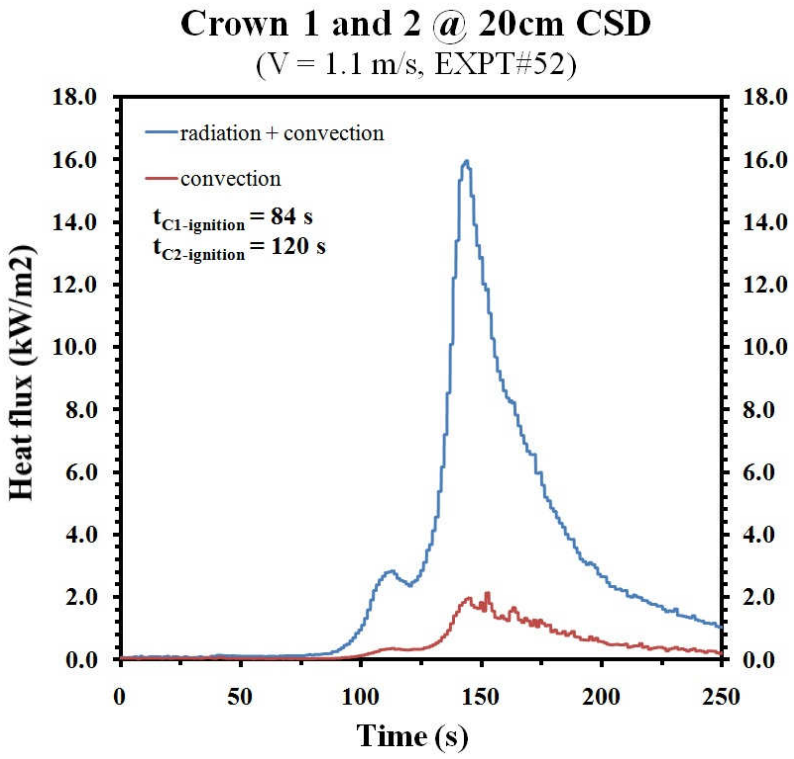


Figure 6.33: Plot for a surface fuel and crown 1 and two configuration at a crown separation distance of 20 cm for a 1.1 m/s wind condition of total heat flux and convection heat flux produced during experiment 52.

Crown Separation Distance of 30 cm with a 1.1 m/s Wind

The following analysis is performed at a CSD of 30 cm at a constant wind speed of 1.1 m/s. Table 6.9 contains data for the average rate of spread, *R*, and average surface fuel mass loss rate, $\dot{m}$, at each thermocouple location along the surface fuel bed. *R* and $\dot{m}$ data is plotted in Figure 6.34. As the fire front approaches and arrives at crown 1, *R* and $\dot{m}$ are 4.0 cm/s (TC4) and 8.0 g/s (TC4), respectively. As heat flux is reallocated to preheat the chamise crown fuel matrix and as heat flux impingement onto the unburned surface fuel diminishes, *R* and $\dot{m}$ decrease to 2.5 cm/s (TC5) and 7.8 g/s (TC5), respectively.

V = 1.1 m/s, Crown 1 and Crown 2 at 30 cm CSD			
TC #	Location (cm)	R (cm/s)	$\dot{m}$ (g/s)
2	60	2.8	6.9
3	80	2.0	7.9
4	100	4.0	8.0
5	120	2.5	7.8
6	140	3.1	9.2
7	160	3.9	11.9
8	180	2.0	8.2
9	200	2.4	11.8
10	220	2.2	9.9

Table 6.9: Average rate of spread and average surface fuel mass loss rate data at each thermocouple location for a crown separation distance of 30 cm during a 1.1 m/s wind condition.

Observation of Figure 6.36 shows that in the region before crown 1 the view factor increases from 0.084 (2.56 m from the downstream edge of the fuel bed) to 0.196 (1.48 m from the downstream edge of the fuel bed). Radiation impingement onto the unburned surface fuel is then obstructed by crown 1 resulting in a lower view factor of 0.073 at 1.53 m from the downstream edge of the fuel bed.

Experiment 38 was chosen to represent fire behavior during experimentation at a CSD of 30 cm at a constant wind speed of 1.1 m/s. Hot gaseous products of combustion impinge on the crown 1 fuel matrix, with a maximum temperature of 1050 K, Figure 6.37b, preheating the unburned chamise branch elements to approximately 380 K. The branch elements undergo a desiccation process, and when a sufficient quantity of water has evaporated, the branch elements will continue to increase in temperature, eventually leading to ignition when the appropriate temperature has been achieved, Figure 6.35a. From the period when crown 1 ignites, and the flame lengths increase exceeding 2.0 m, to when the fire front reaches the downstream edge of the fuel bed, the view factors increase exponentially reaching a maximum value of 0.644.

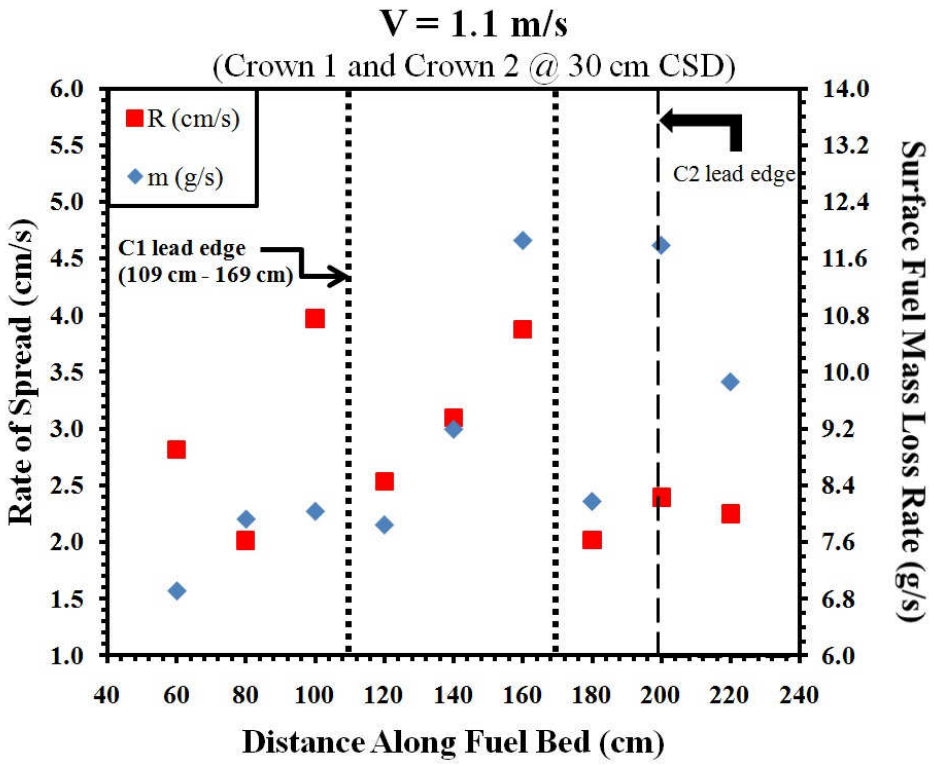
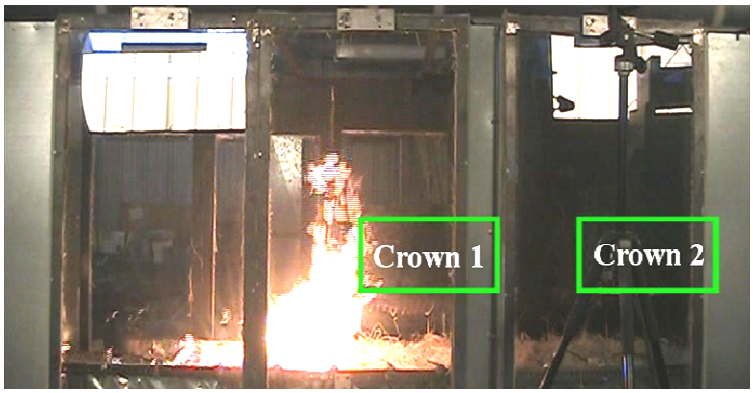
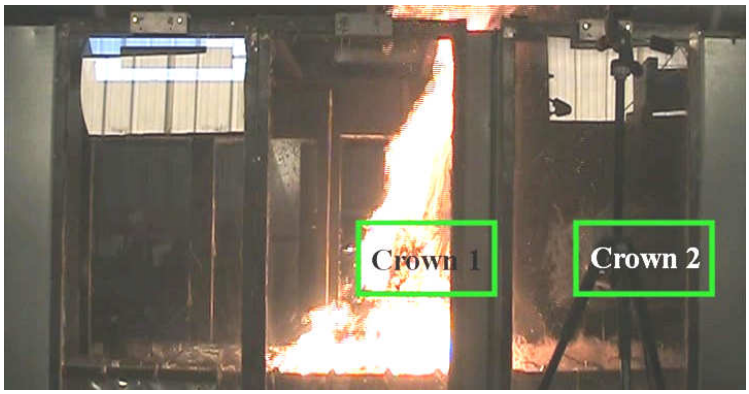


Figure 6.34: Average rate of spread and surface fuel mass loss rate at each thermocouple location plot for a crown separation distance of 30 cm during a 1.1 m/s wind condition. Left axis represents values for rate of spread and right axis represents values for surface fuel mass loss rate; *R* plot containing standard deviation error bars located in Appendix B.

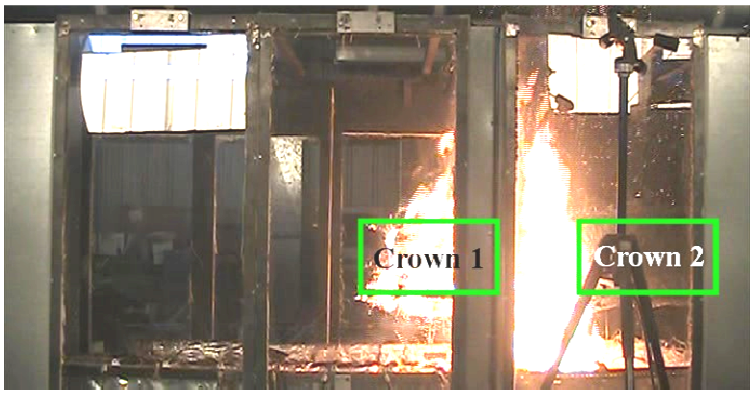
R and $\dot{m}$ increase to 3.9 cm/s (TC7) and 11.9 g/s (TC7), respectively, during the combustion of crown 1. At the peak of crown 1 combustion, Figure 6.35b, 2.52 kW/m^2 and 0.26 kW/m^2 of maximum total and convection heat flux, respectively, impinge onto crown 3 located 150 cm downstream from the center of crown 1, Figure 6.37a. The fire front begins to diminish as the crown 1 and surface fire front progresses in the downstream direction and the crown 1 fuel supply is exhausted. *R* and $\dot{m}$ decrease to 2.0 (TC8) cm/s and 8.2 g/s (TC8), respectively.



(a)



(b)



(C)

Figure 6.35: Images from experiment 38 at (a) t = 99 s at time of crown 1 ignition; (b) t = 115 s during crown 1 combustion; (c) t = 136 s at time of crown 2 ignition.

Crown 1 and 2 @ 30 cm CSD V = 1.1 m/s	
Distance from fuel bed downstream edge (m)	F_{1-2}
2.56	0.084
2.46	0.101
2.30	0.132
2.23	0.130
2.20	0.127
2.11	0.084
2.04	0.116
1.96	0.127
1.91	0.121
1.81	0.139
1.75	0.146
1.66	0.154
1.60	0.162
1.53	0.073
1.48	0.196
1.38	0.130
1.28	0.138
1.18	0.148
1.08	0.170
0.98	0.184
0.88	0.200
0.78	0.219
0.68	0.267
0.58	0.299
0.48	0.338
0.38	0.386
0.28	0.511
0.18	0.596
0.08	0.644

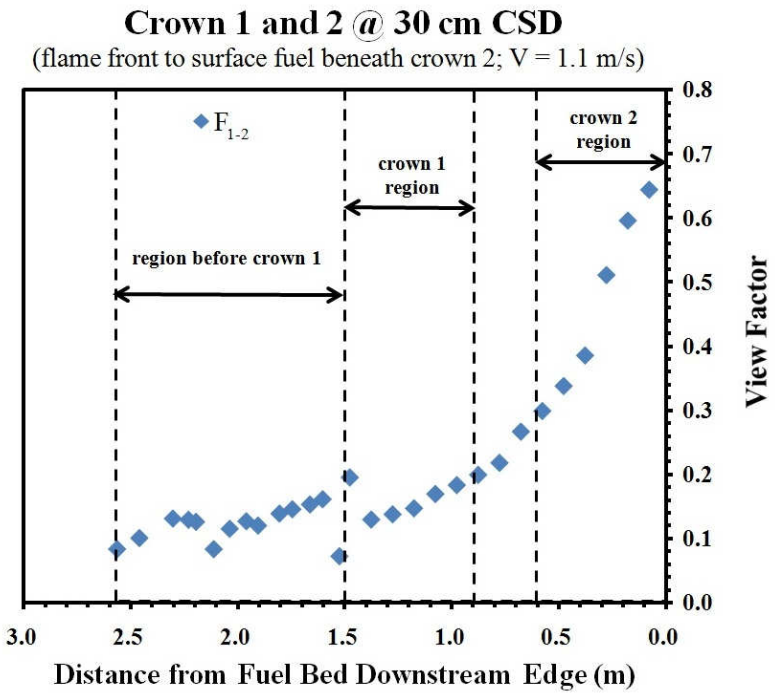


Figure 6.36: Tabulated view factor values and corresponding plot for a crown 1 and crown 2 configuration for a CSD of 30 cm at a wind condition of 1.1 m/s. Left side of plot represents leading edge of fuel bed while right side of plot represents the downstream edge of the fuel bed.

The 30 cm open space between crown 1 and crown 2 allows the fire front to impinge heat flux onto the unburned surface fuel. This allows the unburned fuel to be preheated and R and $\dot{m}$ increases to 2.4 cm/s (TC9) and 11.8 g/s (TC9), respectively. When the fire front arrives at crown 2 heat is reallocated to preheating crown 2 fuel elements and the view factor between the fire front and the unburned surface fuel beneath crown 2 reduces. The result is a decrease of R to 2.2 cm/s (TC10) and $\dot{m}$ to 9.9 g/s (TC10). The 1288 K gaseous products of combustion preheat the chamise branch elements to 380 K, and when sufficient water has evaporated, the branch elements

continue to increase in temperature and ignite when ignition temperature is achieved, Figure 6.35c.

A maximum total and convection heat flux of 17.69 kW/m^2 and 2.11 kW/m^2, respectively, impinge onto crown 3 60 cm downstream from the center of crown 2, Figure 6.37a, during peak crown 2 combustion. Heat flux diminishes as surface and crown 2 fuel is exhausted. The confidence interval for the overall R and $\dot{m}$ along the fuel bed is 2.7 cm/s ± 0.16 cm/s and 9.1 g/s ± 0.79 g/s, respectively. The maximum total heat flux has a confidence interval of 18.10 kW/m^2 ± 0.46 kW/m^2 with a standard deviation of 0.4 kW/m^2, and for the maximum convection heat flux, the confidence interval is 1.97 kW/m^2 ± 0.14 kW/m^2 with a standard deviation of 0.13 kW/m^2.

An analysis is performed using fuel configuration b consisting of the surface fuel and crown 1 to investigate how heat flux impingement onto crown 3 matrix, located 150 cm downstream from the center of crown 1, is affected by the presence of crown 2. Figure 6.38 shows a representation of heat flux which impinges onto crown 3 downstream of crown 1. Analysis show that the average maximum total heat flux and convection flux impinging onto crown 3 is 5.66 kW/m^2 and 0.85 kW/m^2, respectively. In comparison, when crown two is present and CSD is 30 cm, the average maximum total heat flux is 2.73 kW/m^2 and maximum convection flux is 0.29 kW/m^2. The presence of crown two hinders radiation and convection impingement, thus average maximum total and convection heat flux impingement onto crown 3 is reduced by a factor of 2.1 and 3.0, respectively. Low heat flux impingement results in a lower R between crown fuel matrices.

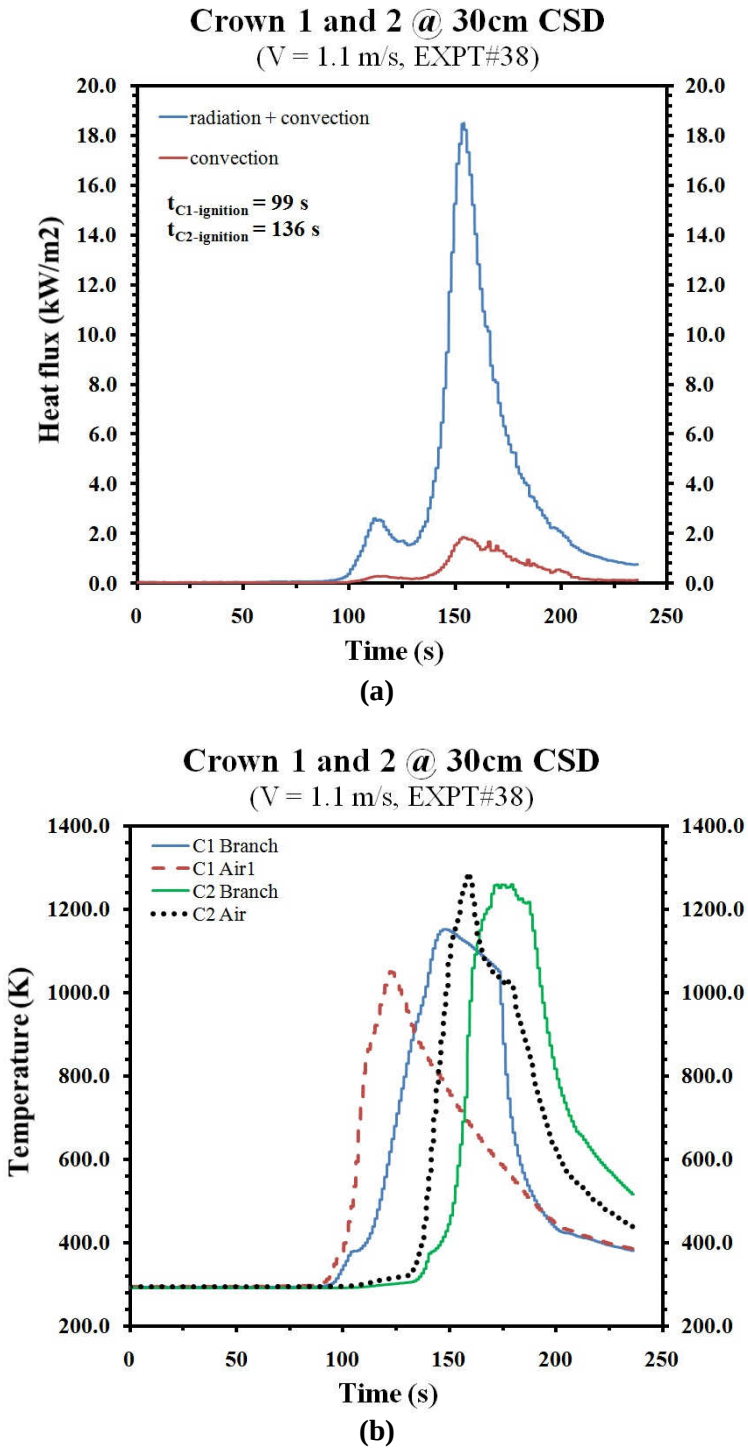


Figure 6.37: Plots for a surface fuel and crown 1 and two configuration at a crown separation distance of 30 cm for a 1.1 m/s wind condition of: (a) total heat flux and convection heat flux produced during experiment 38; (b) branch and air temperature history during experiment 38.

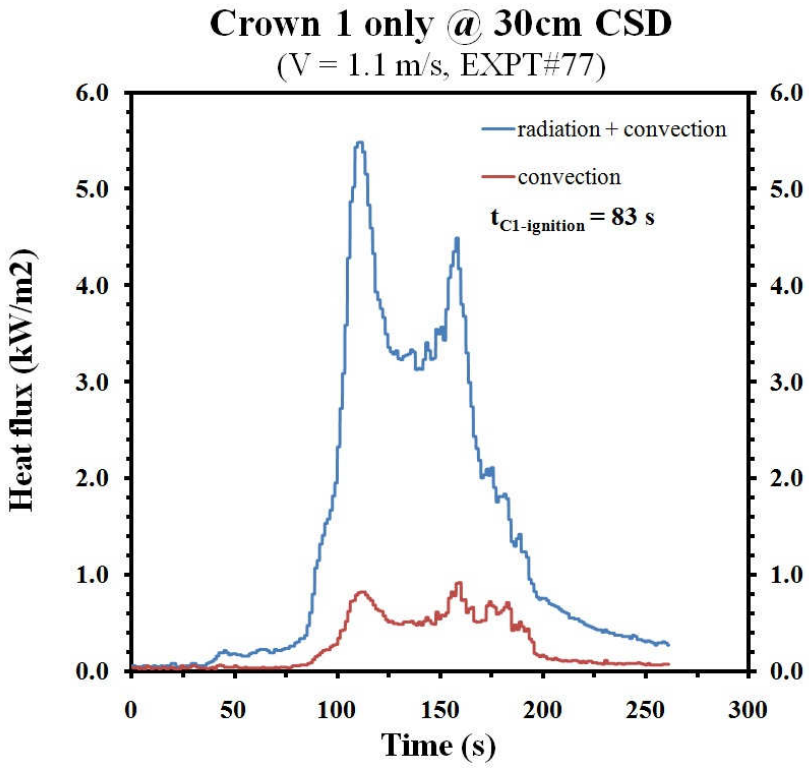


Figure 6.38: Total heat flux and convection heat flux curves for a surface fuel and crown 1 only configuration at a crown separation distance of 30 cm for a 1.1 m/s wind condition during experiment 77.

Crown Separation Distance of 10 cm with a 1.9 m/s Wind

The three crown separation distances of 10 cm, 20 cm and 30 cm are investigated at a constant wind speed of 1.9 m/s. Thermocouples that located 2.5 cm above the surface fuel are used to determine surface fire front rate of spread, while two thermocouples per crown are used to investigate crown fuel ignition as a result of heat transfer from a propagating surface fire and from burning adjacent crown fuel matrices. A heat flux sensor (model RC01) is used to determine heat flux impingement onto crown 3 located 30 cm from the downstream face of crown 2. It is expected that as the wind speed is increase to 1.9 m/s from the previous wind case of 1.1 m/s, the overall rate of

spread along the fuel bed will increase as a result of an augmentation in fuel combustion rate due to the large influx of oxygen to the fire front. This will produce a larger amount of heat flux that will assist in the preheating process of unburned surface and crown fuels.

Table 6.10 contains data for the average rate of spread, R, and average surface fuel mass loss rate, $\dot{m}$, at each thermocouple location along the surface fuel bed, and Figure 6.39 shows the curves of R and $\dot{m}$ plotted together. The instability of R along the surface fuel is apparent by performing a visual inspection of the plotted R values. The range of R is at a minimum 2.4 cm/s and 8.3 cm/s at the maximum with a standard deviation of 2.13 cm/s. At the same fuel configuration, but with wind speeds of 0.0 m/s and 1.1 m/s, the standard deviations are 0.27 cm/s and 1.41 cm/s, respectively. As the wind speed increases the instability of R becomes obvious.

V = 1.9 m/s, Crown 1 and Crown 2 at 10 cm CSD			
TC #	**Location (cm)**	**R (cm/s)**	**$\dot{m}$ (g/s)**
2	60	8.3	11.7
3	80	3.3	11.5
4	100	6.5	9.1
5	120	3.6	14.7
6	140	6.0	11.0
7	160	7.7	13.5
8	180	3.3	16.2
9	200	5.7	17.3
10	220	2.4	14.5

Table 6.10: Average rate of spread and average surface fuel mass loss rate data at each thermocouple location for a crown separation distance of 10 cm during a 1.9 m/s wind condition.

From TC3 to TC4 *R* decreases as the surface fire front approaches crown 1. The combination of heat flux reallocation to preheat the unburned crown 1 chamise fuel and the presence of crown 1, causes *R* and $\dot{m}$ to decrease at the leading edge of crown 1. *R* decreases from 6.5 cm/s (TC4) to 3.6 cm/s (TC5) and $\dot{m}$ decreases from 14.7 g/s (TC5) to 11.0 g/s (TC6). As the fire front approaches crown 1 the view factor increases from 0.175 (2.51 m from the downstream edge of the fuel bed) to 0.222 (1.35 m from the downstream edge of the fuel bed). Crown 1 then starts to obstruct radiation impingement onto the unburned surface fuel resulting in a lower view factor of 0.158 at 1.15 m from the downstream edge of the fuel bed, Figure 6.40.

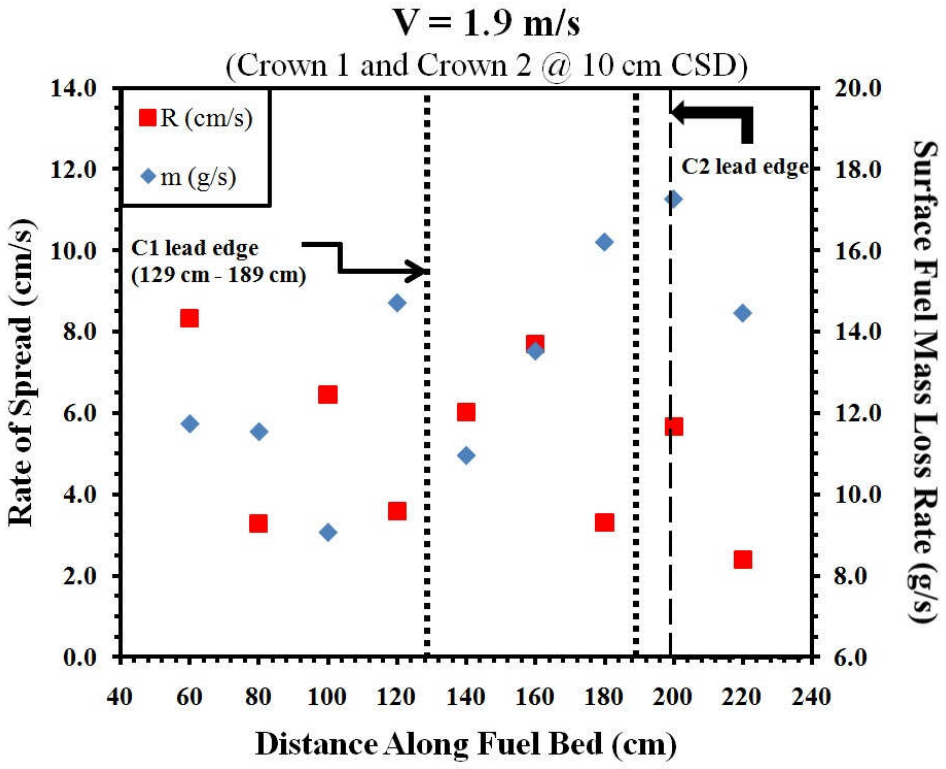


Figure 6.39: Average rate of spread and surface fuel mass loss rate at each thermocouple location plot for a crown separation distance of 10 cm during a 1.9 m/s wind condition. Left axis represents values for rate of spread and right axis represents values for surface fuel mass loss rate; *R* plot containing standard deviation error bars located in Appendix B.

The 913 K hot gaseous products of combustion flow through crown 1 fuel matrix preheating the chamise branch element to 380 K, and cause the water within the chamise fuel to vaporize. Once a sufficient amount of water is expelled, the branch temperature increases to ignition temperature and enters the flaming phase, Figure 6.41a. As crown 1 combusts, R increases to 7.7 cm/s (TC7) and $\dot{m}$ increase to 16.2 g/s (TC8). Since crown 1 and crown 2 are within close proximity of each other, as the fire front propagates and progress towards crown 2, the surface and crown 1 fire front never separate, and instead remain as a large merged fire front growing in intensity as crown 2 is approached. From the moment crown 1 ignites, and the flame lengths increase exceeding 2.4 m, to when the fire front reaches the downstream edge of the fuel bed, the view factors increase exponentially reaching a maximum value of 0.586.

The combustion of crown 1 results in approximately 7.0 kW/m^2 of total heat flux impinging onto crown 3 before crown 2 ignites, Figure 6.41b. The hot gaseous products of combustion, at 1125 K, along with the radiation and convection flux, preheat the crown 2 chamise fuel elements and cause them to ignite, Figure 6.41c. During the preheating of crown 2, R briefly decreases to 3.3 cm/s (TC8), but then increase to 5.7 cm/s (TC9) as crown 2 ignites. At the peak of crown 2 combustion, 23.61 kW/m^2 of maximum total heat flux and 3.98 kW/m^2 of maximum convection flux impinge onto crown 3 with flame heights exceeding 2.4 m, Figure 6.42a.

Crown 1 and 2 @ 10 cm CSD V = 1.9 m/s	
Distance from fuel bed downstream edge (m)	F_{1-2}
2.51	0.175
2.48	0.163
2.39	0.156
2.26	0.195
2.16	0.188
2.15	0.188
2.13	0.173
2.02	0.188
1.99	0.188
1.97	0.188
1.89	0.144
1.85	0.139
1.82	0.222
1.80	0.159
1.72	0.167
1.68	0.167
1.64	0.162
1.63	0.162
1.61	0.255
1.55	0.185
1.46	0.196
1.45	0.210
1.40	0.210
1.35	0.222
1.15	0.158
0.95	0.184
0.75	0.241
0.55	0.299
0.35	0.444
0.15	0.586

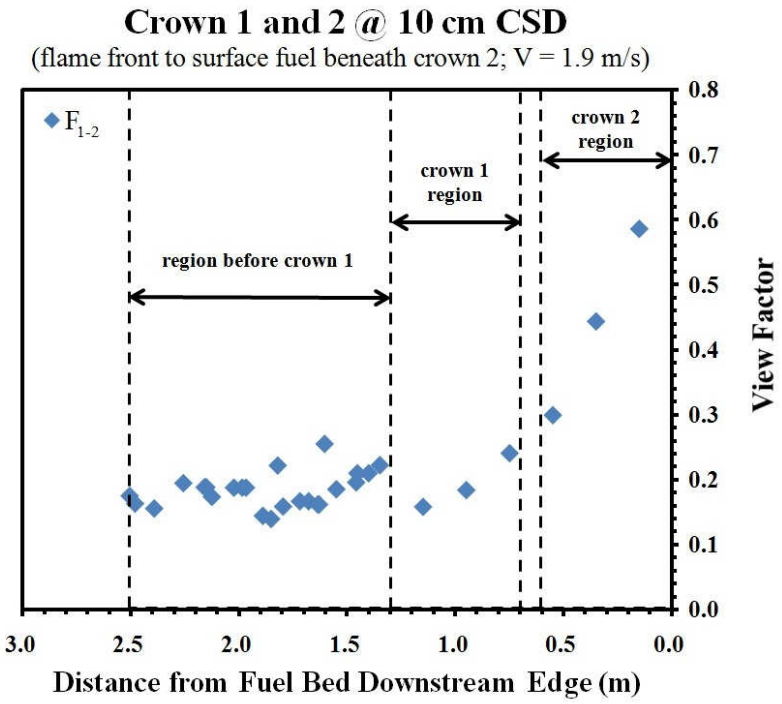
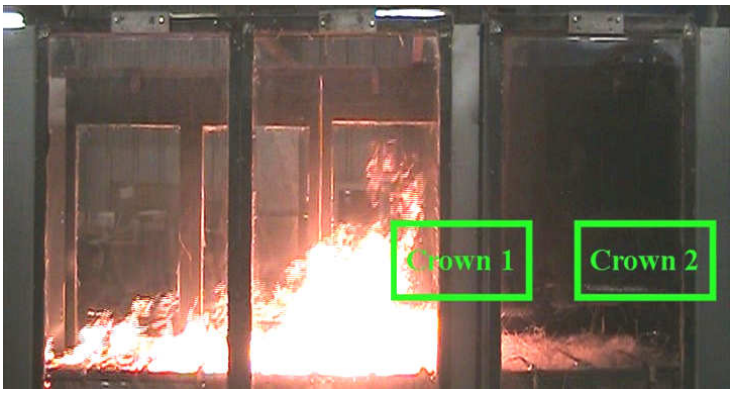
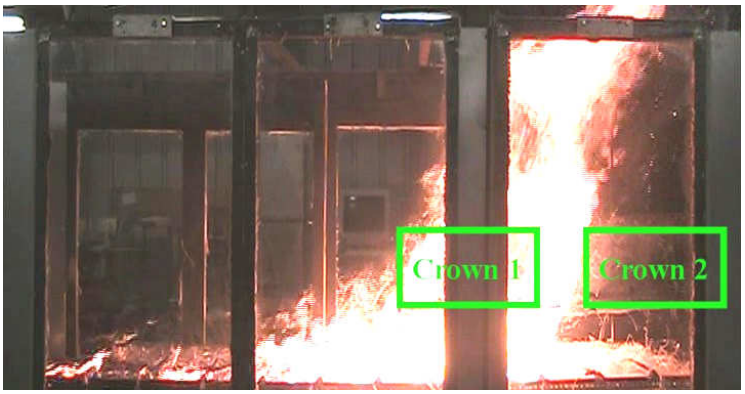


Figure 6.40: Tabulated view factor values and corresponding plot for a crown 1 and crown 2 configuration for a CSD of 10 cm at a wind condition of 1.9 m/s. Left side of plot represents leading edge of fuel bed while right side of plot represents the downstream edge of the fuel bed.

For the case of a crown separation distance of 10 cm at a constant wind speed of 1.9 m/s, a total of four experiments were performed. The overall rate of spread for the four experiments is 4.71 cm/s with a confidence value of ± 0.28 cm/s and a standard deviation of 0.28 cm/s. For the surface fuel mass loss rate, mass loss data was only available for two experiments due to technical difficulties. From those two experiments the average surface fuel mass loss rate is 13.27 g/s with a standard deviation of 0.26 g/s and a confidence value of 0.36 g/s. The confidence interval for the maximum total heat flux and maximum convection flux is 26.16 kW/m^2 ± 3.01 kW/m^2 and 3.98 kW/m^2 ± 0.07 kW/m^2, respectively.



(a)



(b)



(c)

Figure 6.41: Images from experiment 29 at (a) t = 81 s at time of crown 1 ignition; (b) t = 85 s during crown 1 combustion; (c) t = 92 s at time of crown 2 ignition.

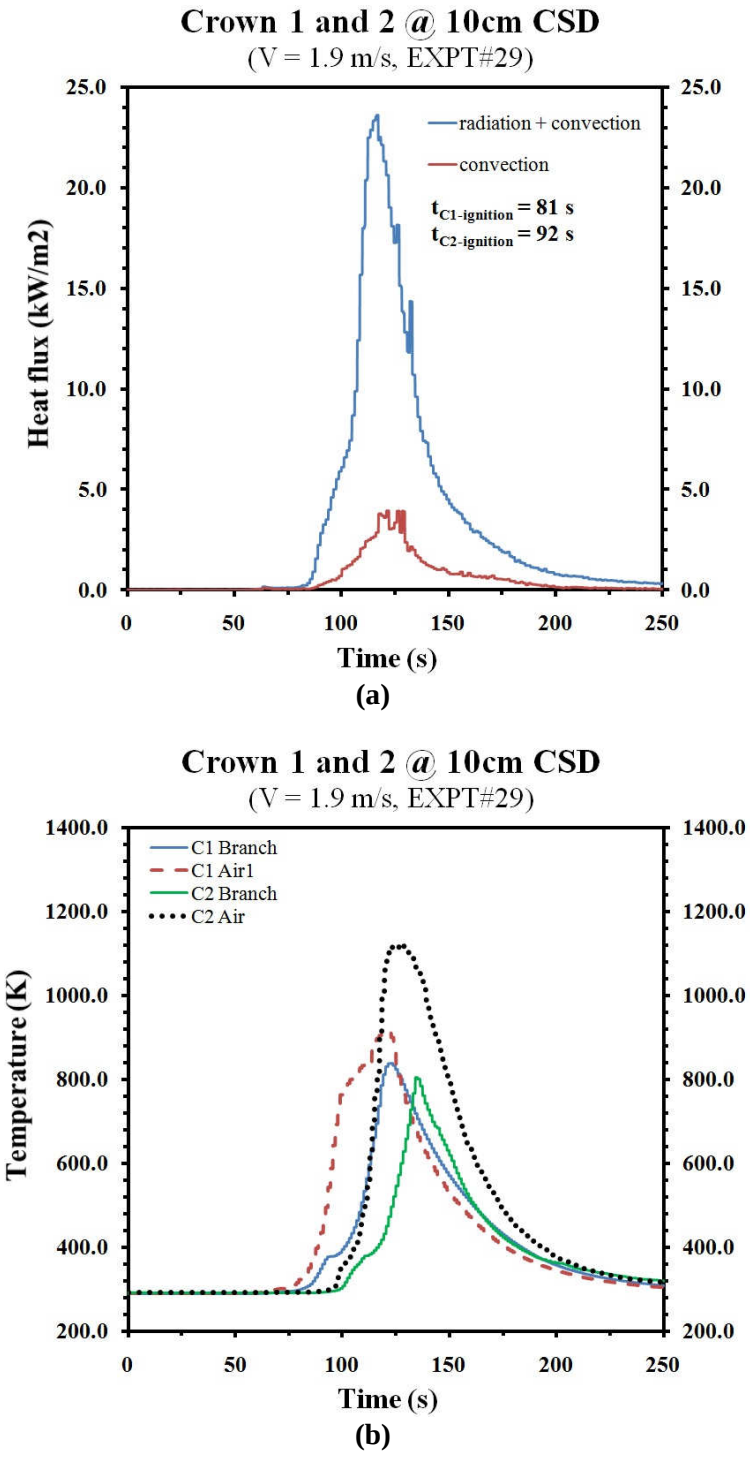


Figure 6.42: Plots for a surface fuel and crown 1 and two configuration at a crown separation distance of 10 cm for a 1.9 m/s wind condition of: (a) total heat flux and convection heat flux produced during experiment 29; (b) branch and air temperature history during experiment 29.

Crown Separation Distance of 20 cm with a 1.9 m/s Wind

The next investigation is performed by adjusting the crown separation distance to 20 cm and keeping the wind constant at 1.9 m/s. Table 6.11 contains data for the average rate of spread and average surface fuel mass loss rate at each thermocouple location calculated from all the experiments performed. Figure 6.43 shows R and $\dot{m}$ plotted together to visually observe spread rate and mass loss behavior as the fire front progresses along the fuel bed.

V = 1.9 m/s, Crown 1 and Crown 2 at 20 cm CSD			
TC #	Location (cm)	R (cm/s)	$\dot{m}$ (g/s)
2	60	8.3	16.4
3	80	2.5	10.1
4	100	6.0	12.4
5	120	5.1	16.6
6	140	5.4	19.0
7	160	12.9	18.0
8	180	3.7	15.8
9	200	4.8	15.6
10	220	3.0	11.3

Table 6.11: Average rate of spread and average surface fuel mass loss rate data at each thermocouple location for a crown separation distance of 20 cm during a 1.9 m/s wind condition.

Similarly to the case of a CSD of 10 cm at 1.1 m/s wind speed, R at each thermocouple, at a 20 cm CSD, varies widely from 2.5 cm/s at the minimum and 12.9 cm/s at the maximum. From TC4 to TC5 R decreases from 6.0 cm/s to 5.1 cm/s as the fire front approaches and arrives at crown 1, Figure 6.44a. The reduction in R is due to the reallocation of heat to preheat crown 1 chamise fuel matrix and decreased heat flux impingement onto the unburned surface fuel due to the presence of crown 1. As the fire front approaches crown 1 the view factor increases from 0.137 (2.5 m from the

downstream edge of the fuel bed) to 0.246 (1.48 m from the downstream edge of the fuel bed). Crown 1 then begins to obstruct radiation impingement onto the unburned surface fuel resulting in a lower view factor of 0.138 at 1.28 m from the downstream edge of the fuel bed, Figure 6.45. Experiment 30 will be used to represent the fire behavior for a CSD 20 cm at a wind speed of 1.9 m/s.

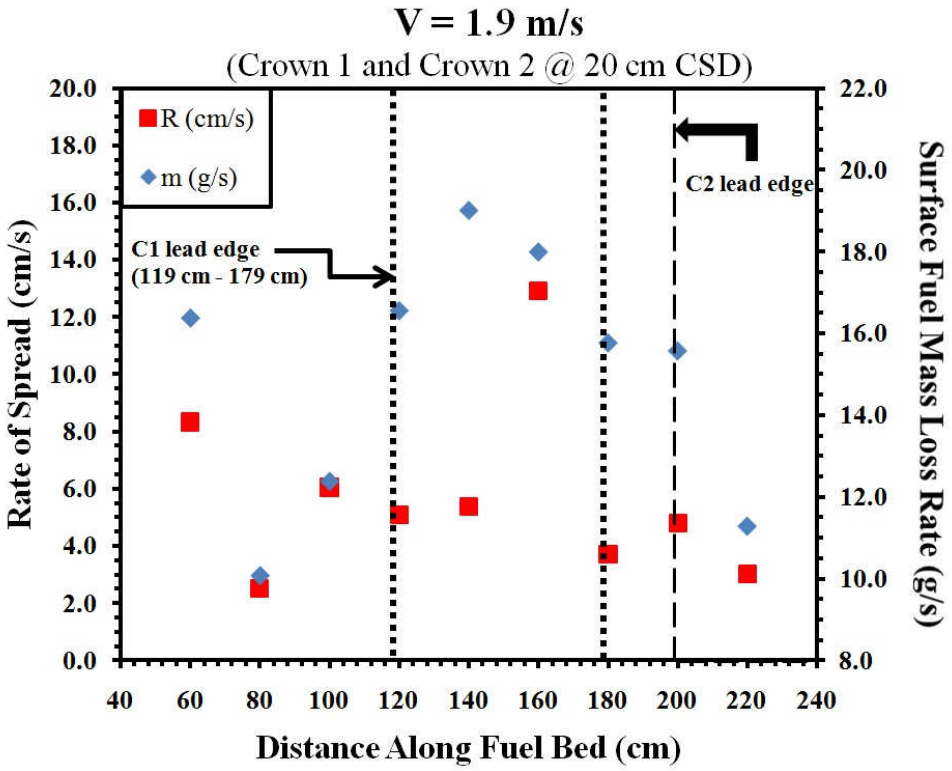


Figure 6.43: Average rate of spread and surface fuel mass loss rate at each thermocouple location plot for a crown separation distance of 20 cm during a 1.9 m/s wind condition. Left axis represents values for rate of spread and right axis represents values for surface fuel mass loss rate; *R* plot containing standard deviation error bars located in Appendix B.

The 1075 K hot gaseous products of combustion flow through crown 1 matrix preheating the chamise fuel elements. The branch elements of the chamise crown 1 matrix are preheated to 380 K, Figure 6.44b. When sufficient water is vaporized, the

chamise branch elements proceed to increase in temperature until ignition temperature is achieved, at which point the branch elements will enter the flaming phase. From the time crown 1 ignites, and the flame lengths increase exceeding 2.4 m, to when the fire front reaches the downstream edge of the fuel bed, the view factors increase exponentially reaching a maximum value of 0.664. R increases to 12.9 cm/s (TC7) as crown 1 combusts and as the surface and crown 1 fire fronts merge and proceed to spread in the downstream direction. $\dot{m}$ continues to increase from 10.1 g/s (TC3) to 19.0 g/s (TC6), Figure 6.43, as the fire front spread along the surface fuel and then ignites crown 1. The increase in $\dot{m}$ is a result of the 1.9 m/s wind causing the fire front depth to increase rapidly.

In the section before crown 1, the fire front increases in intensity because oxygen flow to the fire front is unhindered, feeding the fire front from all direction. Heat from the surface fire front quickly preheats and ignites crown 1 because radiation and convection heat flux is allowed to impinge onto crown 1 without any obstructions. As crown 1 enters the flaming phase, the combined radiation from the merged crown 1 and surface fire fronts impinge large quantities of heat flux onto the unburned surface fuel beneath crown 1. The combination of intense merged fire fronts and quickly combusting fuels, initially causes an increase in R and $\dot{m}$, but as the fire front continues to propagate through crown 1 and surface fuel, R and $\dot{m}$ decrease as a result of the remaining crown 1 and crown 2 fuel that hinders oxygen flow. The result is a reduction in the rate at which oxygen is entrained into merged fire fronts, thus reducing the rate at which the flame

depth grows. The outcome is a decrease of R from 12.9 cm/s (TC7) to 3.7 cm/s (TC8) and a reduction of $\dot{m}$ from 19.0 g/s (TC6) to 15.8 g/s (TC8).



(a)



(b)



(c)

Figure 6.44: Images from experiment 30 at (a) t = 56 s at time of crown 1 ignition; (b) t = 65 s during crown 1 combustion; (c) t = 75 s at time of crown 2 ignition.

Crown 1 and 2 @ 20 cm CSD V = 1.9 m/s	
Distance from fuel bed downstream edge (m)	F_{1-2}
2.50	0.137
2.46	0.171
2.26	0.152
2.22	0.211
2.08	0.249
2.02	0.188
1.95	0.144
1.91	0.212
1.80	0.222
1.80	0.180
1.78	0.214
1.75	0.170
1.74	0.146
1.69	0.243
1.69	0.243
1.67	0.293
1.60	0.261
1.58	0.243
1.55	0.198
1.50	0.222
1.48	0.246
1.28	0.138
1.08	0.170
0.88	0.200
0.68	0.267
0.48	0.338
0.28	0.511
0.08	0.664

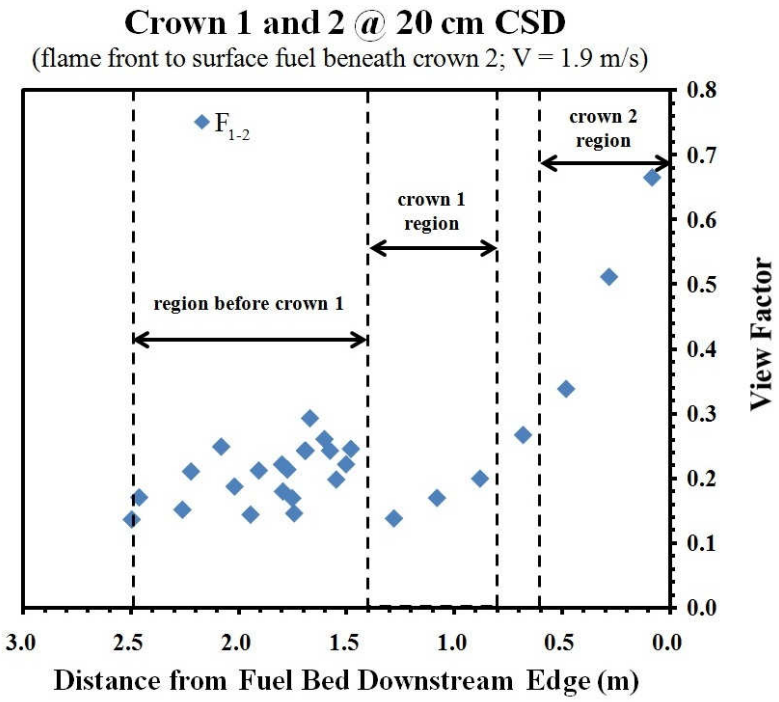


Figure 6.45: Tabulated view factor values and corresponding plot for a crown 1 and crown 2 configuration for a CSD of 20 cm at a wind condition of 1.9 m/s. Left side of plot represents leading edge of fuel bed while right side of plot represents the downstream edge of the fuel bed.

At the peak of crown 1 combustion, 6.66 kW/m^2 of total heat flux impinge onto crown 3 located 140 cm downstream from the center of crown 1. The radiation and convection flux from the burning crown 1 impinge onto crown 2 and onto the unburned surface fuel ahead of the fire front. As the fire front approaches and arrives at crown 2, heat flux is reallocated to preheating the crown 2 fuel matrix, and heat flux impingement onto the unburned surface is reduced due to the presence of crown 2.

The hot gaseous products of combustion, 1066 K, from the merged fire front preheat the chamise fuel elements of crown 2. The branch elements reach a temperature of approximately 380 K and enter the pre-ignition combustion phase. Water from within

the branch elements begin to vaporize and when the branch elements are sufficiently desiccated, the temperature of the branch increases to ignition temperature releasing pyrolysis gases and commencing the flaming phase, Figure 6.44c. R increases to 4.8 cm/s (TC9) as crown 2 undergoes the flaming phase. The surface and crown 2 fuel supply is exhausted as the fire front reaches the downstream edge of the surface fuel bed. R and $\dot{m}$ decrease to 3.0 cm/s (TC10) and 11.3 g/s (TC10) respectively. At the peak of crown 2 combustion, 26.80 kW/m^2 of total heat flux and 3.92 kW/m^2 of convection flux impinge onto crown 3, Figure 6.46a.

Four experiments were performed for the case of a CSD of 20 cm and a constant 1.9 m/s wind speed. R between each thermocouple position has a standard deviation of 3.19 cm/s. The confidence interval for the overall R along the fuel bed is 4.57 cm/s ± 1.01 cm/s while for $\dot{m}$ the confidence interval is 15.0 g/s ± 1.62 g/s. The standard deviation of $\dot{m}$ is 1.65 g/s. Maximum total heat flux and convection flux have confidence intervals of 25.42 kW/m^2 ± 2.38 kW/m^2 and 3.35 kW/m^2 ± 0.32 kW/m^2 with standard deviations of 2.43 kW/m^2 and 0.33 kW/m^2, respectively.

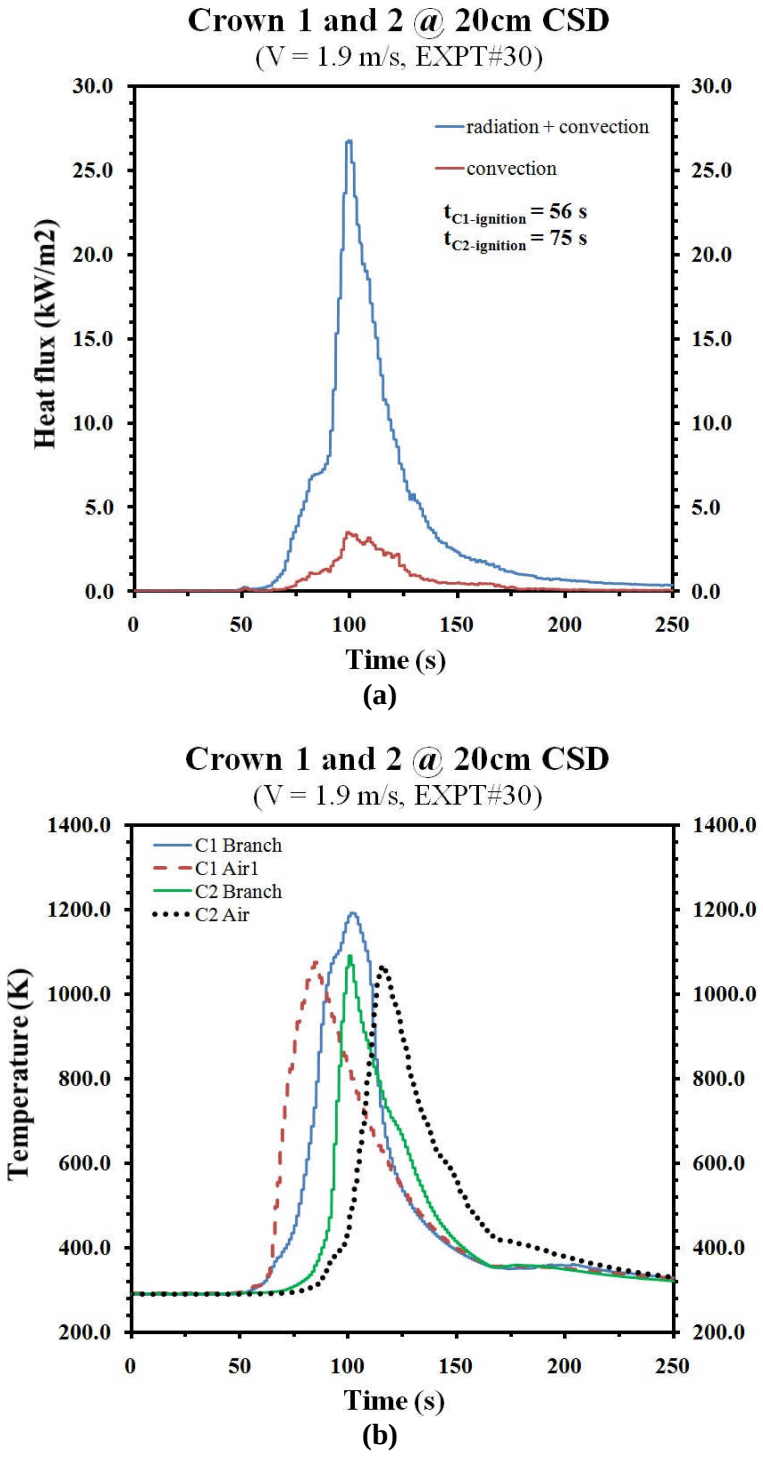


Figure 6.46: Plots for a surface fuel and crown 1 and two configuration at a crown separation distance of 20 cm for a 1.9 m/s wind condition of: (a) total heat flux and convection heat flux produced during experiment 30; (b) branch and air temperature history during experiment 30.

Crown Separation Distance of 30 cm with a 1.9 m/s Wind

The next investigation is performed by increasing the crown separation distance to 30 cm and keeping the wind constant at 1.9 m/s. Table 5.12 is constructed of the average rate of spread and average surface fuel mass loss rate data at each thermocouple location along the surface fuel bed. R and $\dot{m}$ are plotted in Figure 6.47 to visually investigate how the fire front behaves as it propagates along the surface fuel bed. Figure 6.47 shows the instability of R, which has a standard deviation of 1.71 cm/s. At a CSD of 30 cm the standard deviation is larger than at wind speeds of 1.1 m/s and 0.0 m/s, for the same fuel configuration, by a factor of 2.3 and 4.6, respectively.

V = 1.9 m/s, Crown 1 and Crown 2 at 30 cm CSD			
TC #	Location (cm)	R (cm/s)	$\dot{m}$ (g/s)
2	60	5.1	7.8
3	80	2.4	11.9
4	100	7.0	13.6
5	120	3.6	15.0
6	140	5.8	13.9
7	160	6.3	15.4
8	180	4.0	10.8
9	200	3.8	11.9
10	220	2.0	7.6

Table 6.12: Average rate of spread and average surface fuel mass loss rate data at each thermocouple location for a crown separation distance of 30 cm during a 1.9 m/s wind condition.

From TC4 to TC 5 R decrease from 7.0 cm/s to 3.6 cm/s as a result of heat reallocation to preheat crown 1 fuel elements and by the hindering of heat flux impingement onto the unburned surface fuel due to the presence of crown 1, which results in a reduction of the view factor between the entire fire front and the unburned surface fuel beneath crown 1. As the fire front approaches crown 1 the view factor

changes from 0.175 (2.47 m from the downstream edge of the fuel bed) to 0.173 (1.38 m from the downstream edge of the fuel bed). Crown 1 then starts to obstruct radiation impingement onto the unburned surface fuel resulting in a lower view factor of 0.104 at 1.35 m from the downstream edge of the fuel bed, Figure 6.48.

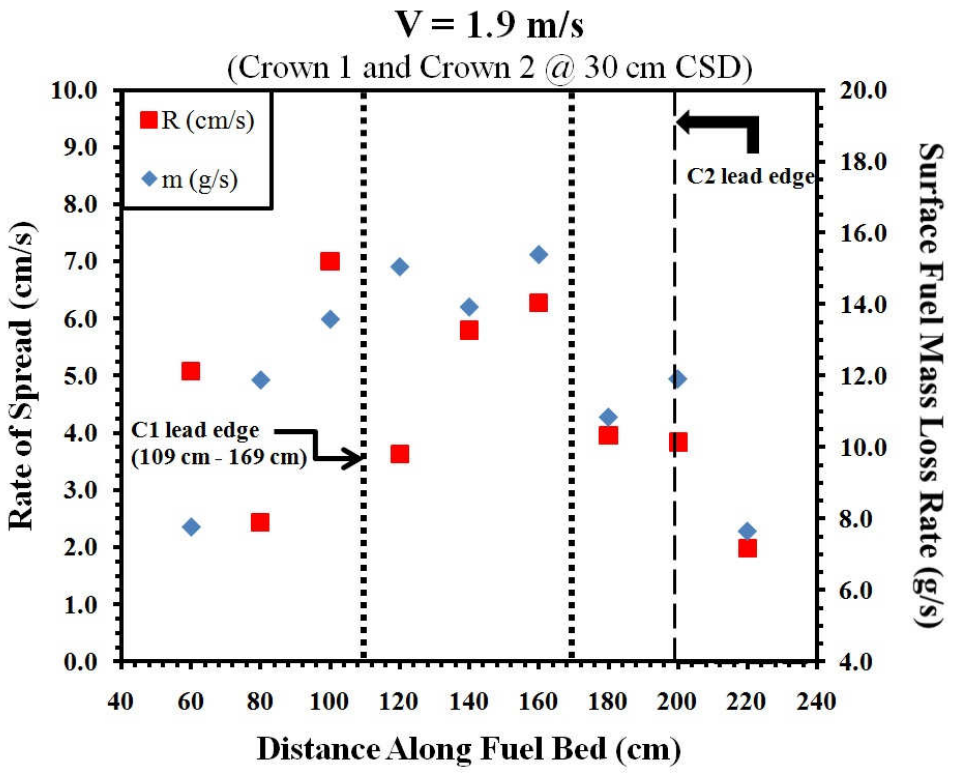


Figure 6.47: Average rate of spread and surface fuel mass loss rate at each thermocouple location plot for a crown separation distance of 30 cm during a 1.9 m/s wind condition. Left axis represents values for rate of spread and right axis represents values for surface fuel mass loss rate; *R* plot containing standard deviation error bars located in Appendix B.

The high 1.9 m/s wind speed causes the flame depth to grow rapidly resulting in $\dot{m}$ increasing from TC2 to TC5 from 7.8 g/s to 15.0 g/s just beyond the leading edge of crown 1. The 1065 K hot gaseous products of combustion flow through the crown 1 matrix preheating the chamise fuel elements. Chamise branch elements are preheated to

approximately 380 K, entering the pre-ignition combustion phase, where water is expelled as vapor and pyrolysis gases are emitted. The pyrolysis gases then mix with incoming oxygen and crown 1 achieves the flaming phase, Figure 6.49a. *R* increases from TC5 to TC7 from 3.6 cm/s to 6.3 cm/s as crown 1 is fully engulfed by the fire front. At the peak of crown 1 combustion, Figure 6.49b, 4.57 kW/m^2 of total heat flux and 0.89 kW/m^2 of convection heat flux impinge onto crown 3 located 150 cm downstream from the center of crown 1. From the instant crown 1 ignites, and the flame lengths increase exceeding 2.4 m, to when the fire front reaches the downstream edge of the fuel bed, the view factors increase exponentially reaching a maximum value of 0.586.

Crown 1 and 2 @ 10 cm CSD V = 1.1 m/s	
Distance from fuel bed downstream edge (m)	F_{1-2}
2.64	0.097
2.58	0.097
2.35	0.104
2.26	0.102
2.14	0.107
1.99	0.127
1.90	0.154
1.80	0.162
1.67	0.173
1.64	0.188
1.52	0.267
1.42	0.123
1.32	0.130
1.22	0.148
1.12	0.158
1.02	0.170
0.92	0.184
0.82	0.219
0.72	0.241
0.62	0.267
0.52	0.299
0.42	0.386
0.32	0.444
0.22	0.511
0.12	0.596

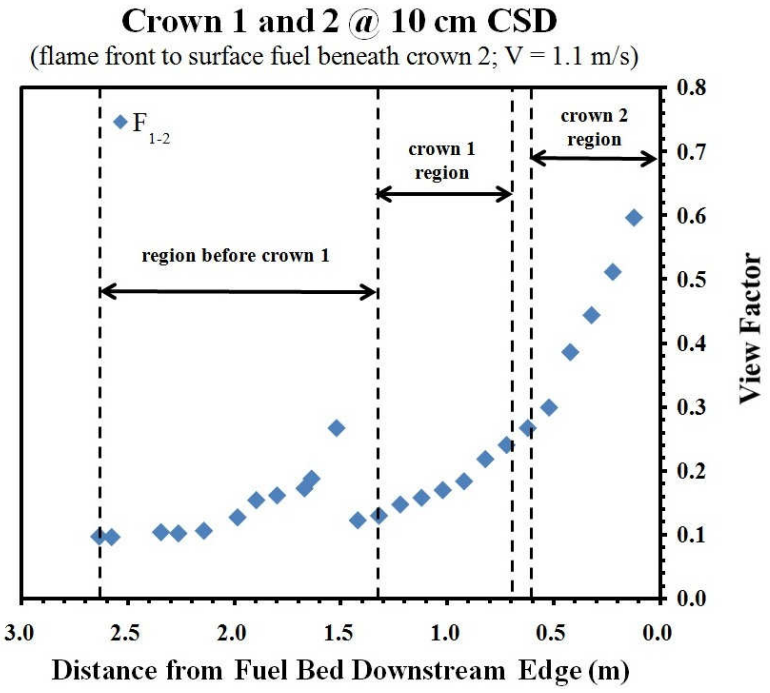
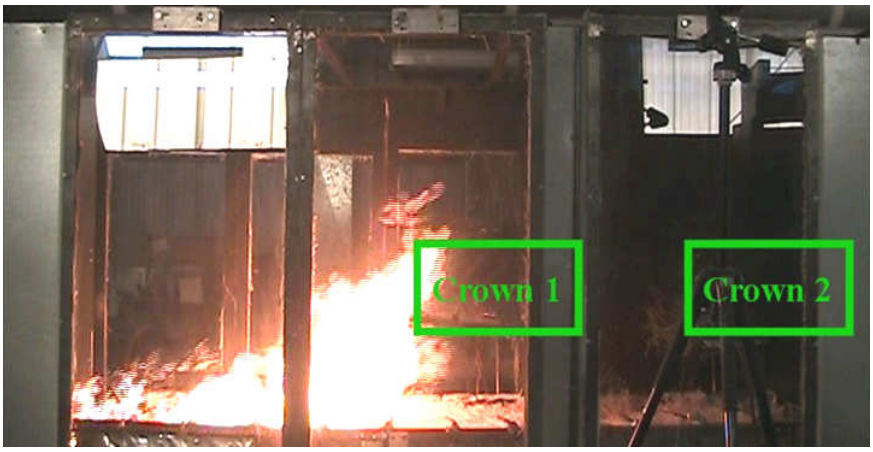


Figure 6.48: Tabulated view factor values and corresponding plot for a crown 1 and crown 2 configuration for a CSD of 30 cm at a wind condition of 1.9 m/s. Left side of plot represents leading edge of fuel bed while right side of plot represents the downstream edge of the fuel bed.

R decreases from TC7 to TC9 from 6.3 cm/s to 3.8 cm/s as the fire front arrives at the location of crown 2. The reallocation of heat to preheat crown 2 fuel elements causes a reduction in *R*. Radiation and convection flux from the merged surface and crown 1 fire front impinge onto the crown 2 fuel matrix preheating the chamise branch element to approximately 380 K. The branch elements undergo a pre-ignition phase where water vaporizes and pyrolysis gases are produced. Pyrolysis gases then mix with incoming oxygen and ignite entering the flaming phase, Figure 6.49c. During the maximum combustion of crown 2, 15.52 kW/m^2 and 3.13 kW/m^2 of total heat flux and convection heat flux impinge onto crown 3, Figure 6.50. *R* and $\dot{m}$ decrease to 2.0 cm/s (TC10) and 7.6 g/s (TC10) as the surface and crown fuel is exhausted.

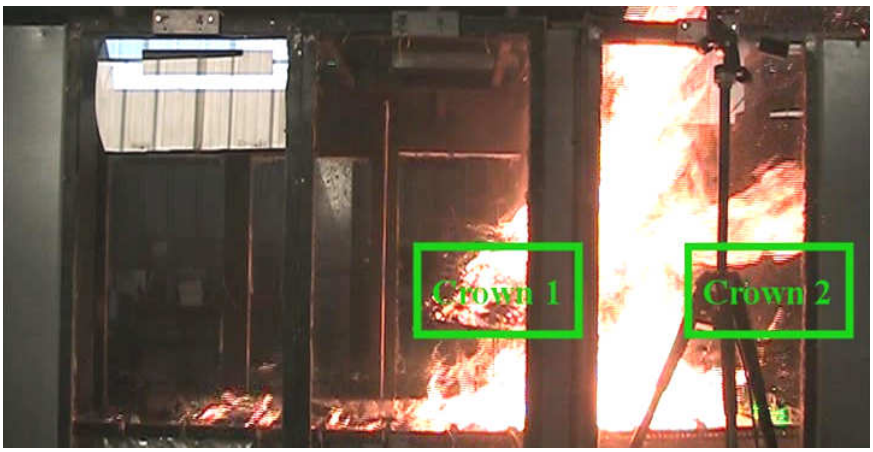
Three experiments were performed at 1.9 m/s wind speed with a 30 cm CSD fuel configuration. The confidence interval for the overall *R* and $\dot{m}$ along the surface fuel bed is 4.4 cm/s ± 0.62 cm/s and 12.0 g/s ± 2.58 g/s, respectively. Maximum total heat flux and maximum convection heat flux have confidence intervals of 17.72 kW/m^2 ± 2.16 kW/m^2 and 3.31 kW/m^2 ± 0.37 kW/m^2, respectively.



(a)



(b)



(c)

Figure 6.49: Images from experiment 30 at (a) t = 56 s at time of crown 1 ignition; (b) t = 65 s during crown 1 combustion; (c) t = 75 s at time of crown 2 ignition.

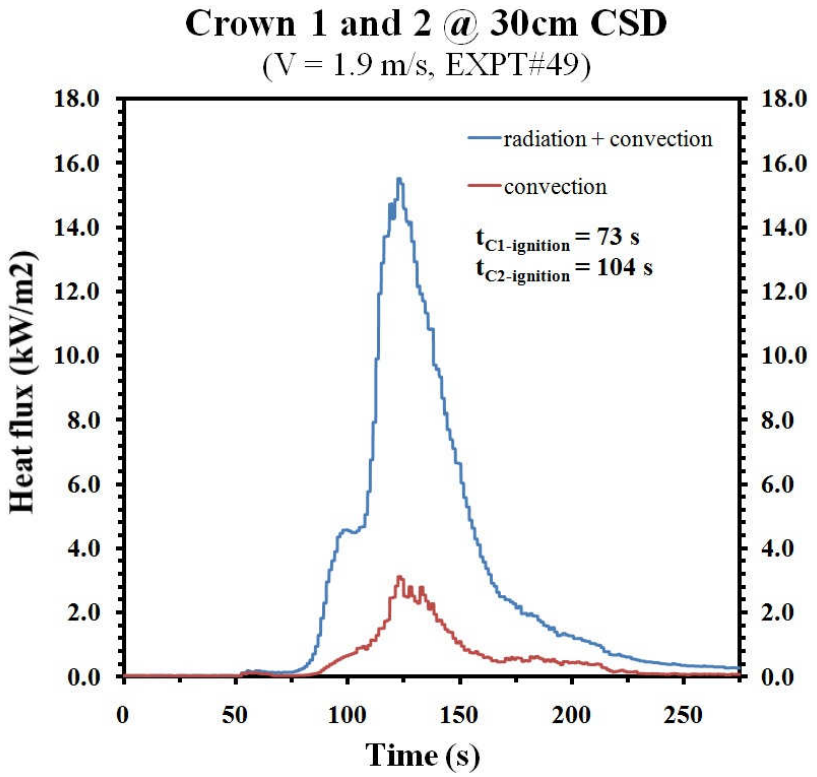


Figure 6.50: Plot for a surface fuel and crown 1 and 2 configuration at a crown separation distance of 30 cm for a 1.9 m/s wind condition of total heat flux and convection heat flux produced during experiment 49.

An analysis is performed to study how heat flux impingement onto crown 3 is affected by the presence of crown 2 using fuel configuration b consisting of the surface fuel and crown 1. The analysis will demonstrate how crown 2 obstructs heat flux impingement onto an adjacent crown fuel matrix. Total heat flux and convection heat flux impinged onto crown 3 is plotted in Figure 6.51 which is data for experiment 73 that closely represents the average heat flux measurements. In the case of a two crown configuration with a CSD of 30 cm experiencing a 1.9 m/s wind speed, the average maximum total heat flux and average maximum convection flux recorded at crown 3 is 3.63 kW/m^2 and 0.68 kW/m^2, respectively. With crown 2 removed and crown 1

maintained at a CSD of 30 cm and at a wind speed of 1.9 m/s, average maximum total heat flux and average maximum convection flux measured at crown 3 is greater by a factor of 3.5 and 3.4, respectively.

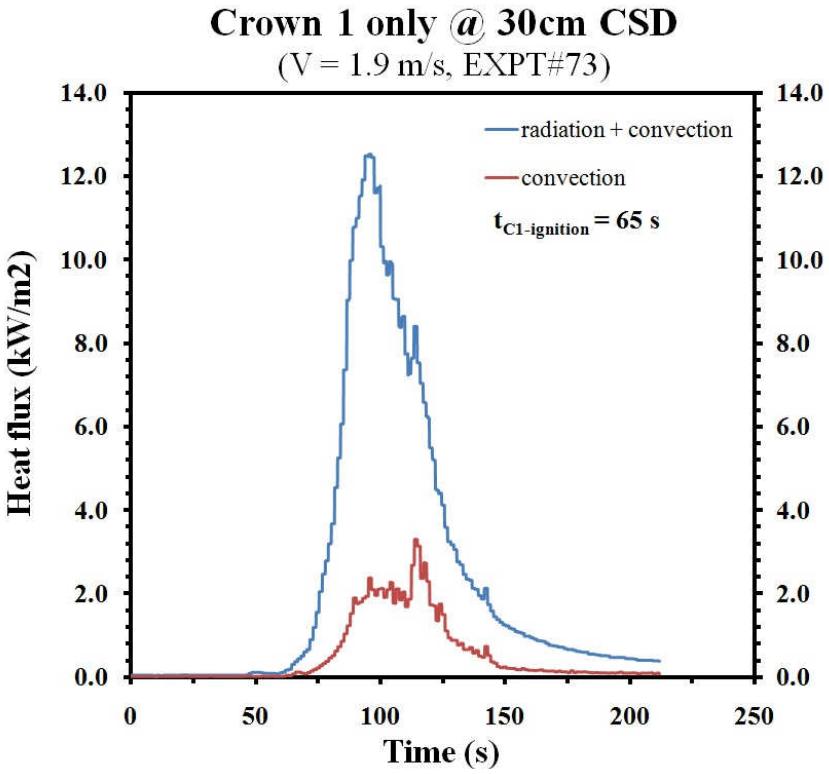


Figure 6.51: Total heat flux and convection heat flux curves for a surface fuel and crown 1 only configuration at a crown separation distance of 30 cm for a 1.9 m/s wind condition during experiment 73.

From this analysis it is determined that the presence of crown 2 significantly hinders heat flux impingement from crown 1 onto crown 3 150 cm downstream from the center of crown 1. It can be inferred from this conclusion, that any crown considerably obstructs heat flux impingement onto adjacent crown fuel matrices and surface fuels, which results in decreasing R and $\dot{m}$ values.

Discussion

Experiments were performed to investigate the influence of crown separation distance on the behavior of a propagating surface fuel fire front. The distance between crowns studied is 10 cm, 20 cm and 30 cm. The wind speed was varied for all sets of experiments to add another dimension and study how the combination of crown separation distance and wind affect fire front propagation behavior. Wind speeds investigated are 0.0 m/s, 1.1 m/s and 1.9 m/s. Heat flux data was collect at a sensor located 30 cm downstream from the downstream face of crown 2, and located to simulate a third crown fuel matrix referred to as crown 3.

In all the cases investigated for all the wind speed variations, it is shown that *R* decreases as the fire front arrives within close proximity of crown 1. The reduction of *R* can be attributed to the reallocation of heat to preheat crown 1 and the hindering of heat flux impingement onto the unburned surface fuel due to the positioning of crown 1 that reduces the view factor between the entire fire front and the unburned surface fuel ahead of the fire front. *R* increases as crown 1 ignites and propagates along the entire crown fuel matrix. Heat flux impingement onto the unburned surface fuel beneath crown 1, from the surface fuel fire front and crown 1 fire front, account for the increase in *R*. As the merged fire front approaches crown 2, *R* decreases, and this decrease is again attributed to the reallocation and hindering of heat flux to preheat crown 1 and preheat the unburned surface fuel ahead of the fire front. In all cases, except for a CSD of 30 cm and 1.9 m/s wind speed, *R* increase within the open space between crown 1 and crown 2. The increase in *R* is due to the open space where no crown fuels are located and thus heat

flux impingement onto the unburned surface fuel is unhindered allowing the surface fuels to be preheated. R and $\dot{m}$ decrease as the merged surface fire front and crown 2 fire front proceed towards the downstream edge of the wind tunnel test section. The decrease in R and $\dot{m}$ is attributed to the fire fronts exhausting the surface and crown fuel supply.

The large R instability in the 1.9 m/s wind speed condition for all the CSD cases investigated can be attributed to the large wind speed causing the flame depth to increase at a larger rate than at 1.1 m/s and 0.0 m/s wind speed conditions. The length of the fuel bed is not sufficiently long to allow the flame depth to stabilize. This phenomena merits further investigation using a significantly longer fuel bed.

Silvani and Morandini (2009) performed field experiments in the Mediterranean region in southern France in an area that ranged from 25 m^2 to 1220 m^2. The fire spread experiments were conducted across fuel beds consisting of pine needles or cut tree branches and leaves and were also conducted through living wild broom shrubs. Wind speeds during experimentation ranged from 0.5 m/s to 3.3 m/s. Heat flux measurements were conducted ahead of the fire front as it spread across the fuel beds and shrubs approaching the heat flux measurement device. In the experiments conducted at a wind speed of 0.5 m/s in a 25 m^2 plot, peak radiant and total heat flux were measured to be 25 kW/m^2 and 40 kW/m^2, respectively. At a wind speed of 2.2 m/s in a 60 m^2 plot, peak radiant and total heat flux were measured to be 36 kW/m^2 and 76 kW/m^2, respectively. In the experiments discussed in this chapter, peak radiant and total heat flux is measured to be 26 kW/m^2 and 30 kW/m^2, respectively, for a CSD of 10 cm at a wind speed of 1.9 m/s. A limitation of these small-scale experiments, in comparison to field experiments, is

that the maximum value of the irradiance of the flame front is naturally lower than in the real-scale fires [87].

7 Results - Particle Image Velocimetry Analysis

A Particle Image Velocimetry (PIV) system is used to investigate the fluid dynamic environment that exists in the region between a two crown fuel configuration as shown in figure 3.6 (Chapter 3: Experimental Setup, section 3.6: Particle Image Velocimetry System Arrangement). The crown fuel separation distances (CSD) studied are 10 cm, 20 cm and 30 cm. The three CSD cases are investigated at three different wind conditions of 0.0 m/s, 1.1 m/s and 1.9 m/s. For each analysis the wind speed is kept constant and the CSD is reconfigured to the three CSD cases. There are two objectives to the PIV analysis. The first objective is to determine if the separation between crown fuel matrices affects the flow speed of the hot gaseous products of combustion as the fire front propagates along the CSD region. The second objective is to observe what, if any, fluid dynamic structures arise due to the various CSD configurations. As is the case with most studies involving PIV, the seeding of the flow field and capturing of PIV images is non-trivial. During experimentation at a 0.0 m/s wind condition only the data at a CSD 10 cm was captured while data for CSD 20 cm and 30 cm was lost due to technical difficulties. At 1.1 m/s and 1.9 m/s, all CSD case data was successfully recorded.

Crown Separation Distance of 10 cm with a 0.0 m/s Wind

The first analysis is performed at a CSD of 10 cm with a 0.0 m/s wind condition. Air is entrained into the fire column as the fire front approaches the region of interest (ROI). During the entrainment period the average horizontal entrainment velocity $\overline{U}_{ent}$ is 0.3 m/s. In Figure 7.1, the dashed red lines represent the 10 cm open area within the ROI

between the crown fuel matrices. The area shown in Figure 7.1 from 0 mm to 100 mm is the region containing crown 1 fuel.

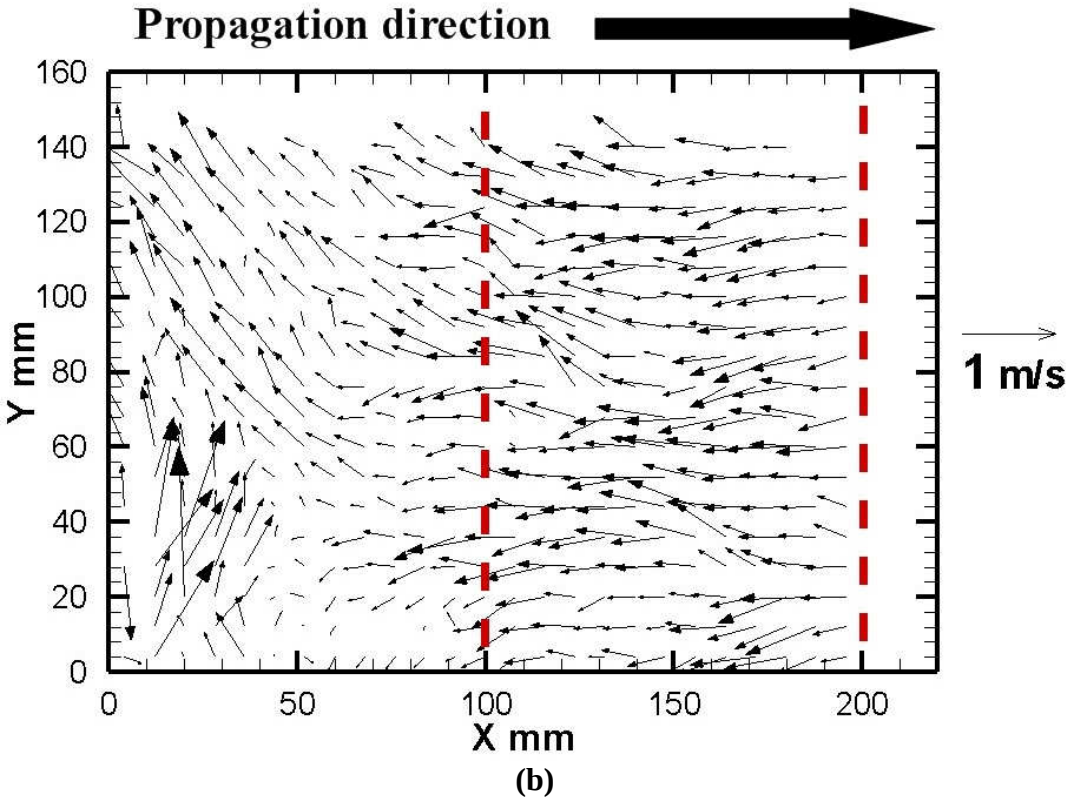


Figure 7.1: Velocity vector field plot for a surface fuel and crown 1 and 2 configuration at a crown separation distance of 10 cm for a 0.0 m/s wind condition during experiment 90 showing ambient air entrainment at t = 9.1 s; Note: time shown here is time during PIV capturing not time during the actual experiment.

The interaction between the high velocities of the hot gaseous products of combustion, the slower velocities of the entrained air, and the presence of the crown 1 fuel elements result in the formation of vortices throughout the ROI and not just at the flame-air interface. In this study, the diameter of a vortex is calculated as per Lozano (2008) and Lozano et al. (2010) where the radius of a vortex structure is defined as the average of the distances from the location of the local peak vorticity magnitude to the

point where its magnitude is 20% of the peak value. The local peak vorticity magnitude is computed using a second-order center differencing of the appropriate velocity components. The distances are measured at increments of 45 degrees starting from 0 to 315 degrees. Twice the average of these distances is calculated and recorded as the diameter of the vortex. Using the measured distances, the local vorticity is calculated using $\omega_i = V_{t_i}/r_i$, where ω_i is the local vorticity, r_i is the radius and $V_{t_i}$is the tangential velocity at the specified location determined utilizing the PIV velocity data. The average vorticity is then calculated using $\bar{\omega} = (1/n)\sum_{i=1}^{n}(V_{t_i}/r_i)$ where $\bar{\omega}$ is the average vorticity, and is henceforth referred to as the vorticity.

Figure 7.2a contains the velocity vector plot showing the formation of a 3.6 cm diameter vortex with a vorticity of 14.9 s^{-1} clockwise at t = 0.7 s and Figure 7.2b contains the corresponding vorticity contour plot used to calculate the vortex diameter and vorticity. The size and location of the vortex suggests that it may assist in preheating the crown 2 fuel elements. A velocity vector plot showing the formation of a 2.1 cm diameter vortex with a vorticity of 19.8 s^{-1} clockwise at t = 3.1 s and its corresponding vorticity contour plot are shown in Figure 7.3a and b, respectively. The size and location of the vortex indicates that it may not be assisting the preheating the fuel elements of crown 2. Three vortices are observed to be generated during the entrainment of the ambient air for the three experiments performed at a 10 cm CSD with a 0.0 m/s wind condition. Two of the vortices generated are shown in Figure 7.2 and Figure 7.3, and the third vortex generated has a diameter of 3.2 cm with a vorticity of 20.9 s^{-1} clockwise.

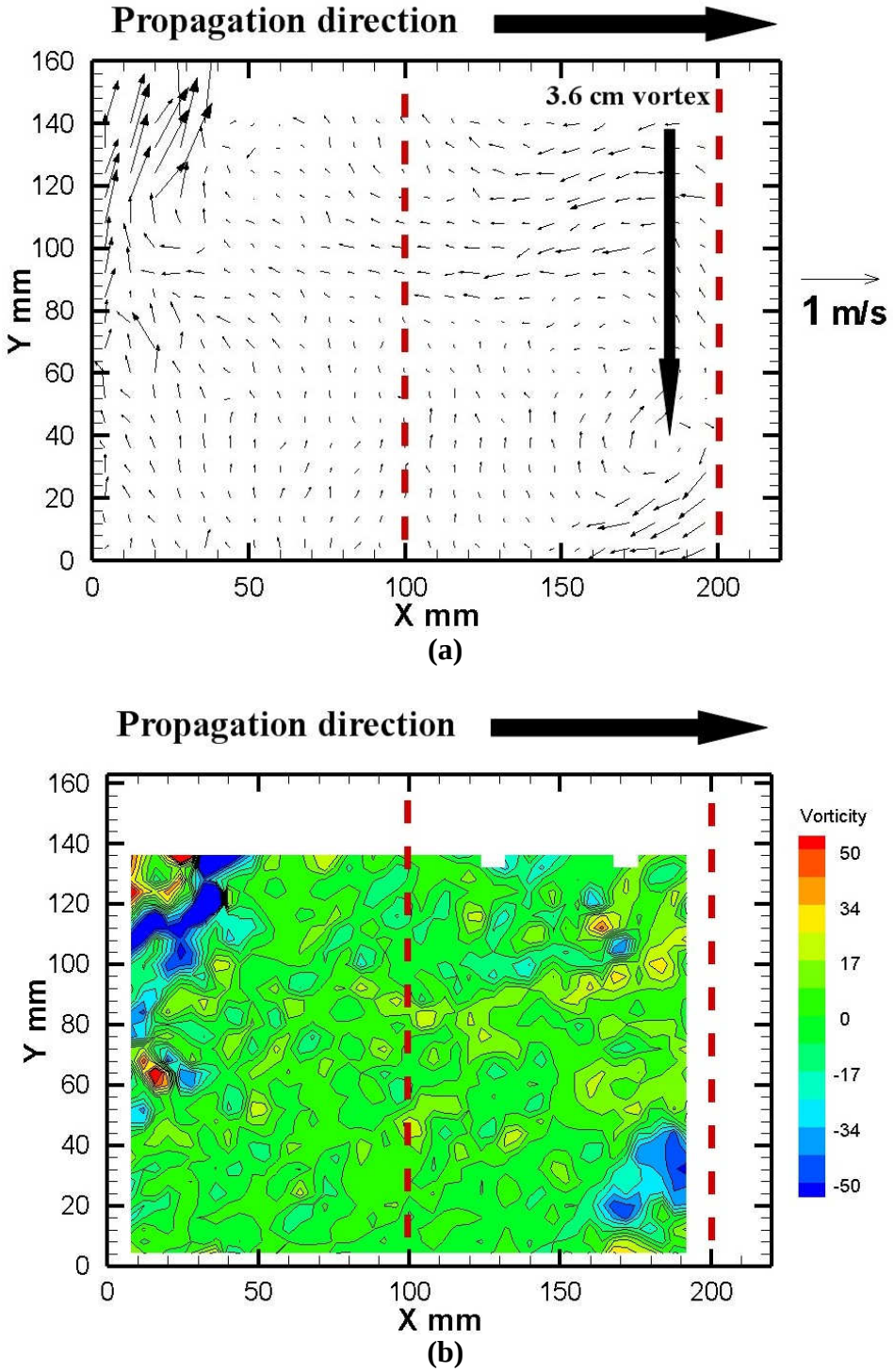


Figure 7.2: (a) Velocity vector plot at t = 0.7 s showing the formation of a 3.6 cm diameter vortex within the open area of a 10 cm CSD and a 0.0 m/s wind condition; (b) corresponding vorticity contour plot used to calculate vorticity of 14.9 s^{-1} clockwise; experiment 90; Note: time shown here is time during PIV capturing not time during the actual experiment.

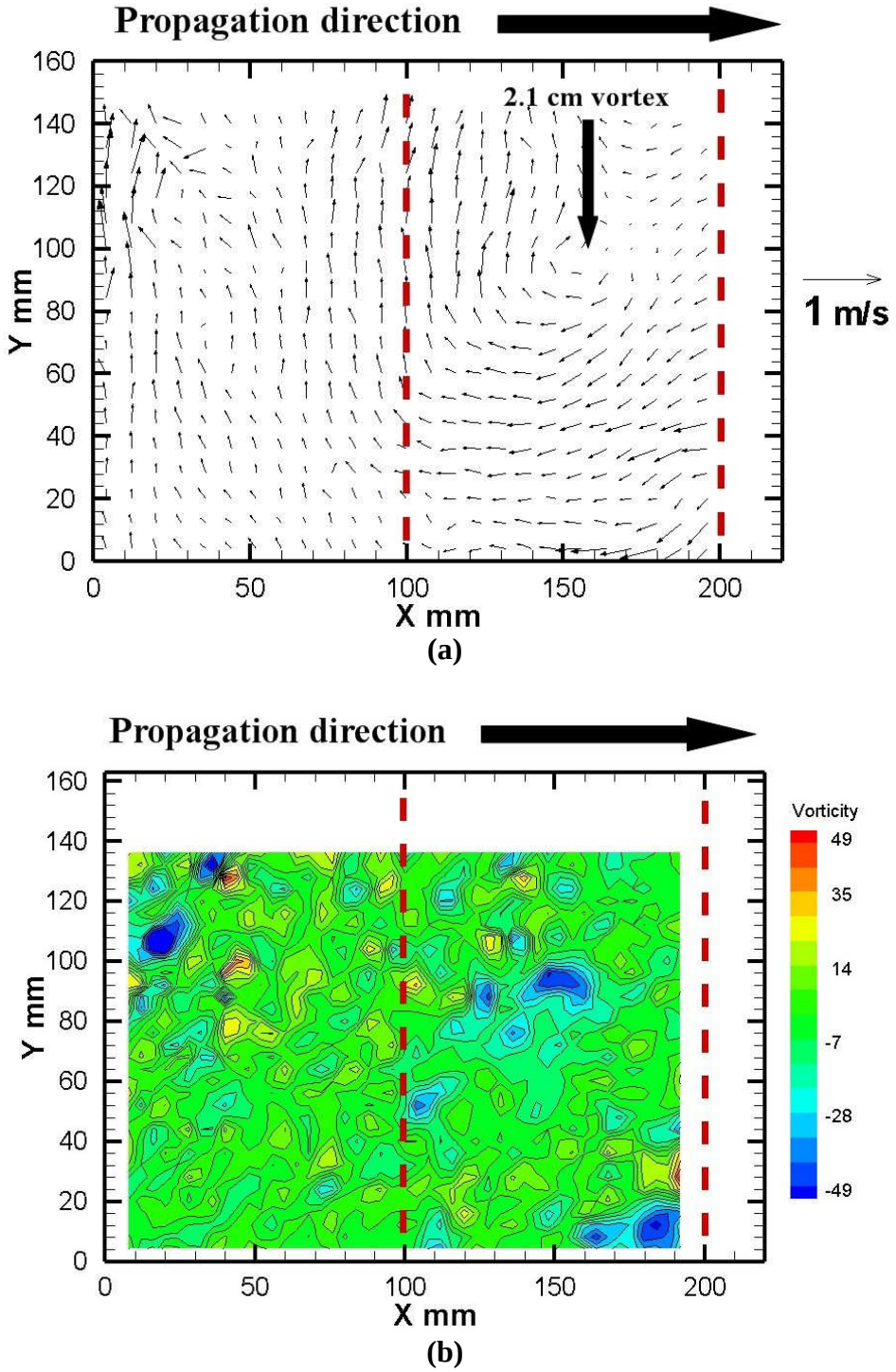


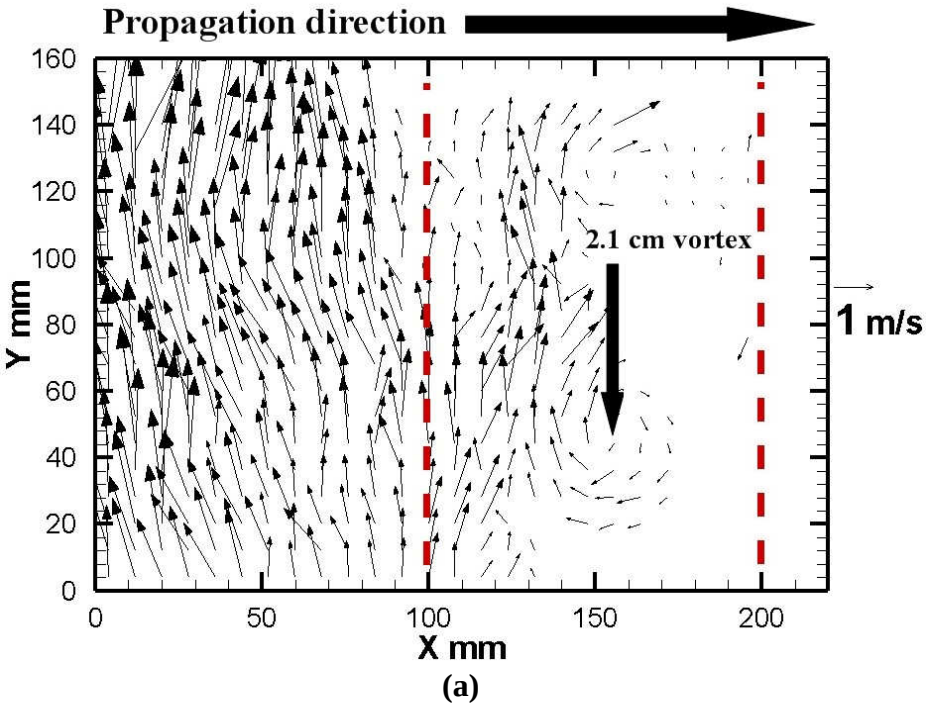
Figure 7.3: (a) Velocity vector plot at t = 3.1 s showing the formation of a 2.1 cm diameter vortex within the open area of a 10 cm CSD and a 0.0 m/s wind condition; (b) corresponding vorticity contour plot used to calculate vorticity of 19.8 s^{-1} clockwise; experiment 90; Note: time shown here is time during PIV capturing not time during the actual experiment.

Only one vortex is observed to occur as the fire front propagated along the 20 cm length of the ROI with an average vertical velocity $\overline{U}_y$ of 1.3 m/s. The shear created between the rising hot gaseous products of combustion and the entrained ambient air resulted in the formation of a 2.1 cm diameter vortex with a vorticity of 65 s^{-1} clockwise, Figure 7.4. The size of the vorticity relative to the size of the CSD indicates that the vortex does not assist in the preheating of the crown 2 fuel matrix.

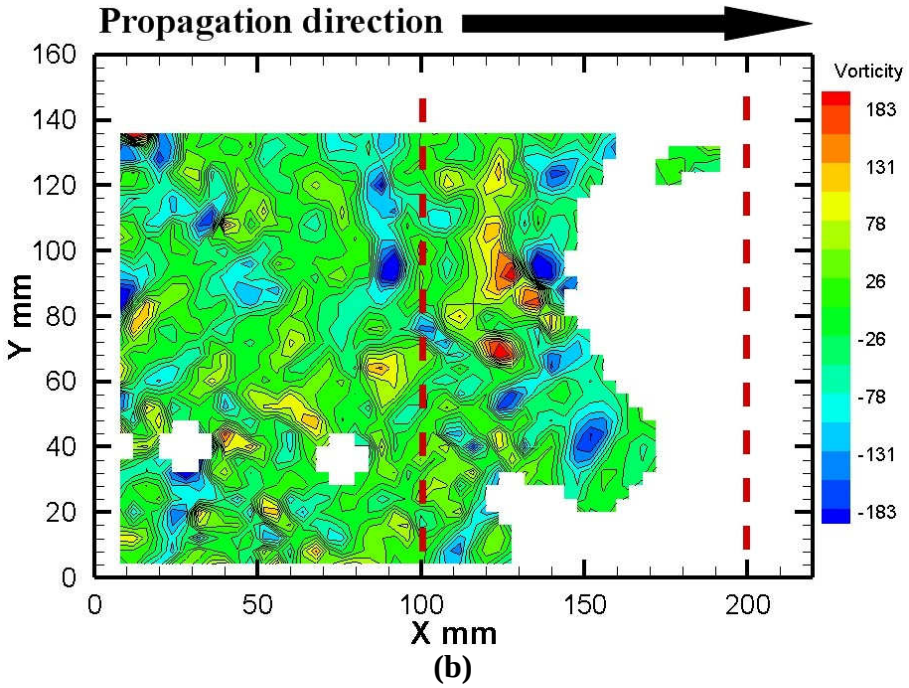
Crown Separation Distance of 10 cm with a 1.1 m/s Wind

The next analysis is performed at a 10 cm CSD with a 1.1 m/s wind condition. During the entrainment of ambient air to the fire column, $\overline{U}_{ent}$ is 0.3 m/s. As the fire front propagates along the ROI, $\overline{U}_y$ is 1.5 m/s. The shear created between the interaction of the rising hot gaseous products of combustion and the entrained air result in the formation of seven vortices in the four experiments that are conducted. These vortices range in diameter from 1.7 cm with a vorticity of 60.5 s^{-1}, Figure 7.5, to 2.5 cm with a vorticity of 46.1 s^{-1}. Vorticity magnitudes range from 34.3 s^{-1} with a diameter of 2.1 cm to 130.6 s^{-1} with a vortex diameter of 2.1 cm/s.

During entrainment of ambient air to the fire column three vortices are observed. The diameter of these vortices is 1.7 cm, 1.7 cm and 2.5 cm with vorticity of 60.5 s^{-1}, 95 s^{-1} and 46.1 s^{-1}, respectively. It is observed that four vortices are generated when the fire front is propagating along the ROI. The diameter of these vortices is 1.8 cm, 1.9 cm, 2.1 cm and 2.1 cm with vorticity of 88.7 s^{-1}, 76 s^{-1}, 34.3 s^{-1} (Figure 7.6) and 130.6 s^{-1}, respectively.



(a)



(b)

Figure 7.4: (a) Velocity vector plot at t = 10.8 s showing the formation of a 2.1 cm diameter vortex within the open area of a 10 cm CSD and a 0.0 m/s wind condition; (b) corresponding vorticity contour plot used to calculate vorticity of 65 s^{-1} clockwise; experiment 91; Note: time shown here is time during PIV capturing not time during the actual experiment.

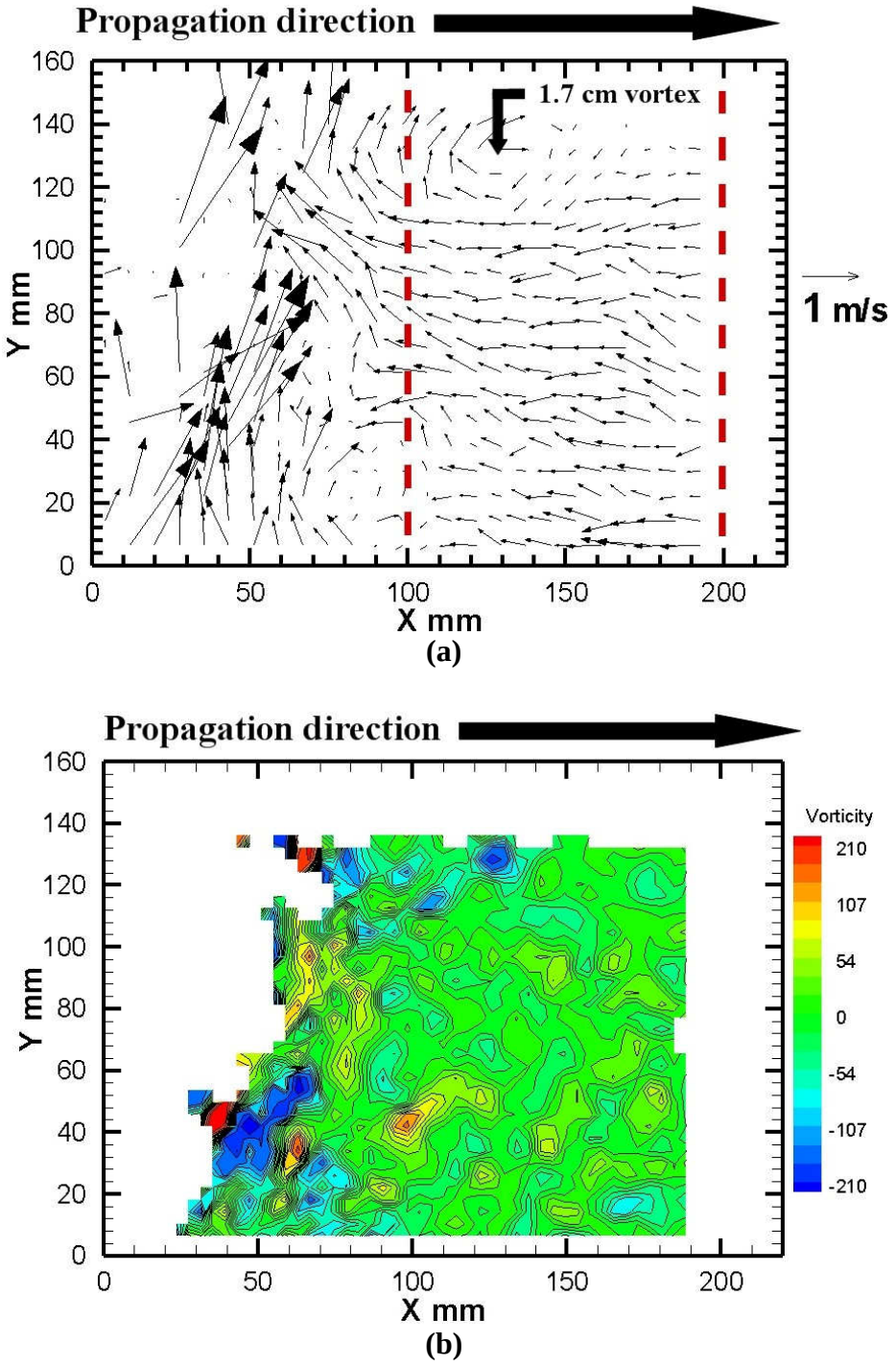


Figure 7.5: (a) Velocity vector plot at t = 3.9 s showing the formation of a 1.7 cm diameter vortex within the open area of a 10 cm CSD and a 1.1 m/s wind condition; (b) corresponding vorticity contour plot used to calculate vorticity of 60.5 s^{-1} clockwise; experiment 57; Note: time shown here is time during PIV capturing not time during the actual experiment.

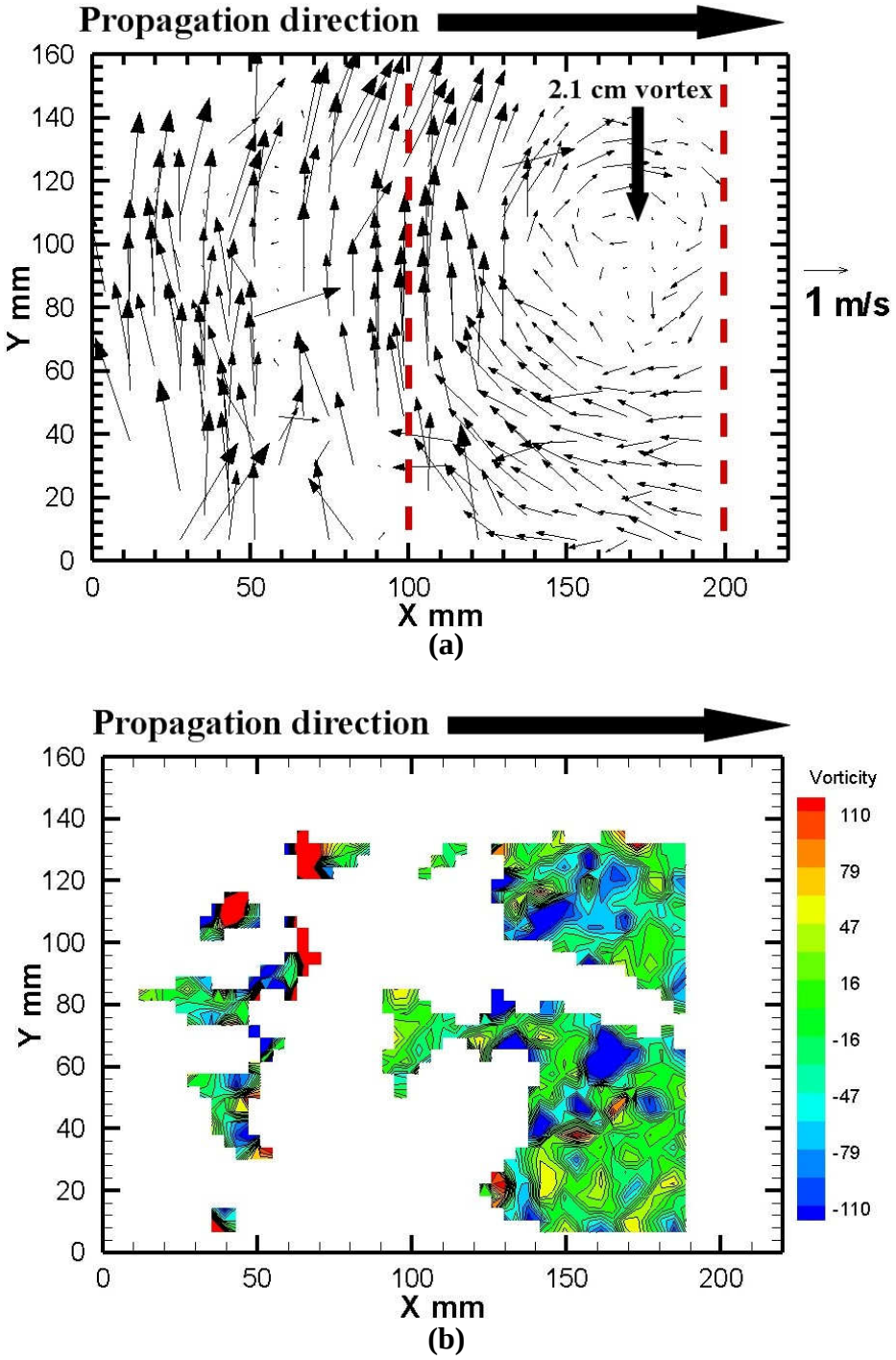
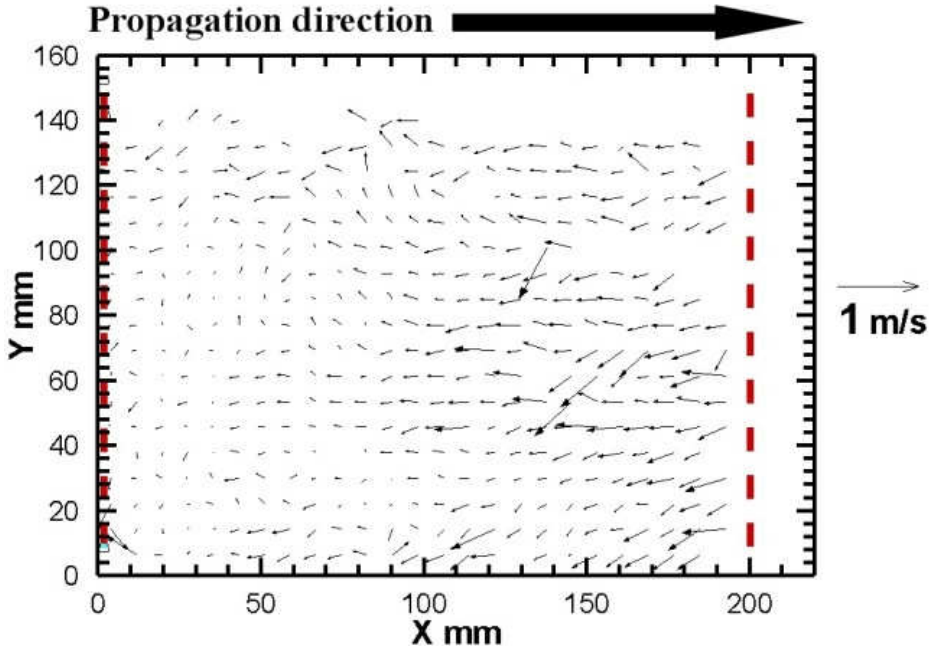


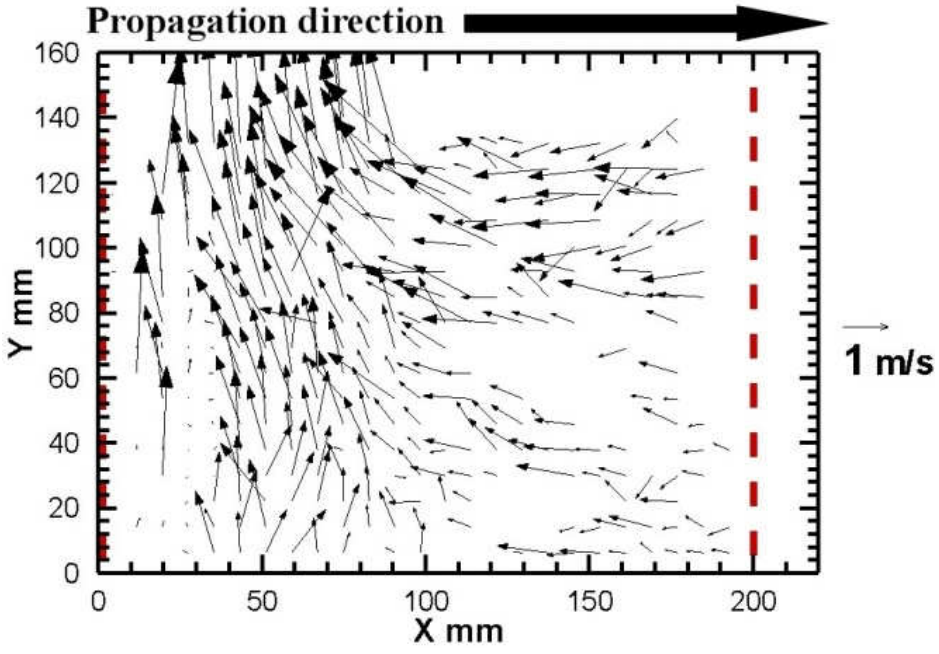
Figure 7.6: (a) Velocity vector plot at t = 12.3 s showing the formation of a 2.1 cm diameter vortex within the open area of a 10 cm CSD and a 1.1 m/s wind condition; (b) corresponding vorticity contour plot used to calculate vorticity of 34.3. s^{-1} clockwise; experiment 57; Note: time shown here is time during PIV capturing not time during the actual experiment.

Crown Separation Distance of 20 cm with a 1.1 m/s Wind

The next analysis is performed by maintaining the wind speed constant at 1.1 m/s and changing the CSD to 20 cm. A total of four experiments are performed. Since the seeding of the flow field and capturing of the necessary images is non-trivial, only two of the experiments have sufficient seed particles to satisfactorily perform an analysis of the flow field. The fire front propagates from left to right. As the fire front approaches the upstream boundary of the ROI, Figure 7.7a, ambient air is entrained into the fire column at an average entrainment horizontal velocity $\overline{U}_{ent}$ of 0.3 m/s. When the fire front enters and propagates along the ROI towards crown 2, Figure 7.7b, the measured mean vertical velocity $\overline{U}_{y}$ of the hot gaseous products of combustion is 1.3 m/s. Analysis of the two experiments performed at a CSD of 20 cm with a 1.1 m/s wind condition yielded no formation of vortices unlike the case of a CSD of 10 cm under the same wind conditions.



(a)



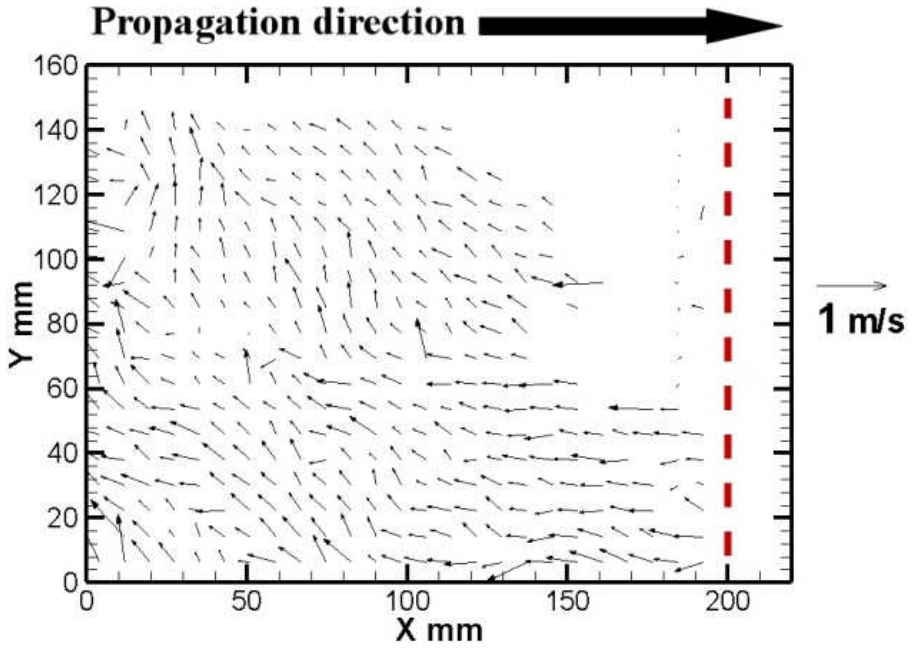
(b)

Figure 7.7: Velocity vector field plots of: (a) ambient air entrainment as the fire front approaches the ROI from the left at t = 0.2 s for experiment 50 (b) fire front propagating along the ROI at t = 4.9 s for experiment 53; Note: times shown here are times during PIV capturing not times during the actual experiment.

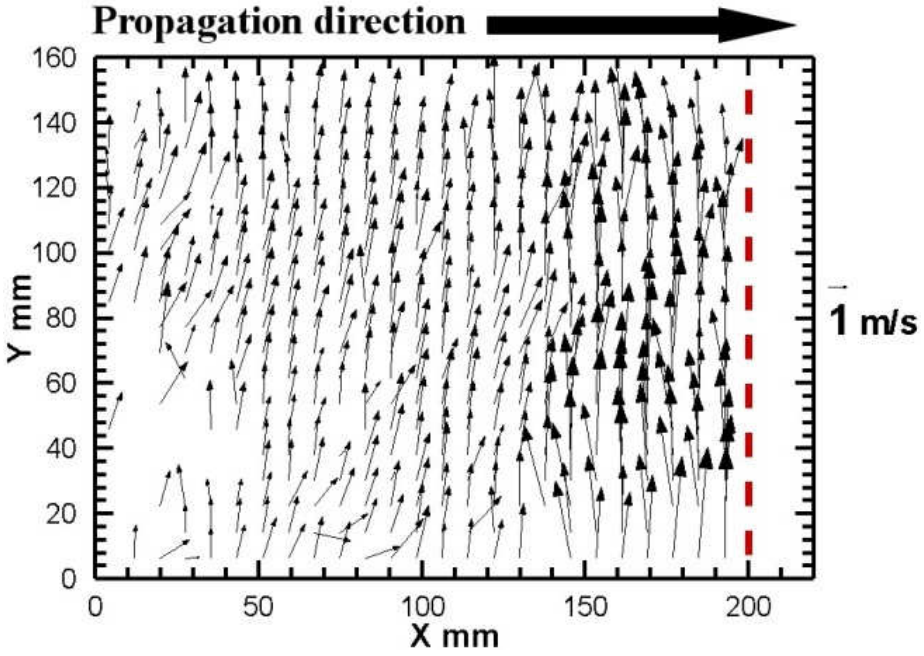
Crown Separation Distance of 30 cm with a 1.1 m/s Wind

At total of four experiments were performed at a CSD of 30 cm with a 1.1 m/s wind condition. Ambient air is entrained into the approaching fire column at an average entrainment velocity $\overline{U}_{ent}$ of 0.4 m/s as the fire front approaches the upstream boundary of the ROI, Figure 7.8a. The measured mean vertical velocity $\overline{U}_{y}$ of the hot gaseous products of combustion is 2.1 m/s as the fire front progress along the ROI, Figure 7.8b. Analysis of the experiments performed for the 30 CSD case and 1.1 m/s wind condition does not show the formation of any vortices as was observed at a 20 cm CSD at the same wind condition.

The overall average of $\overline{U}_{ent}$ and $\overline{U}_{y}$ between all the experiments performed at a wind condition of 1.1 m/s is greater than the overall average of $\overline{U}_{ent}$ and $\overline{U}_{y}$ at a wind condition of 0.0 m/s by a factor of 1.2 and 1.3, respectively. Vortices were observed to only occur at a CSD of 10 cm, similarly to the 0.0 m/s wind condition investigation.



(a)



(b)

Figure 7.8: Velocity vector field plots of: (a) ambient air entrainment as the fire front approaches the ROI from the left at t = 4.7 s for experiment 38 (b) fire front propagating along the ROI at t = 15.3 s for experiment 39; Note: times shown here are times during PIV capturing not times during the actual experiment.

Crown Separation Distance of 10 cm with a 1.9 m/s Wind

The wind speed is increased to 1.9 m/s and the three CSD configurations are investigated starting with a CSD of 10 cm. Four experiments are performed and only vertical velocity data is attained at this CSD configuration. Analysis of the PIV data shows that the average vertical velocity $\overline{U}_y$ as the fire front progresses along the ROI, Figure 7.9, between the four experiments performed is 2.2 m/s with the formation of a single vortex. Figure 7.10 contains the velocity vector plot and vorticity contour plot at time of 1.1 s. Analysis of the PIV data shows the formation of a vortex with a 1.5 cm diameter and a vorticity of 238.1 s^{-1} clockwise. The vortex is a result of the shear experienced at the interface between the fast rising hot gaseous products of combustion and the slow entrained ambient air. The size and location of the vortex suggests that it does not assist in the preheating of crown 2 fuel elements.

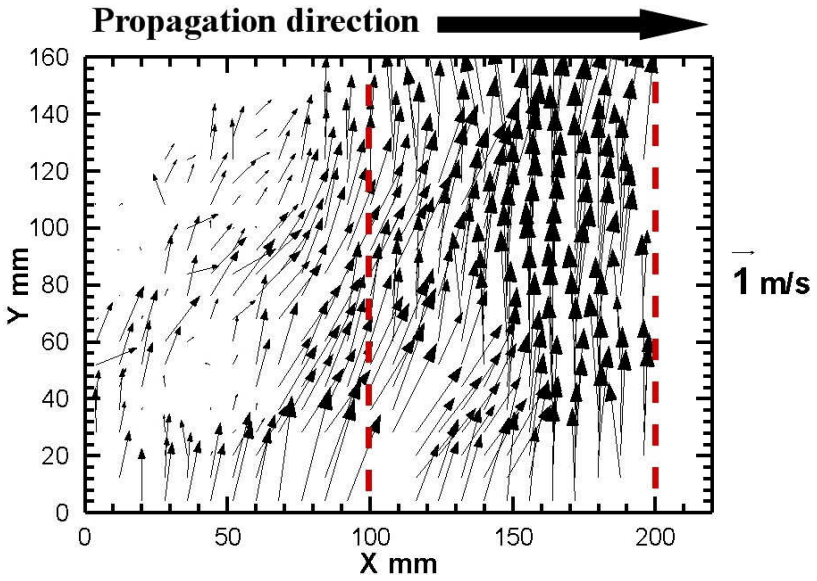


Figure 7.9: Velocity vector plot at t = 1.61 s as the fire front propagates along the ROI for a 10 cm CSD configuration with a 1.9 m/s wind condition.

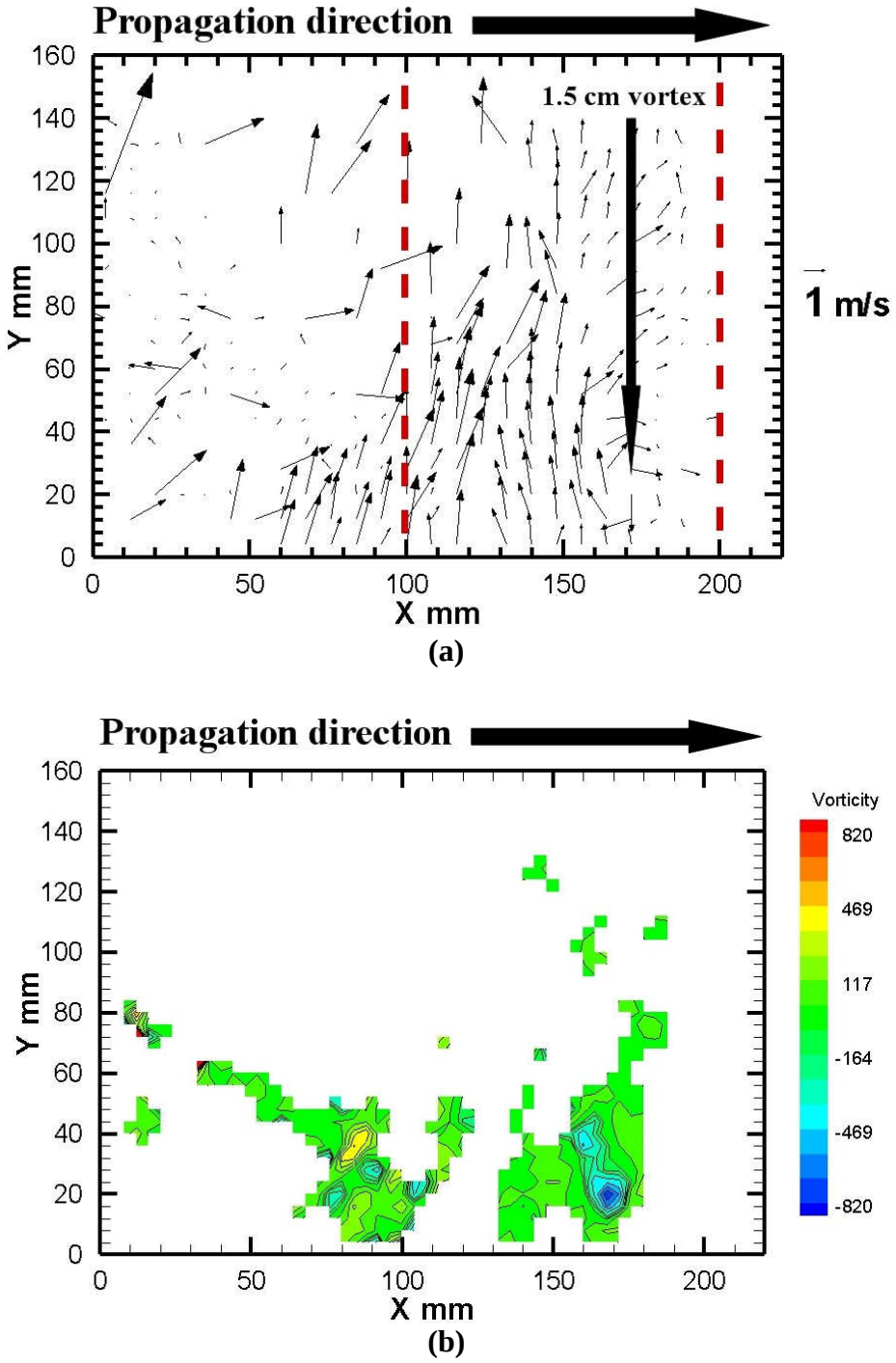
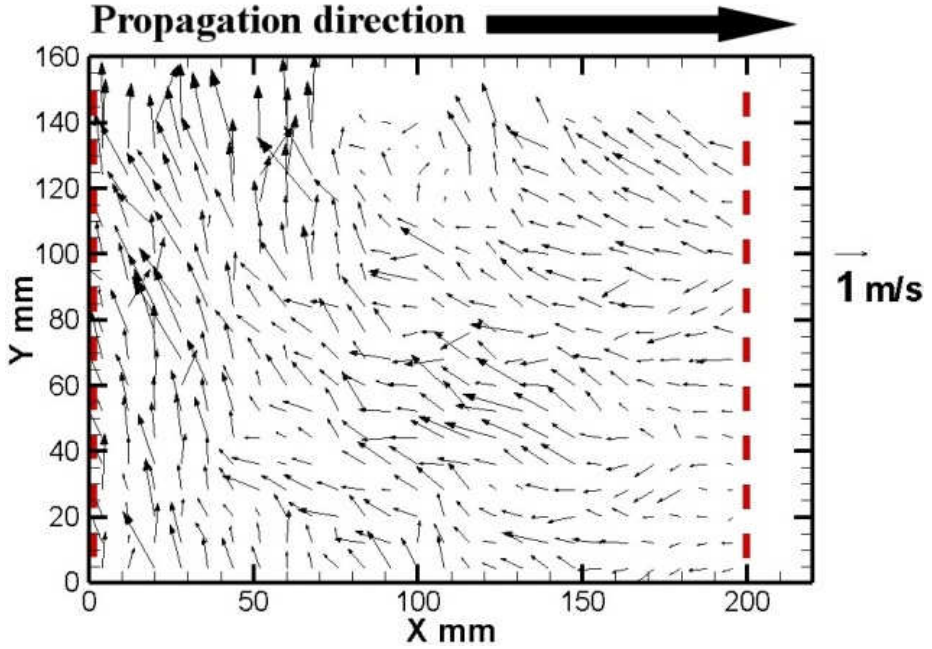


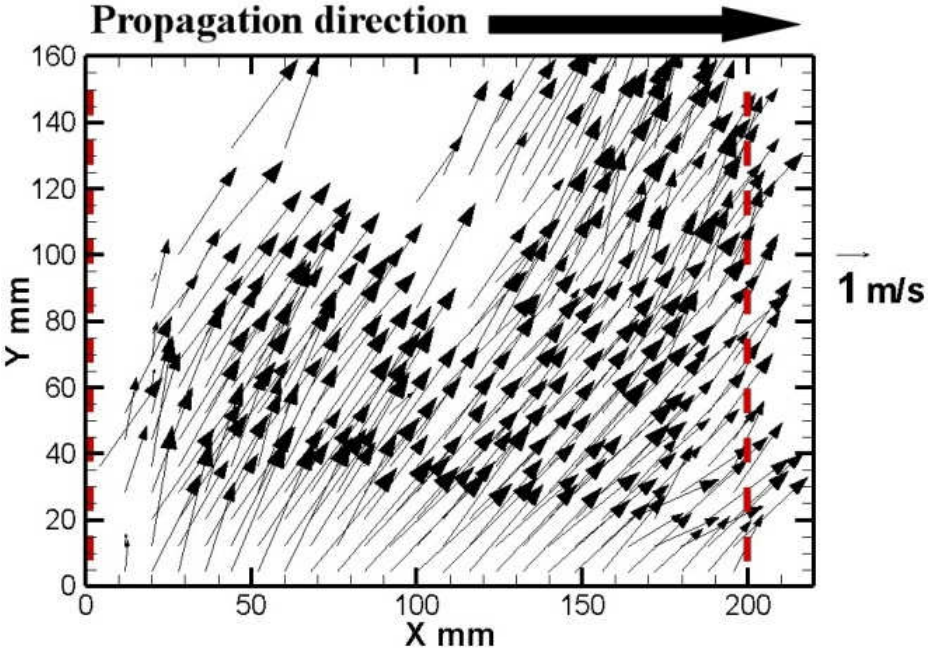
Figure 7.10: (a) Velocity vector plot at t = 1.1 s showing the formation of a 1.5 cm diameter vortex within the open area of a 10 cm CSD and a 1.9 m/s wind condition; (b) corresponding vorticity contour plot used to calculate vorticity of 238.1 s^{-1} clockwise; experiment 88; Note: time shown here is time during PIV capturing not time during the actual experiment.

Crown Separation Distance of 20 cm with a 1.9 m/s Wind

The next analysis is performed by increasing the CSD to 20 cm and maintaining wind speed constant at 1.9 m/s. Similarly to the same CSD at a wind condition of 1.1 m/s, analysis of the PIV data showed no formation of vortices as the fire front approaches the upstream boundary of the ROI or as the fire front propagates along the ROI. Average $\overline{U}_{ent}$ of ambient air is measured to be 0.5 m/s with a maximum value of 1.1 m/s as the fire front approached the upstream boundary of the ROI, Figure 7.11a. The average $\overline{U}_y$ of the hot gaseous products of combustion is measured at 1.9 m/s with a maximum of 5.0 m/s as the fire front progresses through the ROI, Figure 7.11b. Analysis show that at the time Figure 7.11b was captured, the average flame tilt angle from the vertical was approximately 18 degrees.



(a)

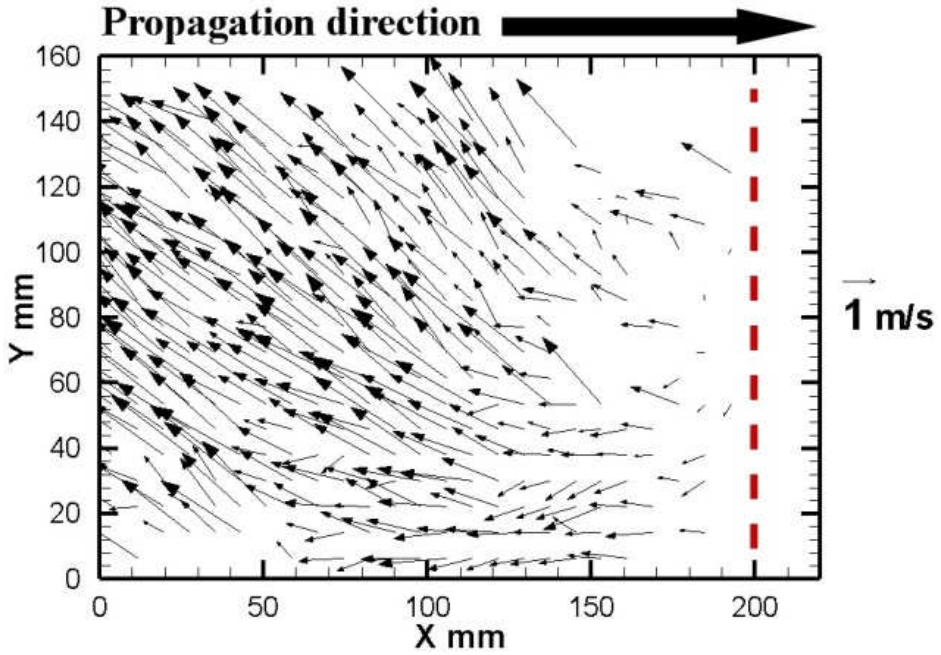


(b)

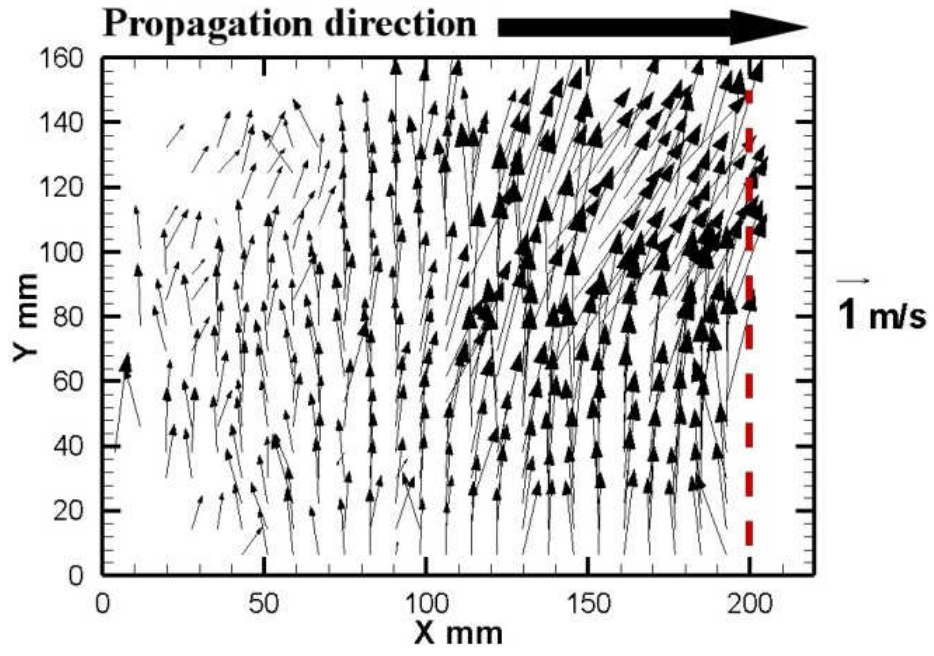
Figure 7.11: Velocity vector field plots of: (a) ambient air entrainment as the fire front approaches the ROI from the left at t = 4.0 s for experiment 85 (b) fire front propagating along the ROI at t = 7.0 s for experiment 85; Note: times shown here are times during PIV capturing not times during the actual experiment.

Crown Separation Distance of 30 cm with a 1.9 m/s Wind

The final PIV analysis is performed at a 30 cm CSD with a 1.9 m/s wind speed. Average $\overline{U}_{ent}$ as the fire front advances towards the upstream side of the ROI is measured to be 0.6 m/s with a maximum of 2.0 m/s, Figure 7.12a. Average $\overline{U}_{y}$ is measured at 2.0 m/s with a maximum velocity of approximately 5.0 m/s as the fire front propagates along the ROI, Figure 7.12b. Analysis of the three experiment performed does not show the formation of any vortices as the fire front advances towards the upstream side of the ROI or as the fire front progresses along the ROI.



(a)



(b)

Figure 7.12: Velocity vector field plots of: (a) ambient air entrainment as the fire front approaches the ROI from the left at t = 2.4 s for experiment 46 (b) fire front propagating along the ROI at t = 1.07 s for experiment 46; Note: times shown here are times during PIV capturing not times during the actual experiment.

Discussion

A total of 21 PIV experiment were performed with the objective to investigate if the flow speed of the hot gaseous products of combustion is affected by the separation distance between adjacent crown fuel matrices and to study any fluid dynamic structures that may arise due to the separation distance between crown fuel matrices. Through analysis it is shown that the formation of vortices between crown fuel matrices only occurs at the lower CSD of 10 cm and not at CSD's of 20 cm and 30 cm. Further, it is suggested that due to their sizes and locations, the resulting vortices do not contribute to the preheating of the unburned crown 2 fuel elements. Comparison of the average $\overline{U}_{ent}$ between all the experiment performed for the three CSD configurations at a given wind condition show that at a wind condition of 1.9 m/s the average $\overline{U}_{ent}$ is greater than at a wind condition of 1.1 m/s and 0.0 m/s by a factor of 1.9 and 2.2, respectively. Performing the same analysis for the average vertical velocity $\overline{U}_y$, shows that the average vertical velocity at a wind condition of 1.9 m/s is greater than at a wind condition of 1.1 m/s and 0.0 m/s by a factor of 1.3 and 1.6, respectively. A similar analysis is conducted for the vorticity values at a 10 cm CSD for the three wind conditions investigated. It is shown that vorticity is greater during a wind condition of 1.9 m/s than at 1.1 m/s and 0.0 m/s by a factor of 3.1 and 7.9 respectively. This hierarchy is expected because at a high wind condition of 1.9 m/s the flame tilt angle is the greatest which results in an increased combustion rate, thus a more intense fire. The more intense fire entrains ambient air at a greater rate resulting in larger horizontal velocities than at lower wind conditions.

8 Results – Large Eddy Simulation

A Large Eddy Simulation (LES) model, described in chapter 2 and chapter 4, is used to study the fluid dynamic environment between two adjacent crown fuels and to investigate the overall fire behavior as a fire front propagates along a surface fuel. Three different crown fuel configurations are studied at two distinct wind conditions. The separation distance between crown fuels is varied while maintaining wind speed constant. Crown separation distances (CSD) studied are 10 cm, 20 cm and 30 cm at a wind condition of 0.0 m/s and 0.8 m/s. The objective of this study is to determine the affect of CSD on the 1) surface fire rate of spread, 2) flow of the hot gaseous products of combustion between adjacent crown fuel matrices.

8.1 Surface Fire Front Rate of Spread

All Crown Fuel Configurations at a 0.0 m/s Wind Condition

Initial baseline cases for the three CSD's are studied at a wind condition of 0.0 m/s. The flame depth, flame tilt and rate of spread *R* are determined from the resulting plots. Radiation energy transfer rate per unit volume (q'''_{rad}) is calculated between 1.7 m and 1.8 m as shown in all the figures. At a CSD of 10 cm average *R* is 1.24 cm/s in the region before the fire front arrives at the leading edge of crown 1. Average *R* increases to 1.43 cm/s after crown 1 ignition, Figure 8.1a, and the fire front continues to propagate along the fuel bed. The increase in average *R* is due to the increased amount of q'''_{rad} that impinges onto the unburned surface fuel ahead of the fire front. Radiation impingement increases from 23.1 kW/m^3 to 287.3 kW/m3 over a period of 12.5.

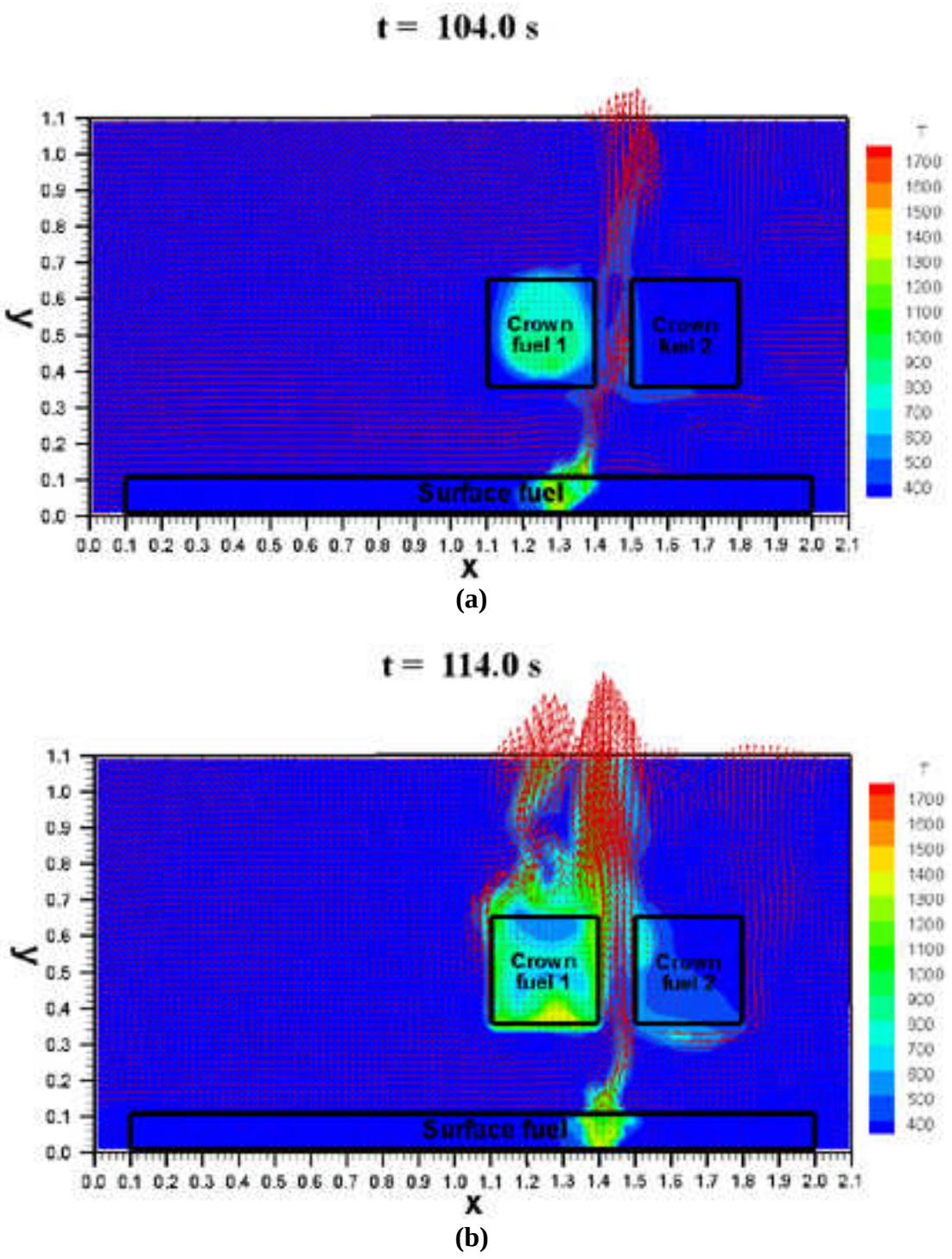


Figure 8.1: LES results at a midplane of air temperature and velocity field for a CSD of 10 cm at: (a) C1 ignition; t = 104.0 s. Instantaneous *R* is 1.8 cm/s and radiation energy transfer rate per unit volume between 1.7 m and 1.8 m is 4.18 kW/m^3; (b) C2 ignition; t = 114.0 s. Instantaneous *R* is 1.4 cm/s and radiation energy transfer rate per unit volume between 1.7 m and 1.8 m is 73.6 kW/m^3.

Before crown 2 ignites the maximum q'''_{rad} calculated is 73.63 kW/m^3. After crown 2 ignites, Figure 8.1b, and before the fire front reaches the radiation energy measurement region, the maximum q'''_{rad} is 287.3 kW/m^3. The combined radiation energy from the two burning crown fuels assists in the desiccation process of the unburned surface fuels that ultimately leads to an increase in *R*. The next baseline case is performed at a CSD of 20 cm.

In the initial portion of the fuel bed before crown 1, average *R* is 1.16 cm/s. Average *R* then increases to 1.24 cm/s after crown 1 ignites and as the fire front continues to propagate beneath the crown fuels, Figure 8.2a. After crown 1 begins vigorous combustion, q'''_{rad} increases from 4.2 kW/m^3 to 213.0 kW/m^3 over a period of 8.8 s. The result is a 7% *R* increase to 1.24 cm/s. Crown 2 ignites as the fire front enters the radiation energy measurement region, Figure 8.2b, thus q'''_{rad} measurements from the burning crown fuels is not possible or would not be representative of actual radiation energy impinging onto the unburned surface fuel.

The final baseline case investigated is at a CSD of 30 cm. Similar to a CSD of 20 cm, average *R* is 1.16 cm/s in the portion of the fuel bed before the fire front reaches the leading edge of crown 1. Within this region the calculated maximum q'''_{rad} is 0.23 kW/m^3. As the fire front continues to propagate along the fuel bed beneath crown 1, average *R* increases slightly to 1.20 cm/s during the time before crown 1 ignition, Figure 8.3a. In the region beneath crown 1 before crown 1 ignites, the calculated maximum q'''_{rad} increases to 0.4 kW/m^3.

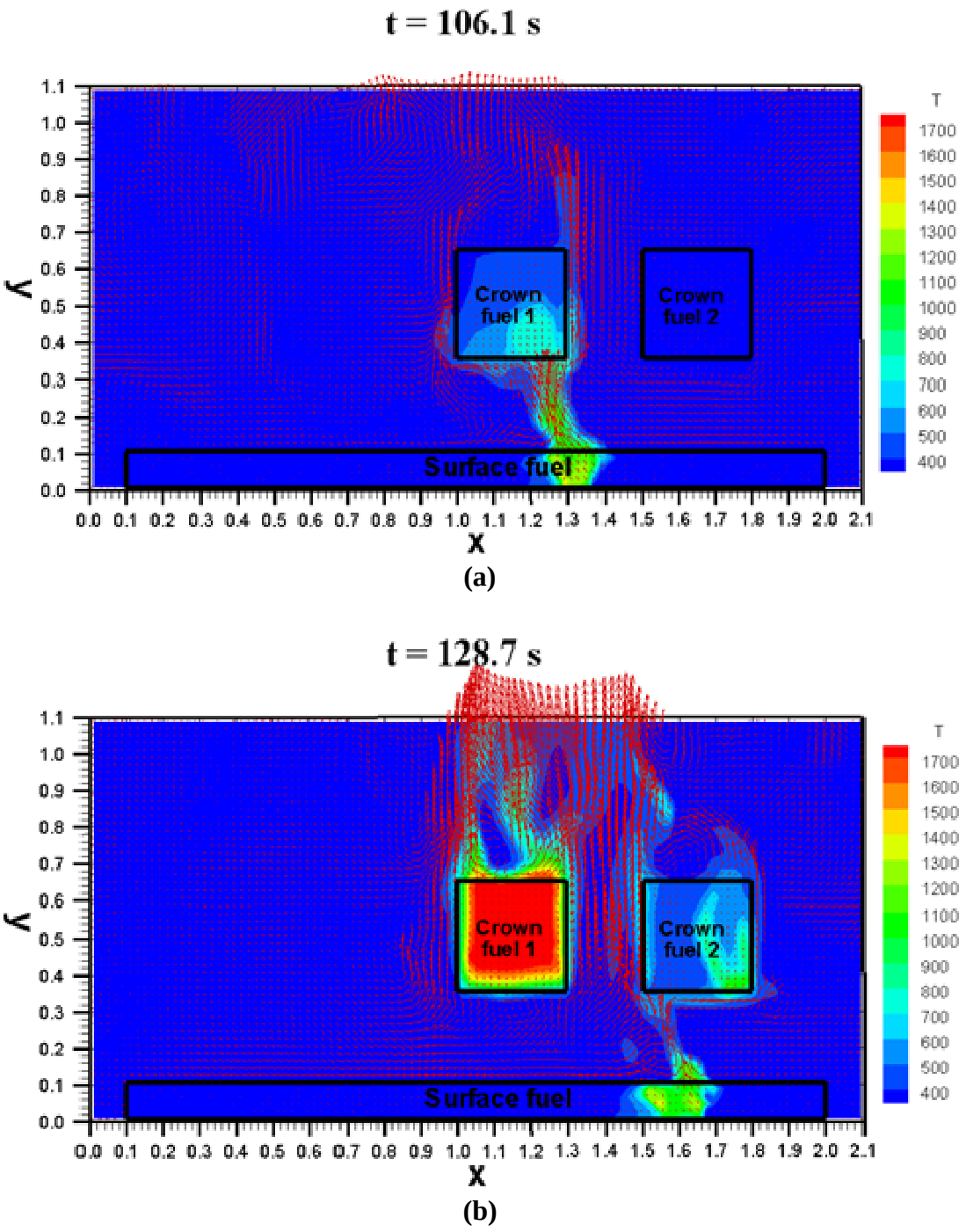


Figure 8.2: LES results at a midplane of air temperature and velocity field for a CSD of 20 cm at: (a) C1 ignition; t = 106.1 s. Instantaneous *R* is 1.4 cm/s and radiation energy transfer rate per unit volume between 1.7 m and 1.8 m is 0.43 kW/m^3; (b) C2 ignition; t = 128.7 s. Instantaneous *R* is 1.4 cm/s and radiation energy transfer rate per unit volume between 1.7 m and 1.8 m is 510.5 kW/m^3.

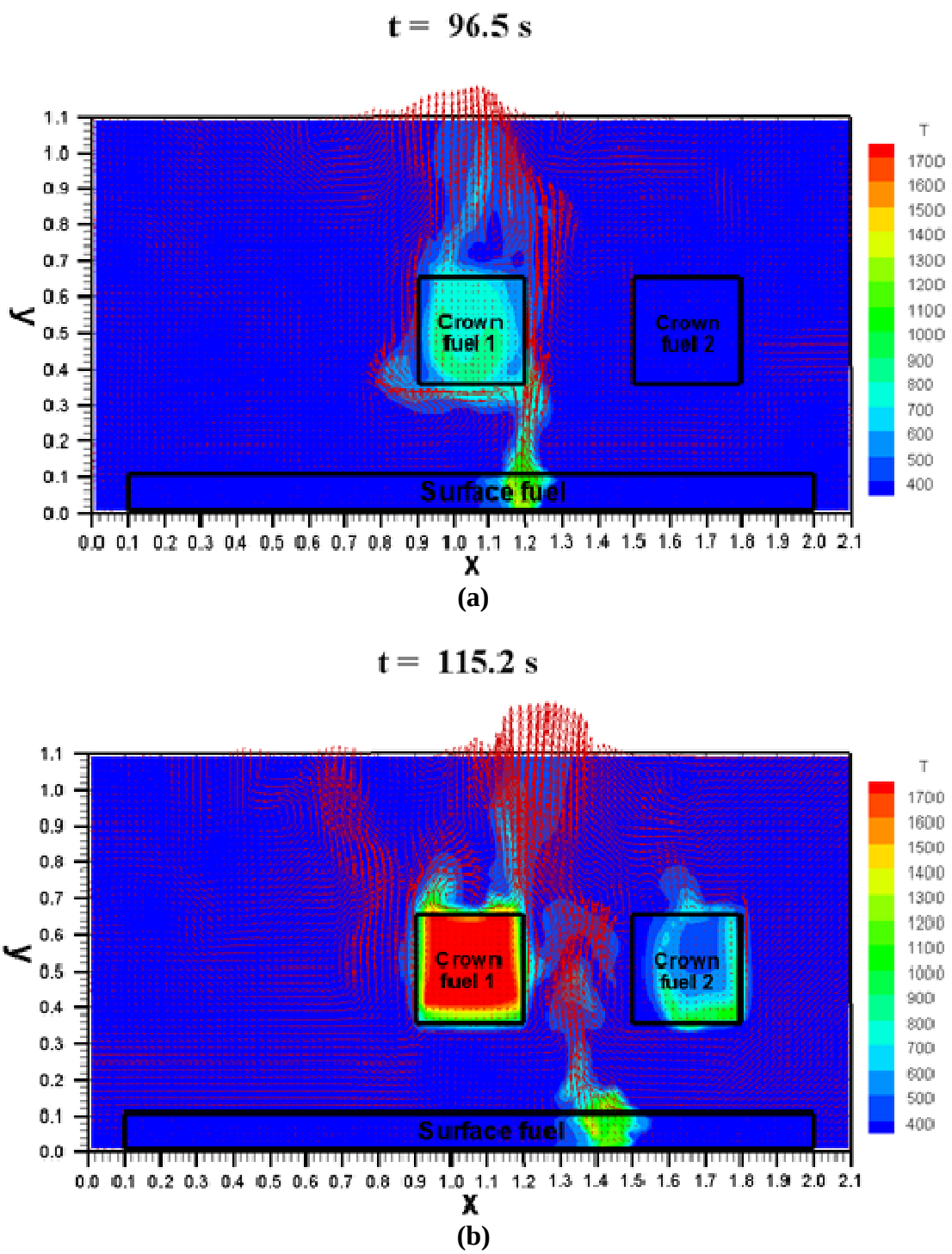


Figure 8.3: LES results at a midplane of air temperature and velocity field for a CSD of 30 cm at: (a) C1 ignition; t = 96.5 s. Instantaneous *R* is 1.2 cm/s and radiation energy transfer rate per unit volume between 1.7 m and 1.8 m is 0.76 kW/m^3; (b) C2 ignition; t = 115.2 s. Instantaneous *R* is 1.2 cm/s and radiation energy transfer rate per unit volume between 1.7 m and 1.8 m is 34.18 kW/m^3.

In this case the increase in radiation energy is due to the decreasing distance between the fire front and the radiation energy measurement region resulting in an increase in view factor. From the instant crown 1 ignites to when crown 2 ignites, average *R* increases to 1.4 cm/s, Figure 8.3b. During this time q'''_{rad} increases to a maximum of 34.18 kW/m^3. During vigorous crown 1 combustion, q'''_{rad} increases from 2.25 kW/m^3 to 34.18 kW/m^3 during a period of 6.2 s. From the time crown 2 ignites to when the fire front arrives at the q'''_{rad} measurement region, average *R* increases to 1.7 cm/s reaching a maximum q'''_{rad} of 353.9 kW/m^3.

All Crown Fuel Configurations at a 0.8 m/s Wind Condition

The next analysis is performed at a wind condition of 0.8 m/s for the three CSD's of 10 cm, 20 cm and 30 cm. The first study is at a CSD of 10cm. Average *R* is 1.37 cm/s in the region before crown 1. During this time the calculated maximum q'''_{rad} is 0.94 kW/m^3. Average *R* increases to 1.46 cm/s during the period when the fire front propagates beneath crown 1 to the instant crown 1 ignites, Figure 8.4a. In this period, the maximum q'''_{rad} is calculated to be 1.88 kW/m^3. After crown 1 ignites the fire front continues to propagate along the surface fuel eventually igniting crown 2, Figure 8.4b. During this period the average *R* decreases to 0.73 cm/s and q'''_{rad} is calculated to be a maximum of 31.98 kW/m^3. The decrease in *R* is due to the reallocation of heat to preheat the unburned crown 2 fuel and the decrease in flame tilt angle (from the vertical). In the region before crown 1, the average flame tilt angle is 49°, and after crown 1 the average flame tilt angle is 47°. The reduction in flame tilt angle results in a decreased view factor between the fire front and the unburned surface fuel.

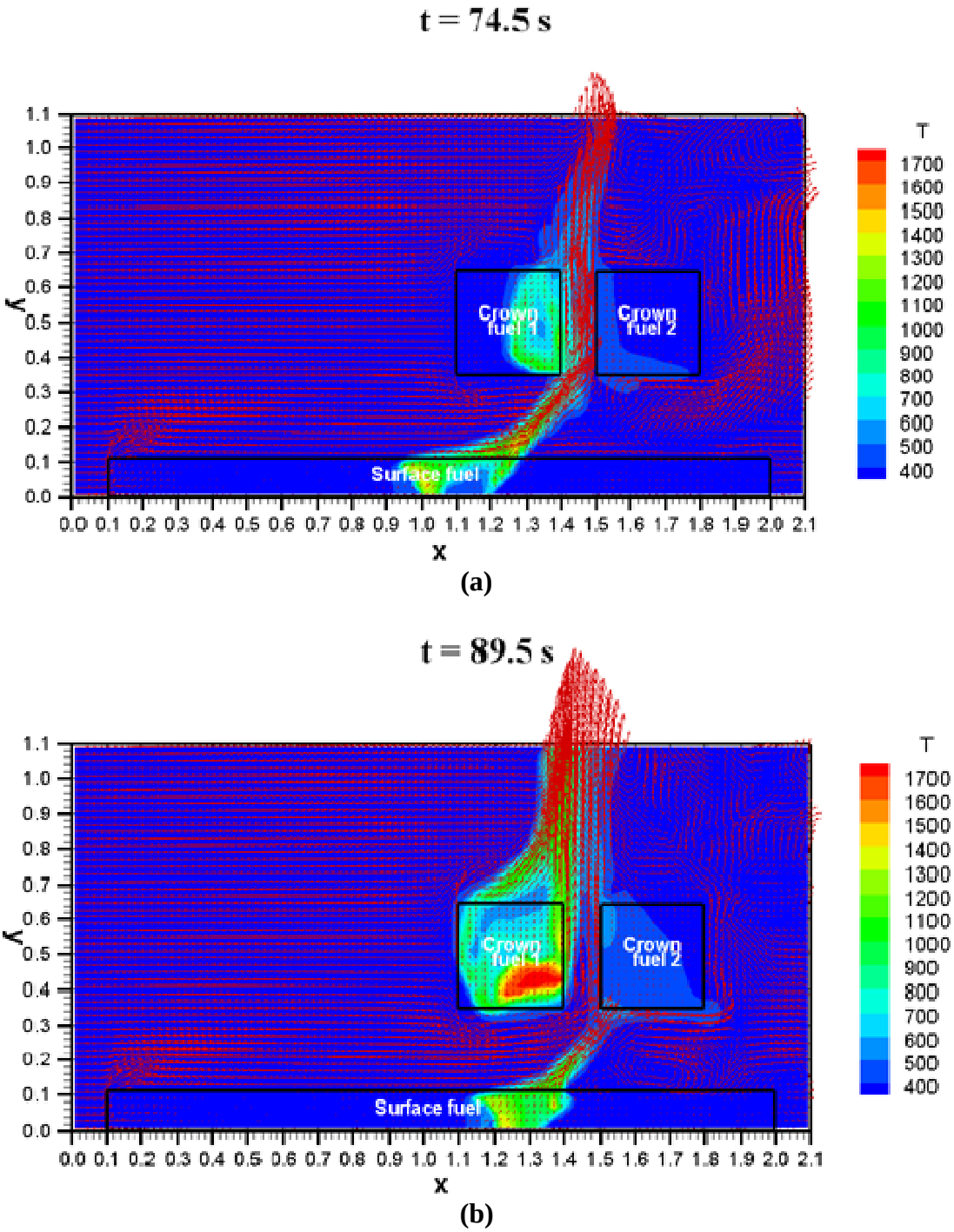
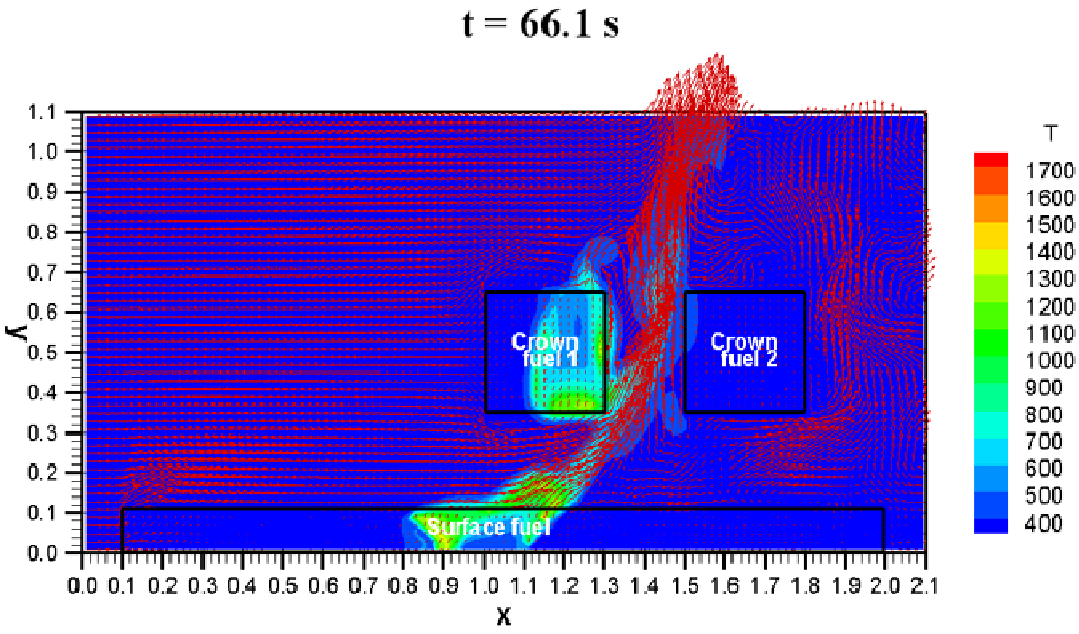


Figure 8.4: LES results at a midplane of air temperature and velocity field for a CSD of 10 cm at: (a) C1 ignition; t = 74.5 s. Instantaneous *R* is 1.0 cm/s and radiation energy transfer rate per unit volume between 1.7 m and 1.8 m is 1.05 kW/m^3; (b) C2 ignition; t = 89.5 s. Instantaneous *R* is 0.6 cm/s and radiation energy transfer rate per unit volume between 1.7 m and 1.8 m is 20.74 kW/m^3.

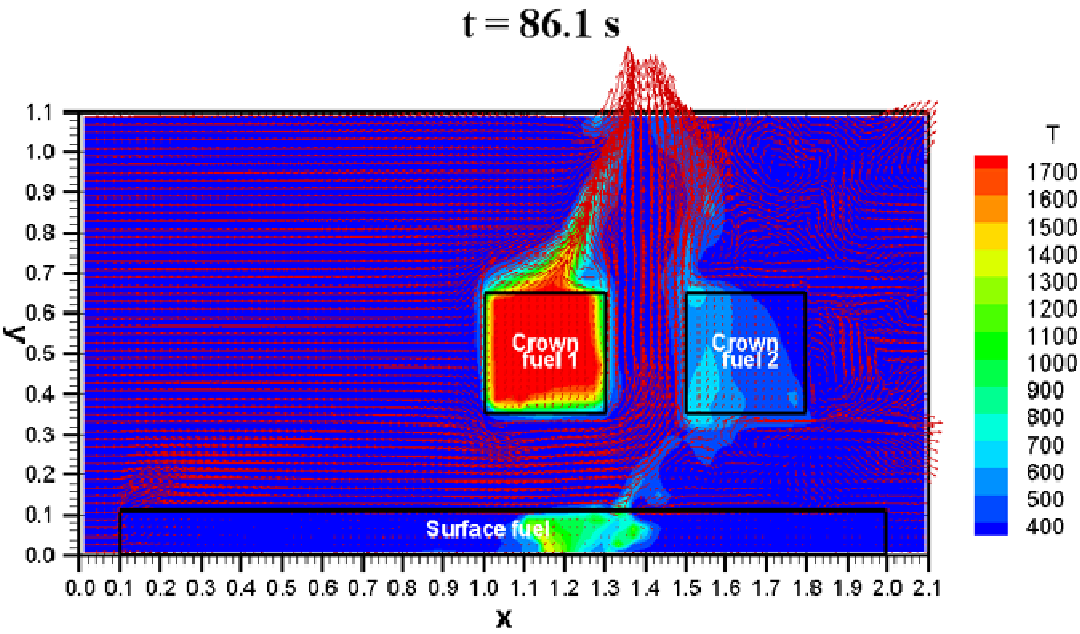
As the fire front continues to propagate along the surface fuel after crown 2 ignition, q'''_{rad} is calculated to increase from 20.74 kW/m^3 to 373.40 kW/m^3 in a period of 8.8 s, resulting in an average *R* increase to 3.46 cm/s.

The CSD is changed to 20 cm while maintaining the wind condition at 0.8 m/s and the same analysis is performed. From t = 0 to t = 45.2 s (time before the fire front arrives at crown 1) average *R* is 1.36 cm/s and the calculated maximum q'''_{rad} is 0.96 kW/m^3. During the period when the fire front propagates beneath crown 1 to when crown 1 ignites, Figure 8.5a, average *R* increases slightly to 1.51 cm/s with a maximum calculated q'''_{rad} of 1.8 kW/m^3. In the period from when crown 1 ignites to when crown 2 ignites, Figure 8.5b, average *R* decrease to 1.05 cm/s with a maximum calculated q'''_{rad} of 104.8 kW/m^3. The decrease in average *R* is attributed to the reallocation of energy to preheat the unburned crown 2 fuel and the decrease in flame tilt angle from an average of 58° in the region before crown 1 to 34° in the region after crown 1. The decrease in flame tilt angle leads to a decreased view factor between the fire front and the unburned surface fuel. After crown 2 ignites and before the fire front reaches the q'''_{rad} measurement area, q'''_{rad} increases from 75.17 kW/m^3 to 393.7 kW/m^3 in a period of 7.5 s leading to an increase of average *R* to 3.2 cm/s.

The final analysis is performed at a CSD of 30 cm. This analysis yields different results from those attained at the previous CSD's of 10 cm and 20 cm. Crown 1 always ignites before crown 2 in all the CSD's at a wind condition of 0.0 m/s and at the CSD's of 10 cm and 20 cm at a wind condition of 0.8 m/s.



(a)



(b)

Figure 8.5: LES results at a midplane of air temperature and velocity field for a CSD of 20 cm at: (a) C1 ignition; t = 66.1 s. Instantaneous *R* is 0.4 cm/s and radiation energy transfer rate per unit volume between 1.7 m and 1.8 m is 0.38 kW/m^3; (b) C2 ignition; t = 86.1 s. Instantaneous *R* is 1.0 cm/s and radiation energy transfer rate per unit volume between 1.7 m and 1.8 m is 75.17 kW/m^3.

At a CSD of 30 cm at a wind condition of 0.8 m/s, Crown 2 ignites prior to crown 1, even though crown 2 is on the downstream side of crown 1. In the region before the fire front arrives at crown 1, average *R* is 0.98 cm/s and the calculated maximum q'''_{rad} is 1.09 kW/m3. The fire front then continues to propagate along the surface fuel bed transferring heat to crown 1 but not causing ignition. Fire front propagation progresses eventually igniting crown 2 at t = 96.4 s, Figure 8.6a. Between the time the fire front arrives at crown 1 and the time crown 2 ignites, average *R* and q'''_{rad} increases to 1.33 cm/s and 5.5 kW/m3, respectively. As the fire front advances, crown 1 ignites 5.4 s later, Figure 8.6b. Between the time of crown 2 combustion and crown 1 combustion, average R decreases to 1.21 cm/s and q'''_{rad} increases to 13.70 kW/m^3. In this case the increase of q'''_{rad} is attributed to the proximity of the fire front to the q'''_{rad} measurement area. In the CSD's of 10 cm and 20 cm at a wind condition of 0.8 m/s, q'''_{rad} increases by a minimum of 30.1 kW/m^3 between crown ignitions, but at a CSD of 30 cm q'''_{rad} increased by 8.2 kW/m^3. The combination of the lower amount of radiation energy impinging onto the unburned surface fuel and the decrease in average flame tilt angle in the region after crown 1, from 51° in the region before the fire front reaches crown 1 to 37° in the region after crown 1, results in the overall decrease of *R*. As crown 1 ignites, q'''_{rad} increases from 13.7 kW/m3 to 570.4 kW/m3 in a period of 7.5 s. Average *R* increase to 2.01 cm/s as a result of the increase in q'''_{rad}.

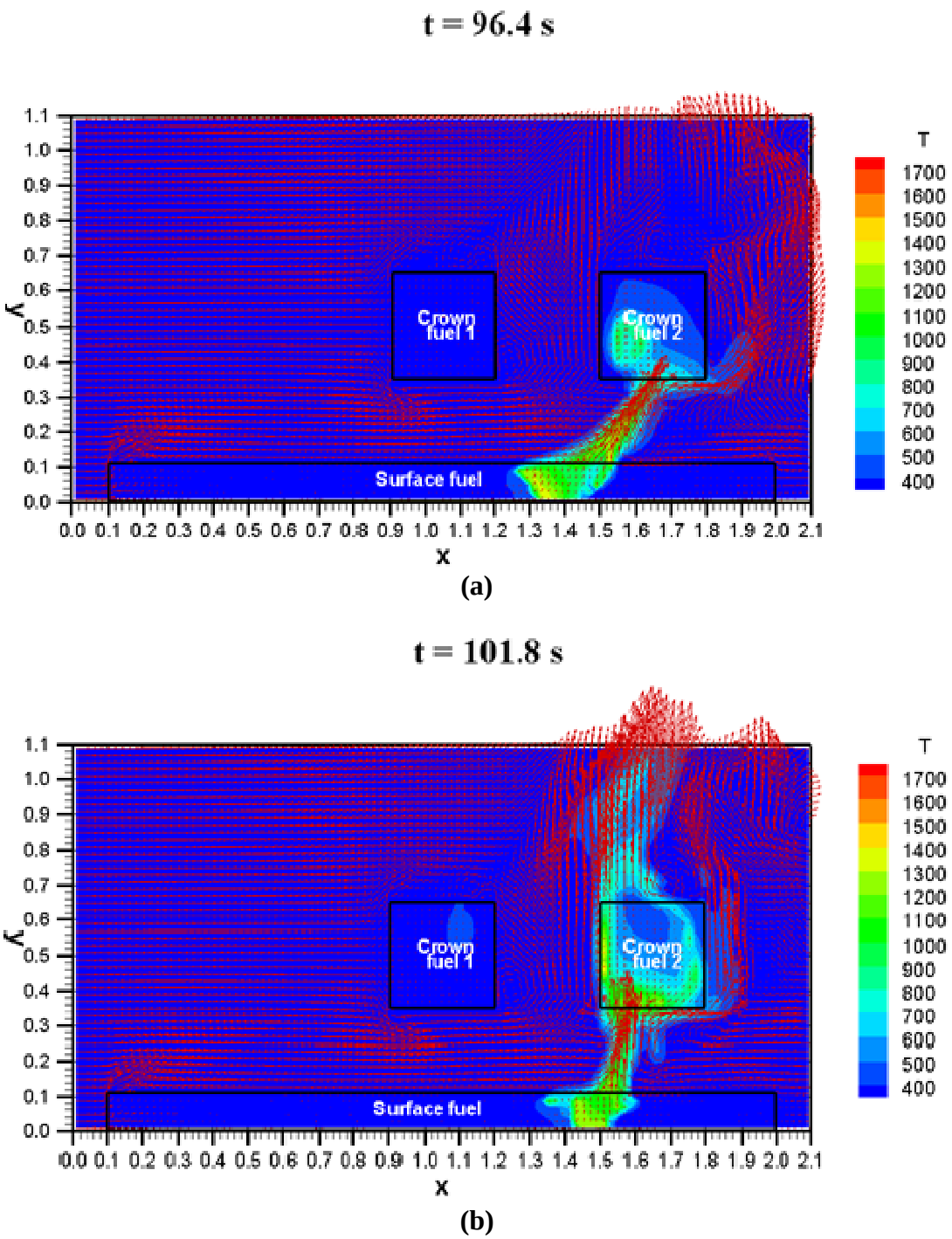


Figure 8.6: LES results at a midplane of air temperature and velocity field for a CSD of 30 cm at: (a) C2 ignition; t = 96.4 s. Instantaneous *R* is 1.4 cm/s and radiation energy transfer rate per unit volume between 1.7 m and 1.8 m is 5.5 kW/m^3; (b) C1 ignition; t = 101.8 s. Instantaneous *R* is 1.2 cm/s and radiation energy transfer rate per unit volume between 1.7 m and 1.8 m is 13.7 kW/m^3.

Discussion

Three fuel configurations are investigated at two distinct wind conditions. In all the cases investigated, except for one, crown 1 ignites before crown 2. In the 0.0 m/s wind speed cases the flame tilt angle does not play a major role in preheating unburned surface fuel. Fire propagation under no wind conditions is primarily driven by radiation heat transfer at the boundary of the combustion zone and unburned surface fuel within the surface fuel bed. The largest flame tilt angle of 10 ° occurs at a CSD of 30 cm. At times the flame tilt angle is negative occurring at a CSD of 20 cm with a flame tilt angle of negative 11°. It is shown that CSD affects the amount of heat that is transferred to the unburned fuels and the duration of the heat transfer process. At a CSD of 10 cm the average *R* after both crowns have ignited is higher than at a CSD of 20 and 30 cm by a factor of 2 and 1.5, respectively. The overall *R* at a CSD of 10 cm is greater than at a CSD of 20 cm and 30 cm by a factor of 1.1.

At a 0.8 m/s wind condition flame tilt angle plays a larger role in preheating unburned fuels. The average flame tilt angle in the region prior to crown 1 is 49°, 58° and 51° for CSD's of 10 cm, 20 cm and 30 cm, respectively. In the region after crown 1, the average flame tilt angle decreases to 47°, 34°, and 37° for CSD's of 10 cm, 20 cm and 30 cm, respectively. The decrease in flame tilt angle before the ignition of crown 2 causes *R* to decrease as the view factor between the propagating fire front and the unburned surface fuel also diminishes. After both crowns ignite, a larger quantity of heat impinges onto the unburned surface fuel resulting in an increase in *R*. A smaller CSD will result in

a larger *R*. At a CSD of 10 cm, average *R* is larger than at CSD of 20 cm and 30 cm by a factor of 1.1 and 1.7, respectively.

At a CSD of 30 cm, the combination of separation distance between crown fuels and the 0.8 m/s wind speed result in the ignition of crown 2 prior to crown 1. This development is due to the proximity of crown 1 to the initial flame source and the large flame tilt angle in the region prior to crown 1 that results in a small residence time in which the surface fire front transfers heat to crown 1. At CSD's of 10 cm and 20 cm, during the 0.8 m/s wind condition, the residence time is 60.4 s and 51.1 s, respectively. Residence time at a CSD of 30 cm is 38.7 s which is an insufficient amount of time to transfer enough heat to crown 1 to cause ignition before crown 2.

8.2 Flow Field between Crown Fuels

All Crown Fuel Configurations at a 0.0 m/s Wind Condition

An analysis is performed to determine how CSD affects vertical flow velocity between adjacent crown fuels. The analysis is performed for three CSD's of 10 cm, 20 cm and 30 cm at two distinct wind conditions of 0.0 m/s and 0.8 m/s. The flow field is investigated as the fire front propagates beneath crown 1 (region 1), through the area between crowns (region 2), and beneath crown 2 (region 3). The first study is performed for a CSD of 10 cm and a 0.0 m/s wind condition. Figure 8.7a demonstrates that as the fire front progresses through region 1, the hot gaseous products of combustion do not easily flow through crown 1 and are instead diverted to flow around it. The average

vertical velocity $\overline{U}_y$ is calculated to be 1.3 m/s with a maximum $U_{y,max}$ of 1.9 m/s as the hot gases flow around crown 1 and into the open area between the crown fuels.

Figure 8.7b shows the fire front propagating through region 2. The average vertical velocity $\overline{U}_y$ of the hot gaseous products of combustion is calculated to be 2.7 m/s with a $U_{y,max}$ of 3.4 m/s. As the fire front continues to propagate and advances through region 3, Figure 8.7c, $\overline{U}_y$ and $U_{y,max}$ are calculated to be 2.3 m/s and 2.8 m/s. The calculated vertical velocities through the area between the crown fuels is greater when the fire front is propagating through region 3 than through region 1, because as the fire front progresses through region 3, crown 1 or both crown 1 and crown 2 will be combusting resulting in an influx of ambient air through region 2 to fuel the combustion process occurring within crown 1 and/or crown 2.

The next analysis is performed at a CSD of 20 cm while maintaining wind constant at 0.0 m/s. The fire front reaches the leading edge of the first crown at t = 69.8 s and requires 40.1 s to traverse the span of region 1, Figure 8.8a. During this time, $\overline{U}_y$ is 0.7 m/s with a $U_{y,max}$ of 1.2 m/s. The fire front then continues to advance through region 2 with $\overline{U}_y$ of 2.3 m/s and a calculated $U_{y,max}$ of 2.7 m/s, Figure 8.8b. At t = 119.9 s the fire front arrives at the leading edge of region 3. The fire front propagates through region 3 in 25 s, Figure 8.8c. In the time that the fire front progresses through region 3, calculated $\overline{U}_y$ and U_{max} are 2.1 m/s and 2.5 m/s, respectively.

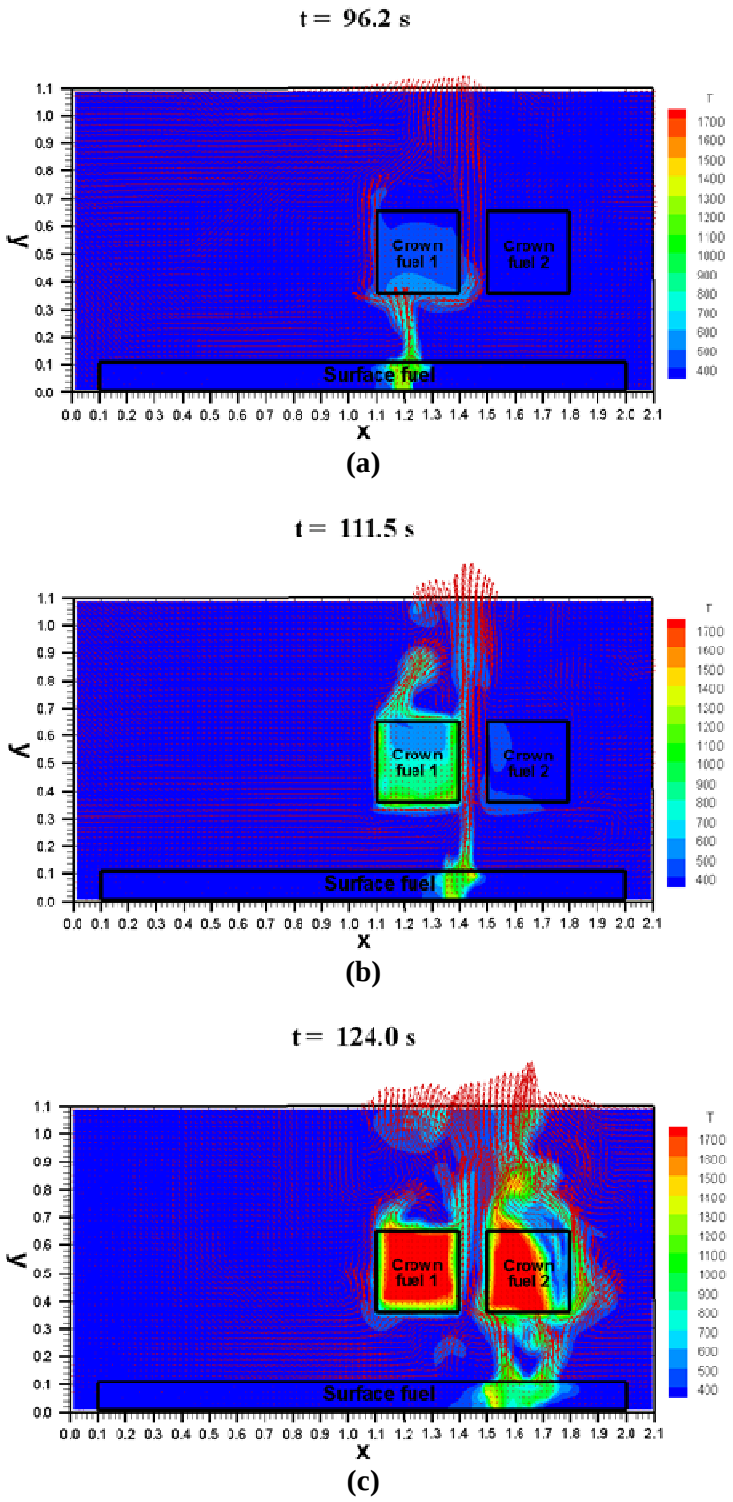


Figure 8.7: LES results at a midplane of air temperature and velocity field for a CSD of 10 cm and a 0.0 m/s wind condition as the fire front propagates: (a) beneath C1; (b) through area between C1 and C2; (c) beneath C2.

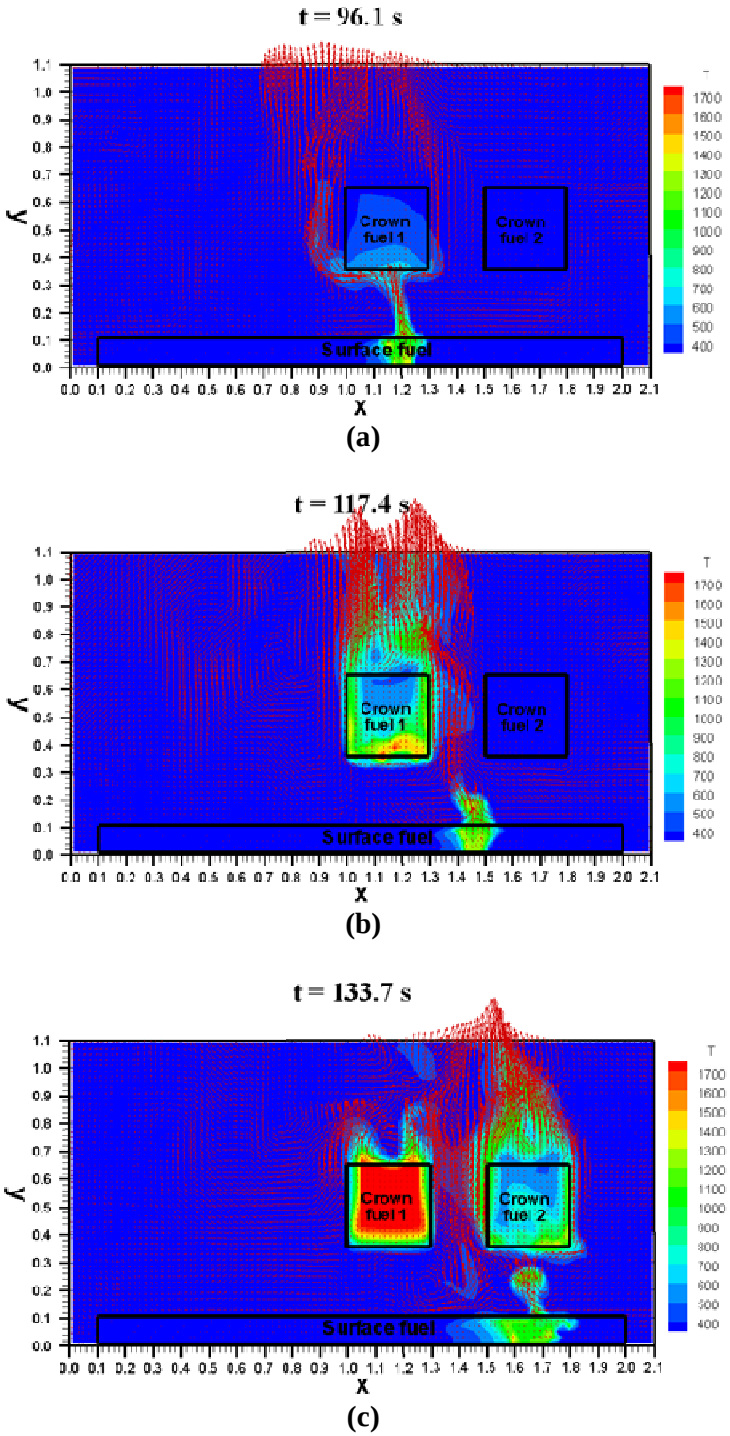


Figure 8.8: LES results at a midplane of air temperature and velocity field for a CSD of 20 cm and a 0.0 m/s wind condition as the fire front propagates: (a) beneath C1; (b) through area between C1 and C2; (c) beneath C2.

The final analysis performed at a wind condition of 0.0 m/s is for a fuel configuration consisting of a CSD of 30 cm. The fire front reaches the leading edge of crown 1 sooner than at CSD's of 10 cm, t = 72.7 s, and 20 cm, t = 69.8 s, as a result of the proximity of crown 1 to the initial ignition source. The fire front reaches region 1 at a time of 68.9 s.

The fire front requires 43.8 s to traverse the span of region 1. During the time in which the fire front propagates through region 1, Figure 8.9a, $\overline{U}_y$ is calculated to be 0.6 m/s while $U_{y,max}$ is 1.0 m/s. The fire front then advances through region 2 with a $\overline{U}_y$ of 1.6 m/s and a $U_{y,max}$ of 2.3 m/s, Figure 8.9b. As the fire front propagates the initial 10 cm through region 2, crown 1 ignites at t = 96.5 s. During crown 1 combustion, the fire front continues to advance through region 2 and into region 3. As the fire front progresses through region 3, Figure 8.9c, crown 2 ignites at t = 115.2 s and $\overline{U}_y$ and $U_{y,max}$ are calculated to be 2.1 m/s and 2.9 m/s, respectively.

All Crown Fuel Configurations at a 0.8 m/s Wind Condition

The next set of investigations is performed at a wind condition of 0.8 m/s and the CSD's studied are 10 cm, 20 cm, and 30 cm. A CSD of 10 cm is initially analyzed. The flames make contact with crown 1 at t = 50.4 s. The hot gaseous products of combustion do not easily flow through the crowns fuels, but instead are diverted to flow around the crown fuels, as was observed at a wind condition of 0.0 m/s. As the fire front propagates through region 1, Figure 8.10a, $\overline{U}_y$ and $U_{y,max}$ of the hot gaseous products of combustion flowing through the area between the crown fuels is calculated to be 1.1 m/s and 2.1 m/s, respectively.

A time of 60.4 s is required for the fire front to traverse the span of region 1. The hot gaseous products of combustion then directly enter region 2 where $\overline{U}_y$ is calculated to be 1.9 m/s and $U_{y,max}$ is computed to be 2.5 m/s, Figure 8.10b. At t = 52.7 s, the fire plume enters region 3. During the time the fire plume is progressing through region 3, Figure 8.10c, $\overline{U}_y$ and $U_{y,max}$ are calculated to be 2.1 m/s and 2.6 m/s, respectively. The plume requires 51.8 s to propagate through region 3.

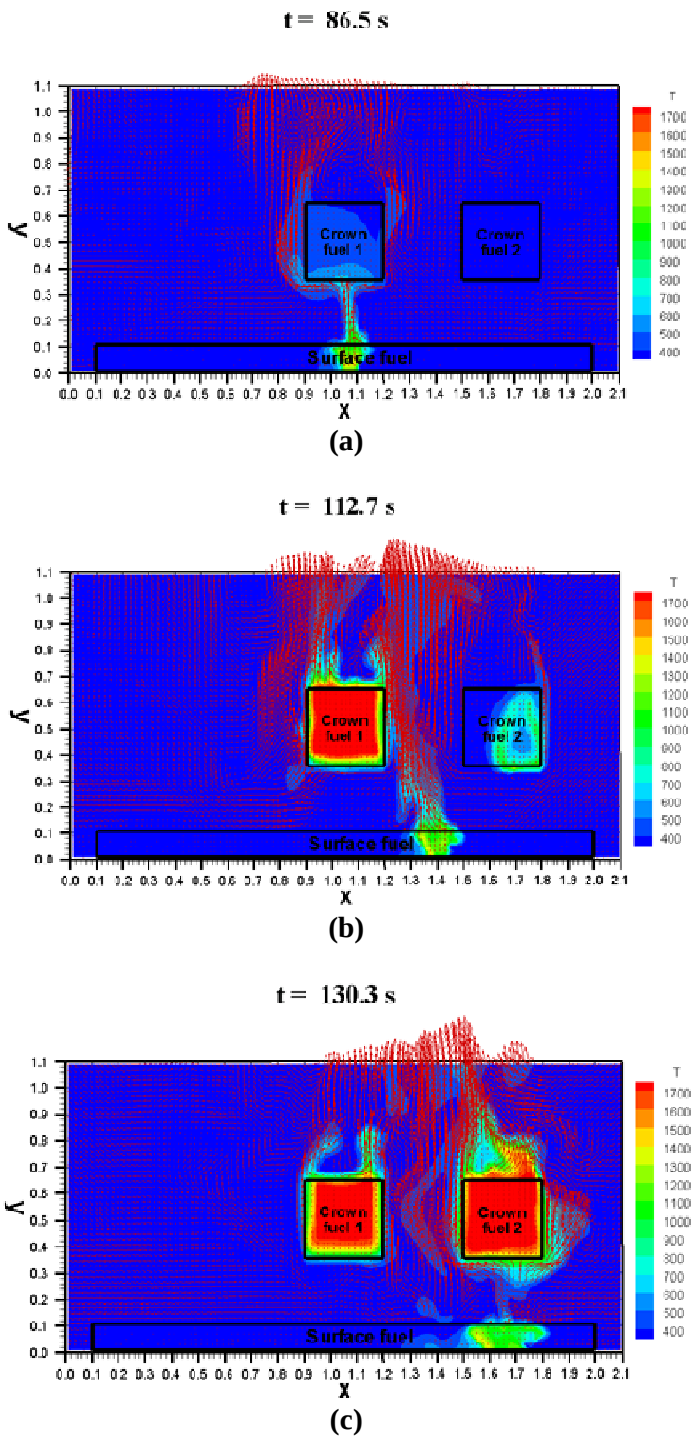
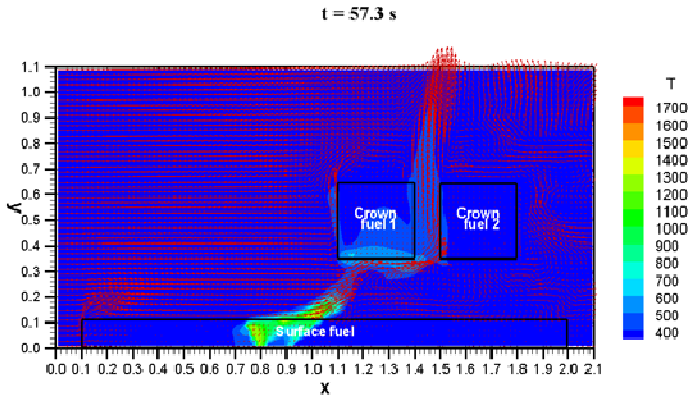
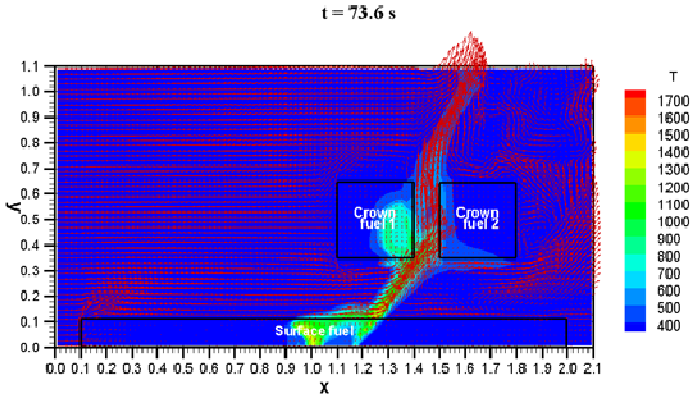


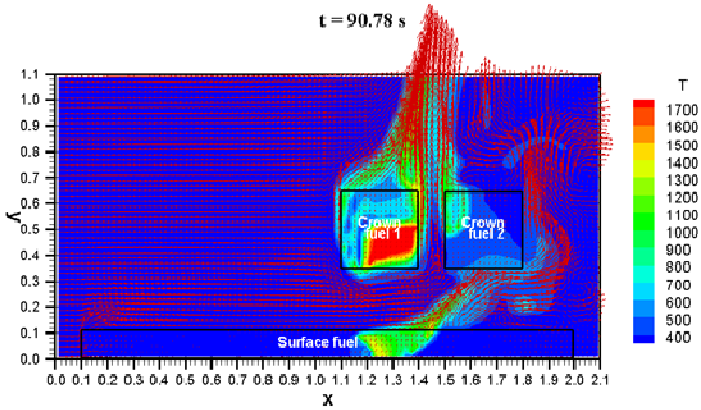
Figure 8.9: LES results at a midplane of air temperature and velocity field for a CSD of 30 cm and a 0.0 m/s wind condition as the fire front propagates: (a) beneath C1; (b) through area between C1 and C2; (c) beneath C2.



(a)



(b)

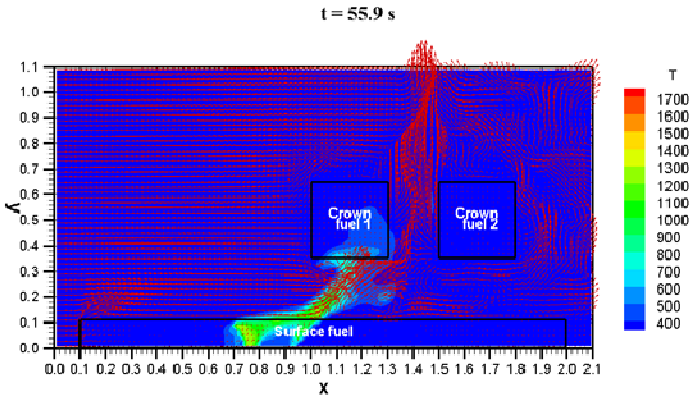


(c)

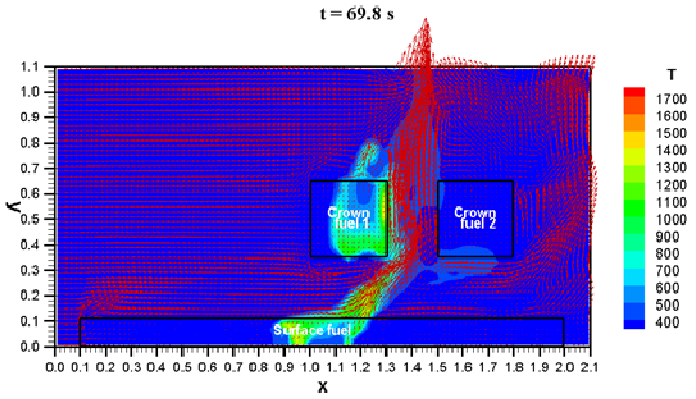
Figure 8.10: LES results at a midplane of air temperature and velocity field for a CSD of 10 cm and a 0.8 m/s wind condition as the fire plume propagates: (a) beneath C1; (b) through area between C1 and C2; (c) beneath C2.

The CSD is increased to 20 cm and the same analysis is implemented. The fire plume makes initial contact with crown 1 at t = 45.2 s. As the fire plume propagates through region 1(Figure 8.11a), which requires 51.5 s, $\overline{U}_y$ and $U_{y,max}$ are calculated to be 1.5 m/s and 2.5 m/s, respectively. The fire plume then proceeds to advance through region 2 (Figure 8.11b) and into region 3, where through region 2 $\overline{U}_y$ is computed to be 2.5 m/s and $U_{y,max}$ is calculated to be 3.0 m/s. Through region 3, Figure 8.11c, $\overline{U}_y$ and U_{max} are computed to be 1.7 m/s and 2.0 m/s, respectively.

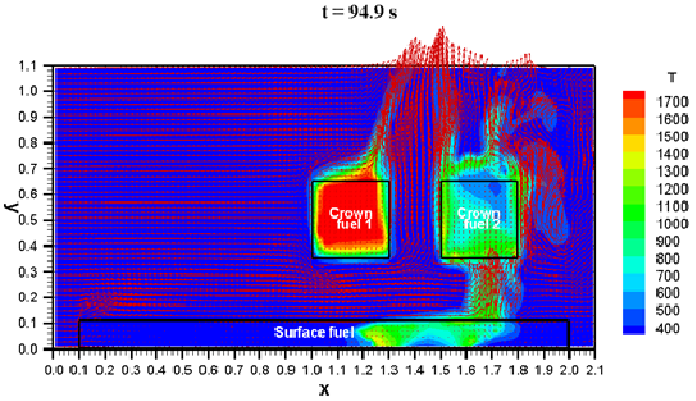
The final analysis is performed for a CSD of 30 cm. At t = 35.9 s, the fire plume make initial contact with crown 1. The fire plume then proceeds to propagate through region 1 (Figure 8.12a) which requires 38.7 s. Through region 1, $\overline{U}_y$ is calculated to be 1.1 m/s and $U_{y,max}$ is computed to be 1.8 m/s. The fire plume then advances towards region 3 through the 30 cm area between the crown fuels. Through region 2 (Figure 8.12b), $\overline{U}_y$ and $U_{y,max}$ are calculated to be 1.8 m/s and 3.1 m/s, respectively. The fire plume requires 58.2 s to propagate through region 3. $\overline{U}_y$ and $U_{y,max}$ are computed to be 1.1 m/s and 2.8 m/s, respectively, through region 3 (Figure 8.12c).



(a)

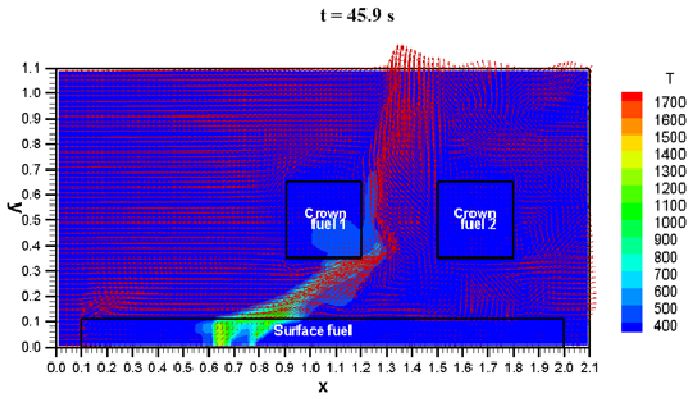


(b)

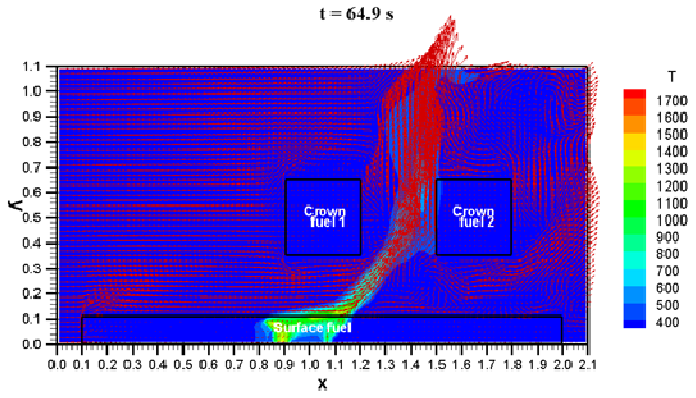


(c)

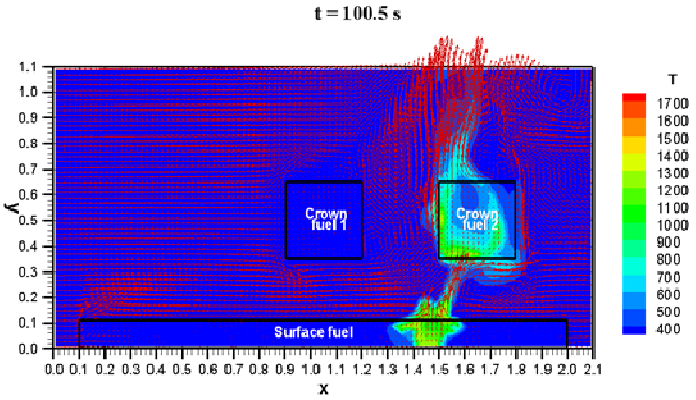
Figure 8.11: LES results at a midplane of air temperature and velocity field for a CSD of 20 cm and a 0.8 m/s wind condition as the fire plume propagates: (a) beneath C1; (b) through area between C1 and C2; (c) beneath C2.



(a)



(b)



(c)

Figure 8.12: LES results at a midplane of air temperature and velocity field for a CSD of 30 cm and a 0.8 m/s wind condition as the fire plume propagates: (a) beneath C1; (b) through area between C1 and C2; (c) beneath C2.

Discussion

An analysis is performed to investigate how CSD affects the flow of hot gaseous products of combustion between adjacent crown fuels. The analysis is performed for CSD's of 10 cm, 20, cm, and 30 cm at wind conditions of 0.0 m/s and 0.8 m/s. By observing the calculated maximum vertical velocities it is possible to determine what affect, if any, CSD has on the flow field. The first analysis was performed for a wind condition of 0.0 m/s.

The maximum vertical velocity $U_{y,max}$ through region 1 at a CSD of 10 cm, 20 cm, and 30 cm is 1.9 m/s, 1.2 m/s and 1.0 m/s, respectively. This order from greatest to least is also observed when calculated the average vertical velocity $\overline{U}_y$ within region 1. The same trend is also recognized when calculating $\overline{U}_y$ and $U_{y,max}$ through region 2 where $\overline{U}_y$ is 2.7 m/s, 2.3, m/s and 1.6 m/s while $U_{y,max}$ is 3.4 m/s, 2.7 m/s and 2.3 m/s for CSD's of 10 cm, 20 cm and 30 cm, respectively. A different trend is observed as the fire plume propagates through region 3.

It is observed that the hot gaseous products of combustion do not easily flow through the crowns fuels. Instead, the flow is diverted to flow primarily beneath the crown fuels, rising at the outer boundaries. All the dimensions that make up the area between the adjacent crown fuels are identical except for the distance between crowns (CSD). A small CSD results in a space between the crown fuels that has a small cross sectional area. For CSD's of 10 cm, 20 cm and 30 cm the cross-sectional area through which the hot gaseous products of combustion must flow through is 0.08 m^2, 0.16 m^2, and 0.24 m^2, respectively. A simple conservation of mass equation $\dot{m}_e = \dot{m}_i$ where

$\dot{m} \propto VA$ demonstrates that to conserve mass as the cross-sectional area decreases the flow velocity must increase. Thus, at a CSD of 10 cm with A = 0.08 m^2, $U_{y,max}$ should be the greatest, followed by a CSD of 20 cm then 30 cm. This trend differs as the fire plume traverses region 3 where $U_{y,max}$ is greatest at a CSD of 30 cm (2.9 m/s), followed by a CSD of 10 cm (2.8 m/s) then 20 cm (2.5 m/s). The difference can be attributed to the surface fire behavior through region 3 as crown 2 undergoes vigorous combustion. As crown 2 combusts the fire plume propagates 0.17 m into region 3 for a CSD of 20 cm, while the fire plume advances 0.12 m into region 3 for a CSD of 10 cm, and for a CSD of 30 cm the fire plume has progresses 0.1 m into region 3. For a CSD of 20 cm, the fire plume transfers heat to crown 2 for the remaining 0.13 m after crown 2 commences vigorous combustion. At a CSD of 10 cm, heat is transferred to crown 2 for the remaining 0.18 m, while for a CSD of 30 cm, heat is transferred to crown 2 for the remaining 0.2 m after crown 2 enter vigorous combustion. The additional quantity and duration of heat transfer to crown 2 from the surface fire causes crown 2 to burn more intensely for a longer period of time, thus entraining air at a greater velocity to fuel the combustion process occurring within the crown fuels.

For a wind condition of 0.8 m/s the results differs from those attained at a wind condition of 0.0 m/s. As the fire plume propagates through region 1, $U_{y,max}$ is 2.5 m/s, 2.1 m/s, and 1.8 m/s for CSD's of 20 cm, 10 cm, and 30 cm, respectively. Hot gaseous products of combustion that are unable to pass through crown 1 are diverted around the crown fuel and flow across the bottom of the crown towards the outer boundaries exiting region 1. At a CSD of 20 cm, the buoyancy of the hot gaseous products of combustion

that exit region 1 has sufficient space, 20 cm, to change the direction of the flow and flow vertically upward. For a CSD of 10 cm the flow that passes the outer boundaries of crown 1 and rises into the open area between the crown fuels exits region 1 with a maximum horizontal velocity $U_{x,max}$ of 2.31 m/s. As a result of the relatively high $U_{x,max}$, the hot gaseous products of combustion that exit region 1 strike the lower portion of the upstream face of crown 2. Flow speed decreases upon striking crown 2 and is then diverted to flow vertically upward. The resulting maximum vertical velocity $U_{y,max}$ is 2.1 m/s. Similarly to a CSD of 20 cm, at a CSD of 30 the buoyancy of the hot gaseous products of combustion that exit region 1 has sufficient space to change the direction of the flow and flow vertically upward. Since the flows at CSD's of 20 cm and 30 cm do not strike crown 2, as is the case at a CSD of 10 cm, the flow is not impeded. Applying the simple conservation of mass equation, it should follow that the flow through region 2 for a CSD of 10 cm should be the greatest followed by flow through region 2 for a CSD of 20 cm then 30 cm. But since the flow is impeded at a CSD of 10 cm, $U_{y,max}$ is greatest at a CSD of 20 cm then at 10 cm and final at 30 cm. The same hierarchy is observed for $\overline{U}_y$.

As the fire plume advances through region 2, crown 2 continues to impede the flow speed of the rising hot gaseous products of combustion. $U_{y,max}$ is 3.1 m/s, 3.0 m/s and 2.5 m/s for CSD's of 30 cm, 20 cm, and 10 cm. CSD of 10 cm, having the longest duration where the flow speed of the hot gaseous products of combustion is directly impeded by crown 2, has the lowest $U_{y,max}$ of 2.5 m/s. From the instant the fire plume enters region 2 to when it exits region 2, the flow of the hot gaseous products of

combustion is making direct contact with crown 2, thus causing the flow to change direction vertically and reducing flow speed. For the first 4 s that the fire plume advances through region 2, for a CSD of 20 cm, the flow is unhampered, but for the remaining 12.5 s required by the fire plume to propagate through the remaining portion of region 2, the hot gaseous products of combustion are directly impeded by crown 2 which results in a $U_{y,max}$ of 3.0 m/s. At a CSD of 30 cm, the flow of the hot gaseous products of combustion is unhindered for the first 12.6 second as the fire plume progresses through region 2. For the remaining 3.7 s before the fire plume exits region 2, the rising hot gaseous products of combustion are making direct contact with crown 2. The result is a $U_{y,max}$ of 3.1 m/s. The fire plume then enters region 3.

For the CSD's of 10 cm and 20 cm, as the fire plume advances through region 3, eventually both crown 1 and crown 2 are burning. The burning of both crown 1 and crown 2 simultaneously causes an influx of ambient air that fuels the combustion processes occurring within the surface and crown fires. In the case of a CSD of 10 cm, because the cross-sectional area through which the hot gaseous products of combustion and ambient air must flow through is smaller than for a CSD of 20 cm, U_{max} is greatest for a CSD of 10 cm (2.6 m/s) followed by a CSD of 20 cm (2.0 m/s). As the fire plume propagates through region 3, for a CSD of 30 cm, only crown 2 is combustion. Crown 1 did not ignite before crown 2 due to the high wind speed that caused the residence time between the surface fire front and crown 1 to reduce significantly. The burning of only crown 2 results in the entrainment of less ambient air than at CSD's of 10 cm and 20 cm, thus less intense crown fires and a lower $U_{y,max}$ of 1.7 m/s.

9 Conclusions and Future Work

The influence of horizontal separation distance between adjacent crown fuel matrices (CSD) on the transition process from surface fires to crown fires and on surface fire rate of spread in chaparral fuels is investigated experimentally and numerically. All experiments are conducted within the confines of a wind tunnel. Various measurement instruments such as a thermocouple system, digital weight scale, heat flux sensors, and a Particle Image Velocimetry system are used to analyze surface fire rate of spread, transition process from surface fire to crown fire, surface fuel mass loss rate, radiation and convection flux impingement onto the surface and crown fuels, and to investigate the flow field between adjacent crown fuels separated by a specified CSD. A Large Eddy Simulation (LES) model is used to further investigate the affect of horizontal separation distance between crown fuel matrices on the overall fire behavior in a multiple crown fuel environment.

9.1 Conclusions

The initial experiment baseline fuel configuration consists of only a surface fuel at three distinct wind conditions. Wind conditions investigated are 0.0 m/s, 1.1 m/s and 1.9 m/s. It is shown that at wind conditions of 0.0 m/s and 1.1 m/s surface fire front rate of spread (R) is quasi-steady as the fire front propagates along the surface fuel bed. At a 1.9 m/s wind condition R is unsteady. An analysis of fire front flame depth is performed and it is shown that at a wind condition of 1.9 m/s the fire front never achieves a steady flame depth as it propagates the full length of the surface fuel bed. The length of the fuel bed is

not sufficiently long to allow the flame depth to stabilize. This phenomena merits further investigation using a significantly longer fuel bed.

In all the remaining experiment fuel configurations for all the wind conditions, it is shown that *R* decreases as the fire front approaches crown 1. This decrease in *R* is a result of the reallocation of energy to preheat the fuel elements of crown 1 and the interference of heat flux impingement onto the unburned surface fuel by crown 1. The hindering of heat flux impingement causes a view factor reduction between the propagating fire front and the unburned surface fuel ahead of the fire front. *R* increases after crown 1 ignites which merges with the surface fuel fire front and propagates along the entire crown fuel matrix. The increase in *R* is a direct result of the addition of heat flux from the crown 1 fire that impinges on the unburned surface fuels in addition to the heat flux already impinging onto the unburned surface fuels from the surface fuel fire front. *R* decrease as the merged fire front approaches crown 2. The decrease in *R* is caused by the reallocation of energy to preheat the fuel elements of crown 2 and the interference of heat flux impingement onto the unburned surface fuel by crown 2. In all cases studied, except for a CSD of 30 cm and 1.9 m/s wind condition, *R* increase through the empty space between crown 1 and crown 2. Heat flux impingement onto the unburned surface fuel is unhindered through the empty space between crowns 1 and 2 allowing the surface fuels to be preheated resulting in an increase in *R*. As the merged surface fire front and crown 2 fire front proceed towards the downstream edge of the wind tunnel test section, *R* and $\dot{m}$ decrease. The decrease in *R* and $\dot{m}$ is attributed to the fire fronts exhausting the surface and crown fuel supply.

Utilizing a Particle Image Velocimetry system the flow field between adjacent crown fuel matrices is studied. The objective is to determine how the flow of the rising hot gaseous products of combustion from a propagating surface fire is influenced by the CSD between crown fuel matrices, and to study any fluid dynamic structures that may arise due to this CSD. Analysis of the PIV data demonstrates that the average horizontal entrainment velocity $\overline{U}_{ent}$ is greatest at a wind condition of 1.9 m/s than at a wind condition of 1.1 m/s and 0.0 m/s by a factor of 1.9 and 2.2, respectively. This same hierarchy applies to the average vertical velocity $\overline{U}_y$ where at a wind condition of 1.9 m/s $\overline{U}_y$ is shown to be greater than at a wind condition of 1.1 m/s and 0.0 m/s by a factor of 1.3 and 1.6, respectively. The propagating surface fire front tilts to a greater extent during a wind condition of 1.9 m/s than at the lower wind conditions of 1.1 and 0.0 m/s. The large flame tilt angle increases the view factor between the propagating surface fire front and the unburned surface fuels resulting in higher rates of spread, thus more intense fires which leads to ambient air entrainment with greater horizontal velocities and larger vertical velocities. Analysis of the fluid dynamic structures arising as a result of the CSD between crown fuel matrices indicates that the development of vortices only occurred at a crown separation distance of 10 cm. It is shown that vorticity is greatest during a wind condition of 1.9 m/s than at 1.1 m/s and 0.0 m/s by a factor of 3.1 and 7.9, respectively. Location and sizes of the resulting vortices demonstrates that these vortices do not contribute to the preheating of the unburned fuel.

Using a Large Eddy Simulation (LES) model, surface fire rate of spread (*R*), flame depth, and flame tilt angle from the vertical are calculated and compared to those

attained from experimentation. The two lowest wind conditions from the experiments (0.0 m/s and 1.1 m/s) are compared to the two lowest wind conditions from the LES models (0.0 m/s and 0.8 m/s). At a 0.0 m/s wind condition, the lowest difference between *R*'s is calculated to be 5% for a CSD of 30 cm with *R* being greater in the LES model results at 1.24 cm/s. The largest difference between *R*'s is calculated to be 18% for a CSD of 10 cm with *R* being greater in the LES model results at 1.32 cm/s. Flame depths and flame tilt angles between the LES models and the experiments vary by a much larger difference than was seen in *R* with the largest differences occurring when contrasting flame tilt angles. The flame tilt angles are calculated during the period before the fire front reaches the upstream edge of crown 1. Percent difference is calculated to be the greatest at a CSD of 20 cm at a difference of 188% with the largest flame tilt computed in the LES model results at 7°. The lowest difference is calculated to be 154% for a CSD of 10 cm with the greatest flame tilt angle being calculated from the LES model results at 5.3°. When contrasting flame depths between the experimental and numerical results, the greatest difference of 102% is computed at a CSD of 20 cm with the greatest flame depth occurring in the LES model results at 10.3 cm. The lowest difference is calculated for a CSD of 10 cm at 80% with flame depth being the greatest in the LES model at 9.9 cm. Although flame tilt angle and flame depth vary by larger percent differences, the resulting lower percent differences calculated for *R* demonstrate that at a 0.0 m/s wind condition the results from the experiments and from the LES models are comparable.

The next contrast between the experimental and LES results is performed at a wind condition of 1.1 m/s for the experiments and at 0.8 m/s for the LES model. The contrast is performed at these two different wind conditions to demonstrate that although wind speed is greater in the experiments than in the LES models by a factor of 1.4, the flame tilt angles calculated are greatest in the LES model when it is expected that flame tilt angle be the greatest under the wind conditions present in the experiments. The lowest difference between *R*'s is computed to be 26% for a CSD of 10 cm with *R* being greater in the experimental results at 2.15 cm/s. The largest difference in *R*'s is calculated to be 58% for a CSD of 30 cm with *R* being greater in the experimental results at 2.5 cm/s. When contrasting results for flame tilt angle, those which calculated from the LES model results are the greatest. The greatest percent difference is calculated at a CSD of 20 cm with a difference of 99% where the largest flame tilt computed is in the LES model results at 57.8°. The lowest difference is calculated to be 83% for a CSD of 10 cm with the greatest flame tilt angle being calculated from the LES model results at 48.8°. The large flame tilt angles calculated in the LES model in comparison to those attained from the experimental results suggest that wind speeds in the LES model should be greater than in the experiments, which is not accurate. Greater wind speeds lead to large flame tilt angles which then lead to larger view factors between the fire front and the unburned surface fuel. This results in greater heat transfer to the unburned fuels and increased combustion rate as a consequence, which then leads in greater *R* results. But as was previously presented, *R* is greatest in the experiments, but in the experiments flame tilt angle is the lowest even though wind speed is greater in the experiments. The lowest

difference between flame depth is calculated to be 130% for a CSD of 10 cm with flame depth being greater in the LES model results at 25.4 cm. The largest difference between flame depths is calculated as 141% for a CSD of 20 cm with flame depth being greater in the LES model results at 28.7 cm. The cause for these great difference merits further investigation to gain a greater understanding of the processes occurring under wind conditions.

9.2 Future Work

In this investigation numerous experiments are performed where the horizontal distance between adjacent crown fuel matrices is varied and studied at three distinct wind conditions. All the experiments discussed are conducted during a southern California winter season. To gain a better and in-depth understanding of fire behavior it is important to further investigate effects due to ambient conditions (e.g. relative humidity, ambient temperature, etc.), crown fuel properties (e.g. fuel moisture content) and variations in terrain conditions (e.g. slopes) on the surface fires to crown fires transition process and on surface fire rate of spread.

The Large Eddy Simulation model is utilized successfully to study fire behavior during no wind conditions in a multiple crown fuel environment, but when used to investigate fire behavior during wind conditions, the results generated by the model diverged from those attained by laboratory experimentation. To gain further insight as to the cause of the discrepancies between numerical and experimental results during wind

conditions, it is necessary to compare and contrast model and experimental results beginning with very basic configurations to increasingly complex configurations.

Bibliography

[1] Adrian, R.J. Review of Particle Image Velocimetry Research in The Symposium on Optical Methods in Flow and Particle Diagnostics, 6th International-Congress on Applications of Lasers and Electro-Optics. 1988, Optics and Lasers in Engineering **9**(3-4): 317-319: San-Diego, California, USA.

[2] Adrian, R. 1991. Particle image techniques for experimental fluid mechanics, Annual Review of Fluid Mechanics **23**: 261-304.

[3] Adrian, R., Yao, C. 1985. Pulsed laser technique application to liquid and gaseous flows and the scattering power of seed materials, Applied Optics **24**(1): 44-52.

[4] Albini, F. 1976. Estimating wildfire behavior and effects, USDA Forest Service, Intermountain Forest and Range Experiment Station, General Technical Report INT-30, pp. 92.

[5] Alexander, M.E. (1988) Crown Fire Thresholds in Exotic Pine Plantations of Australia, Ph.D. Thesis, Australian National University, Canberra, Australia.

[6] Alexander, M.E. Cruz, M. 2006. Evaluating a model for predicting active crown fire rate of spread using wildfire observations. Can. J. Forest Res. **36**: 3015–3028.

[7] Andersen, H.E., McGaughey, R.J., Reutebuch, S.E. 2005. Estimating forest canopy fuel parameters using lidar data, Remote Sens. Environ. **94**: 441–449.

[8] Andrews, P.L. 1986. BEHAVE: Fire Behavior Prediction System – BURN Subsystem, Part 1, USDA Forest Serv., Intermountain Res. Sta., Ogden, Utah, USA.

[9] Andrews, P.L., Queen, L.P. 2001. Fire modeling and information system technology, International Journal of Wildland Fire, **10**, 343–352.

[10] Babrauskas, V., Peacock, R.D. 1992. Heat release rate: the single most important variable in fire hazard, Fire Safety Journal **18**: 255-272.

[11] Barbour, M.G., Major J. 1990. Terrestrial Vegetation of California. Special Publication Number 6, California Native Plant Society, Sacramento, pp. 3-10.

[12] Ballantyne, A., Boon, D.J. 1976. Report 76/3, University of Southampton AASU.

[13] Blevins, L.G., Pitts, W.M. 1999. Modeling of bare and aspirated thermocouples in compartment fires, Fire Safety Journal **33**: 239-259.

[14] Bradstock, R.A., Gill, A.M. 1993. Fire in semi-arid, mallee shrublands: size of flames from discrete fuel arrays and their role in spread of fire, International Journal of Wildland Fire **3**(1): 3-12.

[15] Branbander, O.P., Gruzin, A.D., Grishin, A.M., Vdovina, O.A. 1989. Investigation of the conditions of transition of a surface forest fire to a crown fire, Combustion, Explosion, and Shock Waves **24**(4): 435-440.

[16] Brohez, S., Delvosalle, C., Marlair, G. 2004. A two-thermocouple probe for radiation corrections of measured temperature in compartment fires, Fire Safety Journal **39**: 399-411.

[17] Byram, G.M. 1959. "Combustion of Forest Fuels," in Forest fire control and use. K. P. Davis, Ed. McGraw_Hill: New York, 1959, pp. 61-89.

[18] Carrier, G.F., Fendell, F.E., Wolff, M.F. 1991. Wind-Aided Firespread across Arrays of Discrete Fuel Elements. I. Theory, Combustion Science and Technology **75**: 31-51.

[19] Catchpole, T., de Mestre, N. 1986. Physical models for a spreading line fire, Australian Forestry **49**(2), 102-111.

[20] Clark, T.L., Radke, L., Coen, J., Middleton, D. 1999. Analysis of Small-Scale Convective Dynamics in a Crown Fire Using Infrared Video Camera Imagery, J. Appl. Meteor. **38**, 1401–1420.

[21] Clements, C.B., Zhong, S., Bian, X., Heilman, W.E., Byun, D.W. 2008. First observations of turbulence generated by grass fires, J. Geophy. Res. **113, D22102.**

[22] Cohen J.D. 1986. Estimating Fire Behavior with FIRECAST: User's Manual, USDA General Technical Report PSW-90.

[23] Conard, S.G., Weise, D.R. 1998. Management of fire regime, and fire effects in southern California chaparral: lessons from the past and thoughts for the future. Pages 342-350 in Teresa L. Pruden and Leonard A. Brennan (eds.). Fire in ecosystem management: shifting the paradigm from suppression to prescription. Tall Timbers Fire.

[24] Countryman C., Philpot C. 1970. Physical characteristics of chamise as a wildland fuel, USDA Forest Service Research Paper PSW-66.

[25] Cox, G., Chitty, R. 1985. Some source-dependent effects of unbounded fires, Combustion and Flame **60**: 219-232.

[26] Crimmins, M.A. 2006. Synoptic climatology of extreme fire-weather conditions across the southwest United States, International Journal of Climatology, **26**(8): 1001-1016.

[27] Cruz, M., Alexander, M.E., Wakimoto, R.H. 2003. Assessing Canopy fuel stratum characteristics in crown fire prone fuel types of Western North America, International Journal of Wildland Fire **12**: 39–50.

[28] Cruz, M., Butler, B.W., Alexander, M.E. Forthofer, J.M., Wakimoto, R.H. 2006. Predicting the ignition of crown fuels above a spreading surface fire. Part I: model idealization, International Journal of Wildland Fire, **15**(1): 47-60.

[29] Cruz M., Butler, B.W., Alexander, M.E. 2006. Predicting the ignition of crown fuels above a spreading surface fire. Part II: model evaluation, International Journal of Wildland Fire, **15**(1): 61-72.

[30] Dentoni, M.C. 2001. Atmospheric and fuel conditions related to the Puerto Madryn Fire of 21 January, 1994, Meteorological applications **8**(3): 361-370.

[31] Durst, F., Pereira, C.F., Tropea, C. 1993. The Plane symmetric sudden-expansion flow at low Reynolds numbers, Journal of Fluid Mechanics **248**, 567-581.

[32] Emmons, H.W. 1964. Fire in the forest, Fire Research Abstracts and Reviews **5**(3): 163:178.

[33] Feidas, H. 2002. Temporal simulation of diurnal temperature and relative humidity evolution at a forested mountainous site in Attica, Greece, International Journal of Wildland Fire **11**(2): 95-106.

[34] Feingold, A. 1966. Radiant-interchange configuration factors between various selected plane surfaces, Proceedings of the Royal Society of London, Mathematical and Physical Sciences **292** (1428): 51-60.

[35] Fernandes, P.M. 2001. Fire spread prediction in shrub fuels in Portugal, Forest Ecology and Management **144**: 67-74.

[36] Finney, M.A. 1998. Farsite Users Guide and Technical Documentation, USDA Forest Serv. Res. Paper RMRS-RP-4.

[37] Finney, M.A., McAllister, S.S. 2011. A review of fire interactions and mass fires, Journal of Combustion **2011**, Article ID 548328, 14 pgs.

[38] Frandsen, W.H. 1991. Burning rate of smoldering peat, Northwest Science **65** (4): 166-172.

[39] Glass, M., Kennedy, I.M. 1977. An Improved Seeding Method for High Temperature Laser Doppler Velocimetry, Combustion and Flame **29**: 333-335.

[40] Grant I. 1997. Particle image velocimetry: a review. Journal of Mechanical Engineering Science **211**(1): 55-76(22).

[41] Green, L. 1981. Burning by prescription in chaparral, U.S. For. Serv. Pac. Southwest For. Range Exp. Stn. Res. Pap. GTR-PSW-51.

[42] Hamilton, D.C., Morgan, W.R. 1956. Radiant-interchange configuration factors, National Advisory Committee for Aeronautics, Technical Note **2836**, pgs. 110.

[43] Hawley, L.F. 1926. Theoretical consideration regarding factors which influence forest fires, Journal of Forestry **24(**7): 756-763(8).

[44] Hilbruner, M.W. (1988) Fire behavior modeling for burn prescription specification. MS thesis, Department of Forest and Wood Sciences, Colorado State University, Fort Collins, CO, USA.

[45] Hocker R., Kompenhans J. 1989. Some technical improvements of Particle Image Velocimetry with regards to its application in wind Tunnels. ICIASF: 545-554.

[46] Keane R, Adrian R. 1990. Optimization of particle image velocimeters. Part I: Double pulsed systems, Measurement Science and Technology **1**: 1202-1215.

[47] Keane R., Adrian R. 1992. Theory of cross-correlation analysis of PIV images, Applied Scientific Research **49**: 191-215.

[48] Keane, R.E., Reinhardt, E.D., Scott, J., Gray, K., Reardon, J. 2005. Estimating forest canopy bulk density using six indirect methods, Can. J. Forest Res. **35**: 724–739.

[49] Koo, E., Pagni, P.J., Weise, D.R., Woycheese, J.P. 2010. Firebrands and spotting ignition in large-scale fires, International Journal of Wildland Fire **19**: 818-843.

[50] Lai W., Bjorkquist D., Abbott M., Naqwi A. 1998. Video systems for PIV recording, Measurement Science and Technology **9**: 297-308.

[51] Leonard, B.P. 1979. A stable and accurate convective modeling procedure based on quadratic upstream interpolation, Comp. Meth. Appl. Mech. And Eng. **19**: 59-98.

[52] Lindenmuth, A.W., Davis, J.R. 1973. Predicting fire spread in Arizona's oak chaparral, USDA Forest Service, Rocky Mountain Forest and Range Experiment Station, Research Paper RM-101, pp. 19.

[53] Long, E., Hargrave, G., Jarvis, S., Justham, T., Halliwell, N. 2006. Characterization of the interaction between toroidal vortex structures and flame front propagation, J. Phys., Conference Series **45**: 104-111.

[54] Lozano, J., Tachajapong, W., Pan, H., Swanson, A., Kelley, C., Princevac, M., Mahalingam, S. 2008. Experimental Investigation of the Velocity Field in a Controlled Wind-aided Propagating Fire Using Particle Image Velocimetry. Presented at the 9th International Symposium on Fire Safety Science, Karlsruhe, Germany.

[55] Lozano, J., "Effects of Environmental Conditions on Fire Spread Dynamics," M.S. thesis, University of California Riverside, Riverside, CA, USA 2008.

[56] Lozano, J., Tachajapong, W., Weise, D.R., Mahalingam, S., Princevac, M. 2010. Fluid Dynamic Structures in a Fire Environment Observed in Laboratory Scale Experiments, Combustion Science and Technology **182**, 858-878.

[57] Luo, M. 1997. Effects of radiation on temperature measurement in a fire environment, Journal of Fire Science, **15**(6): 443-461.

[58] Marcelli, T. 2004. Fire spread across pine needle fuel beds: characterization of temperature and velocity distributions within the fire plume, Inter. J. Wildland Fire, **13**(1), 37-48.

[59] Marvin, D. 1972. Forest fuel accumulation – A growing problem, American Association for the Advancement of Science **177**(4044): 139-142.

[60] Meinhart C.D., Prasad A.K., Adrian R.J. 1993. A parallel digital processor system for particle image velocimetry, Measurement Science and Technology **4**: 619-626.

[61] Melling, A. 1997. Tracer Particles and Seeding for Particle Image Velocimetry, Measurement Science and Technology **8**: 1406-1416.

[62] Meroney, R.N. 2007. Fires in porous media: natural and urban canopies. In Gayev YA, Hunt JCR (eds) Flow and transport processes with complex obstructions. NATO Science Series 236. Springer.

[63] Merril, D.F. Alexander, M.E. 1987. Glossary of forest fire management terms. Fourth edition, Natl. Res. Counc. Can., Can. Comm. For. Fire Management, Ottawa, Ont. Publ. NRCC No. 26516, p91.

[64] Milling A., Whitelaw, J.H. 1973. Seeding of gas flows for laser anemometry, DISA Information **15**: 5-14.

[65] Modest M. F., Radiative Heat Transfer, McGraw-Hill, Inc., New York, 1993.

[66] Morvan, D., Tauleigne, V., Dupuy, J.L. 2002. Wind effects on wildfire propagation through a mediterranean shrub, In: Forest Fire Research and Wildland Fire Safety, Viegas (ed.), Millpress, Rotterdam.

[67] Nelson, R.J., Water Relations of Forest Fuels, In Johnson, E.A. Miyanishi, K., (eds.) Forest Fires: Behavior and Ecological Effects, Academic Press, San Diego, CA, USA, Chap. 4 (2001) 79-149.

[68] Ottmar, R.D., Sandberg, D.V., Riccardi C.L., Prichard, S.J. 2007. An overview of the Fuel Characteristic Classification System — Quantifying, classifying, and creating fuelbeds for resource planning, Can. J. Forest Res. **37**(12), 2383–2393.

[69] Parsons, R.A. 2006. FUEL3-D: a spatially explicit fractal fuel distribution model. Pp. 253-272. In Andrews, P.L., and Butler, B.W. (comps.) Fuels management—how to measure success: conference proceedings, USDA Forest Serv. Proc. RMRS-P-41, Ft. Collins, CO.

[70] Pastor, E., Zarate, L., Planas, E., Arnaldos, J. 2003. Mathematical models and calculation systems for wildland fire behavior, Progress in Energy and Combustion Science **29**, 139-153.

[71] Patankar, S.V., Numerical Heat Transfer and Fluid Flow, Hemisphere, New York, 1980.

[72] Pisaric, M.F.J. 2002. Long-distance transport of terrestrial plant material by convection resulting from forest fire, Journal of Paleolimnology **28**, 349-354.

[73] Philpot, C. 1977. Vegetative features as determinants of fire frequency and intensity, Proceedings of the Symposium on the Environmental Consequences of Fire and Fuel Management in Mediterranean Ecosystems, pp. 12-16.

[74] Pitts, W.M. 1991. Wind effects on fires, Progress in Energy and Combustion Science **17**, 83-134.

[75] Pokkunuri, P., "A Study of Turbulent Nonpremixed Hydrogen Combustion With Different Levels of Modelling and Computation," Ph.D dissertation, University of California Riverside, Riverside, CA, USA 2007.

[76] Potter, B.E. 1996. Atmospheric properties associated with large wildfires, International Journal of Wildland Fire **6**(2): 71-76.

[77] Pyne, S.J., Andrews, P.L., Laven, R.J. 1996. Introduction to Wildland Fire, 2nd ed. John Wiley & Sons, New York.

[78] Quénot G.M., Pakleza J., Kowalewski T. 1998. Particle image velocimetry using optical flow for image analysis. 8th International Symposium on Flow Visualization: 47.1 – 47.11.

[79] Raffel, M., Willert, C., Werely, S., Kompenhans, J. 1998. Particle Image Velocimetry: A practical Guide. Springer-Verlag: Berlin.

[80] Reuss, D.L., Bardsley, M., Felton, P.G., Landreth, C.C., Adrian, R.J. 1990. Velocity, vorticity, and strain rate ahead of a flame measured in an engine using particle image velocimetry. SAE Tech. Paper Ser. 900053, SAE Publications Group, Warrendale, Pa.

[81] Rothermel, R.C. 1972. A mathematical model for predicting fire spread in wildland fuels, USDA Forest Service Research Paper INT-115.

[82] Rothermel, R.C. 1983. How to predict the spread and intensity of forest and range fires, USDA Forest Serv., Intermountain Forest and Range Exp. Sta., General Technical Report INT-143.

[83] Rothermel R. C., Philpot C. W. 1973. Predicting changes in chaparral flammability, Journal of Forestry: 640-643.

[84] Santoni, P.A. 2006. Instrumentation of wildland fire: Characterization of a fire spreading through a Mediterranean shrub, Fire Safety Journal **41**(3): 171-184.

[85] Schoennagel, T., Veblen, T., Romme, W. 2004. The interaction of fire, fuels, and climate across rocky mountain forests, BioScience **54(**7): 661-676.

[86] Scott, J.H., Reinhardt, E.D. (2001) Assessing crown fire potential by linking models of surface and crown fire behavior. RMRS-RP-29, USDA Forest Service, Rocky Mountain Forest and Range Experiment Station, Fort Collins, Colorado.

[87] Silvani X., Morandini, F. 2009. Fire spread experiments in the field: Temperature and heat fluxes measurements, Fire Safety Journal **44**: 279-285.

[88] Sullivan, A.L. 2009. Wildland surface fire spread modeling, 1990-2007. 1: Physical and quasi-physical models, International Journal of Wildland Fire **18**: 349-368.

[89] Sullivan, A.L. 2009. Wildland surface fire spread modeling, 1990-2007. 2: Empirical and quasi-emperical models, International Journal of Wildland Fire **18**: 369-386.

[90] Sullivan, A.L. 2009. Wildland surface fire spread modeling, 1990-2007. 3: Simulation and mathematical analogue models, International Journal of Wildland Fire **18**: 387-403.

[91] Sun, L., "Experimental and Theoretical Investigation of Fire Behavior in Live Fuels," Ph.D dissertation, University of California Riverside, Riverside, CA, USA 2006.

[92] Swift, M., Heal, O., Anderson, J. 1979. Decomposition in Terrestrial Ecosystems, (University of California Press, Berkeley).

[93] Tachajapong, W., Lozano, J., Mahalingam, S., Zhou, X., Weise, D.R. 2008. An investigation of crown fuel bulk density effects on the dynamics of crown fire initiation in shrublands, Combustion Science and Technology, **180**(4), 593 – 615.

[94] Tachajapong W., "Understanding Crown Fire Initiation via Experimental and Computational Modeling," Ph.D dissertation, University of California Riverside, Riverside, CA, USA 2008.

[95] Taylor, S.W., Wotton, B.M., Alexander, M.E., Dalrymple, G.N. 2004. Variations in wind and crown fire behavior in a northern jack pine – black spruce forest. Can. J. For. Res. **34**: 1561-1576.

[96] Van Wagner, C.E. 1977. Conditions for the start and spread of crown fire, Can. J. For. Res. **7**, 23–34.

[97] Viegas, D.X. 2004. On the existence of a steady state regime for slope and wind driven fires, International Journal of Wildland Fire **13**: 101-117.

[98] Weber, R.O. 1991. Modeling fire spread through fuel beds. Progress in Energy and Combustion Science **17**, 67-82.

[99] Weise, D.R., Zhou, X., Sun, L., Mahalingam, S. 2005. Fire spread in chaparral-'go or no-go', Inter. J. Wildland Fires **14**: 99-106.

[100] Whitaker, S. 1972. Forced convection heat transfer correlations for flow in pipes, past flat plates, single cylinders, single spheres, and for flow in packed beds and tube bundles, AIChE Journal **18(**2): 361-371.

[101] Willert C.E., Gharib M. 1991. Digital particle image velocimetry, Experiments in Fluids **10:** 181-193.

[102] Williams, F.A. 2008. Mechanistic aspects of the scaling of fires and explosions. In Saito K (ed.), Progress in Scale Modeling. Springer. pp. 29-37.

[103] Williams, F.A. 2008. Modeling of combustion phenomena. In Saito K (ed.), Progress in Scale Modeling. Springer. pp. 179-195.

[104] Williams, R.J, Cook, G.D, Gill, A.M., Moore, P.H.R. 1999. Fire regime, fire intensity and tree survival in a tropical savanna in northern Australia, Austral Ecology **24**(1):50-59.

[105] Wolff, M.F., Carrier, G.F., Fendell, F.E. 1991. Wind-aided firespread across arrays of discrete fuel elements. II. Experiment, Combustion Science Technology **77**, 261-289.

[106] Zhou, M., Garner, C.P. 1995. Flame propagation and laminar burning velocity measurements in a cylindrical combustion chamber using particle image velocimetry. SAE Tech. Paper Ser. 952458, SAE Publications Group, Warrendale, Pa.

[107] Zhou X., Mahalingam S., Weise D.R. 2005. Modeling of marginal burning state of fire spread in live chaparral shrub fuel bed, Combustion and Flame **143** (3): 183-198.

[108] Zhou, X., Mahalingam, S., Weise, D.R. 2007. Experimental Study and Large Eddy Simulation of Effect of Terrain Slope on Marginal Burning in Shrub Fuel Beds, Proceedings of the Combustion Institute **31**: 2547-2555.

Appendix A – Summary of Experimental Data

Experiment No.	Date	Configuration	Wind (m/s)	RH %	Ta (°C)	R (cm/s)
1	Jan-11-2011	surface fuel only	0.0	na	na	1.0
2	Jan-11-2011	surface fuel only	0.0	na	na	1.0
3	Jan-11-2011	surface fuel only	0.0	na	na	1.0
4	Jan-11-2011	surface fuel only	0.0	na	na	0.9
5	Jan-11-2011	na	na	na	na	na
6	Jan-13-2011	crown 2	0.0	na	na	1.2
7	Jan-13-2011	crown 2	0.0	22	26	1.0
8	Jan-13-2011	crown 2	0.0	28	25	1.1
9	Jan-13-2011	crown 2	0.0	30	23	1.1
10	Jan-14-2011	C1NC2@30cm	0.0	25	26	1.5
11	Jan-14-2011	C1NC2@30cm	0.0	25	26	1.4
12	Jan-14-2011	crown 1	0.0	25	27	1.3
13	Jan-20-2011	crown 1	0.0	15	21	1.4
14	Jan-20-2011	C1NC2@30cm	0.0	15	21	1.2
15	Jan-20-2011	C1NC2@30cm	0.0	20	20	1.2
16	Jan-20-2011	C1NC2@30cm	0.0	25	18	1.2
17	Jan-20-2011	C1NC2@30cm	0.0	25	18	1.2
18	Jan-24-2011	C1NC2@20cm	0.0	26	24	1.2
19	Jan-24-2011	C1NC2@20cm	0.0	26	24	1.1
20	Jan-25-2011	C1NC2@20cm	0.0	28	25	1.3
21	Jan-25-2011	C1NC2@20cm	0.0	28	25	1.2
22	Jan-27-2011	C1NC2@10cm	0.0	16	26	1.4
23	Jan-27-2011	C1NC2@10cm	0.0	16	26	1.2
24	Jan-27-2011	C1NC2@10cm	0.0	16	26	1.1
25	Jan-31-2011	C1NC2@10cm	0.0	16	26	1.0
26	Feb-1-2011	C1NC2@10cm	1.9	41	21	4.5
27	Feb-1-2011	C1NC2@10cm	1.9	41	21	4.8
28	Feb-1-2011	C1NC2@10cm	1.9	41	21	5.1
29	Feb-1-2011	C1NC2@10cm	1.9	23	17	4.5
30	Feb-2-2011	C1NC2@20cm	1.9	8	18	3.9
31	Feb-2-2011	C1NC2@20cm	1.9	7	15	5.9
32	Feb-2-2011	C1NC2@20cm	1.9	10	13	4.8
33	Feb-2-2011	C1NC2@20cm	1.9	10	13	3.7
34	Feb-8-2011	surface fuel only	1.1	na	na	2.6
35	Feb-8-2011	surface fuel only	1.1	na	na	3.1
36	Feb-8-2011	surface fuel only	1.1	na	na	2.7
37	Feb-8-2011	surface fuel only	1.1	na	na	2.8

Table A.1: Summary of all experiment parameters and environment conditions; included are the overall rate of spread *R* values calculated for each experiment; na indicates that the specific data in question was not obtained; experiments 81 through 92 were conducted to capture only particle image velocimetry data but are included in the table for completeness.

Table A.1 continued…

Experiment No.	Date	Configuration	Wind (m/s)	RH %	Ta (°C)	R (cm/s)
38	Feb-9-2011	C1NC2@30cm	1.1	na	na	2.9
39	Feb-9-2011	C1NC2@30cm	1.1	na	na	2.6
40	Feb-10-2011	C1NC2@30cm	1.1	na	na	3.0
41	Feb-10-2011	C1NC2@30cm	1.1	na	na	2.9
42	Feb-10-2011	C1NC2@30cm	1.1	na	na	2.6
43	Feb-10-2011	na	na	na	na	na
44	Feb-10-2011	na	na	na	na	na
45	Feb-15-2011	C1NC2@30cm	1.9	na	na	na
46	Feb-15-2011	C1NC2@30cm	1.9	na	na	na
47	Feb-15-2011	C1NC2@30cm	1.9	na	na	4.9
48	Feb-17-2011	C1NC2@30cm	1.9	na	na	3.8
49	Feb-17-2011	C1NC2@30cm	1.9	na	na	4.6
50	Jan-17-2011	C1NC2@20cm	1.1	na	na	2.4
51	Jan-18-2011	C1NC2@20cm	1.1	na	na	2.4
52	Jan-18-2011	C1NC2@20cm	1.1	na	na	2.5
53	Jan-18-2011	C1NC2@20cm	1.1	na	na	2.5
54	Jan-18-2011	C1NC2@20cm	1.1	na	na	2.3
55	Jan-18-2011	C1NC2@20cm	1.1	70	14	2.5
56	Jan-22-2011	C1NC2@10cm	1.1	40	16	2.8
57	Jan-22-2011	C1NC2@10cm	1.1	51	13	2.5
58	Jan-23-2011	C1NC2@10cm	1.1	na	na	3.3
59	Jan-23-2011	C1NC2@10cm	1.1	53	14	2.9
60	Jan-23-2011	C1NC2@10cm	1.1	57	13	2.3
61	Jan-24-2011	crown 2	1.9	na	na	6.4
62	Jan-24-2011	crown 2	1.9	na	na	6.8
63	Jan-24-2011	crown 2	1.9	na	na	6.9
64	Jan-25-2011	crown 2	1.9	59	14	5.3
65	Feb-25-2011	surface fuel only	1.9	66	12	5.7
66	Feb-25-2011	surface fuel only	1.9	71	11	5.1
67	Mar-1-2011	crown 2	1.1	34	19	2.9
68	Mar-1-2011	crown 2	1.1	39	17	2.5
69	Mar-1-2011	crown 2	1.1	39	17	2.5
70	Mar-1-2011	crown 2	1.1	40	14	2.2
71	Mar-1-2011	surface fuel only	1.9	45	14	8.1
72	Mar-1-2011	surface fuel only	1.9	45	14	7.0
73	Mar-10-2011	crown 1	1.9	22	27	13.9
74	Mar-10-2011	crown 1	1.9	25	27	11.6

Table A.1 continued…

Experiment No.	Date	Configuration	Wind (m/s)	RH %	Ta (°C)	R (cm/s)
75	Mar-10-2011	crown 1	1.9	25	27	7.5
76	Mar-10-2011	crown 1	1.1	25	27	2.7
77	Mar-11-2011	crown 1	1.1	52	23	2.6
78	Mar-11-2011	crown 1	1.1	52	23	2.8
79	Mar-11-2011	crown 1	1.9	52	23	7.3
80	Mar-11-2011	crown 1	1.1	52	20	2.4
81	Mar-22-2011	C1NC2@20cm	1.9	na	na	na
82	Mar-22-2011	C1NC2@20cm	1.9	na	na	na
83	Mar-23-2011	C1NC2@20cm	1.9	na	na	na
84	Mar-23-2011	C1NC2@20cm	1.9	na	na	na
85	Mar-23-2011	C1NC2@20cm	1.9	na	na	na
86	Mar-23-2011	C1NC2@20cm	1.9	na	na	na
87	Mar-23-2011	C1NC2@20cm	1.9	na	na	na
88	Mar-24-2011	C1NC2@10cm	1.9	na	na	na
89	Mar-24-2011	C1NC2@10cm	1.9	na	na	na
90	Mar-24-2011	C1NC2@10cm	0.0	na	na	na
91	Mar-24-2011	C1NC2@10cm	0.0	na	na	na
92	Mar-24-2011	C1NC2@10cm	0.0	na	na	na

Heat Flux (HF) units = kW/m^2							
Experiment No.	Date	Configuration	Wind (m/s)	Crown 1 Combustion		Crown 2 Combustion	
				$HF_{max,total}$	$HF_{max,conv}$	$HF_{max,total}$	$HF_{max,conv}$
1	Jan-11-2011	surface fuel only	0.0	3.11	0.30		
2	Jan-11-2011	surface fuel only	0.0	2.32	0.23		
3	Jan-11-2011	surface fuel only	0.0	4.33	0.55		
4	Jan-11-2011	surface fuel only	0.0	2.27	0.27		
5	Jan-11-2011	na	na	na	na	na	na
6	Jan-13-2011	crown 2	0.0			11.58	1.25
7	Jan-13-2011	crown 2	0.0			10.36	1.04
8	Jan-13-2011	crown 2	0.0			13.67	1.36
9	Jan-13-2011	crown 2	0.0			17.37	1.65
10	Jan-14-2011	C1NC2@30cm	0.0	na	na	na	na
11	Jan-14-2011	C1NC2@30cm	0.0	na	na	na	na
12	Jan-14-2011	crown 1	0.0	4.67	0.48		
13	Jan-20-2011	crown 1	0.0	4.71	0.43		
14	Jan-20-2011	C1NC2@30cm	0.0	0.91	0.07	8.32	0.82
15	Jan-20-2011	C1NC2@30cm	0.0	1.08	0.12	9.21	0.85
16	Jan-20-2011	C1NC2@30cm	0.0	1.60	0.14	6.57	0.62
17	Jan-20-2011	C1NC2@30cm	0.0	1.50	0.14	9.77	0.93
18	Jan-24-2011	C1NC2@20cm	0.0	1.12	0.11	5.29	0.54
19	Jan-24-2011	C1NC2@20cm	0.0	1.31	0.11	6.23	0.63
20	Jan-25-2011	C1NC2@20cm	0.0	1.77	0.19	13.93	1.35
21	Jan-25-2011	C1NC2@20cm	0.0	1.39	0.14	7.46	0.78
22	Jan-27-2011	C1NC2@10cm	0.0	1.68	0.16	8.63	0.83
23	Jan-27-2011	C1NC2@10cm	0.0	1.98	0.18	7.16	0.67
24	Jan-27-2011	C1NC2@10cm	0.0	1.62	0.09	11.37	1.10
25	Jan-31-2011	C1NC2@10cm	0.0	1.58	0.14	8.35	0.96
26	Feb-1-2011	C1NC2@10cm	1.9	na	na	29.77	4.00
27	Feb-1-2011	C1NC2@10cm	1.9	na	na	27.65	4.07
28	Feb-1-2011	C1NC2@10cm	1.9	na	na	23.62	3.93
29	Feb-1-2011	C1NC2@10cm	1.9	na	na	23.61	3.92
30	Feb-2-2011	C1NC2@20cm	1.9	6.66	na	26.80	3.50
31	Feb-2-2011	C1NC2@20cm	1.9	6.30	na	24.14	3.66
32	Feb-2-2011	C1NC2@20cm	1.9	4.75	na	22.70	2.89
33	Feb-2-2011	C1NC2@20cm	1.9	5.65	na	28.02	3.35
34	Feb-8-2011	surface fuel only	1.1	4.98	1.90		
35	Feb-8-2011	surface fuel only	1.1	5.43	3.24		
36	Feb-8-2011	surface fuel only	1.1	5.59	1.05		
37	Feb-8-2011	surface fuel only	1.1	4.79	1.62		

Table A.2: Summary of all experiment heat flux measurements; na indicates that the specific data in question was not obtained; for surface fuel only configuration experiments the data in the table represents the maximum total and convection heat flux measured as the fire front propagated along the surface fuel bed with no crown fuels present; in the experiments 81 through 92 were conducted to capture only particle image velocimetry data but are included in the table for completeness.

Table A.2 continued…

Heat Flux (HF) units = kW/m^2							
Experiment No.	Date	Configuration	Wind (m/s)	Crown 1 Combustion		Crown 2 Combustion	
				$HF_{max,total}$	$HF_{max,conv}$	$HF_{max,total}$	$HF_{max,conv}$
38	Feb-9-2011	C1NC2@30cm	1.1	2.60	0.27	18.50	1.86
39	Feb-9-2011	C1NC2@30cm	1.1	2.58	0.27	13.56	2.13
40	Feb-10-2011	C1NC2@30cm	1.1	na	na	na	na
41	Feb-10-2011	C1NC2@30cm	1.1	3.06	0.33	18.10	1.94
42	Feb-10-2011	C1NC2@30cm	1.1	2.52	0.26	17.69	2.11
43	Feb-10-2011	C1NC2@30cm	1.1	na	na	na	na
44	Feb-10-2011	C1NC2@30cm	1.1	na	na	na	na
45	Feb-15-2011	C1NC2@30cm	1.9	na	na	na	na
46	Feb-15-2011	C1NC2@30cm	1.9	na	na	na	na
47	Feb-15-2011	C1NC2@30cm	1.9	3.20	0.69	18.82	3.10
48	Feb-17-2011	C1NC2@30cm	1.9	3.12	0.48	18.83	3.69
49	Feb-17-2011	C1NC2@30cm	1.9	4.57	0.89	15.52	3.13
50	Jan-17-2011	C1NC2@20cm	1.1	2.49	0.30	12.93	1.74
51	Jan-18-2011	C1NC2@20cm	1.1	3.23	0.43	17.42	2.14
52	Jan-18-2011	C1NC2@20cm	1.1	2.83	0.36	15.95	2.13
53	Jan-18-2011	C1NC2@20cm	1.1	3.07	0.38	17.60	2.13
54	Jan-18-2011	C1NC2@20cm	1.1	2.97	0.33	16.95	2.06
55	Jan-18-2011	C1NC2@20cm	1.1	2.67	0.34	12.02	1.78
56	Jan-22-2011	C1NC2@10cm	1.1	2.55	0.33	11.43	1.96
57	Jan-22-2011	C1NC2@10cm	1.1	2.75	0.34	9.91	1.56
58	Jan-23-2011	C1NC2@10cm	1.1	2.89	0.37	11.14	1.54
59	Jan-23-2011	C1NC2@10cm	1.1	3.10	0.38	14.71	1.82
60	Jan-23-2011	C1NC2@10cm	1.1	2.54	0.34	10.28	1.73
61	Jan-24-2011	crown 2	1.9			19.87	5.14
62	Jan-24-2011	crown 2	1.9			19.14	4.23
63	Jan-24-2011	crown 2	1.9			14.56	3.76
64	Jan-25-2011	crown 2	1.9			20.03	4.97
65	Feb-25-2011	surface fuel only	1.9	7.46	2.99		
66	Feb-25-2011	surface fuel only	1.9	9.32	3.79		
67	Mar-1-2011	crown 2	1.1			16.28	2.63
68	Mar-1-2011	crown 2	1.1			16.11	2.76
69	Mar-1-2011	crown 2	1.1			11.74	1.99
70	Mar-1-2011	crown 2	1.1			11.35	2.30
71	Mar-1-2011	surface fuel only	1.9	11.84	3.91		
72	Mar-1-2011	surface fuel only	1.9	8.83	3.21		
73	Mar-10-2011	crown 1	1.9	12.53	2.38		

Table A.2 continued…

Heat Flux (HF) units = kW/m^2							
Experiment No.	Date	Configuration	Wind (m/s)	Crown 1 Combustion		Crown 2 Combustion	
				$HF_{max,total}$	$HF_{max,conv}$	$HF_{max,total}$	$HF_{max,conv}$
74	Mar-10-2011	crown 1	1.9	12.77	2.38		
75	Mar-10-2011	crown 1	1.9	12.50	2.23		
76	Mar-10-2011	crown 1	1.1	6.60	0.97		
77	Mar-11-2011	crown 1	1.1	5.48	0.82		
78	Mar-11-2011	crown 1	1.1	5.88	0.91		
79	Mar-11-2011	crown 1	1.9	8.86	2.09		
80	Mar-11-2011	crown 1	1.1	4.69	0.69		
81	Mar-22-2011	C1NC2@20cm	1.9	na	na	na	na
82	Mar-22-2011	C1NC2@20cm	1.9	na	na	na	na
83	Mar-23-2011	C1NC2@20cm	1.9	na	na	na	na
84	Mar-23-2011	C1NC2@20cm	1.9	na	na	na	na
85	Mar-23-2011	C1NC2@20cm	1.9	na	na	na	na
86	Mar-23-2011	C1NC2@20cm	1.9	na	na	na	na
87	Mar-23-2011	C1NC2@20cm	1.9	na	na	na	na
88	Mar-24-2011	C1NC2@10cm	1.9	na	na	na	na
89	Mar-24-2011	C1NC2@10cm	1.9	na	na	na	na
90	Mar-24-2011	C1NC2@10cm	0.0	na	na	na	na
91	Mar-24-2011	C1NC2@10cm	0.0	na	na	na	na
92	Mar-24-2011	C1NC2@10cm	0.0	na	na	na	na

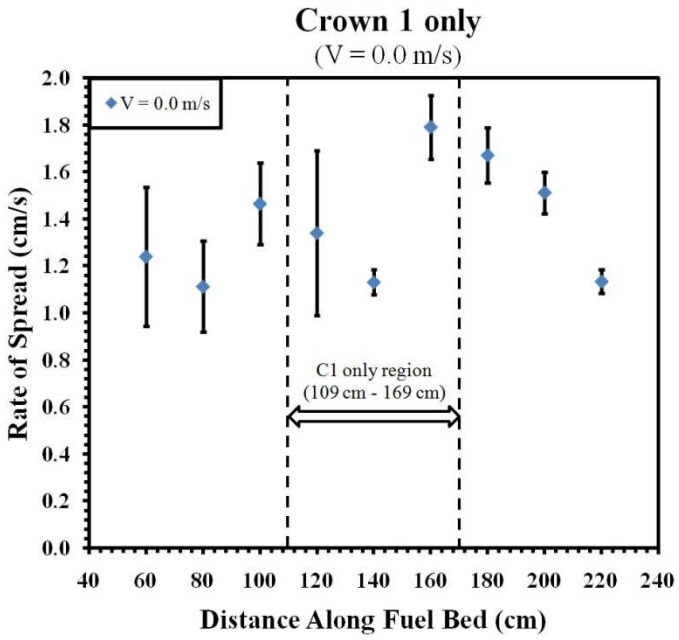
Configuration	Expt. No.	Entrainment when fire front is outside left ROI boundary		Vertical velocity when fire front is within ROI boundaries	
		$U_{ent,min}$ (m/s)	$U_{ent,mean}$ (m/s)	$V_{y,max}$ (m/s)	$V_{y,mean}$ (m/s)
V0_C1N2@10cm	90	-2.0	-0.3	na	na
	91	na	na	6.0	1.3
	92	na	na	5.9	1.3
AVERAGE		**-2.0**	**-0.3**	**6.0**	**1.3**
V1.1_C1N2@10cm	56	-2.0	-0.2	6.0	1.3
	57	-2.0	-0.3	6.0	1.5
	58	na	na	na	na
	60	-1.4	-0.2	6.0	1.6
AVERAGE		**-1.8**	**-0.3**	**6.0**	**1.5**
V1.1_C1N2@20cm	50	-2.0	-0.2	ns	ns
	53	-2.0	-0.3	6.0	1.3
AVERAGE		**-2.0**	**-0.3**	**6.0**	**1.3**
V1.1_C1N2@30cm	38	-2.0	-0.3	na	na
	39	na	na	6.0	2.1
	43	-2.0	-0.6	6.0	1.9
	44	-2.0	-0.4	6.0	2.1
AVERAGE		**-2.0**	**-0.4**	**6.0**	**2.1**
V1.9_C1N2@10cm	88	na	na	6.0	2.5
	89	na	na	6.0	1.7
	82	na	na	6.0	2.5
	83	na	na	6.0	2.2
AVERAGE		**na**	**na**	**6.0**	**2.2**
V1.9_C1N2@20cm	85	-1.1	-0.5	5.0	1.9
AVERAGE		**-1.1**	**-0.5**	**5.0**	**1.9**
V1.9_C1N2@30cm	46	-2.0	-0.8	6.0	2.2
	47	-2.0	-0.4	6.0	1.7
	48	na	na	6.0	2.1
AVERAGE		**-2.0**	**-0.6**	**6.0**	**2.0**

Table A.3: Summary of all experimental data captured using the particle image velocimetry system for the multiple crown fuel configurations for the CSDs of 10 cm, 20 cm and 30 cm for the three wind condition of 0.0 m/s, 1.1 m/s and 1.9 m/s; na indicates that the specific data in question was not obtained; table contains velocity data captured during the entrainment stage when the fire front is to the left of the ROI boundary and vertical velocity data during the period when the fire front is propagating within the ROI boundaries.

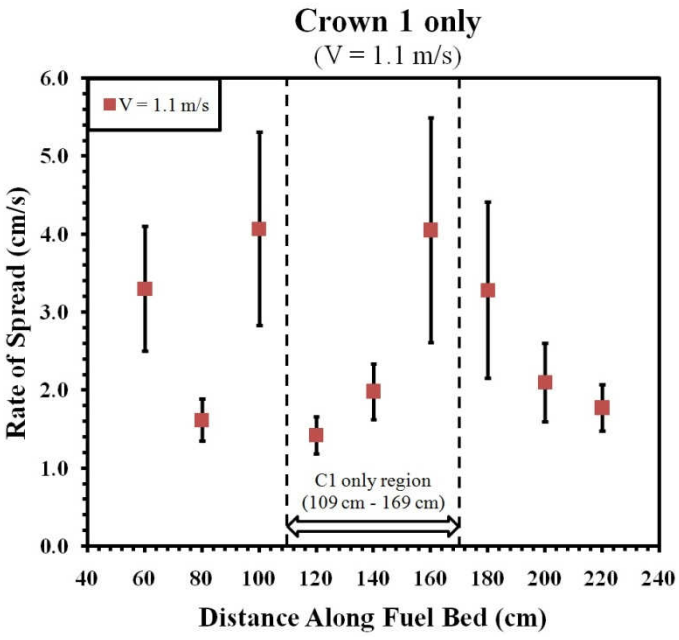
Crown 1 and Crown 2 Fuel Configuration at a CSD of 10 cm				
Wind (m/s)	**Experiment No.**	**Image No.**	**Vortex Diameter (cm)**	**Vorticity (1/s)**
0.0	90	31	2.1	19.8
	91	108	2.1	65.0
	90	96	3.2	20.9
	90	7	3.6	14.9
1.1	57	39	1.7	60.5
	60	53	1.7	95.0
	60	93	1.8	88.7
	56	119	1.9	76.0
	57	123	2.1	34.3
	60	102	2.1	130.6
	57	16	2.5	46.1
1.9	88	11	1.5	238.1

Table A.4: Summary of all the vorticity data obtained using the particle image velocimetry system; vortices were only observed in the multiple crown fuel configuration at a CSD of 10 cm; the table shows the experiment and the corresponding image in which a vortex was observed and the vortex diameters and vorticity values calculated.

Appendix B – Rate of Spread Plots with Standard Deviation Error Bars



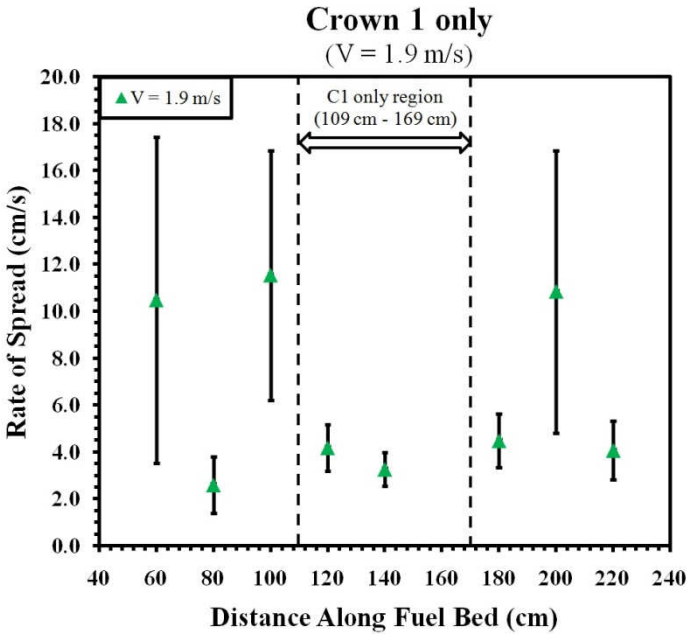
(a)



(b)

Figure B.1: Rate of spread plots with standard deviation error bars for a surface fuel and crown 1 configuration for the three wind speed cases of: (a) 0.0 m/s; (b) 1.1 m/s; and (c) 1.9 m/s.

Figure B.1 continued…



(c)

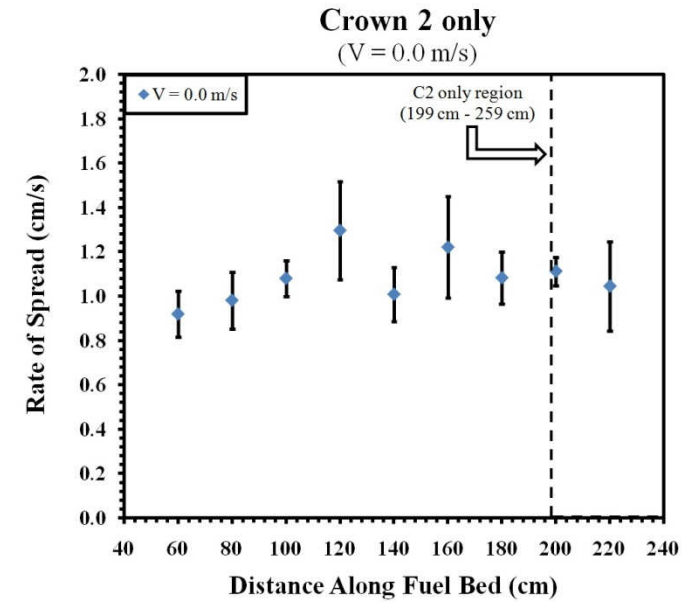
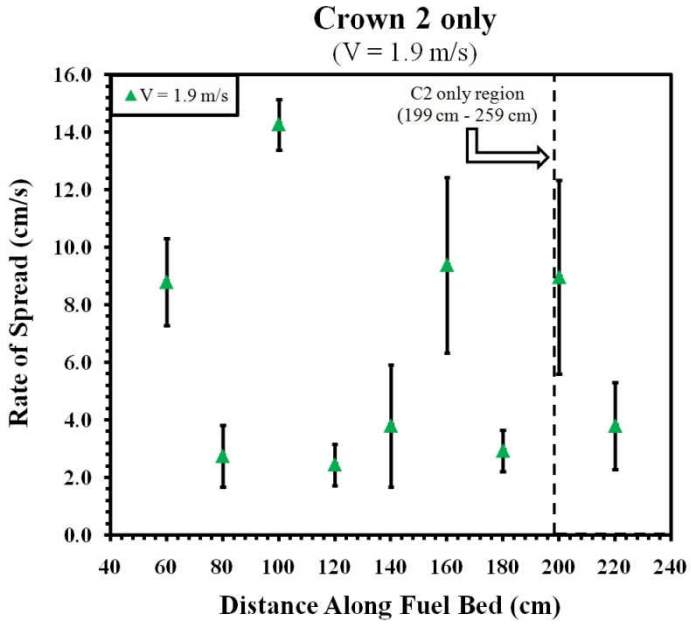
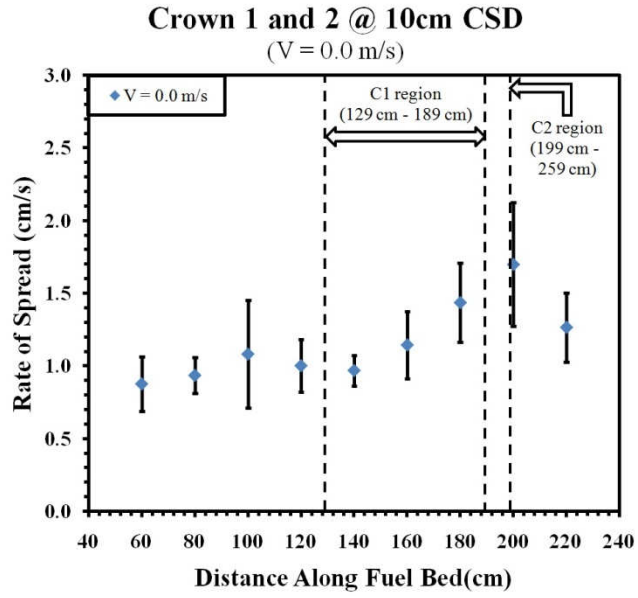


Figure B.2: Rate of spread plots with standard deviation error bars for a surface fuel and crown 2 configuration for the three wind speed cases of: (a) 0.0 m/s; (b) 1.1 m/s; and (c) 1.9 m/s.

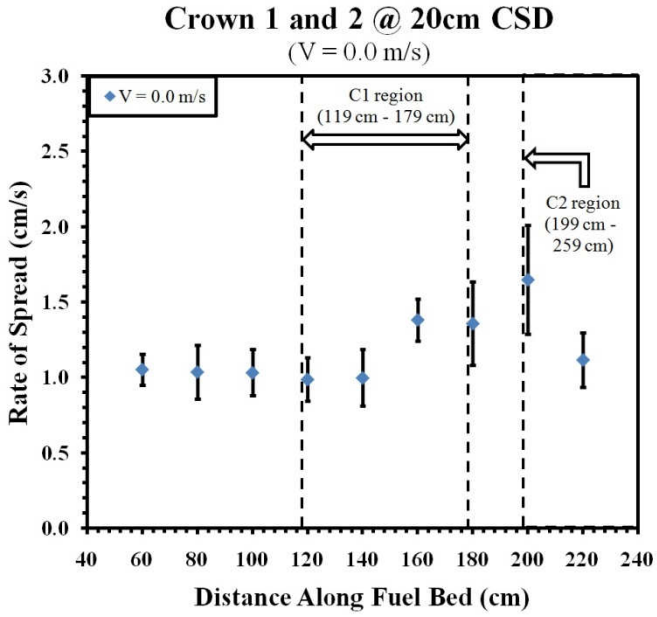
Figure B.2 continued…



(c)



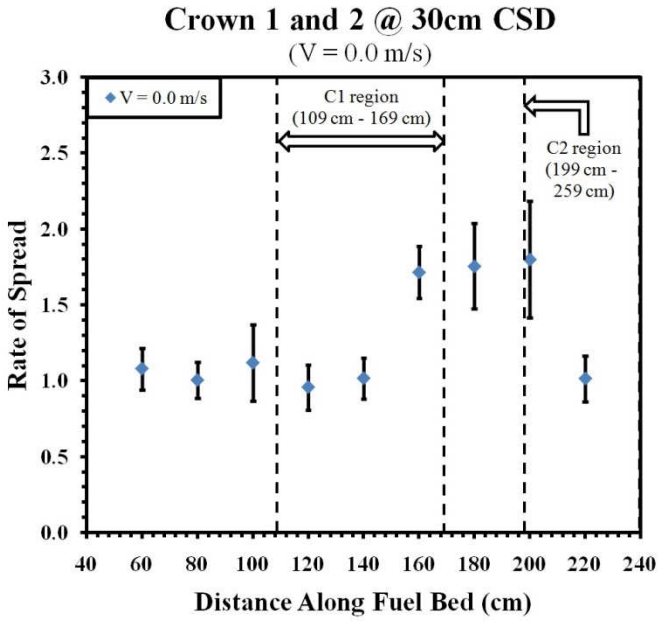
(a)



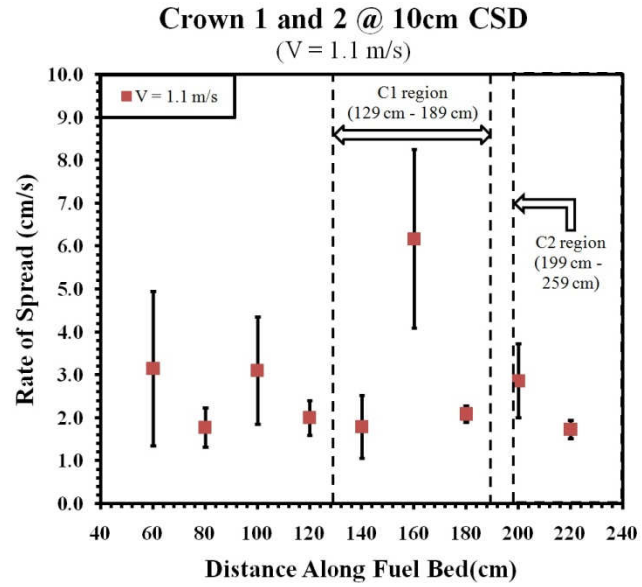
(b)

Figure B.3: Rate of spread plots with standard deviation error bars for a crown 1 and 2 configuration for a wind speed case of 0.0 m/s at a CSD of: (a) 10 cm; (b) 20 cm; and (c) 30 cm.

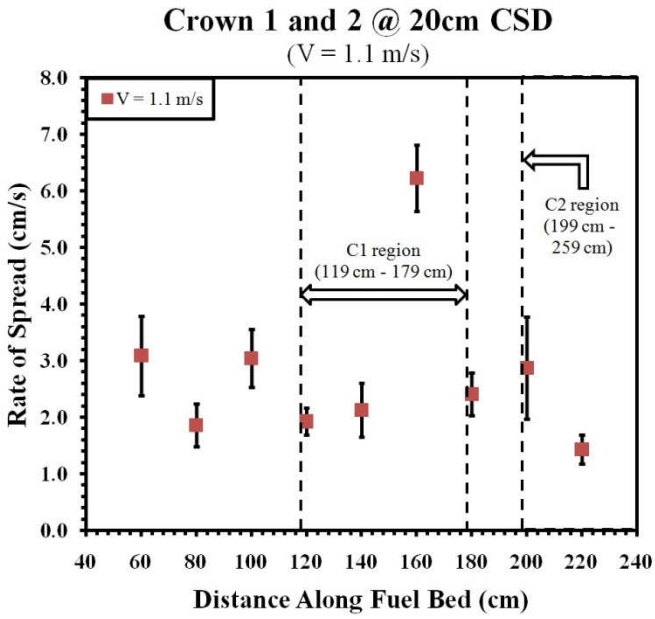
Figure B.3 continued…



(c)



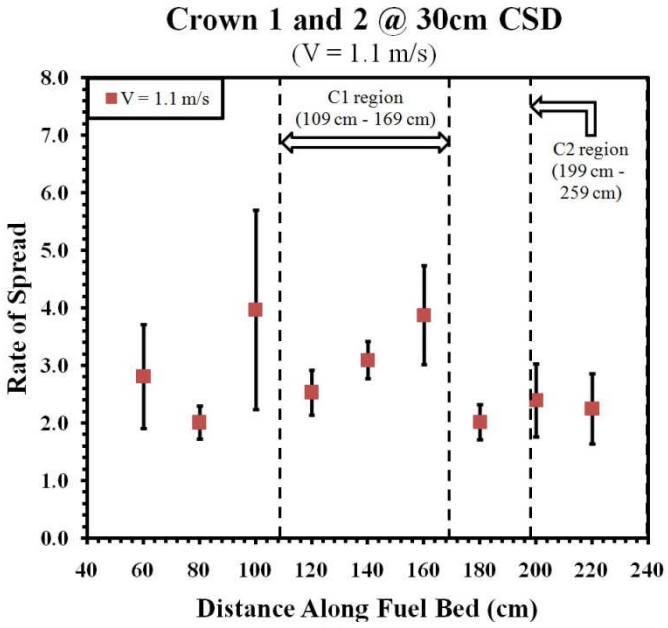
(a)



(b)

Figure B.4: Rate of spread plots with standard deviation error bars for a crown 1 and 2 configuration for a wind speed case of 1.1 m/s at a CSD of: (a) 10 cm; (b) 20 cm; and (c) 30 cm.

Figure B.4 continued…



(c)

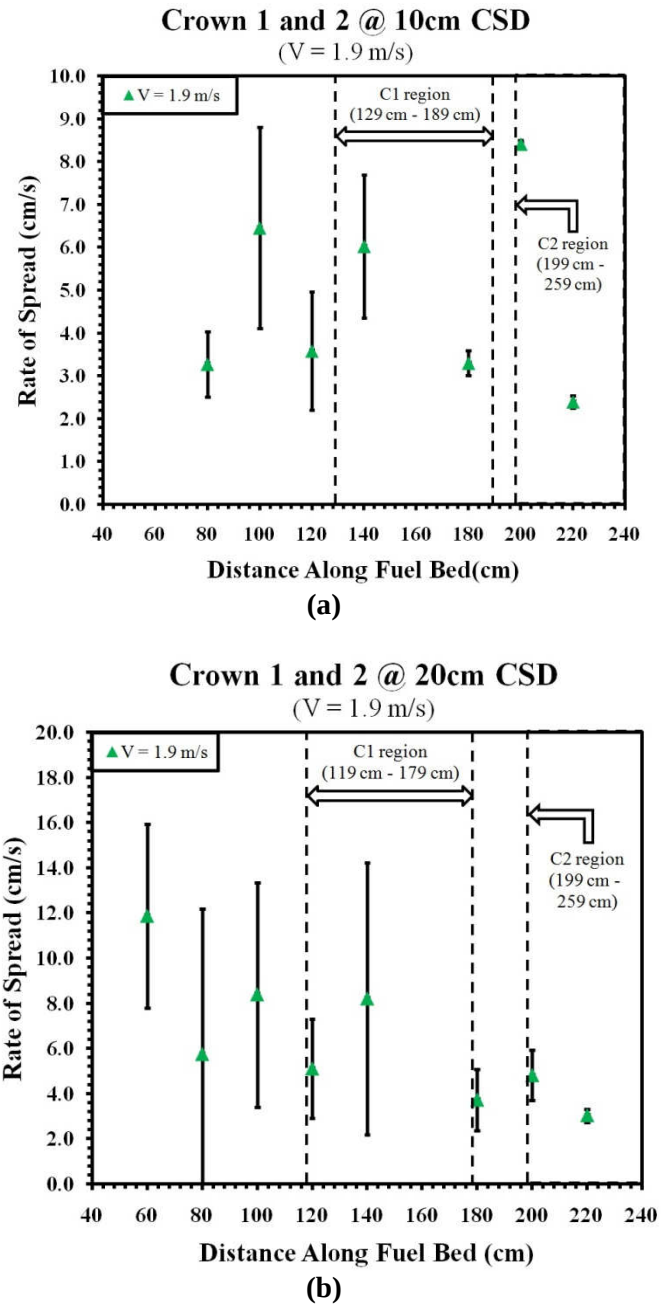
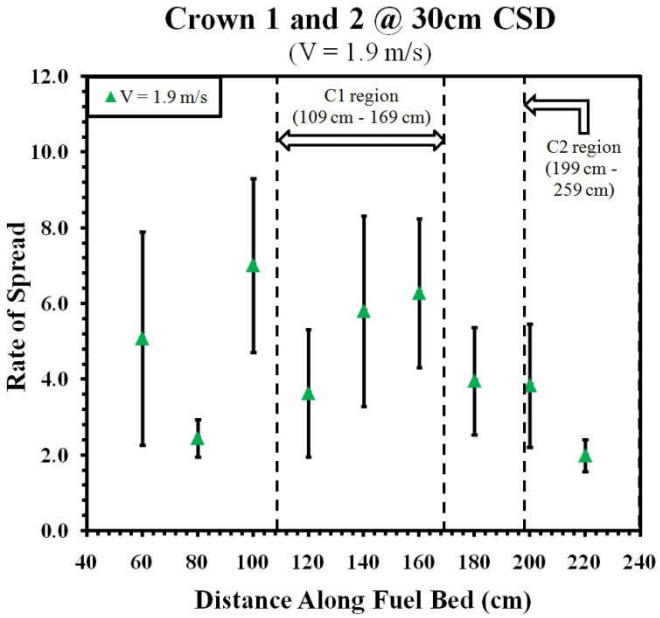


Figure B.5: Rate of spread plots with standard deviation error bars for a crown 1 and 2 configuration for a wind speed case of 1.9 m/s at a CSD of: (a) 10 cm; (b) 20 cm; and (c) 30 cm.

Figure B.5 continued…



(c)